

**IRON NANOPARTICLES
AS MAGNETIC RESONANCE IMAGING
CONTRAST AGENTS**

By

Peter Maurer Ferguson

A thesis

submitted to the Victoria University of Wellington
in fulfilment of the requirements for the degree of
Doctor of Philosophy
in Biomedical Science

Victoria

UNIVERSITY OF WELLINGTON

*Te Whare Wānanga
o te Ūpoko o te Ika a Māui*



Victoria University of Wellington

2011

Dedication

This thesis is dedicated to Martha Goffe Lane and Ian Henry Drummond Ferguson.

As science teacher and citizen soldier, they set examples of determination and a love for learning through which this campaign was realized.

Acknowledgments

This project has been a great leap into the unknown for me.

My supervisors, Ian and Richard, deserve a lot of credit for giving me everything I needed to succeed in this endeavour- strategic vision, support with funding and excellent supervision. They kept faith that I could keep this project afloat on a sea of uncertainty, and knowledge of their belief in me was a strong motivation to succeed. Ian, you never failed to inject enthusiasm and ideas into our weekly meetings and I always left your office feeling uplifted, even after I figured out how much work I was in for! I maintain that I would not have enrolled in this PhD without you as my supervisor and this was the best decision I made. Richard, from our first meeting you have taught me a strategic approach to science and without you none of this project would have existed. I am truly grateful.

Kirk Feindel and Mark Hunter taught me everything I know about NMR, and Bradley Douglass taught me the other 100% (just ask him). It was a great pleasure working with you chaps and I felt welcome in the NMR group from the beginning. It was a very inspiring time to be amongst Sir Paul Callaghan and the Magritek team, and I count myself blessed.

Angie Slocombe has been the guardian angel of this project and she managed to work miracles on a regular basis in providing access to and operation of the clinical scanner. You are a great friend and a true professional. I miss our Thursday night mice sessions already! Matthew MacKay and Trudy Wignall are both brilliant radiologists with a very busy clinical load who gave selflessly of their time and effort to this research.

David Flynn gave me great support with electron microscopy and we lost our youth looking for Nippo worms on Cryo-SEM. We did capture some centrefold images of the little blighters in the end and what fun.

My time at the Malaghan was transformational and there are many people to thank. Graham Le Gros is a passionate leader who is an excellent role model of how a career scientist can effectively run an institute with excellence and vision. I am very grateful to Bridget Stocker and Jacquie Harper for their advice and support. Franca Ronchese shared her wisdom on dendritic cells with generosity and grace. Mike Berridge is a living, breathing science machine who is always up for a stimulating chat on any aspect of biomedical science. Nina Dickgreber and Dianne Sika-Paotonu are patient, effective

tutors and great friends, teaching me everything from using a pipette to making up DCs. Lindsay Ancelet kept me fit and sane. Rob Weinkove and Collin Brooks would dive headlong into a deeply explorative dialogue which could often develop into a night on the lash with a running science commentary - this is a singular pleasure in which I hope we can continue to indulge.

Professors John Carter and Brett Delahunt have selflessly acted as my mentors, encouraging and supporting me to strive for research excellence alongside clinical practice. I am truly grateful for their continued support and guidance.

My family have been a source of continual support and encouragement. Mum and Dad have been very understanding of my need to pursue my dreams in yet another unexpected direction, and their love remains without condition. My brother has always blazed the way forwards. Davey, you made it to Mars with your PhD and I made it to Newtown. I've told you 61 times that when the big fish wriggles out of the pond, he gets swilled by the shark.

To the Arden Street gentlemen: I may have been the the last one to get a PhD but I was the first to RDS; a big bladow to you sirs. To Matthew McDonald: 10 years on and we are still drinking crates of Tui and browsing sherms but now we also fly kites.

I would like to thank GBH-G, the Lord of Misrule, Moz, Croz, Big Hame, Rees "danger-train" Ward, Piley, The Archdeacon, The Dutchman, FDR, Panther, Pearlips, Buckets, Scooby, the Bishop of Fools, the Colonel, Amplexus (retired), Boydie, Craig, Carlos and The Captain's Bar at the Mandarin Oriental in Hong Kong- at the end of it all we should get an apartment and move in together. I miss your musk.

Thank you to my ever-present companions: Leopold and Stephen, Orr and Yossarian, Marcel and Charlus, Faustus and Mephistopheles, Don and Sancho. Let's stay in touch.

And finally, the ultimate thank you goes to my wife, Lina, who has been there through it all. Thank you for trying to talk me out of doing a PhD, and when I persisted, thank you for bringing in dinners and bottles of stout to keep me going. But above all, thank you for the greatest gift ever, the delivery of our precious daughter Ciara.

你们是我的宇宙!

Abstract

Magnetic nanoparticles are effective in a range of biomedical applications including magnetic resonance imaging (MRI) contrast enhancement. The efficacy of nanoparticles as contrast agents depends mainly on the surface chemistry and magnetic properties of the particles, with a large magnetic moment inducing efficient transverse (T_2) relaxation of protons. This results in improved negative enhancement of MRI contrast on T_2 weighted sequences. Iron oxide nanoparticles (FeOx NPs) have been used in MRI for 20 years and are the only commercially available T_2 contrast agents. A significantly larger magnetic moment can potentially be achieved with iron nanoparticles (Fe NPs), but development has been hampered by difficulty in preparing stable particles. In this study, stable Fe NP were prepared by a novel, simple, synthesis and compared with FeOx NP as T_2 contrast agents in a range of MRI-based biomedical applications.

The effectiveness of Fe NPs versus FeOx NPs to negatively enhance MRI contrast on T_2 weighted sequences was first examined in vitro. The Fe NPs and FeOx NPs were characterised by electron microscopy and found to be of similar size (16nm). The Fe NPs possessed a core of highly magnetic α -Fe inside a 3nm shell of FeOx of the same crystal structure as the pure FeOx NPs. Both types of NP were coated with the same molecule, DMSA, to produce aqueous dispersions with similar hydrodynamic particle sizes and pharmacokinetics. When dispersed in gels and examined by MRI, the Fe NPs were found to produce more than twice the amount of T_2 contrast change per unit concentration relative to FeOx NPs. When cells were labelled in vitro, Fe NPs produced greater T_2 contrast enhancement in all cell types tested, whilst there was no significant difference in the uptake of iron or the cytotoxicity between cells labelled with Fe or FeOx NPs.

To assess the clinical applicability of the nanoparticles in vivo, FeOx NPs and Fe NPs were administered to mice and MRI experiments were performed at 1.5 T. Contrast effects of the NPs were examined in the liver, spleen and lymph nodes, as tissues in these organs are rich in phagocytic cells and have a strong tendency to take up circulating NPs. In all three organs studied, the Fe NPs produced noticeably darker contrast than the FeOx NPs, providing twice the contrast improvement.

One of the most intensely researched applications of magnetic nanoparticles in MRI is

improving detection of cancer in the lymph nodes. To model the size and NP uptake of small lymph node metastases in humans, a mouse model was developed by injecting 4T1 breast cancer cells directly into the mouse spleen. Analysis of mice bearing 4T1 tumours performed at 1.5 T showed that Fe NPs produced better contrast than FeOx NPs and improved the detection of small tumours in the spleen as determined by two blinded radiologists. Indeed, the heightened sensitivity and specificity improved the threshold of cancer detection on previous studies performed at 1.5 T.

It was then examined whether the improved T_2 contrast could enable new MRI applications in vivo. A novel assay to detect induced immune responses following dendritic cell-based vaccination using MRI was developed. By tracking cells labelled with iron nanoparticles, a difference in contrast could be detected between nave mice and those that had developed a strong immune response after vaccination. This assay only reached statistical significance with Fe NPs and not with FeOx NPs.

As a consequence of these studies, another MRI-based technique for assessing induction of an immune response was developed, based on the simple observation that lymph nodes draining the injection site became enlarged. This enlargement was seen as early as 12 hours after vaccination and was caused by a cellular infiltrate dominated by lymphoid cells. In experiments where vaccination was performed multiple times using different tumours as a source of antigen, incremental increases in lymph node size were detectable by MRI, which was shown to be a highly antigen-specific response. In the vaccine model studied, the increase in lymph node size was associated with protection from a tumour challenge.

Thus, Fe NPs produce a significant improvement of T_2 contrast over FeOx NPs in a range of applications without any differences found in uptake or cytotoxicity. These findings are substantial enough to justify further investigations into the application of Fe NPs in a variety of clinical settings.

Contents

Abstract	7
List of figures and tables	13
Glossary	16
1 General introduction	19
1.1 Basic principles of nuclear magnetic resonance	20
1.1.1 Nuclear spin and the Zeeman interaction	20
1.1.2 Generation of the free induction decay	22
1.1.3 Relaxation processes cause decay of the MR signal	22
1.1.4 Image formation: slice selection	26
1.1.5 Image formation: frequency and phase encoding	26
1.1.6 Image formation: Fourier transformation of k-space	28
1.1.7 Image formation: resolution	30
1.1.8 Image contrast: introduction	32
1.1.9 Image contrast: T_1 relaxation	33
1.1.10 Image contrast: T_2 relaxation	35
1.1.11 Image contrast: weighting an image to emphasize different MR characteristics	36
1.1.12 Summary	39
1.2 Magnetic nanoparticles as T_2 contrast agents	39
1.2.1 Clinical applications of magnetic NPs	40
1.2.2 Tracking dendritic cells with Fe NPs	41
1.2.3 The role of dendritic cells in cancer immunotherapy	42
1.2.4 Summary	44

2	Materials and methods	45
2.1	MRI scanning	45
2.2	Statistics	46
2.3	Methods from Chapter 3	48
2.3.1	Synthesis of Fe NPs	48
2.3.2	Synthesis of FeOx NPs	48
2.3.3	Transmission electron microscopy	48
2.3.4	Ligand exchange with meso-2,3-dimercaptosuccinic acid	49
2.3.5	Measurements of hydrodynamic size with dynamic light scattering	49
2.3.6	Determination of iron content by flame atomic absorption spec-	
	troscopy	50
2.3.7	Measurements of T_2 relaxivity and MRI at 9.4T	50
2.3.8	Culture of cancer cell lines	51
2.3.9	Labelling cancer cells with NPs	51
2.3.10	Perl's stain	52
2.4	Methods from Chapter 4	52
2.4.1	Mice	52
2.4.2	Administration of NPs for in-vivo MRI	53
2.4.3	In-vivo MRI	53
2.4.4	Histology	53
2.4.5	Administration of subcutaneous B16 tumours	54
2.4.6	Addition of Herceptin-conjugated to Fe NPs to HeLa cells	54
2.4.7	Administration of intrasplenic tumours	54
2.4.8	Scoring tumours	55
2.5	Methods from Chapter 5	55
2.5.1	Bone marrow-derived dendritic cell culture	55
2.5.2	Cytotoxicity assays	56
2.5.3	Flow cytometry	56
2.5.4	DC/peptide vaccine preparation	57
2.5.5	VITAL assay	58
2.5.6	DC migration by CFSE labelling	58
2.5.7	Lymph nodes ex vivo at 9.4 T in agar	59
2.5.8	Tumour lysate preparation	59
2.6	Methods from Chapter 6	60
2.6.1	In vivo lymph node measurement	60

2.6.2	Cell gating strategies for flow cytometry of lymph nodes	60
2.6.3	Tumour protection studies	60
3	Characterisation of Fe NPs for biomedical applications	63
3.1	Introduction	63
3.1.1	Characterisation of magnetic NPs	63
3.1.2	Synthesis of Fe NPs	65
3.1.3	Aims	66
3.2	Results	66
3.2.1	TEM characterisation of Fe and FeOx NPs	66
3.2.2	Electron diffraction pattern confirms Fe NP and FeOx NP crystal structure	67
3.2.3	DMSA ligand exchange to produce water dispersible NPs	70
3.2.4	The importance of pH adjustments during DMSA coating of NPs	72
3.2.5	Stability of Fe NPs over time	73
3.2.6	T_2 relaxation of Fe NP dispersions	73
3.2.7	T_2 relaxivity of Fe NPs	77
3.2.8	In vitro MRI contrast in cells labelled with NPs	77
3.2.9	Fe uptake into cells	79
3.3	Discussion	81
3.3.1	Principle findings	81
3.3.2	Implications of the study	82
3.3.3	Remaining questions	83
3.3.4	Conclusion	84
4	Improving the diagnosis of small tumours by MRI with Fe nanoparticles	85
4.1	Introduction	85
4.1.1	Mechanisms of cellular uptake of magnetic NPs	86
4.1.2	Aims	87
4.2	Results	88
4.2.1	Fe NPs produce greater T_2 contrast in the liver, spleen and lymph nodes in vivo	88
4.2.2	Histology of NP uptake into the liver	89
4.2.3	Direct tumour imaging in vivo with a subcutaneous melanoma model	92
4.2.4	Investigating the central, hypointense regions of tumours observed in a subset of mice following Fe NP administration	94

4.2.5	T_2 contrast in smaller tumours after intravenous administration of Fe NPs	97
4.2.6	Antibody conjugation of Fe NPs to improve tumour specific uptake	99
4.2.7	Detection of intrasplenic tumours following intravenous Fe NPs	100
4.2.8	Histology of spleens and tumours	101
4.2.9	Effect of Fe NPs on tumour detection by blinded radiologists	104
4.2.10	Intra-observer accuracy and variability	105
4.3	Discussion	108
4.3.1	Principle findings	108
4.3.2	Mechanism of improved tumour diagnosis	108
4.3.3	Implications of this study	109
4.3.4	Conclusion	111
5	MRI tracking of DC/peptide vaccines labelled with Fe NPs to determine antigen-specific responses	113
5.1	Introduction	113
5.1.1	Mechanisms of tumor suppression and escape from the immune system	113
5.1.2	DC elimination assay	115
5.1.3	Aims	117
5.2	Results	117
5.2.1	Fe nanoparticles improve sensitivity of dendritic cell detection	117
5.2.2	Fe NPs and FeOx NPs do not effect DC viability, metabolism or activation at the dose used for MRI labelling	120
5.2.3	VITAL assay demonstrates antigen-specific cell elimination in vaccinated mice	122
5.2.4	Fe NPs and FeOx NPs do not affect DC migration or antigen presentation to cytotoxic T cells	125
5.2.5	DC migration can be detected ex vivo by MRI at 9.4 T	125
5.2.6	Only Fe NPs are effective for tracking DC migration in naïve versus primed mice	127
5.2.7	Dose of Fe NPs injected without cells detectable at inguinal lymph node	129
5.2.8	DC/lysate vaccines fail to induce DC elimination	129
5.3	Discussion	130

5.3.1	Principle findings	130
5.3.2	Mechanism of DC elimination	132
5.3.3	Implications of the study	134
5.3.4	Remaining questions	136
5.3.5	Conclusion	137
6	Assessing antigen-specific responses to vaccination by monitoring enlargement of draining lymph nodes by MRI	139
6.1	Introduction	139
6.1.1	The advantages of lysate-based vaccines	140
6.1.2	The need for an assay to detect an immune response to multiple (unknown) antigens	141
6.1.3	Enlargement of the draining lymph node following DC/lysate vaccination	142
6.1.4	Aims	142
6.2	Results	143
6.2.1	Lymph node enlargement is an antigen-specific response to vaccination	143
6.2.2	Time course of the draining lymph node enlargement	145
6.2.3	Re-challenge vaccination produces re-enlargement	148
6.2.4	Cell types involved in lymph node infiltration	148
6.2.5	Lymph node enlargement correlates with tumour protection . . .	151
6.3	Discussion	151
6.3.1	Principle findings	151
6.3.2	Mechanism of the draining lymph node enlargement	154
6.3.3	Implications of the study	157
6.3.4	Remaining questions	159
6.3.5	Conclusion	161
7	General discussion	163
	Appendix - publications arising from this thesis	171
	Bibliography	186

List of Figures

1.1	Zeeman splitting	21
1.2	Generation of the FID	23
1.3	T_2 and T_2^* relaxation	25
1.4	Slice selection by application of a magnetic field gradient	27
1.5	Frequency and phase encoding	29
1.6	Filling k-space	31
1.7	The effect of echo time (TE) on T_2 contrast	38
2.1	Non-parametric distribution of T_2 contrast in lymph nodes	47
2.2	Flow cytometry gating strategies for cells recovered from lymph nodes . .	61
3.1	Beam diagram of a transmission electron microscope	68
3.2	TEM images of Fe and FeOx NPs	69
3.3	Electron diffraction patterns of Fe and FeOx NPs	70
3.4	Schematic of synthesis and DMSA coating of Fe NPs	71
3.5	Meso-2,3-dimercaptosuccinic acid (DMSA)	71
3.6	Hydrodynamic size of NPs in aqueous solution	74
3.7	Stability of Fe NPs after DMSA coating	75
3.8	T_2 relaxation of Fe and FeOx NP dispersions at 9.4T	76
3.9	Relaxivity of Fe NPs and FeOx NPs at 9.4T	78
3.10	T_2 contrast in diverse cell types labelled with NPs in vitro	79
3.11	Fe content of cancer cells after labelling with Fe and FeOx NPs	80
4.1	Contrast in the liver with intravenous Fe NPs	90
4.2	Contrast in the spleen and lymph nodes with intravenous Fe NPs	91
4.3	Fe content in liver tissue following administration of NPs	93
4.4	T_2 contrast in large tumours following intravenous Fe NPs	95
4.5	Histology of hypointense regions of tumours on T_2 imaging	96

4.6	T_2 contrast in small tumours following intravenous Fe NPs	98
4.7	Uptake of Herceptin conjugated Fe NPs into HeLa cells	100
4.8	Imaging intrasplenic tumours with Fe and FeOx NPs	102
4.9	Histology of intrasplenic tumours with intravenous Fe NPs	103
4.10	Receiver operator curve of in vivo tumour detection	106
4.11	Changes in tumour scoring with observer training	107
5.1	Detection of DCs labelled with Fe NPs at 9.4T	119
5.2	Fe NP and FeOx NP uptake into DCs	119
5.3	Cytotoxicity of Fe NPs versus FeOx NPs in DCs	121
5.4	DC maturation after incubation with Fe NPs	123
5.5	VITAL assay demonstrates antigen-specific cell lysis	124
5.6	Migration of DC/peptide vaccines by ex vivo flow cytometry	126
5.7	MRI of draining lymph nodes ex vivo at 9.4T	127
5.8	MRI of draining lymph nodes in vivo at 1.5T	128
5.9	Inguinal nodes after s.c. injection of Fe	130
5.10	Migration of DC/lysate vaccines to the draining lymph node by ex vivo flow cytometry	131
5.11	MRI of draining lymph nodes in vivo following DC/lysate vaccine	131
6.1	Area of lymph nodes following DC/lysate vaccination	146
6.2	Difference in the area between draining and contralateral lymph nodes following DC/peptide vaccination	147
6.3	Time course of draining lymph node enlargement	147
6.4	Area of draining lymph nodes following re-challenge	149
6.5	Cell types involved in lymph node infiltration	152
6.6	Subcutaneous thymoma tumour challenge following vaccination	153

List of Tables

1.1	Proton density, T_1 and T_2 times of different tissues and lesions at 1.5T . .	36
1.2	The effect of TE and TR on image weighting	39
1.3	FeOx NPs developed for clinical applications	41
2.1	Antibodies and fluorophores used in this thesis	57
4.1	Scoring system for intrasplenic tumours	104

Glossary

T_1 longitudinal or spin-lattice relaxation. 32

T_2 transverse or spin-spin relaxation. 32

T_2^* loss of spin coherence due to magnetic inhomogeneity and spin-spin relaxation. 24

4T1 4T1 breast carcinoma cells. 51

AAS atomic absorption spectroscopy. 50

B16 B16F10 melanoma cells. 51

BMDC bone marrow derived dendritic cell. 55

CFSE carboxy-fluorescein succinimidyl ester. 58

CTL Cytotoxic T lymphocytes. 42

DC dendritic cell. 42

DI de-ionised. 49

DLS dynamic light scattering. 64

DMSA meso-2,3-dimercaptosuccinic acid. 49

EG7ova EG7-OVA chicken ovalbumin-expressing thymoma cells. 51

FeOx NPs iron oxide nanoparticles. 35

FID free induction decay. 22

GBCA gadolinium based contrast agents. 34

GL261 GL261 glioblastoma cells. 51

HeLa Henrietta Lacks cervical adenocarcinoma cells. 51

IP intra-peritoneal. 53

MDSC myeloid derived suppressor cells. 115

MHC major histocompatibility complex. 43

MRI magnetic resonance imaging. 20

MTT 3-(4,5-Dimethylthiazol-2-yl)-2,5-diphenyltetrazolium bromide. 120

NMR nuclear magnetic resonance. 20

NMV nuclear magnetic vector. 22

NPs nanoparticles. 19

OLA oleylamine. 48

PBS phosphate-buffered saline. 49

RF radio-frequency. 22

ROI region of interest. 53

Tcm Central memory T cells. 150

TE echo time. 36

TEM transmission electron microscopy. 48

Tem effector memory T cells. 150

TR repetition time. 36

Chapter 1

General introduction

Magnetic Resonance Imaging (MRI) is a powerful and versatile technique that has produced significant benefits for medical imaging. It has several key advantages over other imaging modalities. In contrast to computed tomography and positron emission tomography, MRI produces excellent soft-tissue contrast resolution without exposing the patient to ionizing radiation¹⁻³. Unlike ultrasound or fluorescent imaging techniques, MRI can be used effectively to assess deep tissues⁴⁻⁶. Several biomedical applications of MRI can be further improved with the use of magnetic nanoparticles (NPs) as contrast agents. These include imaging small tumors in the liver and lymph nodes and tracking cells in vivo. Improving cancer imaging can result in more effective clinical treatment whereas enhanced cell tracking can lead to advances in emerging cellular therapies, such as cancer immunotherapy with cell-based vaccines.

This chapter introduces the key concepts involved in producing a diagnostic image with MRI and how this can be improved with the use of magnetic NPs as contrast agents. The clinical applications of magnetic NPs are reviewed followed by a basic introduction to the principles of cancer immunotherapy with cell-based vaccines. These concepts form the foundation of the experimental work presented in this thesis.

1.1 Basic principles of nuclear magnetic resonance

The basic principles of nuclear magnetic resonance (NMR) have been well covered in the scientific literature and several excellent sources were used in the preparation of this chapter⁷⁻¹¹. The purpose of this section is to provide the non-specialist with an introduction to the principles of NMR, which underpin the magnetic resonance imaging (MRI) experiments described in this thesis. This section covers the key concepts of how an NMR response can be produced and manipulated such that information collected from the response can be used to generate an image. Different tissues and pathology can be distinguished with MRI contrast, which can be improved with the use of contrast agents.

1.1.1 Nuclear spin and the Zeeman interaction

Atomic nuclei possess an intrinsic, quantum mechanical property called spin⁷. Nuclear spin angular momentum m_l is quantised and is related to the nuclear magnetic moment μ by the magnetogyric ratio γ :

$$\mu = \gamma \hbar m_l \text{ (Equation 1)}$$

where \hbar is the modified Plancks constant $\frac{h}{2\pi}$. The ^1H nucleus is often termed a proton as it consists of just a single proton. Protons have a positive magnetogyric ratio, which means that the direction of their spin angular momentum and magnetic moment are the same. The vast majority of imaging experiments are done with protons because they produce the best signal to noise ratio. This is due to their large magnetogyric ratio and natural abundance both as an isotope (nearly 100%)¹² and in water molecules in biological tissue (human adults are up to 60% water by mass). Although an increasing amount of MRI research is performed on atomic nuclei other than ^1H (such as ^{23}Na , ^{31}P and ^{19}F), discussion of other nuclei is beyond the scope of this thesis.

In the absence of an applied magnetic field, the proton spins in a sample are randomly oriented in all directions and no energy difference exists between different orientations. When an external magnetic field (B_0) is applied, there are two important effects on the nuclear spins in a sample. Firstly, a difference is created between the two allowed energy states of those spins that are aligned parallel and those that are aligned antiparallel to the direction of B_0 . Quantum mechanics has determined that the projection of the spin

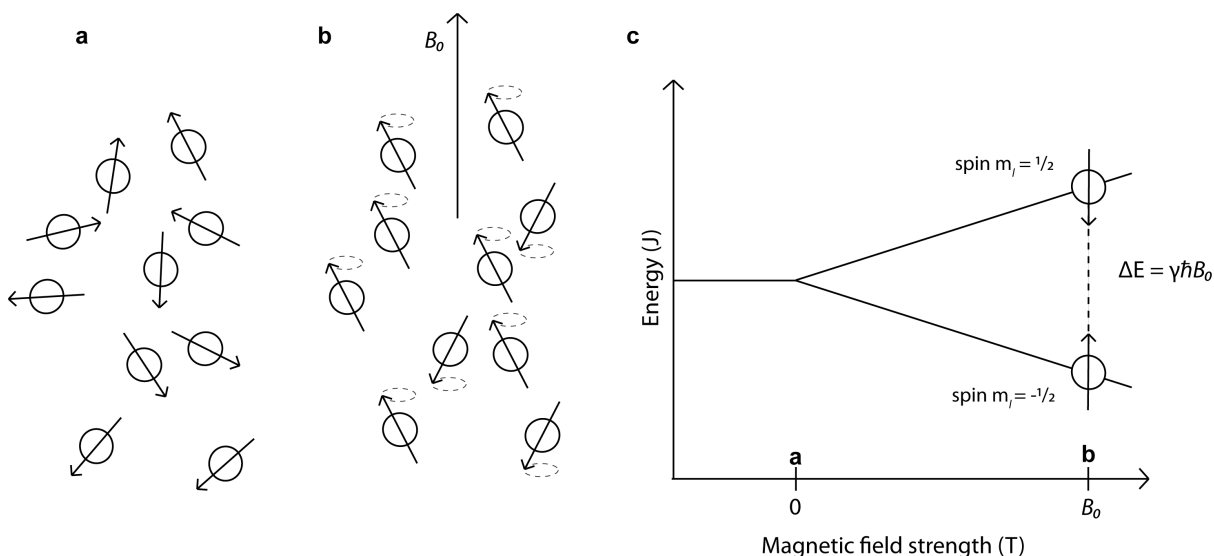


Figure 1.1: Zeeman splitting. Before an external magnetic field B_0 is applied, the directions of the magnetic dipole moments of the nuclear spins have an isotropic distribution (a). After B_0 is applied (b), the proton spins precess at their Larmor frequency and there is net spin polarisation in the direction of B_0 with the population of aligned spins exaggerated for illustration. The application of B_0 splits the two different spin states ($m_l = \pm \frac{1}{2}$) into two different energy levels (c).

angular momentum on a magnetic field is quantised with the two permitted values¹¹ of $m_l = +\frac{1}{2}$. The splitting of these energy states is called Zeeman splitting and is illustrated in Figure 1-1. The second important effect is that the nuclear spins precess about the axis of the applied field, B_0 , at a frequency relative to the strength of B_0 and the magnetogyric ratio γ of the nuclei. The Larmor equation defines this relationship:

$$\Delta E = \gamma \hbar B_0 = h \nu_L \text{ (Equation 2)}$$

ΔE is the difference between in energy between the two spin eigenstates and ν_L is the frequency of precession, known as the Larmor frequency. The result is that the energy state of the spin polarization can take only one of two discrete values for protons at a given B_0 (Figure 1-1).

The energy difference between the two spin alignments is small compared to thermal energy even at large applied fields. For example, at 9.4T (the largest B_0 employed in this thesis), the difference in energy for a single ^1H proton aligned with ($m_l = -\frac{1}{2}$) versus against ($m_l = +\frac{1}{2}$) B_0 is $2.5 \times 10^{-25} \text{ J}$ compared to the thermal energy available at room temperature of $4.1 \times 10^{-21} \text{ J}$. As a result, at thermal equilibrium, there is a fractional population difference between the spins that are aligned with B_0 (and hence at a lower energy state) and those that are aligned against it. At 9.4T there is

approximately 0.007% excess in the populations of proton spins aligned with B_0 . Although it is a relatively small proportion, the difference in the alignment of the proton spin populations forms a net magnetisation vector aligned with B_0 , precessing at the Larmor frequency. Manipulation of this nuclear magnetisation vector (NMV) is the basis of NMR experiments. The remainder of this chapter uses a descriptive approach with semiclassical mechanics, as opposed to quantum mechanics, to explain how manipulation of the NMV results can produce an image.

1.1.2 Generation of the free induction decay

The nuclear magnetic vector (NMV) is difficult to detect at thermal equilibrium when it is aligned along B_0 , as it is many orders of magnitude smaller than B_0 . However, the NMV can be measured when it is disturbed away from its equilibrium orientation along B_0 . An electromagnetic pulse applied perpendicular to B_0 at the same frequency as the frequency of precession (the Larmor frequency) can disturb the equilibrium and rotate the NMV. This is a simple result of the torque felt by the NMV resulting from the applied electromagnetic pulse.

The Larmor frequencies of protons at B_0 fields used for imaging are in the radio-frequency (RF) range. Therefore if an RF pulse is at the Larmor frequency and perpendicular to B_0 , it can rotate the NMV towards the transverse plane. If the RF pulse is of adequate strength and duration, the NMV can be rotated 90° so that it precesses entirely in the transverse plane (Figure 1-2). Such an RF pulse is termed a 90° pulse. The precessing of the NMV in the transverse plane induces an electromotive force, producing an electric current in an RF receiver coil. This signal known as free induction decay (FID), is the measurable basis of NMR.

1.1.3 Relaxation processes cause decay of the MR signal

After the NMV is rotated into the transverse plane by a 90° RF pulse, the NMV loses its transverse component and is restored to its original precession about B_0 . This is caused by relaxation which indicates a return of the nuclear spins to thermal equilibrium. In a non-homogenous sample, nuclear spins in different regions of a sample may have different rates of relaxation according to their local environment. This is a fundamental concept that is exploited in MRI to produce image contrast.

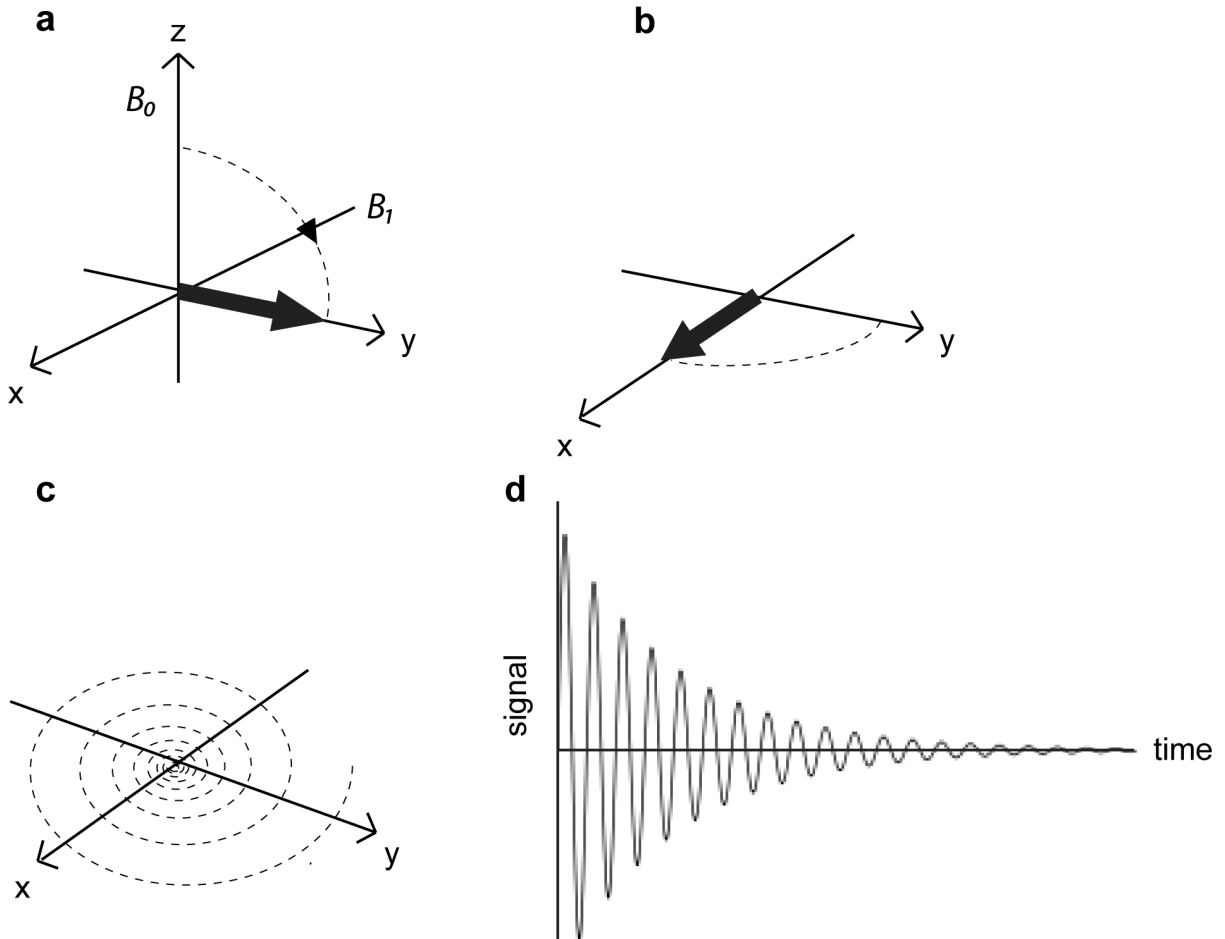


Figure 1.2: Generation of the Free Induction Decay. The application of a 90° RF pulse about the x -axis (B_1) rotates the net magnetization of the spins into the transverse plane (a) where they precess at their Larmor frequency (b). The rotating frame rotates in the plane perpendicular to B_0 at the Larmor frequency, so that the precession of the NMV about B_0 is not apparent (a). The laboratory frame represents the fixed space in which the FID is recorded, and thus shows the precession of the NMV around B_0 (b). Over time, the magnetisation vector decays in the transverse plane (c), as shown in the laboratory frame. The precession and decay can both be seen in the induced signal (d), called the free induction decay (FID). Note that the rate of decay relative to the number of precessions in the transverse plane has been exaggerated for illustrative purposes.

As spins precess together, their magnetic fields interact which makes a slight change to their rate of precession. These spin-spin interactions are temporary and random and they result in a loss of phase coherence. This process is called transverse or T_2 relaxation and it causes irreversible decay of the NMV in the transverse plane (Figure 1-2). The rate of T_2 relaxation is dependent on the local environment of the proton nuclei and is related to the NMR signal S at time t by:

$$S(t) = S_0 \exp(-t/T_2) \text{ (Equation 3)}$$

S_0 is the (maximum) signal at time = 0, immediately after the 90° pulse is applied as seen in Figure 1-3. The T_2 time is when 63% ($\frac{1}{e}$) of the signal has decayed.

After removal of a 90° RF pulse, thermal equilibrium will be gradually restored and the slight population surplus of nuclear spins aligned with B_0 will be re-established. As this happens, the NMV returns to its thermodynamic equilibrium along the z -axis in the laboratory frame (Figure 1-2). This process is called longitudinal or T_1 relaxation. The effects of these relaxation processes on image contrast are discussed in section 1.1.8 below.

It has been shown in Equation 2 that the Larmor frequency of spin precession is dependent on the strength of the applied magnetic field B_0 . B_0 is never perfectly homogenous which results in macroscopic variations in the magnetic field as experienced by nuclear spins within the sample. Also non-homogeneous samples may have regions with different magnetic susceptibility that also cause magnetic field variations experienced by spins within the sample. The inhomogeneity in B_0 and within the sample causes nuclear spins to precess at different Larmor frequencies, which in turn cause the NMV to lose coherence and its transverse magnetization to decay. This process is called loss of spin coherence due to magnetic inhomogeneity and spin-spin relaxation (T_2^*). T_2^* relaxation can be reversed by application of an RF pulse to rotate the NMV by 180° . After the 180° pulse is applied, the nuclear spins will come back into coherence generating an echo signal in the RF receiver (Figure 1-3). The echo time is the time between the application of the 90° pulse and the generation of an echo. Further echoes can be generated by applying successive 180° pulses, one echo time apart. T_2 relaxation causes the signal in each successive echo to diminish. The basic concept of this pulse sequence is called a spin echo and it is often used to produce images with T_2 contrast that have not been degraded by T_2^* effects. All of the imaging performed in this thesis incorporates the spin echo technique.

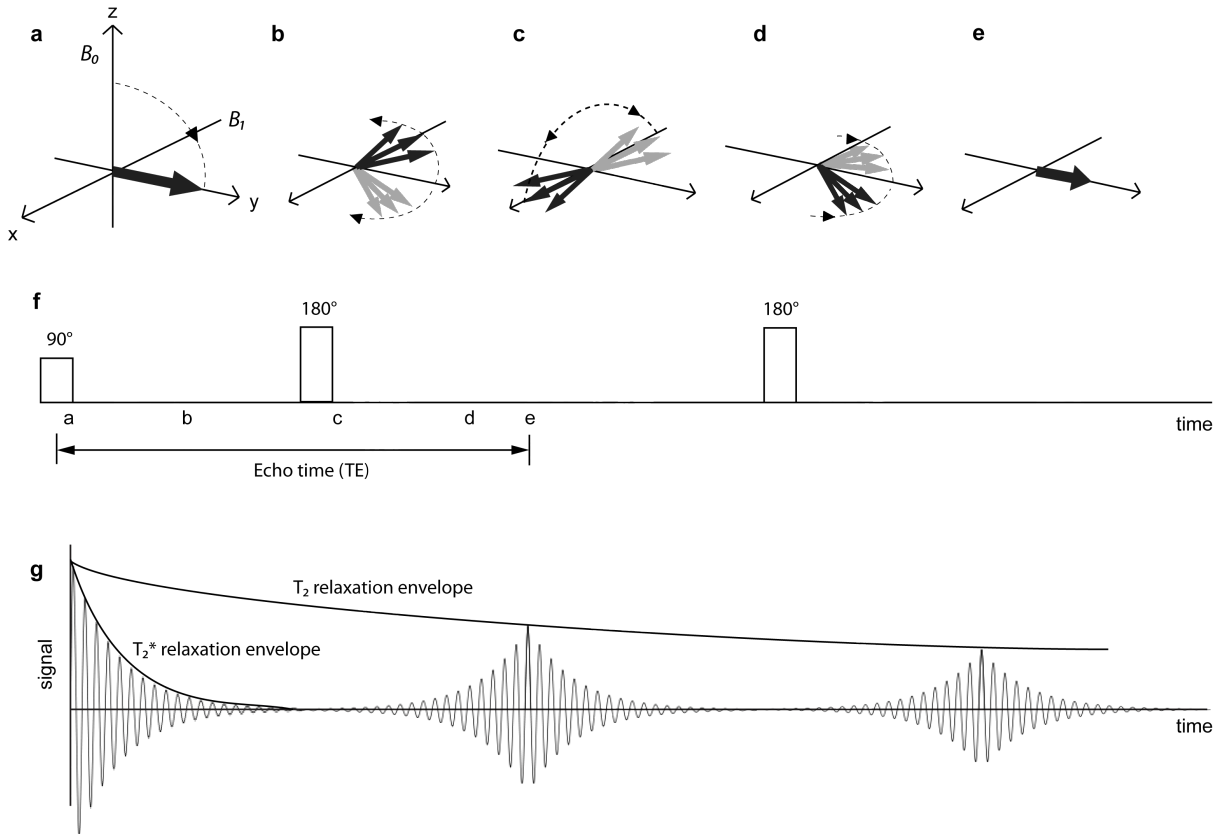


Figure 1.3: T_2 and T_2^* relaxation. As shown in the rotating frame, a 90° pulse about B_1 brings the nuclear magnetization vector into the transverse plane (a). Due to magnetic field inhomogeneity, different spins in the sample precess at different Larmor frequencies in the transverse plane shown in the laboratory frame (b) higher frequencies in grey, lower frequencies in black). This causes T_2^* decay of the FID (g). A 180° pulse is applied to flip the magnetisation vectors about the x -axis (c), which reverses the effects of the magnetic field inhomogeneity (d,e) such that phase coherence occurs (e) and produces an echo detectable in the transverse plane. Each successive echo has less signal and due to irreversible T_2 relaxation (g). The RF pulse sequence (f) is shown in synchrony with the echoes produced (g).

1.1.4 Image formation: slice selection

In the absence of externally applied magnetic field gradients, a 90° pulse will cause the nuclear spins distributed across the whole sample to rotate into the transverse plane and contribute to the FID. For imaging applications, it is often desirable to examine only part of the sample. This can be done by selectively rotating the nuclear spins from only a slice of the sample by applying a magnetic field gradient in combination with an appropriate RF pulse.

If a homogenous magnetic field gradient is applied along the axis of B_0 , the nuclear spins will experience a different magnetic field according to their position along the axis. Therefore they will precess at a different Larmor frequency according to their position along B_0 (Figure 1-4). If an RF pulse is applied transverse to B_0 in the presence of such a gradient, only the proton spins in the sample that are precessing at the same frequency as the RF pulse will be rotated towards the transverse plane. This technique is called slice selection and is used to examine the NMV of select regions of the sample according to their position along B_0 . The thickness of the slice is determined by the bandwidth of the RF pulse and the strength of the magnetic field gradient (G) applied simultaneously by:

$$\text{slice thickness} = \frac{\text{RF pulse bandwidth}}{\gamma G} \quad (\text{Equation 4})$$

Therefore to achieve selection of a thinner slice, a larger gradient can be applied or the width of the RF bandwidth can be reduced.

1.1.5 Image formation: frequency and phase encoding

By the slice selection technique, the NMV from protons in the region of interest along the B_0 axis (defined as the z -axis by convention) can be rotated into the transverse plane. After slice selection, if a magnetic field gradient is applied along one of the transverse axes, such as the x axis, the frequency of the precessing spins will vary along the x -axis according to position. An echo recorded whilst the gradient is applied will contain information about the position of spins along the x -axis, as encoded by frequency along the gradient (Figure 1-5). This is known as the read, or frequency encoding gradient.

To produce a 2D image, information about spins along the y -axis is required. After a 90° slice selection pulse, a gradient is applied across the y -axis. Once the gradient is

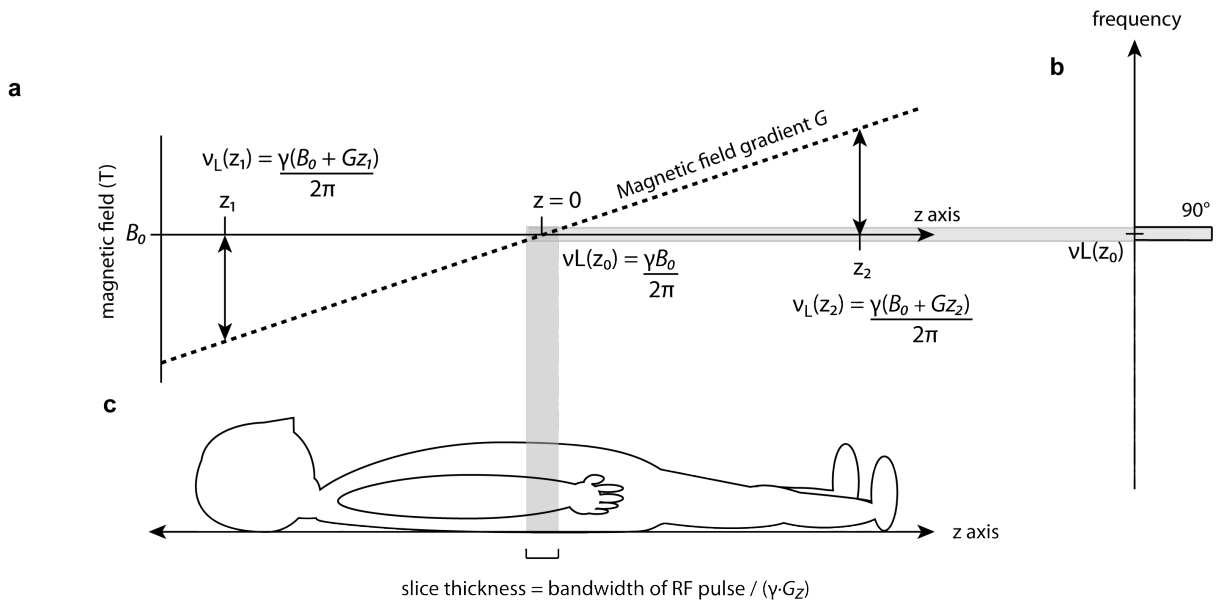


Figure 1.4: Slice selection by application of a magnetic field gradient. When a magnetic field gradient is applied along the z -axis (a), proton spins in the sample will precess at different Larmor frequencies ν_L corresponding to their position along the axis. Regions of the sample can be selected by applying a 90° pulse at a frequency corresponding to the region of interest along the z -axis (a). In this example, only spins in a slice in the middle of the patient (grey rectangle) at $z = 0$ would be rotated into the transverse plane by a 90° pulse at frequency ν_L (c). To select spins in a slice corresponding to the head or the feet, a RF pulse of lower or higher frequency would be required, respectively. Note that for a fixed bandwidth, increasing the strength of the gradient (G) would reduce the slice thickness (Equation 4).

removed the spins will return to precessing at the Larmor frequency but with a phase shift relative to their position along the y -axis. This is known as the phase encoding gradient. The echo is then recorded in the presence of the frequency encoding gradient (along the x -axis). This sequence is repeated for a number of steps changing the strength of the phase encoding gradient (along the y -axis) by the same increment each time (Figure 1-5). The resulting data set contains a series of echoes containing information about the nuclear spins in the sample according to their position in the z -axis (slice selection), x -axis (frequency encoding) and y -axis (phase encoding). It is important to note that MRI is completely flexible as to which method of encoding is used along which axis. Many alternative strategies exist such as in 3D imaging where no slice selection and three different phase encoding gradients or one frequency and two phase encoding gradients can be used.

1.1.6 Image formation: Fourier transformation of k-space

How is a series of FIDs, generated under conditions such as those seen in Figure 1-5, used to form an image? To convert the raw signal into an image, the recorded FIDs are first converted into a digital signal and stored in a matrix, containing what is known as k-space data. K-space is known as a reciprocal space because it maps directly to the spin density ρ of the sample in real space, by a Fourier transform:

$$\rho(x, y) = \int S(k_x, k_y) \exp[-i2\pi(k_x x + k_y y)] dk_x dk_y \quad (\text{Equation 5})$$

A Fourier transform is an operation that decomposes a signal into its complex constituent frequencies with their respective amplitudes. Therefore, by performing a 2D Fourier transform on k-space, an image is produced with the number of pixels equivalent to the number of points acquired in k-space. In two dimensions, k-space has two axes, k_x and k_y corresponding to the frequency encoding gradient (G_F) and the phase encoding gradient (G_P) as follows:

$$k_x = k_F = (\gamma G_F n \Delta t) / 2\pi \quad (\text{Equation 6})$$

$$k_y = k_P = \gamma (G_{min} + m \Delta G_P) \tau / 2\pi \quad (\text{Equation 7})$$

G_F is the strength of the frequency encoding gradient, n is sample number along the k_x axis and Δt is the sampling time (or reciprocal of the sampling frequency) of the FID as the G_F is applied. ΔG_P is the difference between increments in the phase encoding gradient, G_{min} is the minimum strength of the phase encoding gradient, m is the sample number along the k_y axis and τ is the duration of the G_P in a given direction along the

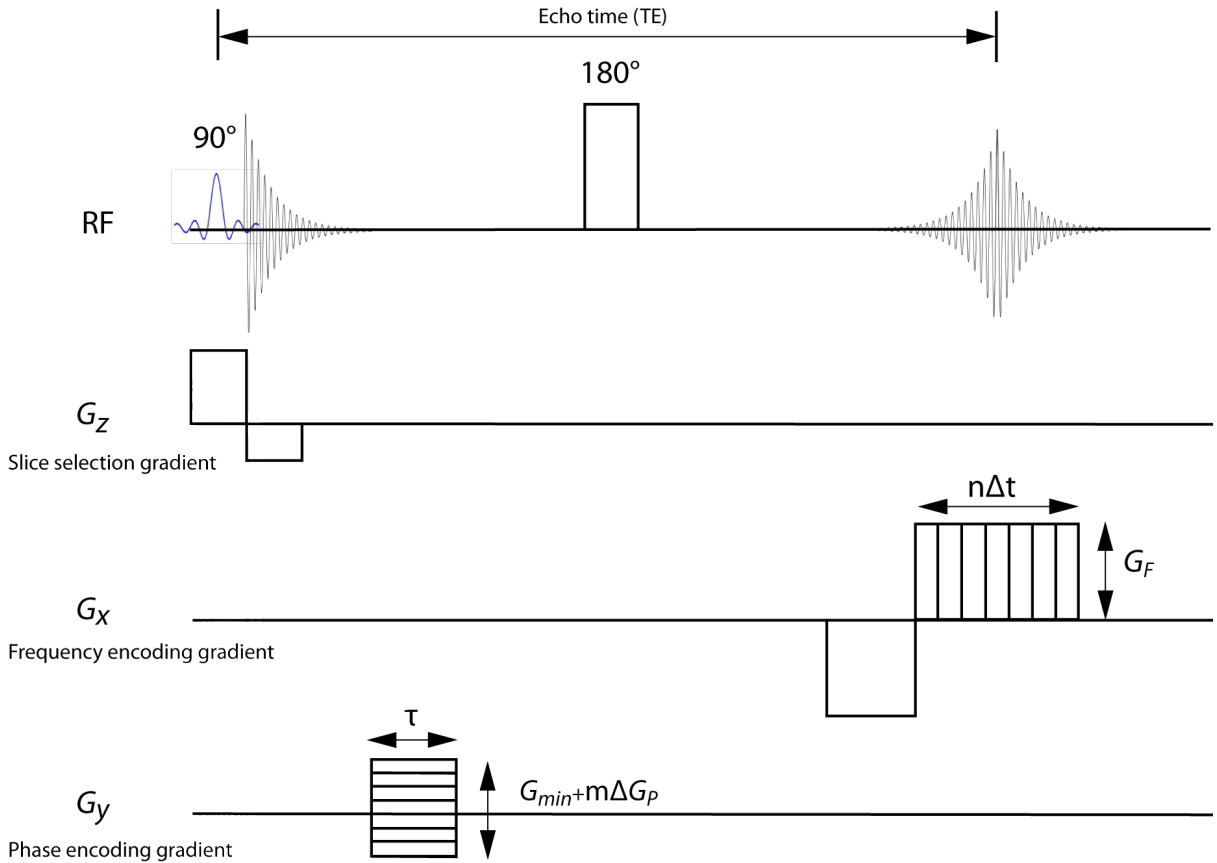


Figure 1.5: Frequency and phase encoding. After slice selection, by application of the G_z gradient during a 90° pulse, frequency and phase encoding are performed to obtain spatial information about the specimen along its x - and y - axis respectively. Frequency encoding is performed by applying a constant gradient G_F whilst recording the echo at n intervals of increasing duration Δt . Phase encoding is performed by varying the strength of the G_P gradient by m intervals, each applied once per echo for a fixed time period τ . Note that n steps of Δt are obtained for every echo, whereas for each step of G_P , this pulse sequence is repeated a total of m times.

phase encoding axis. Figure 1-6 illustrates how the axes of k-space can be filled by incrementing Δt for each value of m in $m\Delta G_P$.

There are two key properties of k space worth noting here. Firstly, every point in k-space contains information from an FID with signal contributions drawn from the entire 2D slice. Secondly, at the centre of k-space ($(k_x, k_y) = (0, 0)$) is data of low spatial frequency related to signal to noise ratio and contrast (Figure 1-6). The data at this point represents the MR signal that is unaffected by the phase or frequency encoding gradients. Conversely, data with higher spatial frequency relating to resolution is found towards the periphery.

1.1.7 Image formation: resolution

Given that the number of points in k-space determines the number of pixels in the final image, what determines the pixel size? The pixel size is determined by the physical field of view (FOV) and the number of points acquired across the field of view. For example, the pixel size Δx across the x -axis is:

$$\Delta x = \frac{FOV_x}{N_x} \text{ (Equation 8)}$$

N_x represents the number of points acquired across the x -axis. The spatial resolution $\frac{1}{\Delta x}$ can be improved by increasing N_x through an increase in the strength of gradient applied along the k_x -axis (e.g. G_F). There are potential drawbacks with increasing resolution, including increased imaging time and decreased signal to noise ratio. If resolution is increased along the frequency encoding gradient then there will not be an increase in imaging time required because the increase in N_x , corresponding to an increase in the number of points along the k_x -axis, is made by increasing the strength of G_F (see Equation 6). However, as is often the case, if a corresponding increase in resolution is required across the phase encoding axis, this will increase the number of acquisitions required, as each change in G_P requires a separate acquisition (see Equation 7 and Figure 1-5). As a consequence, imaging time will be lengthened in direct proportion to the increase in resolution across the phase encoding gradient. Therefore, to double the resolution with the same FOV along the phase encoding gradient, twice the time is required.

Another drawback and one of the ultimate limitations in increasing the image resolution is the associated decrease in signal to noise ratio (SNR). The SNR decreases in proportion to the voxel volume. A voxel is the 3D volume element from which the MRI

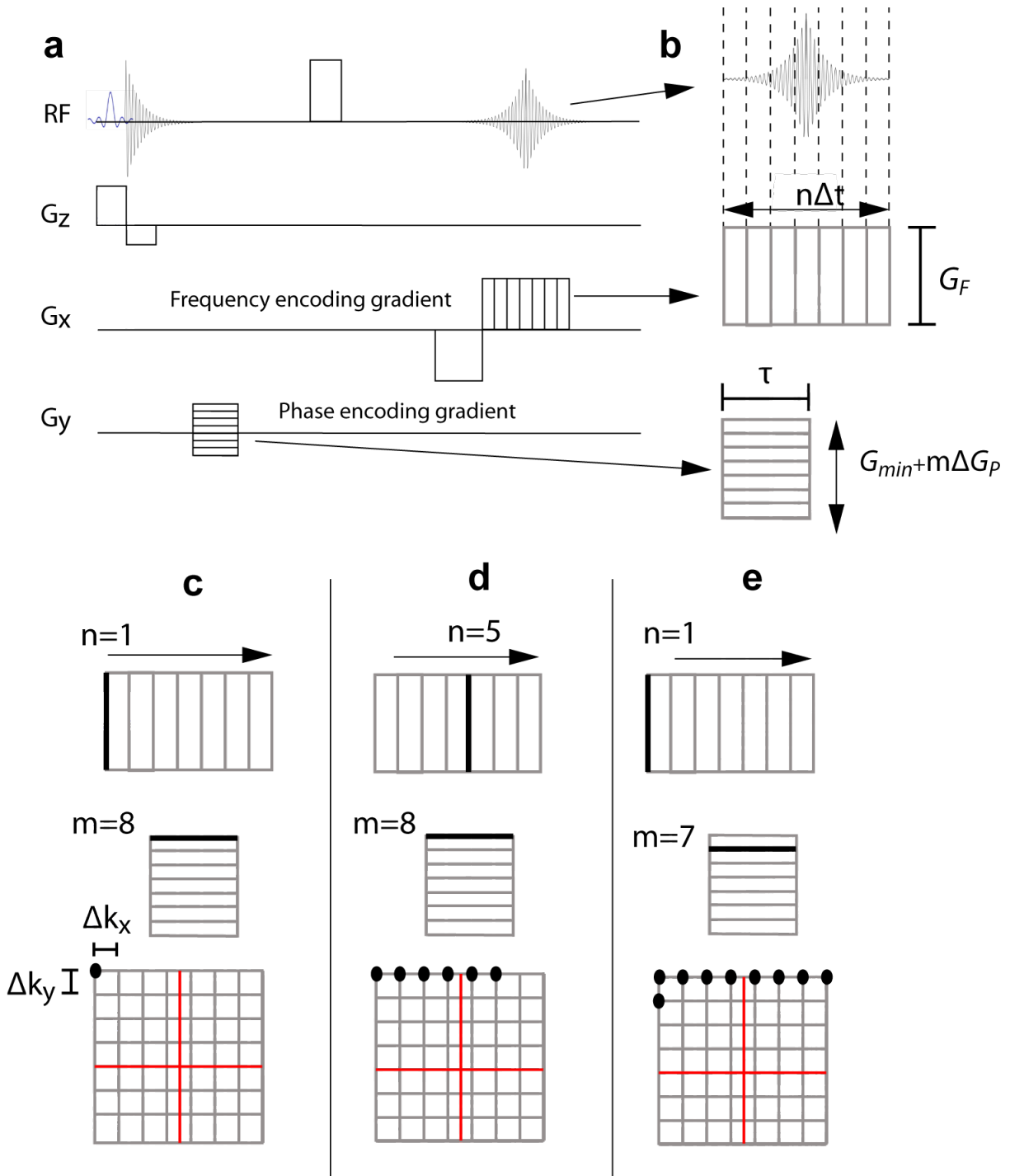


Figure 1.6: Filling k-space. A spin echo pulse sequence is shown with slice selection, frequency and phase encoding steps (a) with the echo signal and frequency and phase encoding steps enlarged (b). A line of k-space is filled along the k_x axis by incrementing the time duration of signal capture Δt by n steps (c,d). This is done during a single echo whilst keeping the frequency encoding gradient G_F constant. To fill a new line of k-space with a different value along the k_y axis, the process is repeated with the strength of the phase encoding gradient modified by an increment ΔG_P (e). Note that the intersection of the axes (c-e in red) represents the center of k-space, where $k_x = k_y = 0$.

signal was drawn, in other words it is product of the area of a pixel and the slice thickness. Therefore by halving the slice thickness, the SNR will be approximately halved. One strategy to increase the SNR is to increase the number of signals acquired to average the signal, which increases it relative to the noise. The SNR is proportional to the square root of the number of echoes acquired, so by doubling the number of FIDs acquired (and hence the imaging time), SNR can be improved a factor of $\sqrt{2}$. Another strategy to improve the SNR is to decrease the size of the RF probe. SNR is proportional to voxel volume/probe volume so that the closer the probe is to volume of the sample, the larger the SNR. This principle was applied in this thesis by using a wrist coil to image mice rather than the integrated RF coils in the body of the magnet, improving SNR by a factor of approximately 65.

A balance exists between image resolution, signal to noise and the amount of time taken to acquire the image. If the image resolution is too low, significant volume averaging can occur where volume elements (i.e. collections of nuclear spins) with different signal intensities within a voxel become averaged. If the SNR is too low, the image will be of poor quality with limited sensitivity. In a clinical setting, strong pressure on MRI scanner time makes the duration of each image sequence a key consideration. Understanding the balance of these basic principles is key to designing an imaging sequence appropriate for the specific needs of the operator.

1.1.8 Image contrast: introduction

Magnetic resonance imaging provides an excellent tool for clinical diagnosis. The advantages of MRI over other imaging modalities include its excellent spatial resolution and the degree of tissue characterisation possible without exposure to ionizing radiation¹³. There are five different variables that can be used to characterise different tissues with MRI. These include the proton density, longitudinal or spin-lattice relaxation (T_1) and transverse or spin-spin relaxation (T_2) relaxation times, diffusion and chemical shifts¹⁴. This section will describe how MRI contrast is produced and how it can be augmented with the use of contrast agents.

The three intrinsic characteristics of biological tissue that are exploited most commonly in clinical MRI are the proton density, the T_1 and the T_2 relaxation times. Two further characteristics include chemical shift and diffusion. Chemical shift imaging can produce spectral information about the chemical content of each voxel. An example of its use is

in studies of tissue metabolites¹⁵. Diffusion based imaging techniques are used predominantly in neurological studies and can provide information about tissue physiology, microvascular circulation and advanced anatomical pathways¹⁶. Although the latter two techniques are used increasingly in the clinical setting¹⁷, their detailed description is outside the scope of this thesis. The experimental work that follows is concerned primarily with contrast produced by enhancing T_2 relaxation, but T_1 relaxation and proton density will also be explored in this chapter.

1.1.9 Image contrast: T_1 relaxation

T_1 or longitudinal relaxation is the return of the nuclear magnetization vector to alignment with the applied magnetic field B_0 , as discussed in section 1.1.3. The T_1 time is defined as the time at which 63% ($\frac{1}{e}$) of the longitudinal magnetization is restored after being disturbed from thermal equilibrium. Therefore, the faster the rate of T_1 relaxation in a given tissue, the shorter its T_1 time.

So what causes variation in the rates of T_1 relaxation? T_1 relaxation is affected by thermal interactions between the precessing ^1H nuclear spins and other magnetic nuclei in the surrounding magnetic environment. These interactions allow the energy absorbed by the nuclei during the application of the RF pulse to be dispersed to other nuclei in the environment. T_1 relaxation therefore reflects the rate of energy dispersal from the proton spins to their environment.

The rate of energy dispersal from protons spins is related to their speed of molecular motion and their Larmor frequency. When the Larmor frequency is close to the speed of molecular motion of water protons, their dispersal of energy becomes more efficient which increases the rate of T_1 relaxation and decreases the T_1 time¹⁴. Protons in water molecules move rapidly with a frequency that is greater than the Larmor frequency of their spin at the strength of B_0 used for clinical imaging. Therefore bulk aqueous fluid such as cerebrospinal fluid (CSF) has a long T_1 time as seen in Table 1-1.

When the movement of water molecules is constrained, their frequency of motion is reduced. This occurs if water molecules are bound in hydration layers such as in proteinaceous fluids (i.e. abscesses) or around myelin protein (i.e. periventricular oedema)¹⁸. In these cases the frequency of protons moving in water molecules is reduced so that it is closer to the Larmor frequency, resulting in increased energy dissipation and a shorter T_1 time.

In addition to the frequency of molecular motion, T_1 relaxation is also affected by the presence of paramagnetic substances. Paramagnetic substances have magnetism that is induced in the presence of a magnetic field. They produce T_1 shortening by an interaction between their unpaired electrons and the proton in the ^1H nucleus. An important example is the iron-containing haemoglobin molecule. When haemoglobin is oxygenated as oxyhaemoglobin, it is not paramagnetic and does not enhance T_1 contrast. When it becomes deoxygenated as deoxyhaemoglobin, it becomes paramagnetic and is able to produce T_1 shortening. This is exploited in functional MRI (fMRI) where the difference in contrast between oxyhaemoglobin and deoxyhaemoglobin gives information about oxygen consumption of specific regions of the brain¹⁹.

Another important paramagnetic substance that enhances T_1 relaxation is gadolinium. Gadolinium is a lanthanide rare-earth metal with seven unpaired electrons, which bestow it with a large magnetic moment. Free gadolinium ions are a similar size to calcium ions and act as calcium antagonists in the body, producing toxic effects which impair cellular metabolism, muscle contraction and blood clotting¹¹. For this reason, gadolinium is administered clinically only as a chelated ion. Chelated gadolinium complexes have a low rate of dissociation of free gadolinium, the log of the dissociation constant measured in vitro is between 16-26²⁰ for various chelation agents. Therefore the administration of gadolinium chelates was long thought to be safe²¹ and up to 2007 they were used to enhance an estimated total of 130 million MRI scans worldwide²².

The popularity of gadolinium based contrast agents (GBCA) is due to their effectiveness as extracellular contrast agents that remain intravascular except in regions of abnormal vascular permeability, such as breakdown of the blood-brain barrier such as in tumours²⁰. Other central nervous system pathology can be identified on MRI with GBCA including active demyelination plaques in multiple sclerosis versus chronic quiescent ones²³, early ischaemia²⁴, parenchymal and meningeal brain infections²⁵.

Gadolinium based contrast agents can be used for dynamic imaging whereby a series of images is taken within the first few minutes of administration of the contrast agent.

This type of imaging is useful for distinguishing lesions such as breast cancer vs benign fibroadenoma; hepatic hemangiomas vs hepatocellular carcinoma. The overall utility of GBCAs means they are used in approximately one third of MRI scans²⁶. An aspersion has been cast recently on the safety profile of GBCAs, as they have been found to be strongly associated with a multi-organ fibrotic disorder called nephrogenic systemic fibrosis²⁷ in patients with renal impairment. The implications of this finding to the clinical use of GBCAs will be discussed in Chapter 7.

1.1.10 Image contrast: T_2 relaxation

T_2 or "transverse" relaxation time occurs simultaneously with T_1 relaxation but they are distinct processes. T_2 relaxation is a measure of how long the transverse magnetization of the nuclear magnetization vector persists after a 90° RF pulse, which is equivalent to how long the precessing nuclear spins remain in phase. T_2 relaxation is a result of the magnetic interactions that occur between precessing nuclear spins. Unlike T_1 relaxation, T_2 relaxation does not involve energy transfer²⁸ but instead a change in the phase of precessing spins, which leads to a loss of their coherence. T_2 relaxation is accelerated by static magnetic fields in the local environment. In substances such as bulk water, the rapid motion of ^1H nuclei tends to average out the magnetic fields producing a more uniform magnetic environment, which slows down the rate of T_2 relaxation.

Coated nanocrystals of iron oxides, are a type of magnetic nanoparticle that can produce enhanced T_2^* , T_2 and to a lesser extent, T_1 relaxation²⁹. All iron oxide based nanoparticle systems will be referred to in this thesis as iron oxide nanoparticles (FeOx NPs). FeOx NPs have been used as contrast agents in clinical MRI for over 20 years²⁸ and remain the focus of a highly active field of research^{30,31}.

FeOx NPs can cause a rapid loss of coherence by producing strong inhomogeneities in the local magnetic field. This causes increased T_2^* relaxation, which is a direct result of the magnetic field inhomogeneity and is reversible by a spin-echo technique as seen in Figure 1-3. FeOx NPs enhance T_2 relaxation by a mechanism known as the outer sphere theory³². This theory states that the refocusing 180° RF pulse in a spin-echo pulse sequence (see Figure 1-3) will reverse the decay of transverse magnetisation due to static magnetic fields as long as no proton spins have encountered FeOx NPs between RF pulses³³. If water protons have diffused across the magnetic field associated with a FeOx NP, this will result in a phase change in their rate of precession. If this phase change was not present when the 90° RF pulse was applied, then the 180° RF pulse will not bring them back into coherence with the other proton spins in the sample, resulting in irreversible decay of transverse magnetization. The relationship between the physical and chemical characteristics of FeOx NPs and the enhancement of T_2 contrast will be discussed in detail in Chapter 3.

Table 1.1: Proton density, T_1 and T_2 times of different tissues and lesions at 1.5T. This table illustrates the variation in proton density, T_1 and T_2 relaxation times between different tissues and disease processes, compiled from multiple sources^{11,14,34-37}. Incomplete or inconsistent data is replaced by “/”.

Tissue/lesion	Proton density	T_1 (ms)	T_2 (ms)
Aqueous liquid (e.g. CSF)	100	> 4000	> 2000
Fat	100	260	80
Air	0	0	0
Skeletal muscle	80	760	30
Grey matter	85	920	100
White matter	70	780	90
Multiple sclerosis lesions	/	1200-1800	110-150
Cerebral infarction	100	/	120
Meningioma	90	400	80
Metastasis	85	1800	85

1.1.11 Image contrast: weighting an image to emphasize different MR characteristics

Different tissues and disease processes have different rates of T_1 and T_2 relaxation, as seen in Table 1-1. How are these differences exploited to produce contrast in an image? The amplitude of signal intensity on an MR image is related to both the proton density and the relaxation rates of the protons in the region imaged. Differences in proton density, T_1 or T_2 relaxation can be emphasized through the use of different pulse sequences and by varying the echo (TE) and repetition time (TR).

The echo time (TE) is the interval between the application of the excitatory 90° RF pulse and the collection of the MR signal. The TE determines the degree to which T_2 relaxation affects image contrast. To illustrate this concept, an example of three different tissues, each with a different T_2 relaxation rate, is shown in Figure 1-7. The graph shows the MR signal intensity versus time following a spin echo pulse sequence. The tissues all had the same initial signal intensity, which has been normalized. The T_2 time of each of the tissues can be taken from the graph where the signal intensity has decayed to 63% ($= \frac{1}{e}$) of the original (Figure 1-7b, solid grey horizontal line), and it is apparent that the T_2 time of tissue 1 > 2 > 3. A more accurate way of determining the T_2 time of a tissue is to extract the value from the mono exponential fit of the graph shown in Figure 1-7b. The former method was used throughout this thesis for in vivo

imaging at 1.5T, where T_2 mapping was not available. The latter method of producing a value of T_2 from a fit of the exponential signal decay was used in all other circumstances.

Consider the signal remaining in each of the tissues if a short TE of 1ms was used, for example. There would be less than a 10% difference in the MR signal from any of the tissues. In this case, the tissues would all appear bright as less than 10% of their original signal had decayed by T_2 relaxation. As can be seen in the image (Figure 1-7a, far left), there is little contrast between the tissues. Now consider a longer TE of 8ms (Figure 1-7b, dotted vertical line). At this echo time there is $\approx 45\%$ difference in the MR signal between tissue 1 and 2 and $\approx 30\%$ difference between tissue 2 and 3. The resulting images captured at this echo time are shown in Figure 1-7c. The MR image with a TE of 8ms can be said to have more T_2 weighting than the image with a TE of 1ms. A shorter TE produces less T_2 weighting and a longer TE increases the T_2 weighting. Another way of expressing this is that a T_2 weighted image has a TE greater than or equal to the tissue specific T_2 . Therefore, by selecting the TE, the degree of T_2 weighting in the resulting MR image can be modified.

Consider again the simulated image at the far left of Figure 1-7a, where a TE of 1ms was modeled. In this case, differences in the image contrast would be mostly due to differences in the density of the protons in the tissues, as not enough time has passed (relative to the T_2 values of the tissues) for significant signal decay to have occurred by T_2 relaxation. This type of weighting is called proton density weighting and it can be used to distinguish between tissues that have low proton density (i.e. lung) and those that have T_2 times that are very short (i.e. liver). These tissues would both appear dark on an image that had a TE $> T_2$ time of liver (as can be seen in many of the images in chapter 4).

MR images can also be weighted so that their contrast emphasizes differences in T_1 relaxation rates. This can be achieved by shortening the repeat time (TR). The TR is the interval between two successive 90° RF pulses. Application of a 90° pulse rotates the NMV 90° from the longitudinal into the transverse orientation, and as a result the longitudinal component of the NMV is totally lost. The longitudinal component of the NMV must be allowed to recover before another signal can be generated. The amount of longitudinal magnetization that is recovered depends on the T_1 relaxation rate and the time allowed for recovery to occur, which is the TR. Tissues with a shorter T_1 time will recover their longitudinal magnetization faster and will have a larger longitudinal component of their NMV available to rotate into the transverse plane at an earlier time

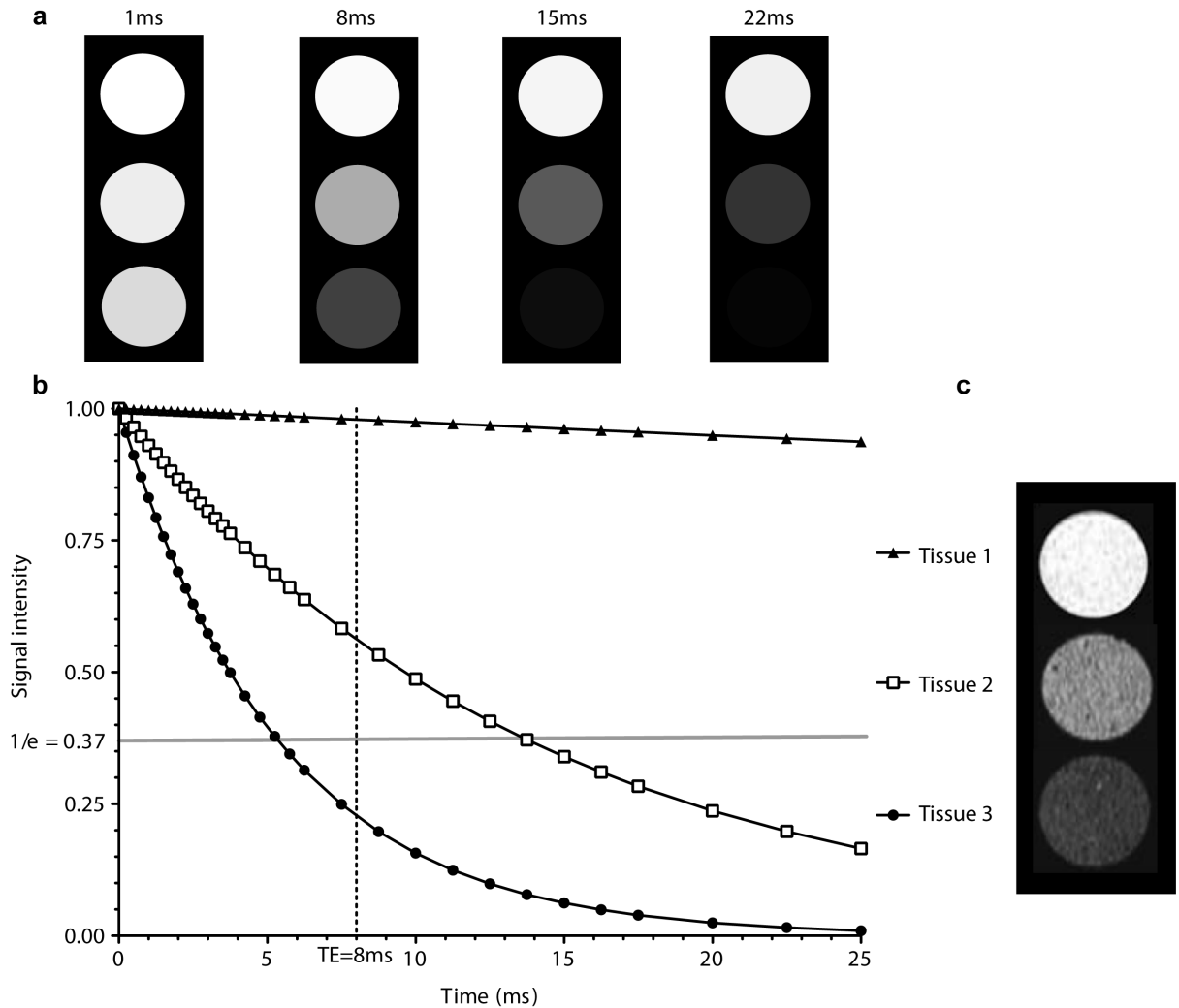


Figure 1.7: The effect of echo time (TE) on T_2 contrast. The transverse relaxation of three different tissues (1% agar gels containing FeOx NPs in tissue 2, and Fe NPs in tissue 3) were analysed at 9.4T using a spin-echo sequence (b,c). Each point represents the signal intensity at a given echo time relative to the initial signal intensity (at $t = 0$). Curves were fitted by using a monoexponential decay. The point where each curve intercepts the line drawn at signal = $\frac{1}{e}$ (b, solid horizontal line), represents the T_2 time of the tissue. The line drawn at 8 ms (b, dashed vertical line) represents the echo time (TE) used for imaging the tissues shown in (c). A simulation shows the contrast of each tissue at different echo times (a). (This figure contains data from Figure 3-8b and 3-9c, which is used here for illustrative purposes).

Table 1.2: The effect of TE and TR on image weighting.

Weighting	TE	TR
Proton density	short ($\leq T_2$ time)	long ($\gg T_1$ time)
T_1	short ($\geq T_2$ time)	short ($\leq T_1$ time)
T_2	long ($\leq T_2$ time)	long ($\leq T_1$ time)

point compared to another tissue with a longer T_1 time. If the TR is set to be equal or less than the T_1 time of the tissue of interest, any tissues with a longer T_1 time will have less signal rotated into the transverse plane by the second 90° pulse and will appear darker in the MR image. This is called T_1 weighting and can be defined by the use of a TR T_1 time of the tissue of interest. Table 1-2 summarises the differences in TE and TR used to weight image contrast for proton density, T_1 or T_2 relaxation.

1.1.12 Summary

MRI is versatile in its ability to distinguish different tissue types and disease processes with image contrast. Image contrast can be weighted to emphasize different tissue characteristics, such as T_1 and T_2 relaxation rates, by varying the echo time (TE) and the repeat time (TR) of the pulse sequence. Further image contrast can be produced with the use of contrast agents. Gadolinium based contrast agents enhance T_1 contrast and are the most widely used contrast agent, although concerns with their toxicity have emerged in recent years. T_2 contrast can be enhanced with the use of magnetic nanoparticles, which are the main focus of this thesis. In summary, these principles form the basis of MRI contrast and they are applied throughout this thesis.

1.2 Magnetic nanoparticles as T_2 contrast agents

Magnetic NPs play a significant role in many biomedical applications of magnetic resonance imaging (MRI), including liver imaging²⁸, detection of lymph node metastases³⁸, tracking of therapeutic cells³⁹ and imaging macrophages in diverse processes from strokes^{40,41} to organ graft rejections^{42,43}. The only commercially available T_2 contrast agents are FeOx NPs, due to their biocompatibility⁴⁴, ease of synthesis⁴⁵ and adaptability by alteration of their surface coating⁴⁶. Owing to a

significantly larger magnetic moment, Fe NPs have the potential to be more effective T_2 contrast agents but have proven very difficult to synthesize⁴⁷.

Each Fe NP contains a single crystal of Fe that is superparamagnetic, which refers to its large magnetic moment in the presence of an external magnetic field.

Superparamagnetic NPs possess a large magnetic susceptibility, which is the ability to align with and strengthen the external magnetic field they are exposed to. This is because the entire NP crystal aligns with the external magnetic field, due to its single crystal nature. Superparamagnetism can exist when the size of the single crystal NP is less than its ferromagnetic domain. For Fe NPs, this superparamagnetic size limit is less than 30nm³⁰. This is in contrast to paramagnetic materials, in which each atom aligns their individual magnetic dipoles with an external magnetic field, resulting in small magnetic susceptibilities with random orientations when there is no magnetic field present.

Through their large magnetic moments, Fe NPs can produce large changes in the local magnetic field, which causes a rapid dephasing of the spins of neighbouring protons, resulting in more efficient transverse relaxation. This can be seen as areas of signal hypointensity (i.e. dark region) on a T_2 weighted scan, as discussed in section 1.1. It is worth noting that superparamagnetic NPs do not directly cause a change in MRI contrast, rather they influence the MRI signal produced by proton spins in their vicinity. Although they are also able to affect longitudinal relaxation and produce T1 contrast, superparamagnetic NPs are primarily applied for their effects on T_2 contrast⁴⁸. The characterization of Fe NPs, including their size, crystal pattern, and effects on T_2 contrast are examined and contrasted with those of FeOx NPs in chapter 3.

1.2.1 Clinical applications of magnetic NPs

FeOx NPs that are clinically approved as intravenous MRI contrast agents in Europe or the US are shown in Table 1-3. Some FeOx NPs in later stages of clinical development are shown for comparison as are the Fe NPs and the FeOx NPs examined in this thesis. Note that the FeOx NPs used for lymph node imaging, Sinerem, have a size of less than 50nm (although the size of their FeOx core without the coating is only 6nm⁴⁹).

Sinerem's smaller size facilitates a longer circulation time in the blood, enabling them to reach macrophages in the lymph nodes, whereas the larger NPs are rapidly taken up in the liver and spleen, which are both rich in macrophages and have more permeable

Table 1.3: FeOx NPs developed for clinical applications (adapted from sources^{49,52})

Name	Approval	Application	T_2 relaxivity	size(nm)
Endorem/Feridex	US	liver/spleen	120	120-180
Sinerem	clinical	lymph nodes	65	15-30
Resovist	clinical	liver/cell labelling	189	60
FeOx NPs	preclinical	all of the above	145	65-75
Fe NPs	preclinical	all of the above	324	60-70

blood vessels⁵⁰. Despite this characteristic, Sinerem recently failed to gain approval for use in imaging lymph nodes from the European Medicines Agency following a large clinical trial due in part to its failure to improve the sensitivity of detecting cancer in lymph nodes by MRI⁵¹.

Early and accurate detection of lymph node involvement can improve the outcomes in a number of different cancers^{53–55}, and one of the most intensely researched applications of magnetic nanoparticles is in improving the MRI detection of cancer in the lymph nodes^{56,57}. FeOx NPs have been shown to improve the MRI diagnosis of metastatic tumours in the lymph nodes when the tumours are greater than 5mm^{57,58} or cause lymph node enlargement⁵⁹. However the sensitivity of detecting tumours that are smaller than 5mm with FeOx NPs decreases from 96% to 41%. Fe NPs, with a greater magnetic moment, have the potential to improve the sensitivity of MRI detection of smaller tumours in the macrophage-rich tissues of the liver, spleen and lymph nodes. The ability of Fe NPs to improve the MRI detection of small tumors above that of FeOx NPs is examined in chapter 4.

1.2.2 Tracking dendritic cells with Fe NPs

When applied to track therapeutic cells, MRI can provide important information to assist the development of novel cellular therapies. With their relatively long half life and low toxicity in labelled cells^{60,61}, FeOx NPs have been applied to track many

different cell types, including stem cells^{62,63} and immune cells^{64,65} involved in regenerative medicine and cellular immunotherapy respectively.

Cancer immunotherapy with dendritic cell (DC)-based vaccines has demonstrated tumour regression and prolonged survival in a modest number of patients with metastatic cancer^{66,67}. Evaluating the generation of specific immune responses following DC-based immunotherapy has proved challenging and potentially limits the development of more effective vaccines⁶⁸. In chapter 5, a novel *in vivo* strategy is developed which employs Fe NPs to assist DC tracking by MRI in order to detect an induced antigen-specific immune response to a DC-based vaccine.

1.2.3 The role of dendritic cells in cancer immunotherapy

DCs are immune cells present throughout the body that are critical for the induction of powerful and enduring immune responses by the adaptive immune system⁶⁹. DCs belong to a subset of cells called antigen presenting cells that are able to effectively take up and process molecules from the extracellular environment, migrate to lymphoid tissues and present them to cells of the adaptive immune system in a manner that can stimulate immunity⁷⁰. Collectively, the acquired molecules are known as antigens. The adaptive immune system has the ability to recognize and respond to specific antigens, then form long lasting memory that can enables a rapid immune response on re-exposure to the antigen.

The adaptive immune system evolved to protect the host from infectious pathogens through the generation of a diverse repertoire of antigen-specific cells that can respond to almost any antigen to which they are exposed. Two major divisions of the adaptive immune system correspond to the type of immune response that they produce.

Cytotoxic T lymphocytes (CTL), which are a specialised subset of CD8⁺ T cells, can directly eliminate cells infected with intracellular pathogens or tumour cells through a cytotoxic immune response. B cells can generate antibodies that recognise pathogen-associated antigens and promote the removal of the pathogen. These processes both require the participation of CD4⁺ T cells, also known as T helper cells, which produce cytokines that can support CTL⁷¹ and or B cell⁷² differentiation and proliferation. Furthermore, CD4⁺ T cells can produce effector responses in their own right⁷³.

Virtually all nucleated cells can process intracellular proteins, break them into peptides, and display them on their surface complexed to major histocompatibility complex (MHC) class I molecules⁷⁴. DCs, and other antigen presenting cells such as B cells, can process extracellular proteins in their environment and present them as peptides on MHC class II molecules. DCs can also present exogenous antigens on MHC class I molecules, which is known as cross-presentation⁷⁵. CTLs can recognize infected or malignant cells through binding between their T cell receptor (TCR) and specific peptide molecules presented on MHC class I molecules on the target cell. $CD4^+$ T cells bind specific peptides that are presented on MHC class II molecules by antigen presenting cells. These binding events are assisted by the CD8 and CD4 co-receptors, respectively⁷⁶. Depending upon the co-stimulatory signals from the environment, including DCs, antigen recognition by TCRs can result in a cascade of signaling events that can ultimately differentiate T and B cells to produce cytotoxic and humoral immune responses, proliferate, and form long lasting memory cells^{77,78}.

The hazard of having an adaptive immune system that can recognize and eliminate diverse antigens is that the antigen-specific T and B cell repertoire contains cells that recognize self-antigens and could potentially attack the host's own tissues. Control mechanisms exist to prevent immune responses to self-antigens and DCs are at the center of controlling the regulation and promotion of antigen-specific adaptive immune responses. Tissue-resident DCs that process pathogen-associated antigens are activated by "danger signals" associated with infection⁷⁹ (e.g. bacterial cell wall components) or tissue damage⁸⁰ (e.g. uric acid). When DCs become activated, they change from being benign regulators of immune homeostasis to pro-inflammatory cells with the ability to induce differentiation and proliferation of antigen-specific T cells. Activated DCs change their expression of surface molecules such as CD86, which have the ability to "co-stimulate" T cells that bind to the antigen presented on MHC molecules on the surface of the DC. This second signal is important in translating the danger signal to potent activation of antigen-specific T cells⁸¹. There are also positive feedback mechanisms whereby molecules expressed on stimulated T cells can produce further DC activation and release of cytokines that support T cell differentiation⁸². Activated DCs migrate from the tissues to draining lymph nodes, where they encounter a high concentration of lymphocytes. This facilitates the interaction of DCs with lymphocytes expressing receptors specific for the MHC molecules and antigen expressed on the surface of the DC. This migration of activated DCs from the tissues to the draining

lymph nodes is tracked using MRI assisted with Fe NPs in chapter 5.

Tumours can become targets for T cells when they express mutated proteins, known as tumour antigens, that the immune system regards as "foreign"⁸³. Unlike infectious pathogens however, tumours do not usually produce the correct "danger signals" required to activate DCs⁸⁴, resulting in an ineffective immune response⁸⁵. DC-based vaccines can overcome this obstacle through the administration of DCs that have been loaded with tumour antigen(s) and activation molecules in vitro. These DCs can produce potent immunostimulatory effects in vivo, resulting in antigen-specific CTLs that are able to eliminate tumour cells^{67,86}. The source of tumour antigens can consist of single peptides from defined tumour-associated proteins, whole tumour-associated proteins, tumour lysates or antibody complexes with proteins or cellular material⁸⁷. The goal of vaccination in cancer immunotherapy is to induce immunity against tumours through selectively stimulating antigen-specific CTLs and CD4⁺ T cells. DCs have been used as the basis of cellular vaccines against metastatic cancer for over a decade⁸⁸ in more than 1000 patients and 100 published studies⁸⁹. However, further testing is required to improve the response rate to beyond 10%⁹⁰. To address this need, two novel, MRI-based assays are presented in chapter 5 and 6 to detect the presence of an antigen specific response following DC vaccination.

1.2.4 Summary

The effectiveness of MRI in detecting small tumors and tracking therapeutic cells can be augmented with the use of magnetic nanoparticles as T_2 contrast agents. Fe NPs, with their larger magnetic moment, have the potential to further improve these applications beyond FeOx NPs, which are the current commercial standard. The application of Fe NPs to enhance T_2 contrast, cancer detection, cell tracking and the detection of immune responses following DC-based vaccination comprises the four experimental chapters which form the body of this thesis.

Chapter 2

Materials and methods

This chapter provides further details regarding the materials and methods used in this thesis. The information is presented in the order of its appearance in the figures from the results chapters 3, 4, 5 and 6. The methods are not repeated in later chapters unless there are modifications. A justification is given for the MRI sequences and statistical methods used in this thesis. As this was a multidisciplinary body of work with a large degree of variation in content between chapters, a discussion structure modelled on Docherty and Smith⁹¹ was applied to the results chapters in an attempt to maintain a cohesive structure throughout the thesis.

2.1 MRI scanning

The comparison between imaging at 9.4T and 1.5T was limited by the fact that in vivo scanning was not possible at 9.4 T, and T_2 mapping was not possible at 1.5T. These measurements are perfectly feasible in general but they were not possible in this study for logistical reasons concerning the access arrangements to the 9.4T NMR spectrometer and the 1.5T clinical MRI scanner. Comparisons were still able to be made between T_2 weighted images, and this explains why the in vivo data is presented as % reduction in T_2 contrast as opposed to a % reduction in T_2 time.

MRI pulse sequences used in this study were all weighted for T_2 contrast, using spin-echo based sequences. The question may be raised why T_2^* contrast, such as can be produced with a gradient echo pulse sequence, was not used. Magnetic nanoparticles

are known to produce strong T_2^* contrast through their magnetic susceptibility⁹². When gradient echo pulse sequences were applied at 1.5T, the contrast to noise ratio was significantly reduced compared to spin-echo sequences with the same resolution. Reduced contrast to noise ratio is an expected feature of T_2^* versus T_2 weighted sequences as there is accelerated decay of the transverse magnetization with T_2^* (as seen in Figure 1-3). The result was that the T_2^* weighted images were too poor for any gains in contrast sensitivity to be of benefit. A further reason for using T_2 measurements was for comparison with the literature, where T_2 values (such as T_2 relaxation time and T_2 relaxivity = r_2) are predominantly reported^{30,49}.

2.2 Statistics

For most of the experiments in this thesis, a normal (or Gaussian) distribution was assumed for the measured variables. This assumption was made in the context of a highly controlled biomedical environment with the use of congenic mice, sterile technique, the use of clonal cancer cell lines and the use of cellular vaccine aliquots from a common pool. These controls were made to decrease the chance of unmeasured variables influencing the measured variable in a non-random way. Each data set was checked by examining its scatter plot for any evidence of a deviation from a normal distribution. In all instances except one, there was no evidence of deviation from a normal population distribution of the sampled variables. Therefore parametric statistical tests were applied including student's t-test for two group comparisons and one-way analysis of variance (ANOVA) with a Bonferonni post-test for multiple group comparisons.

The analysis of T_2 weighted MR contrast in the lymph nodes (Figure 5-8) was prone to volume averaging effects due to the presence of adjacent subcutaneous tissue along the slice selection axis (which was three times as thick as the other two dimensions in order to increase contrast to noise ratio). These effects were not seen when the lymph nodes were imaged at 9.4T ex vivo in the context of better resolution (0.1 x 0.1mm with a 0.5 mm slice thickness and dissection of the peripheral tissue away from the lymph node. This finding suggests that the variation seen in the T_2 contrast in the lymph nodes in vivo was not an intrinsic property of the lymph nodes themselves.

The subcutaneous tissue surrounding the lymph nodes had a different rate of T_2 relaxation as the lymph nodes, so if it was averaged into the T_2 weighted contrast it

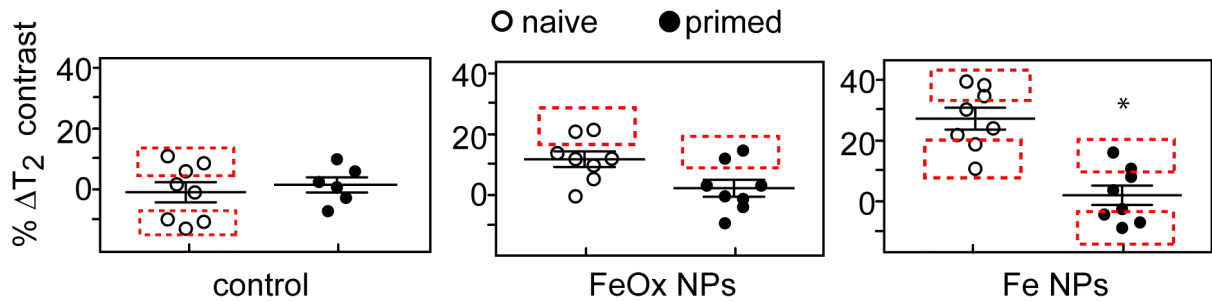


Figure 2.1: Non-parametric distribution of T_2 contrast in lymph nodes. T_2 contrast was measured in lymph nodes at 1.5T in vivo (Figure 5-8c) using a resolution of $0.3 \times 0.3\text{mm}$ with a slice thickness of 1.0mm . The red boxes indicate populations that deviate from a normal distribution, with two boxes per group indicating a bimodal population and one box indicating a skew population.

could change the measured T_2 contrast of the lymph node. This resulted in a non-normal distribution of T_2 contrast in the lymph nodes. The sampled populations possessed either a bimodal or a skewed distribution (Figure 2-1), presumably depending on the amount of subcutaneous tissue sampling in the slice selection axis. This was evident in most of the populations including control mice that received no injections of dendritic cells or NP contrast. This did not affect the measurements of the lymph node area in Chapter 6 because the distinction between the border of the lymph node and the subcutaneous tissue was clearly discernible in the plane of the image where area was measured (see Figure 6-1a). This could not be prevented with the use of fat saturation techniques, which suppress the signal from protons in lipid molecules, indicating that there were contributions to the volume averaging of the T_2 signal from water protons in the subcutaneous tissue.

It was therefore deemed appropriate to apply non-parametric statistics to the analysis of T_2 weighted MR contrast measurements in vivo. The Mann-Whitney rank sum test was applied to all two group comparisons with the Kruskal-Wallis test with a Dunn's post-test applied to multiple group comparisons. Unless otherwise stated, all error bars shown in graphs represent the standard error of the mean. All statistical calculations were produced with Graphpad Prism Version 4 (Graphpad Software Inc).

2.3 Methods from Chapter 3

2.3.1 Synthesis of Fe NPs

This method is the same as published by Cheong et al⁹³. All reagents were used as received without further purification. The iron precursor $\text{Fe}(\text{C}_5\text{H}_5)(\text{C}_6\text{H}_7)$ was prepared according to a previously described method⁹⁴. For the synthesis of iron nanocrystals, the iron precursor (0.4 g, ≈ 2 mmol), oleylamine (OLA) (2 mL, ≈ 6 mmol, Aldrich, 98%) and mesitylene (8 mL, Aldrich, 98%) were added to a closed reaction vessel (Fischer-Porter bottle), which was then flushed three times with hydrogen gas (H_2) before being filled with 100 kPa H_2 , and sealed. The bottle was placed into an oven heated at 130°C and remained for 2 days. The reaction was allowed to cool to room temperature naturally before the reaction vessel was opened to air. Each synthesis typically produced 60 mg Fe, which gave $\approx 50\%$ yield.

2.3.2 Synthesis of FeOx NPs

The nanoparticles were synthesized following a commonly adopted method⁹⁵. Briefly, under vigorous stirring, two solutions, (i) FeCl_3 (5.406 g, Aldrich, 99%) in 20 mL deionized (DI) water, and (ii) FeCl_2 (1.988 g, Aldrich, 98%) in 5 mL of HCl (2 M), were added to 100 mL DI water, to which 120 mL of ammonia solution (2 M) was added, and remained under stirring for 5 minutes. Black precipitate was purified by centrifugation at 3500 rpm for 20 minutes, and redispersed in DI water. The same purification process was repeated 4 additional times and the resulting precipitate was redispersed in 35 mL DI water. DMSA coating was applied using the same ligand exchange procedure for the core/shell nanoparticles.

2.3.3 Transmission electron microscopy

The transmission electron microscopy (TEM) images and electron diffraction patterns were taken on a JEOL 2010, with a LaB_6 filament operated at an acceleration voltage of 200 keV. TEM samples were prepared by dipping a carbon-coated TEM grid into the nanoparticle dispersion in toluene or water and allowing the solvent to evaporate under

ambient conditions. The size distributions were determined by counting 100 NPs of each type. The electron diffraction patterns were taken with a camera length of 30cm.

2.3.4 Ligand exchange with meso-2,3-dimercaptosuccinic acid

Ligand exchange to replace OLA with meso-2,3-dimercaptosuccinic acid (DMSA) was carried out based on known methods⁹⁶. The as-synthesized nanoparticle solution was sonicated briefly and divided into four equal portions. For each aliquot, the solution was dried in vacuum overnight to leave a powder, which was then dispersed in 20 mL of deionized de-ionised (DI) water. Separately, DMSA (20 mg, Aldrich, 98%) was added to 20 ml of DI water. The pH of both solutions was adjusted to 3.0 with HCl, prior to mixing the solutions. After adding the DMSA solution to the nanoparticle solution the pH was again adjusted to 3.0 with HCl under vigorous stirring and constant nitrogen bubbling, and remained for 30 minutes. The resulting mixture was centrifuged at 3500 rpm for 10 minutes, to give a black precipitate, which was redispersed in 20 ml DI water. The supernatant, comprising aqueous and oil (OLA) layers, was discarded. The pH of the product dispersion was adjusted with NaOH to 9.25-9.5 under constant stirring and was maintained for 30 minutes before lowering the pH to 7.4 with HCl. The resulting solution was centrifuged at 3500 rpm for 10 minutes. The supernatant was discarded, and the nanoparticles were dispersed in water or sterile phosphate-buffered saline (PBS), which was sterile filtered. The dispersion in PBS was used as stock solution and was stored at 4°C. The iron content of each stock solution was determined by atomic absorption spectrometry.

2.3.5 Measurements of hydrodynamic size with dynamic light scattering

DMSA coated Fe NPs or FeOx NPs were dispersed in water and filtered with a 0.2m syringe filter to remove dust particles and large aggregates. Their hydrodynamic sizes were measured by DLS at 20°C with a Malvern Zetasizer Nano ZS.

2.3.6 Determination of iron content by flame atomic absorption spectroscopy

All samples for measurement of iron concentration by flame atomic absorption spectroscopy (AAS) were first dissolved in 0.5ml of concentrated hydrochloric acid and diluted up to 3mL with de-ionized water. Standard concentrations of 2, 4, 10 and 20 $\mu\text{g ml}^{-1}$ of iron were prepared by dissolving iron wire in hydrochloric acid and serial dilution in de-ionized water. The measurements were made with a GBC 906AA spectrometer using an air-acetylene flame. A standard curve was made with the four standard concentrations and further dilutions were made of any sample that was not within the range of the standard curve. Measurements were made in triplicate and if there was more than 5% variation between instances then the measurement was discarded and performed again.

2.3.7 Measurements of T_2 relaxivity and MRI at 9.4T

Preparation of nanoparticle dispersion in agar: 2% agar was made up from dissolving agar powder (Aldrich) in de-ionized water and heating in a microwave until it reached a boil. The stock solution of Fe NPs or FeOX NPs was diluted with PBS to give concentrations of 1, 2, 3, 4, 10 and 20 $\mu\text{g ml}^{-1}$ of Fe in PBS. To 100 μl of each of the dilutions, 100 μl of 2% agar was added to give concentrations of 0.5, 1.0, 1.5, 2.0, 5.0 and 10.0 $\mu\text{g Fe ml}^{-1}$ in 1% agar. The control was prepared by adding 100 μl of 2% agar to 100 μl PBS. All samples were pipetted into plastic micro-PCR tubes (capacity 250 μl).

MRI of nanoparticles: MRI was performed using a Bruker Instruments AVANCE400 nuclear magnetic resonance (NMR) spectrometer, equipped with a Bruker Micro 2.5 imaging module. MR images were acquired at 9.4 T using a 2D multi-slice spin-echo sequence, at room temperature, with the following parameters: echo time (TE) = 8 ms, repetition time (TR) = 2000 ms, pixel size = 100 μm x 100 μm , slice thickness = 0.5 mm, number of echoes = 64, 4 averages, total experiment time = 16 minutes.

Measurements were repeated on four separate samples for each iron concentration for consistency.

Determination of transverse relaxivity (r_2) and imaging at 9.4T: Paravision software (Bruker) was used for MR image reconstruction and analysis. A region of interest was manually selected within the axial image of each nanoparticle, cell or

lymph node dispersion in agar. A plot of the signal intensity against the echo time was fitted with an exponential function: $S(t) = S_0 \exp(\frac{-t}{T_2})$; where $S(t)$ = signal intensity at time t , S_0 = signal intensity at 0ms, and the transverse time T_2 was then calculated. The plot of $\frac{1}{T_2}(\text{sample}) - \frac{1}{T_2}(\text{control})$ against iron concentration ($[\text{Fe}]$, in mM) was fitted with a linear function: $\frac{1}{T_2}(\text{sample}) - \frac{1}{T_2}(\text{control}) = r_2 \times [\text{Fe}]$; where the relaxivity r_2 was determined as the slope of the fit. This procedure was repeated four times for the Fe NP and the FeOx NP dispersions to determine the average and the standard error of the mean (SEM).

2.3.8 Culture of cancer cell lines

All cell culture was performed at 37°C, with 5% CO₂ and 95% humidity. The culture medium used was Iscove's Minimum Essential Medium (IMDM) supplemented with 5% foetal calf serum (Aldrich), 2mM glutamax, 100U/ml penicillin, 100µg ml⁻¹ streptomycin and 50µM 2-mercaptoethanol (all Invitrogen). This medium will be referred to in this thesis as complete medium and incomplete medium indicates the same medium without the foetal calf serum. All washing steps included centrifugation at 472 x g for 4 minutes in a Megafuge 2.0R (Heraeus Instruments) with the supernatant discarded and the cells re-suspended in the appropriate medium. The tumour cell lines used were based on lines originally from the American Tissue Culture Centre (ATCC). These cancer lines were not subject to genotypic confirmation for this study. The cell lines GL261 glioblastoma cells (GL261), B16F10 melanoma cells (B16), Henrietta Lacks cervical adenocarcinoma cells (HeLa), 4T1 breast carcinoma cells (4T1), EG7-OVA chicken ovalbumin-expressing thymoma cells (EG7ova) were cultured in medium described above. Gentecin selective antibiotic (Gibco, Invitrogen) was added to EG7ova culture at 0.5 mg/ml to maintain ovalbumin expression.

2.3.9 Labelling cancer cells with NPs

Fe NPs or FeOx NPs at 2µg Fe ml⁻¹ were added to cancer cells. The total amount of iron added was 50µg as the cells were cultured in 25mL media/flask. After incubation for four h, the media was removed from the flask and the cells were washed with sterile phosphate buffered saline (PBS). The adherent cells were detached with 0.25% Trypsin/EDTA (Gibco, Invitrogen), counted with a haemocytometer and dispersed at

500 cells μl^{-1} in 100ml PBS. A modification to this procedure was necessary for EG7ova cells as they are semi-adherent. After incubation with NPs, the cells were removed with the media from their flask, washed twice in PBS before being dispersed in PBS. 100ml of 2% agar was added to all of the cell dispersions followed by thoroughly mixing by repetitive aspiration with a micropipette.

2.3.10 Perl's stain

Two stock solutions of reagents were made with:

- 1) 20ml of concentrated HCl with 80ml of distilled water
- 2) 10g of potassium ferrocyanide trihydrate powder (Aldrich) with 100 ml of distilled water.

Cells were fixed in 10% buffered formalin (4% formaldehyde, Aldrich) on polylysine covered glass microscope slides. Perl staining was performed by first mixing equal volumes of reagents 1 and 2 and placing the slides in a Coplin jar containing the reagent mixture. The slides were removed after 10 minutes and placed in a dilute (0.1%) solution of Safranin-O in distilled water as a counterstain for 5 minutes. The slides were then successively dehydrated by 1 minute submersion in ascending gradients of ethyl alcohol - 70%, 80%, 90%, 100%. The slides are then cleared in xylol (Aldrich) for 30 seconds. Mounting media (Vision Mount, Thermo Scientific) and cover slip were then applied.

2.4 Methods from Chapter 4

2.4.1 Mice

All mice were handled in accordance with the Animal Ethics Policy 2008R7M, approved by the Animal Ethics Committee of Victoria University of Wellington. All mice were bred and maintained in the Biomedical Research Unit of the Malaghan Institute of Medical Research. Mice were not used in experiments until they reached 6 weeks of age. Breeding pairs of C57Bl/6 mice were originally sourced from the Jackson Laboratories, Bar Harbour, ME, USA. Balb/c breeding pairs were originally sourced from the Australian Research Council, Canberra, ACT, Australia.

2.4.2 Administration of NPs for in-vivo MRI

Nanoparticles dispersed in PBS (200 μ l) were administered either intravenously through the tail vein or subcutaneously into the hind limb of 6 week-old C57BL/6 mice. A control mouse was injected with the same volume of PBS, without the presence of nanoparticles. Doses of 3 μ mol Fe kg⁻¹ were employed for imaging the liver and 120 μ mol Fe kg⁻¹ for the spleen and lymph nodes.

2.4.3 In-vivo MRI

24 hours after injection of NPs, the mice were anaesthetized by intra-peritoneal (IP) injection of a ketamine/xylazine mixture in PBS (100/10 mg kg⁻¹, both from Phoenix Pharm). Lacrilube (Allergan) was applied to the cornea to prevent dessication. MRI was performed using a clinical 1.5 Tesla MR scanner (Philips Medical Systems), equipped with a wrist solenoid coil. The mice were positioned in the centre of the wrist coil and the same protocols were used for all images. T_2 -weighted multi-slice, multi-echo, spin-echo images were acquired with the following parameters: TE = 54 ms, TR = 2000 ms, pixel size = 300 μ m x 300 μ m, thickness = 1 mm, number of echoes = 8, averaged from a total of 3 scans, total experiment time = 4 minutes 24 seconds. Both an axial and coronal series of images were performed. Images were analyzed with ImageJ (National Institutes of Health) by manually selecting a region of interest (ROI) corresponding to the liver, spleen, upper hind limb muscles or inguinal lymph nodes and integrating the signal intensity of each ROI.

2.4.4 Histology

After MR imaging, the mice were euthanized by cervical dislocation and their tissues (liver, spleen or tumours) were removed and placed in formalin. They were then sent to the Wellington School of Medicine where they were embedded in paraffin and sectioned at 5 μ m thickness using a cryotome. Haematoxylin and Eosin (H&E) and Perl stains were performed on the sections as described in 2.3.10. Slides were examined under an Olympus IX51 optical microscope, with digital images recorded.

2.4.5 Administration of subcutaneous B16 tumours

B16 cells were cultured as in 2.2.8, and a dispersion of either 10^6 cells (Figure 4-4) or 10^5 cells (Figure 4-6) in $100\mu\text{l}$ of PBS was injected into the left flank of C57Bl/6 mice. Mice were checked daily for the development of tumours. Tumours were measured by calipers daily to ensure that no mouse had ulceration or a tumour measurement of more than 200mm^2 by day 7.

2.4.6 Addition of Herceptin-conjugated to Fe NPs to HeLa cells

Herceptin conjugation to Fe NPs: 10mg of EDC (1-ethyl-3-[3-dimethylaminopropyl]carbodiimide hydrochloride, Thermo Scientific) was added to 1ml of de-ionized water. Separately, $100\mu\text{g}$ of Fe NPs and $500\mu\text{g}$ of Herceptin (trastuzumab, Genentech) were added to 1ml of de-ionized water. The solutions were then combined, vortexed for 20 seconds and left at 4°C for 40 minutes. The solution was centrifuged at $1000 \times g$ for 10 minutes. The supernatant was discarded and the Fe NPs were resuspended in PBS. The iron concentration was determined by flame atomic absorption spectroscopy (Section 2.3.6).

Addition of conjugated NPs: HeLa cells were added to a 96 well plate at 5000 cells/well in PBS. The Herceptin-conjugated Fe NPs were added to the cells in triplicate at concentrations of 5, 12.5, 25 and $50\mu\text{g ml}^{-1}$ of Fe. As a control, unconjugated Fe NPs were added in triplicate to HeLa cells at the same concentration. After 100 minutes of incubation, the supernatant was removed from the plate. The cells were washed with PBS three times before being harvested for analysis by MRI and AAS.

2.4.7 Administration of intrasplenic tumours

For the tumor studies, 6 week-old BALB/c mice were anaesthetized by IP injection as described above. 10 and 5 mm incisions were made through the skin in the left hypochondrium and the peritoneum, respectively. The spleen was exposed and injected with 10^6 4T1 breast cancer cells. The peritoneum and skin were closed with 5.0 vicryl sutures (Ethicon) and the mice were given buprenorphine (0.1 mg kg^{-1} single dose, Phoenix Pharm) and carprofen (5 mg ml^{-1} , 2 doses 12 hours apart, Phoenix Pharm)

subcutaneously for analgesia. 72 hours after the cancer cell implantation the mice were anaesthetized by IP injection of ketamine/xylazine and MRI was performed (Section 2.4.3).

2.4.8 Scoring tumours

Two consultant radiologists were recruited to the study, both of whom had extensive experience reading MRI scans at a tertiary centre in New Zealand, and neither of whom had interpreted images with FeOx based contrast agents previously. They were given an example (Figure 4-8) of pre and post contrast images for mice with splenic tumours given Fe NPs or FeOx NPs intravenously. Their instructions were to score the mice with an integer from one to five (Table 4-1) according to the probability of an intrasplenic tumour being present. The images were on a DVD and were identified with only the scan number. They were advised to look through a dozen of the images at random to get an idea of the range of appearances before commencing scoring. Their scoring sheets were sent to an un-blinded investigator who analysed the results. No feedback was given to the radiologists on their accuracy until they had performed their second reading, which was at least one month from the first, and was performed without reference to their previous scoring.

2.5 Methods from Chapter 5

2.5.1 Bone marrow-derived dendritic cell culture

Preparation of BMDC culture: The bone marrow derived dendritic cell (BMDC) cell culture was prepared by first flushing the marrow cavity of the femur and tibia bones removed from 6 week-old C57Bl/6 mice using a 25-gauge needle and a syringe filled with complete medium, then passed through a 70 μ m cell strainer. Cells were cultured in complete medium supplemented with IL-4 and GM-CSF in 6 well plates at 2×10^6 cells in 5ml per well, according to the method developed by Lutz⁹⁷. IL-4 and GM-CSF were derived from the culture supernatants of Chinese hamster ovary mIL-4 and X63/GM-CSF cells, respectively, with optimal concentrations determined by titration. Non-adherent cells were harvested on Day 7 by gentle aspiration and

expulsion (5 times for each well) with an auto-pipette. The following substances were often added to BMDCs in culture, according to the specific experiment.

Addition of NPs: Fe NPs or FeOx NP labelling was performed by addition of 5g Fe ml⁻¹ on Day 5.

Addition of alpha-galactosylceramide: α -gal (α -galactosylceramide) was synthesized by Gavin Painter at Industrial Research Limited (Lower Hutt, New Zealand) according to a published method⁹⁸. α -gal was added to BMDCs as a vaccine adjuvant at a concentration of 200ng ml⁻¹.

Addition of LPS: To mature cells, a total of 500ng (=100ng ml⁻¹) of bacterial lipopolysaccharide (LPS, Sigma) was added to each well of the BMDC cultures on Day 6.

2.5.2 Cytotoxicity assays

Setting up BMDCS in a 96 well plate: BMDCs were cultured as in Section 2.5.1 but on Day 5 were transferred to a 96 well plate at 5000 cells/well in complete medium. Fe NPs and FeOx NPs were added at concentrations ranging from 0-200 μ g Fe ml⁻¹ in triplicate wells. As a control, wells with media only (no cells) were set up for every concentration of NPs.

Trypan blue exclusion for viability: On Day 7, 10 μ l aliquots were removed from each well and counted using a haemocytometer. Live cells were distinguished by the exclusion of trypan blue dye (Invitrogen).

MTT for metabolism: To test cellular metabolism, 20 μ l of 5mgml⁻¹ MTT (3-(4,5-dimethylthiazol-2-yl)-2,5-diphenyltetrazolium bromide, Invitrogen) was added to each well of the 96 well plate. The cells were incubated at 37°C for a further 4 hours then the medium was carefully removed. 150 μ l of DMSO (Aldrich) was added to each well to dissolve the crystals completely. The absorbance of the each well at 570 nm was then measured through a spectrophotometer (Versamax Plate Reader). Cell viability was expressed as a percentage of the control - absorbance of NPs only.

2.5.3 Flow cytometry

Antibody staining: Cells were stained with antibodies in 96 well plates at 4°C. The medium used was PBS containing 1% foetal calf serum, 0.01% sodium azide and 2mM

Table 2.1: Antibodies and fluorophores used in this thesis. The fluorophores in the table include PerCP (peridinin-chlorophyll-protein), PacBlue (Pacific Blue), FITC (fluorescein isothiocyanate), PE (phycoerythrin), Cy7 (cyanine 7), PETR (phycoerythrin texas red), APC (allophycocyanin), V450 and V500 (Horizon 450 and 500).

Antigen	Fluorophore	Source	Clone number
CD4	PerCP	BD	RM4-5
CD8	PacBlue	Biolegend	SK-1
NK1.1	FITC	BD	PK136
CD3	PE-Cy7	BD	145-2C11
CD62L	PE	BD	MEL-14
CD44	APC	BD	IM7
B220(CD45R)	PETR	BD	RA3-6B
CD11b	PE	eBioscience	M1/70
CD11c	APC-Cy7	eBioscience	N418
CD8	V500	BD	53-6.7
F480	PerCP	RD Systems	521204
Ly6c	PE-Cy7	Biolegend	RB6-8C5
CD86	V450	BD	GL1

EDTA. Non-specific Fc-receptor mediated antibody binding was blocked by incubation with anti-CD16/32 antibody (2.4G2, in house production). After blocking, cells were resuspended in medium with antibodies (Table 2-1) and incubated for 15 minutes. Cells were washed twice in medium and to distinguish dead cells, 50ng ml⁻¹ of propidium iodide (PI, BD Pharmigen) or 0.1μg ml⁻¹ DAPI (4,6-diamidino-2-phenylindole, BD Pharmigen) was added to the cells before acquisition.

Analysis: Flow cytometry was performed using a BD FACScalibur or BD LSRII SORP (Becton Dickinson) and analysed using FlowJo software (Treestar).

2.5.4 DC/peptide vaccine preparation

BMDCs were prepared as in Section 2.5.1 and were pulsed with SIINFEKL peptide (Ovalbumin peptide257-264, Genscript Corp) in complete medium for two hours. The cells were then washed twice in incomplete medium, then resuspended in PBS. Mice were vaccinated by intravenous injection of 10⁶ cells in 200μl of PBS through the tail vein.

2.5.5 VITAL assay

Peptide loading: The cytotoxic activity of CD8+ T cells induced by vaccinations was measured by the VITAL assay as originally described by Hermans et al⁹⁹. Syngeneic splenocyte populations were loaded with 50nM, 5 nM, and 0.5 nM SIINFEKL peptide in complete medium for two hours. Two washes in incomplete medium were performed to remove excess peptide and once in PBS.

CFSE labelling of cells loaded with peptide: Splenocytes with increasing peptide concentrations were then labelled with increasing concentrations (up to 2 μ M determined by titration of each batch) of carboxy-fluorescein succinimidyl ester (CFSE) (Molecular Probes) for 8 mins at room temperature. After incubation, an equal volume of foetal calf serum was added and cells were washed twice in complete medium and once in IMDM before injection into mice.

CTO labelling of control cells: As a control, splenocytes unlabelled with peptide were suspended in pre-warmed complete medium and CTO (Cell Tracker Orange, Molecular Probes) was added at a final concentration of 10 μ M. After incubation for 15 minutes at 37°C and centrifugation at 472 x g, cells were washed in complete medium and washed twice in incomplete medium. Equal proportions of all four cell populations were mixed together and 10⁷ cells were injected intravenously into groups of immunized and naïve mice.

Lymph node harvesting: The assessment of specific lysis of the peptide-loaded targets was assessed 24 hours later by euthanizing the mice by cervical dislocation and removing the axillary, brachial and inguinal lymph nodes. The lymph nodes were processed into a single cell suspension by passing through a fine (40 μ m) gauze mesh. The cells were analysed by flow cytometry (Section 2.5.3).

2.5.6 DC migration by CFSE labelling

BMDCs were prepared into a vaccine (Section 2.5.4) and were labelled with CFSE (Section 2.5.5) before subcutaneous injection at 10⁶ cells in 50 μ l of PBS into the upper hind limb of C57Bl/6 mice. The draining inguinal lymph nodes (on the same side as the injection) were harvested (Section 2.5.5) at 48 hours and analysed by flow cytometry (Section 2.5.3).

2.5.7 Lymph nodes ex vivo at 9.4 T in agar

BMDCs labelled with NPs (Section 2.5.1) and loaded with peptide (Section 2.5.5) were injected into the upper hind limb. The draining lymph nodes were harvested from mice (Section 2.3.6) 48 hours later and placed in PBS without being passed through gauze. The lymph nodes were dispersed intact into a 1% agar gel matrix and the T_2 relaxation time was determined at 9.4T (Section 2.3.7).

2.5.8 Tumour lysate preparation

Preparation of lysate: Tumour lysate from cancer cells was prepared by first harvesting GL261 or EG7ova cells in culture (Section 2.3.8), washing twice in PBS then placing 5×10^6 cells in 200 μ l of PBS in a plastic cryotube. The cells were snap frozen by immersion of the cryo tube into liquid Nitrogen. After 1 minute they were removed and placed in a hot water bath at 37°C. This freeze-thaw was repeated four times. After the final cycle, it was confirmed that no viable cells remained by trypan blue exclusion (Section 2.5.2). The protein content of the lysate was determined then the lysate was added at appropriate concentrations to BMDCs at Day 5 of their in culture (Section 2.5.1).

Determination of protein content: A Biorad Protein assay kit (BioRad) was used to determine the protein concentration of the tumour lysate. 5 ml of lysate and protein (bovine serum albumin, BioRad) standards were aliquoted to 96 well plate in triplicate. 25 μ l of Biorad Protein Assay Reagent A, then 200 μ l of Biorad Protein Assay Reagent B was added into each well. \approx 15 minutes was allowed for the reaction to proceed, with some colour change occurring immediately after the addition of Reagent B. Absorbance was analyzed at 750nm with a spectrophotometer (Versamax Plate Reader) and the lysate concentrations were determined with reference to a standard curve of the protein control.

2.6 Methods from Chapter 6

2.6.1 In vivo lymph node measurement

MRI scans were performed as described (Section 2.4.3). Measurement of the inguinal lymph nodes was performed using ImageJ. The area was measured by tracing around the border of the lymph node and its surrounding fat on a coronal slice. The area of each lymph node was taken from on the coronal slice in which it had the greatest area.

2.6.2 Cell gating strategies for flow cytometry of lymph nodes

Lymph nodes were harvested, processed (Section 2.5.5), counted and stained with antibodies for examination by flow cytometry (Section 2.5.3). Compensation was performed with anti-rat and anti-hamster compensation beads (BD). Cell types were defined by the gating strategy defined by the flow plots in Figure 2-2. The gates were set using flow data from the contralateral lymph nodes of the DC only group as these were the closest to a true naïve cell population. All cells went through two gates for singlets (to remove clumped cells) based on forward scatter area versus height then side scatter area versus height. All cells then went through a gate for forward and side scatter area to remove debris, and a DAPI negative gate to remove dead cells. Different cell types were then gated in the following way: CD4⁺ T cells (B220⁻/CD4⁺), CD8⁺ T cells (B220⁻/CD4⁺), B cells (B220⁺), NK cells (B220⁻/CD4⁻/CD3⁻/NK1.1⁺), NKT cells (B220⁻/CD3⁺/NK1.1⁺), DCs (B220⁻/CD11c⁺), monocytes (B220⁻/CD11c⁻/Ly6C^{Hi}) and macrophages (B220⁻/CD11c⁻/F480⁺). >95% of events were recorded from each lymph node for analysis as determined by comparison with cell counts using a haemocytometer.

2.6.3 Tumour protection studies

C57Bl/6 mice received a subcutaneous injection containing 10⁶ EG7ova cells in 100µl of PBS into the left flank, one week following vaccination. Mice were examined daily from day 6 and deemed to be positive for tumours when they developed a mass measuring greater than 4mm² by external calliper measurements. Mice were euthanized by CO₂

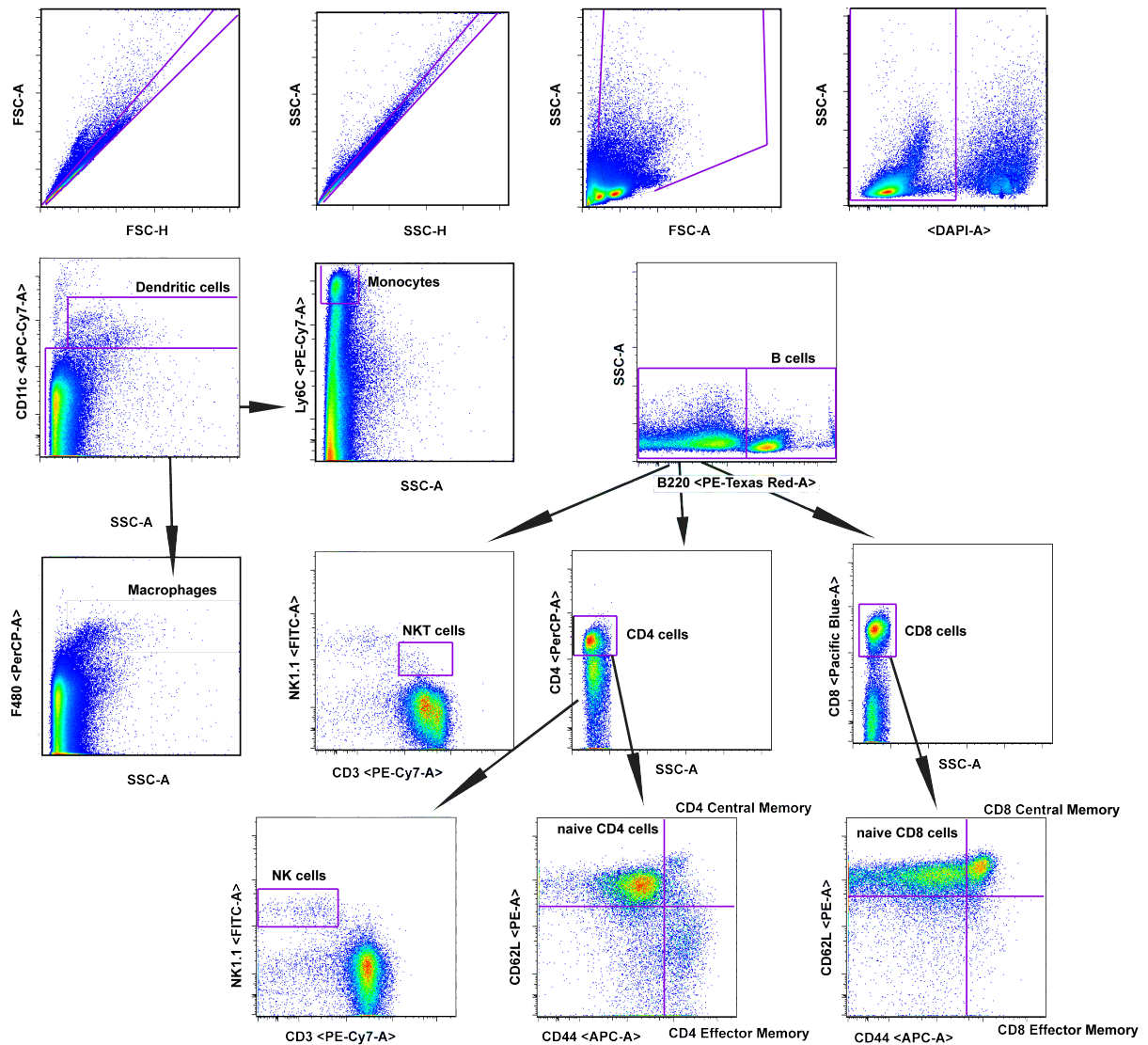


Figure 2.2: Flow cytometry gating strategies for cells recovered from lymph nodes. Gates are shown as polygons with purple boundaries, drawn on the flow plots from samples from contralateral lymph nodes in the DC only group. The top line shows the gates that all cells went through to exclude cell clumping, debris and dead cells. From the second line, arrows indicate the passage through a gate. Cell types are labelled next to the final gate they went through. The axes show the detector associated with the fluorophore-labelled antibody (Table 2-1).

asphyxiation or cervical dislocation when their tumour reached 200mm² or at the end of 60 days.

Chapter 3

Characterisation of Fe NPs for biomedical applications

3.1 Introduction

Magnetic nanoparticles (NPs) are effective in a range of biomedical applications including magnetic resonance imaging (MRI) contrast enhancement. For more than 20 years, iron oxide nanoparticles (FeOx NPs) have been used to enhance T_2 contrast in clinical MRI²⁸. A significantly larger magnetic moment and T_2 contrast effect can potentially be achieved with iron nanoparticles (Fe NPs), but development has been limited by difficulty in preparing stable particles. In this chapter, stable Fe NP prepared by a novel, simple, synthesis are characterised and compared with FeOx NPs as T_2 contrast agents in vitro.

3.1.1 Characterisation of magnetic NPs

There are multiple factors that determine the efficacy of MRI contrast produced by magnetic NPs applied in vitro^{46,100} and in vivo¹⁰¹. In addition, synthesis of NPs is complex because they are colloids¹⁰². Although the relationship between a NP's physicochemical characteristics and its efficacy as an MRI contrast agent are not yet well understood¹⁰³, the accurate characterization of size, crystal structure, hydrodynamic size as well as the effects on MRI contrast in vitro can be helpful in

assessing how a NP might perform as a contrast agent in vivo. This is particularly important in determining the reproducibility of a novel synthetic method³⁰.

The crystalline size of NPs can be measured by transmission electron microscopy (TEM). TEM allows the imaging of individual particles and by sizing significant numbers of NPs, the mean NP size can be estimated. The crystal size of NPs can be also be determined by X-ray diffraction where it is calculated from the line broadening on the diffraction pattern using the Scherrer formula^{104,105}. The size of a NP affects both its relaxivity and its biodistribution. Larger particles tend to have greater effects on T_2 relaxation within a certain range¹⁰⁶. Increasing a NP's size also increases its uptake into the liver and spleen¹⁰⁶ (see Chapter 4 for mechanisms).

The crystal structure of a NP can be determined by the electron diffraction produced using a TEM. The crystal structure has a large impact on the magnetic properties of a NP, and thus its effectiveness in producing MRI contrast by enhancing transverse relaxation. The different crystal structures of iron oxides have a wide range of magnetic susceptibility values and effects on T_2 relaxation, ranging from 0.3 emu g⁻¹ for haematite, 7-20 emu g⁻¹ for ferrihydrite to 92 emu g⁻¹ for magnetite¹⁰⁷. For the purposes of this thesis FeOx NPs refers to NPs containing a core of maghemite or magnetite. The crystal composition of the NP also affects its cytotoxicity, in particular when the NP contains transition metals or lanthanides, such as Co¹⁰⁸, Mn¹⁰⁹ or Gd¹¹⁰, with proven toxicity in humans.

The hydrodynamic size is commonly measured by photon correlation spectroscopy¹⁰³, otherwise known as dynamic light scattering (DLS). This gives the size of a NP including its surface coating. The hydrodynamic radius distinguishes the two main classes of commercial FeOx NPs, where NPs smaller than 50nm are referred to as ultrasmall superparamagnetic iron oxide (USPIO) particles and those larger than 50nm are referred to as merely superparamagnetic iron oxide nanoparticles (SPIO)¹¹¹. SPIO particles are used predominantly for liver imaging³⁰, as they are rapidly taken up by liver macrophages. USPIO, with their smaller size, have been used for blood pool and lymph node imaging as they have a longer elimination half-life from blood allowing them to reach deeper compartments¹¹².

The magnetic susceptibility of NPs can be measured in a superconducting quantum interfering (SQUID) magnetometer¹⁰⁵. A NP's magnetic susceptibility is related to its ability to enhance T_2 relaxation, in that NPs with a larger magnetic susceptibility can

induce more efficient T_2 relaxation of protons, resulting in greater T_2 contrast enhancement^{113,114}.

3.1.2 Synthesis of Fe NPs

Fe has the highest saturation magnetization at room temperature among all elements¹¹⁵ and is biocompatible, making it an ideal candidate for MRI contrast enhancement. Nevertheless, the development of Fe NPs for biomedical applications has been limited due to the difficulty in preparing Fe NPs that are stable to oxidation using simple synthetic methods and precursors^{115,116}.

Under ambient conditions, Fe NPs of 8 nm or smaller oxidize completely upon exposure to air¹¹⁷. For larger NPs, an oxide shell of 3-4 nm forms instantly on the surface, forming Fe/FeOx core/shell NPs. The synthesis of Fe NPs larger than 8 nm has been achieved by the decomposition of iron pentacarbonyl, $[\text{Fe}(\text{CO})_5]$ ¹¹⁶. Additional reports include the use of other precursors in forming iron nanocubes¹¹⁸. However, all of these processes are limited in terms of ease of synthesis and scalability; $[\text{Fe}(\text{CO})_5]$ is volatile and highly toxic¹¹⁵, and other processes involve precursors that are expensive and air-sensitive¹¹⁹, or require high decomposition temperatures¹¹⁸.

This thesis employs Fe NPs that have been prepared by a simple synthesis involving the decomposition of the Fe precursor, $\text{Fe}(\text{C}_5\text{H}_5)(\text{C}_6\text{H}_7)$, in the presence of oleylamine (OLA) stabilizing molecules¹⁰⁵. The sandwich compound was chosen for its simple preparation and ease of decomposition compared to other more stable sandwich compounds such as ferrocene¹²⁰. The synthesis was carried out in a closed reaction vessel under a mild hydrogen atmosphere, at 130°C. The temperature required was lower than the temperatures (150-300°C) required for decomposition of other iron precursors in previous studies. Once synthesized, the Fe NPs were exposed to air to allow oxidation of the surface, forming Fe/FeOx core/shell NPs. The oxide layer can be exploited as a passivation shell that prevents further oxidation¹¹⁷ and enables functional adaptation for biomedical applications using protocols established for iron oxides⁴⁵.

3.1.3 Aims

The aim of this chapter is to test the hypothesis that Fe NPs can produce more effective T_2 contrast than FeOx NPs by:

1. Characterising Fe NPs and FeOx NPs produced by simple synthetic methods in terms of their size, crystal structure and hydrodynamic radius
2. Developing a ligand exchange strategy and apply it to both Fe NPs and FeOx NPs to make them water dispersible and biocompatible
3. Examining the T_2 relaxivity of Fe NPs and FeOx NPs
4. Measuring the uptake of Fe NPs versus FeOx in multiple cell lines in vitro
5. Investigating the ability of Fe and FeOx NPs to improve T_2 contrast of labelled cancer cells in vitro

3.2 Results

3.2.1 TEM characterisation of Fe and FeOx NPs

The size and crystal composition of Fe-based NPs are important factors in determining their induction of transverse relaxation of water protons⁴⁹. This study was primarily concerned with how the addition of a Fe core affects the T_2 MRI contrast versus pure iron oxide particles and whether this could improve the biomedical applications of MRI. It was therefore important to compare the Fe NPs to FeOx NPs of similar size so that any differences observed in T_2 relaxation could be attributed to differences in their crystal composition and not their size. The size and crystal composition of the synthesized Fe NPs and FeOx NPs were examined by transmission electron microscopy (TEM) to produce images (Figure 3-2) and electron diffraction patterns (Figure 3-3).

The transmission electron microscope (TEM) has similar optics to a light microscope with several important differences (Figure 3-1). Firstly, the TEM uses a beam of accelerated electrons travelling in a vacuum with a wavelength of 2.5pm instead of visible light with wavelengths down to 400nm. This enables the TEM to resolve distances as small as several angstroms (10^{-10} m). Secondly, the lenses in the TEM are electromagnetic instead of glass and are able to focus the electrons into a very narrow

beam. When the electron beam hits the sample, electrons are transmitted through the sample and can be made to form an image after enlargement by passing through electromagnetic lenses.

As the distances between atoms in a crystal is of the same order as the wavelength of the electrons, the lattice planes of the crystal can act as diffraction gratings so that some electrons will be diffracted at the lattice planes producing an electron diffraction pattern. Lattice planes can be labelled using Miller indices which consist of a three integers h , k , and l , written (hkl) , which describe how the plane intersects the main axes of the crystal.

To determine the spacing of the lattice planes, the Bragg law describes the relationship between interplanar distance d and diffraction angle θ : $n\lambda = 2d\sin 2\theta$. Since the wavelength (λ) of the electrons is known, the distances between the lattice planes can be determined from the diffraction patterns (as seen in Figure 3-3). These distances are related to the size and position of atoms in the crystal and can be used to determine the crystal structure of the sample.

When imaged by TEM (Figure 3-2), the Fe NPs had a mean diameter of 16.1nm with a central dark core of 9nm. The FeOx NPs had a mean diameter of 15.4nm and there was a uniform density within each particle. The FeOx NPs were not as monodisperse as the Fe NPs, however 90% of the FeOx NPs (versus 100% of the Fe NPs) were within 2 nm of the mean of the Fe NPs.

3.2.2 Electron diffraction pattern confirms Fe NP and FeOx NP crystal structure

The electron diffraction pattern of Fe NPs (Figure 3-3a) showed ring patterns consistent with α -Fe assigned to the (110), (200), (211) and (310) lattice planes, and FeOx of spinel structure: either magnetite (Fe_3O_4) or maghemite ($\gamma\text{-Fe}_2\text{O}_3$) assigned to the (311) plane. Electron diffraction patterns produced using a TEM, called selective area electron diffraction (SAED), can not differentiate between magnetite and maghemite¹²². The spinel structure assigned to FeOx within the Fe NPs is consistent with the structure of the passive FeOx film that forms on the surface of Fe¹²³.

This is a key finding because it verifies the presence of α -Fe in the Fe NPs, which is highly magnetic. Pure α -Fe NPs of a similar size have a reported magnetisation of 190

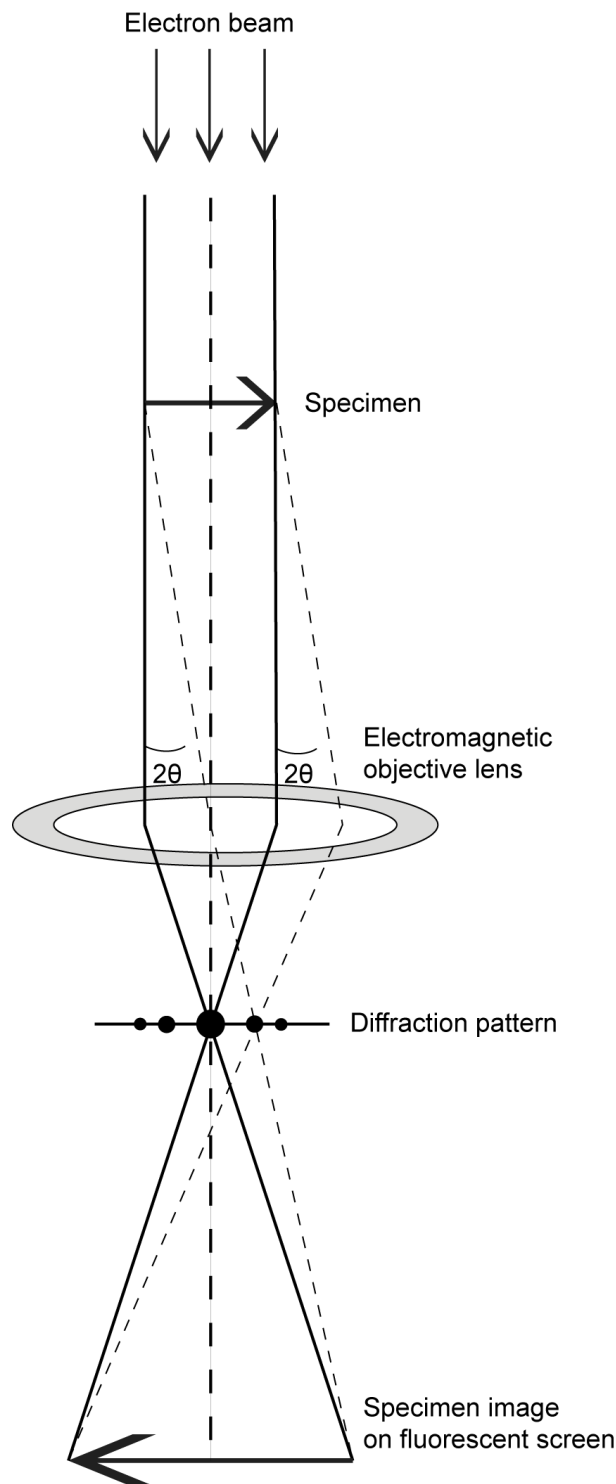


Figure 3.1: Beam diagram of a transmission electron microscope. The TEM electron beam is generated from an emission source such as a LaB6 filament and travels in a vacuum through a series of condenser lenses (not shown) before reaching the sample. Electrons transmitted through the sample are focused at the objective lens and are then magnified by a projector lens (not shown) to form an image on a fluorescent screen at the base of the TEM. Electrons diffracted by the sample form a diffraction pattern at the back focal plane of the objective lens. This pattern can be viewed on the fluorescent screen by adjusting the back focal plane of the objective lens to act as the objective plane for the projector lens. Diagram adapted from source¹²¹.

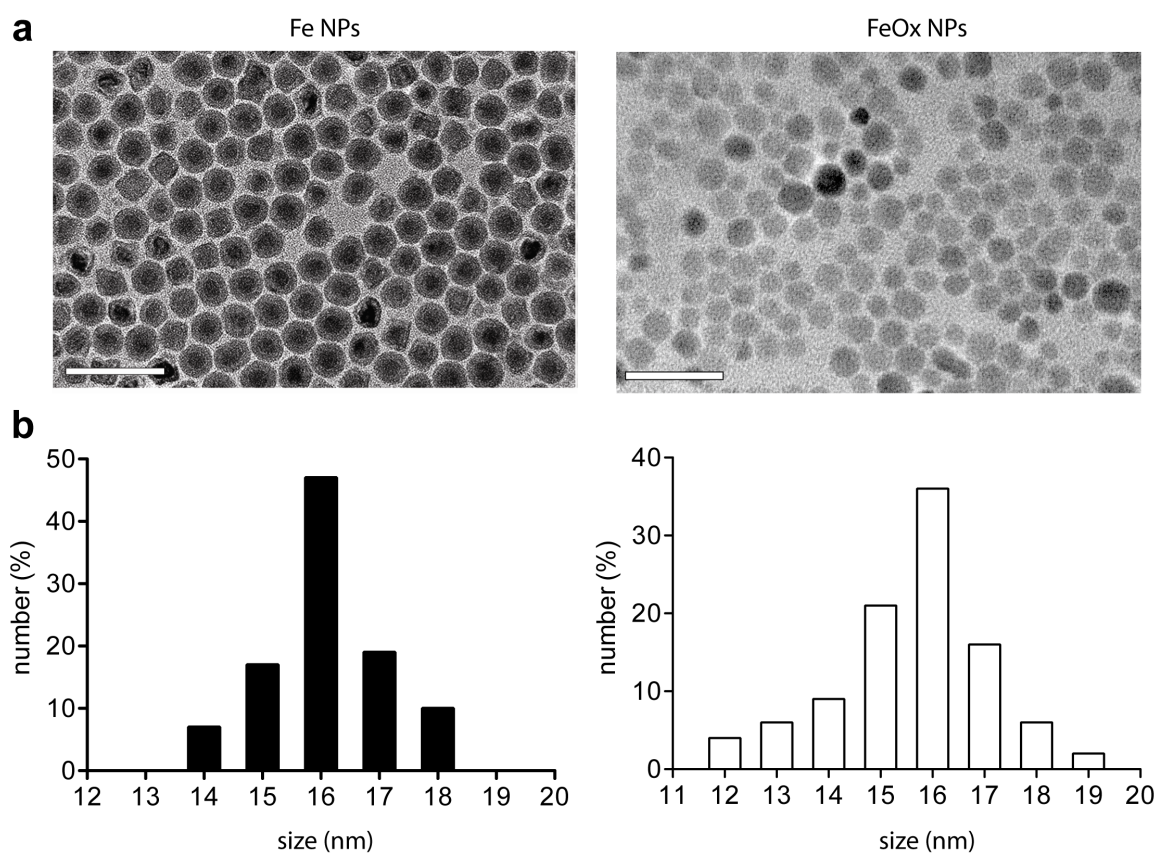


Figure 3.2: TEM images of Fe and FeOx NPs. Carbon coated TEM grids were dipped into toluene dispersions of Fe and FeOx NPs and were dried at ambient conditions before imaging at 200keV (**a**). The size distributions (**b**) were determined by counting 100 NPs of each type. (scale bar = 50nm, TEM image of Fe NPs taken by Soshan Cheong). The TEM measurement of Fe NPs was performed on multiple (>10) specimens with a representative result shown.

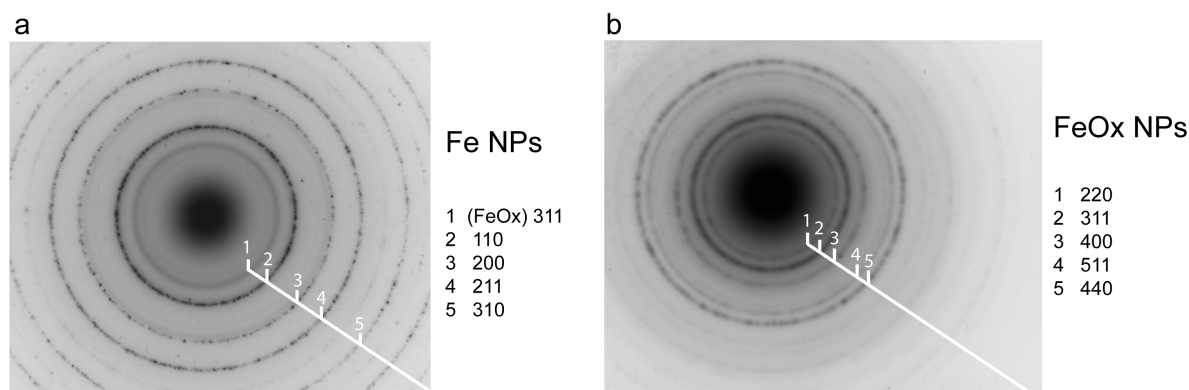


Figure 3.3: Electron diffraction patterns of Fe and FeOx NPs. Electron diffraction was performed on Fe NPs and FeOx NPs using a 200keV TEM. The ring patterns for Fe NPs (a) are assigned to planes of the crystal structures of α -Fe and spinel FeOx. The ring patterns for FeOx (b) are assigned to planes of spinel FeOx. (Electron diffraction pattern for Fe NPs taken by David Herman)

emu/g¹²⁴. The Fe NPs with the FeOx shell synthesized here had a magnetisation of 140 emu/g when measured at 2T in a superconducting quantum interfering (SQUID) magnetometer¹⁰⁵. This is a much higher magnetisation than that of 40-70 emu/g reported for pure FeOx¹²⁵.

The FeOx NPs synthesized were also subject to analysis electron diffraction pattern (Figure 3-3b). These NPs had a ring pattern consistent with the same spinel structure as Fe NPs, indicating magnetite or maghemite. This important finding suggests that the FeOx present in both types of NPs is of the same crystal structure. Sharing the same surface has important implications, as it may mean that pharmacokinetics will be similar, and that strategies for surface modification may be applicable to both types of NP.

3.2.3 DMSA ligand exchange to produce water dispersible NPs

After synthesis in an organic solvent (mesitylene) and coated with a hydrophobic stabilising molecule (oleylamine), Fe NPs require surface modification before they will readily disperse in aqueous solutions (Figure 3-4). This involves exchanging the hydrophobic oleylamine molecules on their surface with a hydrophilic ligand. There are a multitude of different molecules that have been chemically attached to the surface of

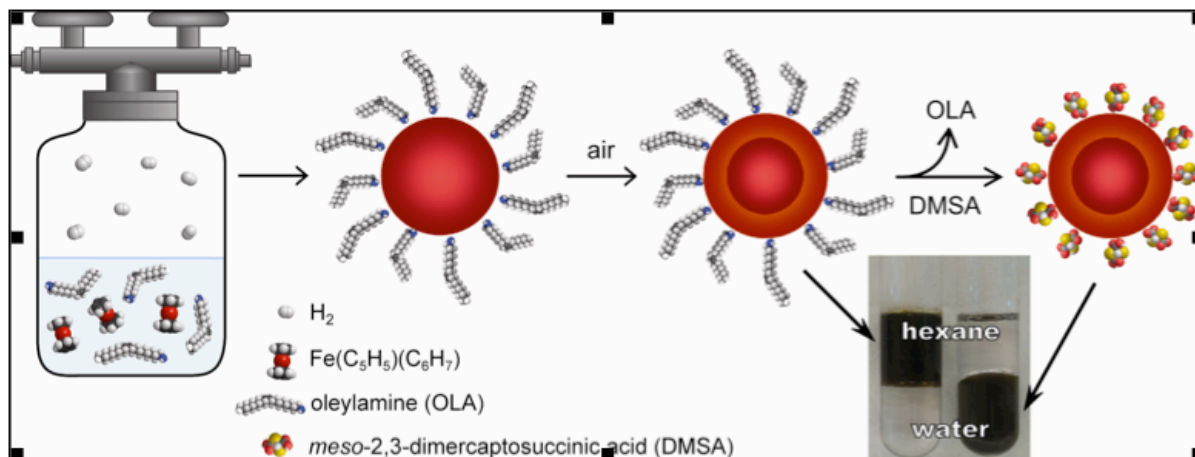


Figure 3.4: Schematic of synthesis and DMSA coating of Fe NPs Fe NPs were synthesized from a sandwich Fe precursor molecule in a closed container in the presence of oleylamine (OLA) and a hydrogen atmosphere. After exposure to ambient conditions an oxide shell forms. These NPs are dispersible in organic solvents such as hexane but not dispersible in water. Following ligand exchange with DMSA, the Fe NPs disperse readily in water. Schematic designed with Soshan Cheong.

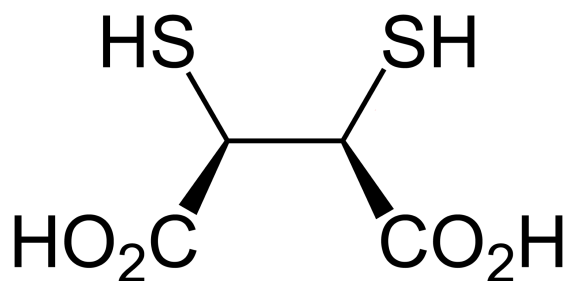


Figure 3.5: Meso-2,3-dimercaptosuccinic acid (DMSA). DMSA is an organic acid containing two carboxyl (COOH) and sulfhydryl (SH) groups. It can bind to Fe atoms on the FeOx surface of NPs through its carboxyl groups.

FeOx NPs to improve their stability in aqueous dispersions and to alter their pharmacokinetics⁵⁰. A water soluble, sulfhydryl containing compound, meso-2,3-dimercaptosuccinic acid (DMSA, Figure 3-5) was chosen as a coating molecule as it has an excellent safety profile in humans¹²⁶, having been used as a chelator for heavy metal poisoning since the 1950s¹²⁷. DMSA binds through its carboxyl group to Fe atoms on the FeOx surface of the NP¹²⁸, which assists in displacing oleylamine. Furthermore, DMSA has two different functional groups (a thiol and a carboxyl group) to which other molecules, such as antibodies can be readily attached for further functional specialisation^{129,130}.

3.2.4 The importance of pH adjustments during DMSA coating of NPs

One of the strategies used to assess the ligand coating of NPs is to determine their hydrodynamic size when dispersed in water by dynamic light scattering (DLS). Dynamic light scattering is performed by illuminating particles in a solvent with a laser and recording the scattering produced. The intensity of the laser scattering fluctuates at a rate that is dependent on particle diffusion in the solvent with smaller particles producing more rapid fluctuations due to Brownian motion. If the viscosity of the solvent is known then the hydrodynamic radius of the particles can be calculated from analysis of the time dependence of the intensity fluctuation. Comparing the hydrodynamic size of coated NPs to their TEM size before coating gives an indication of the coating thickness and to a larger extent, particle aggregation¹³¹.

To coat Fe NPs with DMSA, a method from the recent literature for FeOx NPs was adopted¹³². Fe NPs coated by DMSA using this method dispersed poorly in water with a mean hydrodynamic diameter of $> 1\mu\text{m}$ (Figure 3-6a), indicating significant aggregation of NPs. An earlier paper by Fauconnier et al detailed the importance of sequential pH changes to increase the stability of DMSA coated FeOx NPs in aqueous dispersions⁹⁶. The first pH adjustment (to pH 3) was shown to produce the maximum amount of adsorbed DMSA to the surface of the FeOx NPs. The next step is to remove the excess unbound DMSA by centrifugation and discarding the supernatant. The NPs are redispersed in water and the second pH adjustment is made to 9.25. This assists in the formation of disulfide linkages between adjacent molecules of DMSA to further stabilise them on the surface of the NPs. At this pH, the carboxyl groups on the unbound ends of DMSA are de-protonated and have a net negative charge which helps prevent particle aggregation by electrostatic repulsion of like charges. By applying these pH adjustments during the coating process, a superior aqueous dispersion was produced with a mean hydrodynamic radius of 62nm (Figure 3-6b). The same DMSA ligand exchange method was applied to FeOx NPs producing an aqueous dispersion with a hydrodynamic radius of 76nm (Figure 3-6c).

The Fe NPs and FeOx NPs coated by the improved DMSA method here have a similar hydrodynamic size to the 60nm commercial Resovist NPs which are FeOx with a dextran coating¹³³. These hydrodynamic sizes were much smaller than those reported for DMSA coating methods without pH adjustment¹³² where 10nm FeOx NPs had a

hydrodynamic diameter of 280nm after coating. The ratio of TEM pre coating to hydrodynamic radius post-coating reported here was 1:4, which compares with results reported with other coating molecules, such as dextran, where ratios of 1:3 up to 1:30 have been achieved^{30,125}.

3.2.5 Stability of Fe NPs over time

After producing a stable dispersion of Fe NPs in water, it was important to check for further oxidation of the Fe core, which would reduce its magnetisation and utility as an MRI contrast agent. Under ambient conditions, Fe NPs of 8 nm or smaller have been shown to oxidize completely upon exposure to air¹³⁴. Fe NPs were imaged by TEM before coating with DMSA (Figure 3-7a). After coating with DMSA the Fe NPs were dispersed in water and stored at 4 °C for six months. There were no changes observed in the overall size of the NPs or in the size of the FeOx shell (Figure 3-7b). This suggests that oxide shell is acting as a passivation layer preventing further oxidation which is a well described phenomenon in bulk Fe¹²³. Note that the size of the DMSA coated NPs measured by TEM (Figure 3-7) is significantly smaller than the measurements obtained by DLS (Figure 3-6). This can be explained by the loss of the hydration shell surrounding the NPs during the dehydration required for TEM, which is performed in a vacuum.

3.2.6 T_2 relaxation of Fe NP dispersions

The measurements performed up to this point had shown that the 16nm Fe NPs possessed a highly magnetic α -Fe core, were covered in an FeOx shell preventing further oxidation, and they dispersed in water after coating with DMSA. FeOx NPs had also been synthesized with the same crystal structure as the outer shell of the Fe NPs; they were of a similar size to the Fe NPs and they had been coated with the same molecule (DMSA). The efficacy of Fe NPs as T_2 contrast agents could now be directly compared to the FeOx NPs, and any major differences between the two NPs could be ascribed to the α -Fe core of the Fe NPs. The efficacy of T_2 contrast agents is assessed by measuring their effect on the transverse relaxation of the nuclear magnetic spins of water protons. This effect is known as T_2 relaxivity and it is defined as the amount of change in T_2 relaxation produced per unit concentration of contrast agent (unit: $\text{mM}^{-1}\text{s}^{-1}$). T_2

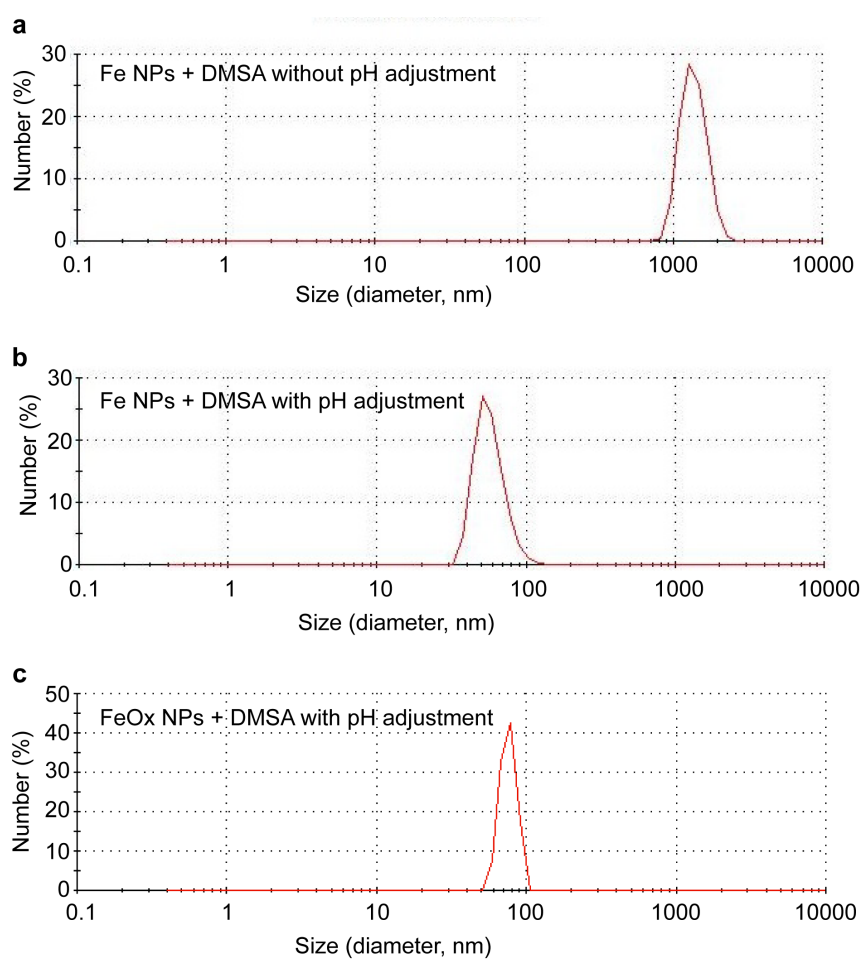


Figure 3.6: Hydrodynamic size of NPs in aqueous solution. The hydrodynamic size of NPs were analysed by dynamic light scattering (DLS) following coating with DMSA. Fe NPs were sized before (a) or after (b) adjusting the pH during coating as described in the text. FeOx NPs were sized after DMSA coating with pH adjustment (c).

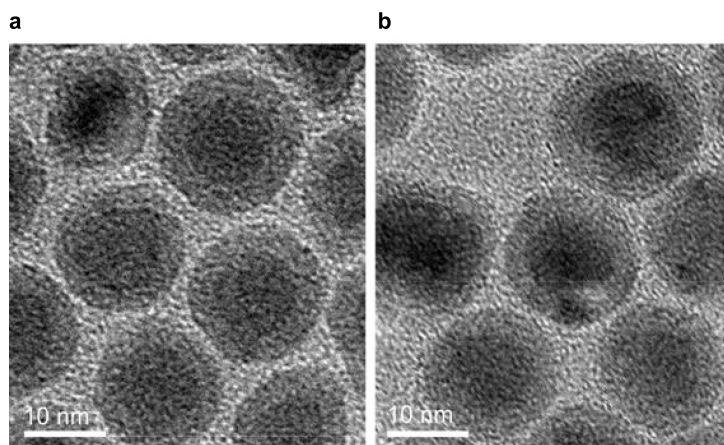


Figure 3.7: Stability of Fe NPs after DMSA coating. TEM images were taken of Fe NPs dispersed in hexane before coating with DMSA (**a**). The NPs were then coated in DMSA and dispersed in water for six months before being imaged (**b**). (scale bar = 10nm, images taken by Sujay Prakabar.)

relaxation can be measured by dispersing the NPs in an aqueous gel then analysing the gel by nuclear magnetic resonance (NMR). For these measurements, the gradients used in MRI to produce an image are not required because signal from the entire gel can be taken with no slice selection being necessary.

Fe NPs and FeOx NPs were dispersed at $5\mu\text{g Fe ml}^{-1}$ in 1% agar and analysed at 9.4T by a spin echo pulse sequence. This sequence corrects for magnetic field inhomogeneities by the use of 180° pulses so that T_2 relaxation and not T_2^* relaxation is being measured (refer Chapter 1). The T_2 times were calculated by using the monoexponential curve fit $S(t) = S_0 \exp(-t/T_2)$, where $S(t)$ is the signal at time = t and S_0 is the initial signal intensity at time = 0. The T_2 times for the Fe NP and FeOx NP groups can be seen on the graph where their curves intercept the horizontal line at signal = $\frac{1}{e}$. At this point the signal has decayed $\frac{1}{e} = 63\%$, such that the $S(t) = S_0 \exp(-1)$ and $t = T_2$. The vertical line at time = 8 ms is shown as this was the echo time at which the images in Figure 3-9a were taken. Fe NPs produced enhanced transverse relaxation relative to FeOx NPs with T_2 times of 5.4 ms versus 13.9 ms respectively (Figure 3-8). Both types of NPs produced large changes in T_2 relative to the control gel at 385 ms.

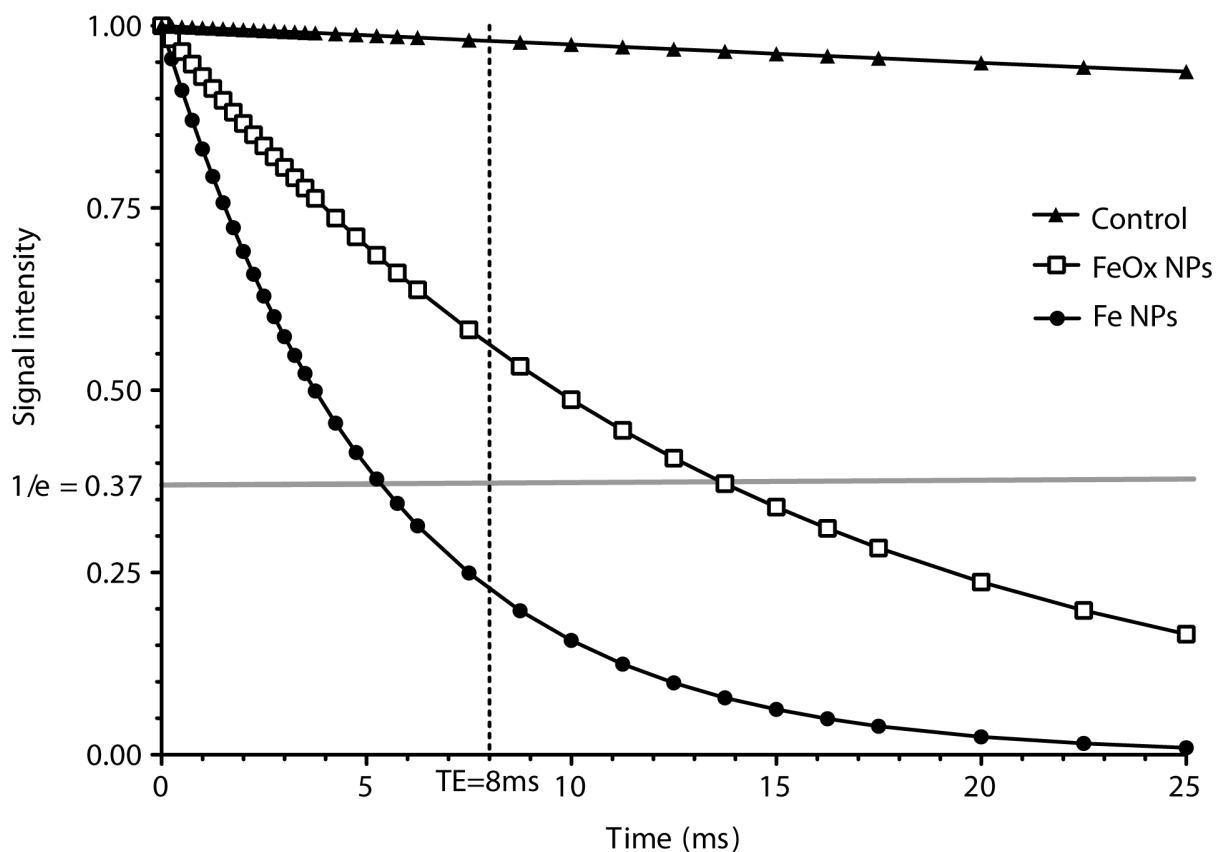


Figure 3.8: T_2 relaxation of Fe and FeOx NP dispersions at 9.4T. The transverse relaxation of dispersions of Fe NPs and FeOx NPs in agar were analysed at 9.4T using a spin-echo sequence. Each point represents the signal intensity at a given echo time relative to the initial signal intensity (at $t = 0$). Curves were fitted by using a monoexponential decay. The horizontal line drawn at signal = $\frac{1}{e}$ represents the intercept where time = T_2 . The vertical line drawn at $t = 8$ ms represents the echo time used for imaging in later Figure 3-9a.

3.2.7 T_2 relaxivity of Fe NPs

To calculate the T_2 relaxivity (r_2) for each type of NP, multiple measurements of T_2 relaxation were taken at varying concentrations of the NP dispersed in gel. Five concentrations of NPs were used to determine their r_2 (0, 0.5, 1.0, 2.0 and 5.0 $\mu\text{g Fe ml}^{-1}$), as seen in Figure 3-9. A linear relationship between the change in T_2 relaxation of the gels versus the concentration of NPs was observed as reported elsewhere¹³⁵.

The r_2 of Fe NPs taken from the slope of Figure 3-9b were plotted versus FeOx NPs in Figure 3-9c. The result was that Fe NPs had an r_2 value of 324 $\text{mM}^{-1}\text{s}^{-1}$ compared to 145 $\text{mM}^{-1}\text{s}^{-1}$ for FeOx NPs. Fe NPs therefore produce more than twice the amount of contrast as FeOx NPs on T_2 weighted images, which can be detected visually as darker images at each concentration relative to FeOx NPs in Figure 3-9a.

These r_2 measurements were taken after the Fe NPs had been in aqueous solution at 4°C for up to six months. There was no trend towards a reduction in r_2 over time (data not shown) suggesting that the highly magnetic α -Fe core remained intact. This observation, combined with the TEM data in Figure 3-7, is evidence that the Fe NPs are stable against oxidation for months in solution.

3.2.8 In vitro MRI contrast in cells labelled with NPs

To improve cellular imaging with MRI, it was necessary to show that the greater T_2 contrast effect of Fe NPs over FeOx NPs observed from dispersions of NPs was applicable also to dispersions of cells labelled with NPs. To undertake this analysis, cells from diverse tissue types were used, including cervix (HeLa adenocarcinoma cells), brain (GL261 glioma cells), immune system (bone marrow derived dendritic cells, BMDCs) and skin (B16 melanoma cells). These cells were cultured in the presence of Fe NPs or FeOx NPs at 2 $\mu\text{g Fe ml}^{-1}$. The cells were then washed, harvested, dispersed at 500 cells μl^{-1} in 1% agar and imaged at 9.4T.

In all cell types tested, labelling with Fe NPs resulted in at least twice the T_2 contrast versus labelling with FeOx NPs (Figure 3-10). This difference in T_2 contrast can be seen in the image of B16 cell dispersions in Figure 3-10a. It is interesting to note that there was no increase in T_2 contrast in the BMDCs versus the other types of cells, which are all cancer cells. BMDCs have phagocytic activity related to their function as antigen

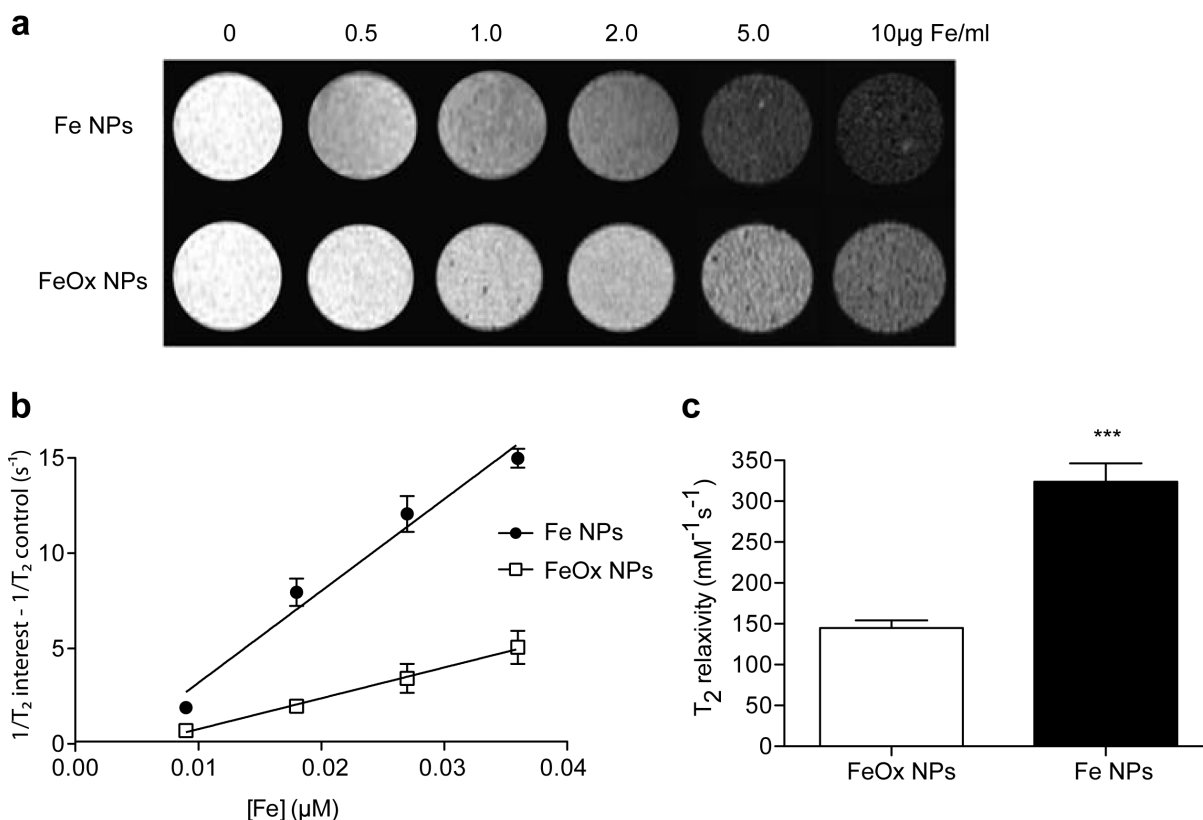


Figure 3.9: Relaxivity of Fe NPs and FeOx NPs at 9.4T. The T_2 relaxation of dispersions of Fe NPs and FeOx NPs in 1% agar were analysed at 9.4T using a spin-echo sequence. The images in (a) were taken at an echo time of 8 ms. The T_2 of each concentration of NP was determined as in Figure 3-8 and plotted as $(\frac{1}{T_2} \text{ sample} - \frac{1}{T_2} \text{ control})$ versus the concentration of NPs in the observed gel (b). A linear fit was made of the data in (b) and the slopes were plotted as r_2 in (c). A different slope was fitted for each batch of NPs to produce the standard error in (c). (***) $p < 0.001$ by two tailed t test).

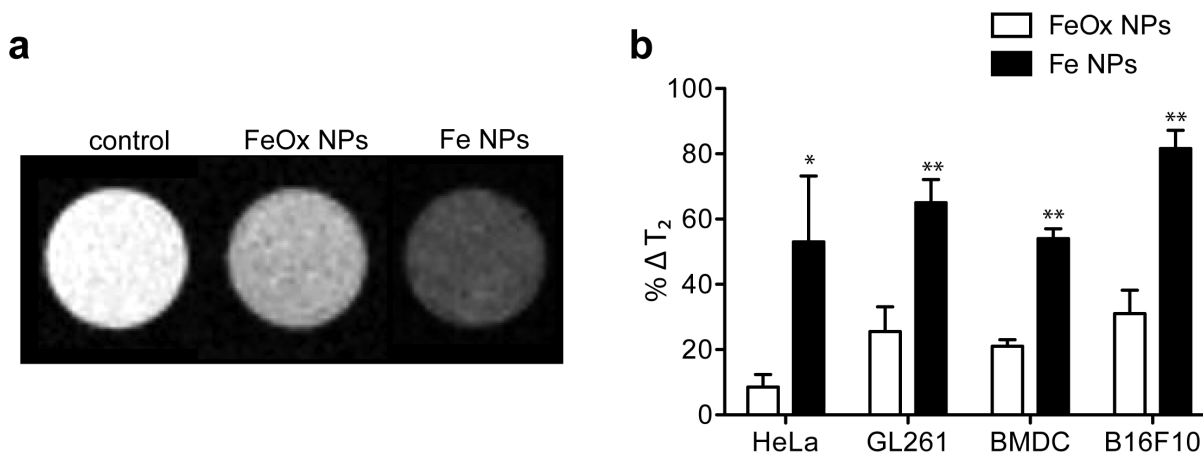


Figure 3.10: T_2 contrast in diverse cell types labelled with NPs in vitro. Cell dispersions of $500 \text{ cells} \mu\text{l}^{-1}$ in 1% agar were imaged at 9.4T using a multi-slice spin echo sequence with an echo time of 8ms. The T_2 times of the cell dispersions were determined by manually selecting a region of interest within the cell dispersion then plotting the T_2 relaxation as in Figure 3-8. (a) Images of B16 cell dispersions labelled with Fe NPs, FeOx NPs or PBS control. (b) The T_2 times were compared to that of the control cell layer and plotted as $\% \Delta T_2 = (T_2 \text{ control} - T_2 \text{ sample}) / T_2 \text{ control}$. (* $p < 0.05$, ** $p < 0.01$ by two tailed t test).

presenting cells and it is known that phagocytic cells such as macrophages are responsible for the majority of FeOx NP uptake in vivo. The in vivo uptake of Fe NPs will be examined in Chapter 4 and BMDCs will be discussed in further detail in Chapter 5.

In summary, the magnitude of cellular T_2 contrast improvement of Fe NPs over FeOx NPs is similar to the differences in their r_2 values, supporting the hypothesis that the improved r_2 of Fe NPs can be translated into improving the biomedical applications of FeOx NPs.

3.2.9 Fe uptake into cells

An alternative explanation could be proposed for the improved T_2 contrast of cells labelled with Fe NPs in Figure 3-8. Instead of Fe NPs producing more efficient transverse relaxation of water protons than FeOx NPs at the same dose of Fe, as indicated by a larger r_2 value, the intracellular uptake of Fe NPs could be more efficient, producing a greater concentration of Fe per cell. Therefore it was important to examine the Fe content of cells after incubation in the same dose of Fe NPs or FeOx NPs. B16

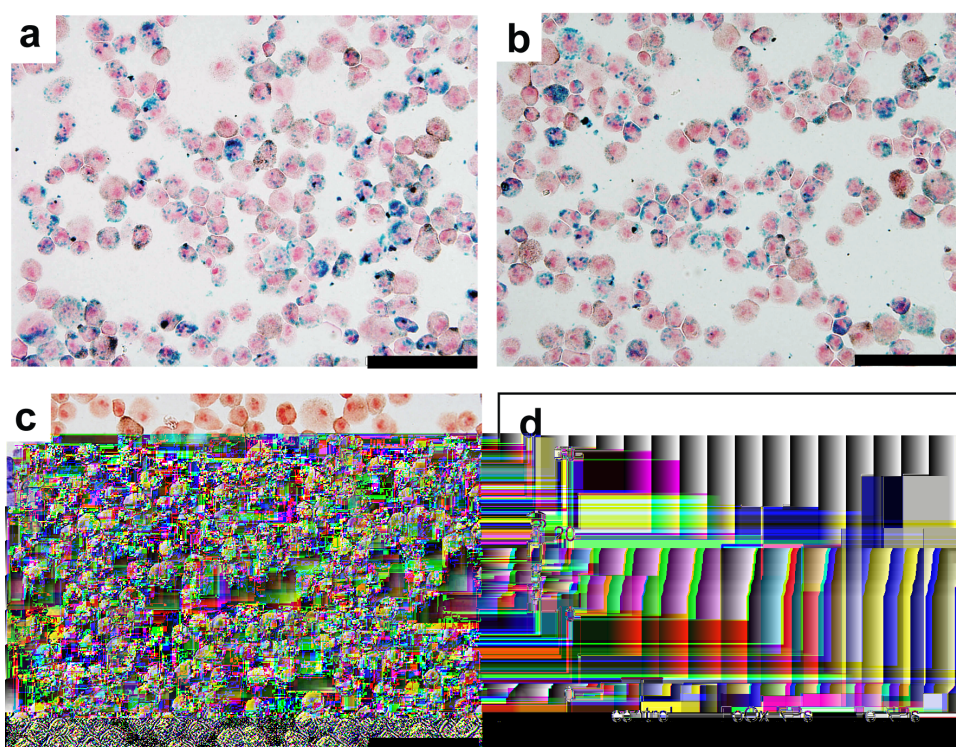


Figure 3.11: Fe content of cancer cells after labelling with Fe and FeOx NPs. B16 cells incubated with $2\mu\text{g}$ Fe/ml of Fe NPs (a) or FeOx NPs (b) were washed, harvested, fixed and stained with Perl's stain for Fe. A group incubated with PBS only was used as a control (c). Atomic absorption spectroscopy was performed on the three groups of cells to determine the quantitative Fe content per cell (d). (scale bar = $100\mu\text{m}$)

cells were incubated in NPs using the same method as for the cells imaged in Figure 3-10. After washing and harvesting, B16 cells were fixed and stained for Fe with Perl's stain. Images taken from light microscopy can be seen in Figure 3-11a-c. Fe uptake was qualitatively the same in cells labelled with either Fe NPs (a) or FeOx NPs (b), whereas no Fe was seen in the control cells that had not been exposed to NPs (c).

To produce a quantitative analysis of cellular Fe, flame atomic absorption spectrometry was performed where samples were dissolved in concentrated hydrochloric acid and atomised under an air/acetylene flame. Light of a specific wavelength, which is absorbed only by the atom of interest, is radiated through the stream of atoms in the flame. The amount of light absorbed at the specific wavelength is proportional to the concentration of the atom. The result of this analysis again showed that there was no significant difference in the amount of Fe acquired by cells incubated with either Fe NPS or FeOx NPs (d).

The findings from microscopy and atomic absorption spectroscopy show that there is a similar cellular uptake of Fe NPs and FeOx NPs in vitro. This finding is important because it provides further evidence that there is a qualitative difference in T_2 contrast produced by Fe NPs. Although there are severe limitations in making comparisons between in vitro and in vivo uptake, if a different rate of cellular Fe uptake was seen in vitro it would have cast doubt on the hypothesis that these Fe NPs and FeOx NPs, with the same outer shell and DMSA coating, would possess similar pharmacokinetics in vivo.

3.3 Discussion

3.3.1 Principle findings

Fe NPs were synthesized by a novel, simple technique and found to have a core of highly magnetic α -Fe surrounded by a shell of FeOx. Water-dispersible Fe NPs and FeOx NPs of a similar hydrodynamic size were prepared by ligand exchange with DMSA, and compared as MRI contrast agents. Fe NPs were found to have more than twice the T_2 relaxivity as FeOx NPs. When added to cancer cells in vitro, Fe NPs produced twice the T_2 weighted signal change per cell than FeOx NPs, despite the same amount of cellular NP uptake.

3.3.2 Implications of the study

A significant contribution to the field of MRI contrast agents from this research is the application of Fe NPs in biological systems. Fe NPs have been produced by other synthetic methods, but have had minimal testing in cell culture or animal models. Most studies of Fe NPs include magnetization data but no T_2 relaxivity or bioapplication data^{47,116,118,119,134,136–138}.

A comparison was recently performed of Fe NPs with different FeOx shells and doping with cobalt (Co) or manganese (Mn)¹³⁹. In this study, Yoon and colleagues measured the T_2 relaxivity of various Fe NPs and applied them to a cell detection assay in blood. They found that Fe NPs with the same overall size (16nm), oxide shell (magnetite/maghemite) and surface coating (DMSA) as used in this study, proved more sensitive when applied to the T_2 contrast-based assay than FeOx NPs, including those doped with manganese and cobalt. These findings were published in the same issue of *Angewandte Chemie* as work from this thesis¹⁰⁵ (see appendix). The strengths of the paper by Yoon et al were the comparisons of multiple NPs and the detailed magnetic studies with mathematical modelling. The paper from this thesis provided significant additional information by confirming that T_2 contrast differences were not due to varying uptake of NPs and that Fe NPs could improve the MRI diagnosis of small tumours in vivo (Chapter 4).

A criticism that could be raised against both of these papers is that they did not make comparisons with commercial FeOx NPs. The primary concern of both papers was to examine the effects of NPs with different metallic cores on T_2 contrast. As the relaxivity and cellular uptake of NPs is strongly affected by their size and coating molecules^{100,125,138}, it is important to compare NPs of the same size coated with the same coating technique. Furthermore, the T_2 relaxivity (r_2) values of the FeOx NPs used in these studies were similar or superior to all of the commercial FeOx NPs contrast agents currently on the market⁴⁹.

Although Fe NPs can induce more effective T_2 relaxation than pure FeOx NPs, there are FeOx NPs containing other metals and possess higher reported r_2 values than the Fe NPs in this study. Specifically, magnetic NPs have been synthesized with pure cobalt metal¹⁴⁰ and alloys such as FePt¹⁴¹, FeZn¹⁴², CoPt₃¹⁴³. FeOx NPs have also been doped with metals to improve their magnetic properties^{114,144}, forming structures with the general formula MFe_2O_4 , where M is a +2 cation such as Mn, Co, nickel (Ni) or Fe.

MnFe₂O₄ has reported r_2 values of similar magnitude to the Fe NPs in this study¹¹⁴, 358 versus 324 mM⁻¹s⁻¹ at 1.5T, respectively. When directly compared at 0.47T, Fe core/MnFe₂O₄ shell particles had a higher r_2 than Fe NPs similar to those used in this study¹³⁹. While these metal doped magnetic NPs may make excellent in vitro MRI contrast agents, cobalt¹⁰⁸, nickel¹⁴⁵, and manganese metals¹⁰⁹ have proven toxicity, making them unlikely candidates for clinical application. In contrast, Fe-based NPs degrade to non-toxic Fe and oxygen components, which is evidenced by their excellent safety profile in clinical studies¹⁴⁶.

The improvement of T_2 contrast with Fe NPs over FeOx NPs reported in this chapter has implications not only for clinical applications but also pre-clinical applications, such as stem cell tracking. There is increasing research involved with tracking stem cells in vivo by MRI after in vitro labeling with FeOx NPs, and several different types of applications have already been examined in clinical studies¹⁴⁷. The injection of mesenchymal stem cells (MSCs) represents a promising new therapy for regenerative medicine¹⁰⁶. There is a need to determine the fate of these cells after implantation, to ensure that they migrate to their intended location and do not become oncogenic following injection¹⁴⁸. It has been shown that MSCs maintain their pluripotent capabilities, including the ability to differentiate into functional cell lineages, after labelling with FeOx NPs^{149,150}. However, the sensitivity of detecting labeled cells by MRI is low, making it only possible to identify large clusters of cells in some studies^{151,152}. As shown in this chapter, labeling cells with Fe NPs improves the sensitivity of their detection by MRI, compared with cells labeled with FeOx NPs. Substituting Fe NPs for FeOx NPs could enable fewer cells to be detected or enable studies to be performed at MRI with lower field strength where sensitivity can be reduced by a lower signal to noise ratio¹⁵³.

3.3.3 Remaining questions

The aim of this thesis is to investigate whether Fe NPs can improve the biomedical applications of MRI. For this reason, Fe NPs are compared with FeOx NPs with the same surface coating across a range of applications. A question that remains unanswered is whether the same differences in T_2 relaxivity and the same similarities in cellular uptake, between Fe NPs and FeOx NPs, would have been observed if a different coating strategy was employed.

The coating molecules of a magnetic NP can affect the motion of water molecules near its surface by hindering water diffusion, immobilizing water molecules by forming hydrogen bonds, or exclude water molecules by hydrophobic interactions, all of which may affect the nuclear relaxation of water protons¹³¹. Although it is not well understood, the coating molecules can affect the T_2 relaxation and large differences in r_2 have been observed between different coating schemes, even when the core magnetic NPs are of the same crystalline structure and size¹⁵⁴. Although it is hypothesized that Fe NPs would still have a larger r_2 value than FeOx NPs, it is uncertain whether the difference in the r_2 values would have the same magnitude if a different coating strategy were employed.

A further question raised by the work performed in this chapter is whether Fe NPs and FeOx NPs will have a similar biodistribution in vivo. Very few studies have compared the uptake of Fe NPs and its effect on T_2 relaxation in different organs versus FeOx NPs in vivo. Differences in biodistribution compared to FeOx NPs could result in the failure of Fe NPs to produce effective T_2 contrast enhancement in various tissues. For example, if Fe NPs were to be rapidly removed from the blood by uptake into the liver, they may prove ineffective at imaging other tissues such as lymph nodes. This question will be addressed in the next Chapter.

3.3.4 Conclusion

Fe NPs were found to be twice as effective than FeOx NPs at producing T_2 contrast, when administered at the same dose, with the same surface coating and with a similar hydrodynamic size. Fe NPs have the potential to improve a range of MRI-based biomedical applications including cell tracking and tumour detection. Further studies with Fe NPs are required to investigate their cytotoxicity, pharmacokinetics and T_2 contrast enhancement in vivo.

Chapter 4

Improving the diagnosis of small tumours by MRI with Fe nanoparticles

4.1 Introduction

The early and accurate detection of a wide range of cancers can improve the prognosis and therapeutic options for the patient. Due to the characteristics of their cellular uptake in the body, FeOx NPs have been used to improve the diagnosis of cancer in the liver for more than 20 years. An active field of research is addressing whether FeOx NPs can improve the diagnosis of cancer that has spread to involve lymph nodes. This would have a large benefit to patients suffering from a range of cancers. Although there has been modest success in this endeavour, there is a suggestion that MRI with FeOx NPs is not able to effectively detect tumours in the lymph nodes at an early stage when they are smaller than 5mm. Fe NPs produce more effective contrast than FeOx NPs in vitro and therefore have the potential to improve the MRI diagnosis of smaller tumours in vivo. In this chapter, a mouse model involving tumours with a diameter of 1-3mm is employed to test whether Fe NPs can improve the diagnosis of small tumours⁵⁸ above that of Fe Ox NPs by two blinded, independent radiologists.

4.1.1 Mechanisms of cellular uptake of magnetic NPs

Fe NPs and FeOx NPs can be readily taken up *in vitro* by a number of different cell types without the use of transfection agents to improve uptake^{155,156}, as seen in Chapter 3. This is one of the advantages of their use in MRI-based cell tracking studies. However, following intravenous injection, the uptake of Fe NPs and FeOx NPs is primarily into the macrophage-rich tissues of the liver, spleen and lymph nodes^{157,158}. The mechanisms of cellular uptake of FeOx NPs has been studied in a range of cell types, and there are important implications for *in vivo* applications.

Labelling of cells with magnetic NPs is predominantly through surface attachment¹⁵⁹ or by endocytosis, a complex process with at least ten different pathways identified¹⁶⁰. Cellular uptake of magnetic NPs can occur via fluid phase endocytosis¹⁶¹, receptor-mediated endocytosis¹⁶⁶ or phagocytosis¹⁵⁸. Phagocytosis is the predominant pathway for uptake of large particles, such that FeOx NPs are more efficiently phagocytosed with a size >50nm¹⁶². Phagocytosis is enhanced when NPs are coated with antibodies or complement molecules, acting through the crystallizable fragment (Fc) of an antibody molecule or the C3b complement molecule, respectively. This process can be seen *in vivo* when the immune system reacts to a NP coating molecule, such as dextran, by producing anti-dextran antibodies¹⁶³.

Professional phagocytic cells, such as macrophages, are responsible for the majority of cellular uptake of FeOx NPs after intravenous administration³⁰. FeOx NPs accumulate in tissues with a large macrophage population and abundant vascular access, such as the liver and spleen¹⁶⁴, although their uptake into macrophages in other tissues such as transplanted organs can be identified¹⁶⁵. Macrophages possess scavenger receptors that are able to endocytose a wide array of NPs³⁰. *In vitro*, FeOx NP endocytosis by mouse peritoneal macrophages was dose-dependently inhibited by polyinosinic acid and fucoidan, suggesting that a scavenger receptor SR-A-mediated endocytosis is involved for this contrast agent¹⁶⁶.

Using human activated monocyte THP-1 cells, Feridex (120-180nm dextran coated FeOx NPs) was shown to undergo more intense macrophage uptake than Sinerem (15-30 nm dextran coated FeOx NPs), probably due to its larger size¹⁶⁶. Besides particle size, phagocytic uptake is also dependent on the surface properties of the NPs, as ionic carboxy-dextran coating of FeOx NPs of varying sizes leads to a higher uptake than nonionic dextran coating¹⁶⁷.

NPs can also be taken up by target cells via receptor-mediated endocytosis. Ligands, including monoclonal antibodies, can be conjugated to the surface of NPs to facilitate receptor-mediated endocytosis of the particles. Other targeting molecules including transferrin¹⁶⁸, ceruloplasmin¹⁶⁹, folic acid¹⁷⁰ and epidermal growth factor¹⁷¹ have been demonstrated to target cell surface receptors and improve endocytosis of FeOx NPs.

Uptake of NPs also occurs in vivo in cell types other than macrophages. Endothelial cells can endocytose FeOx NPs conjugated to molecules that target cell surface molecules¹⁷², T cells can be labelled in vitro with FeOx NPs without the use of vectors¹⁰⁰. Various cancer cells also uptake FeOx NPs without the use of vectors¹⁷³, in fact uptake has been shown to be more rapid in cells which proliferate quickly, which may be due to an increased rate of endocytosis¹⁷⁴. In Chapter 3 (Figure 3-11) and later in Chapter 5 (Figure 5-2), it is shown that cancer cells and dendritic cells can efficiently uptake both Fe NPs and FeOx NPs to a similar extent.

The cellular uptake properties of Fe NPs and FeOx NPs are important for their clinical application. In particular, the tendency of NPs larger than 50nm to be rapidly internalized by macrophages determines in which organs they can produce effective contrast. In all the cell types tested in vitro in this thesis, Fe NPs and FeOx NPs had similar uptake characteristics, which is likely due to their similar size and surface coating.

4.1.2 Aims

The working hypothesis in this chapter is that Fe NPs can produce better T_2 contrast in vivo than FeOx NPs that not only enhances contrast in the liver, spleen and lymph nodes but can improve diagnosis of tumours within these organs. This hypothesis will be tested in C57Bl/6 and Balb/c mouse models, using melanoma (B16) and breast cancer (4T1) cells, with MR imaging performed in a clinical scanner at 1.5T with interpretation performed by two consultant radiologists in an independent, blinded analysis. The following questions will be addressed:

1. Does Fe produce better in vivo contrast than FeOx in organs rich in macrophages?
2. How long does this contrast last for?
3. Can improved contrast be achieved by direct tumour uptake of Fe NPs?

4. To what degree does antibody-conjugation affect the specific uptake of Fe NPs?
5. Can Fe enable greater detection of tumours (in a splenic tumour model) than FeOx and/or no contrast control?
6. Can tumours smaller than 5mm be detected with Fe NP or FeOx NP contrast at 1.5T?
7. What is the inter-observer and intra-observer variability of NP-assisted MRI tumour diagnosis, and does diagnostic accuracy improve with training?

4.2 Results

4.2.1 Fe NPs produce greater T_2 contrast in the liver, spleen and lymph nodes in vivo

FeOx NPs have been used for over a decade as T_2 contrast agents for clinical imaging of the liver¹⁷⁵. Therefore the first evaluation of Fe NPs in vivo was to see how they compared to FeOx NPs in producing T_2 contrast in the liver after intravenous administration. A working hypothesis from the in vitro studies was that Fe NPs could produce around twice the change in T_2 contrast as FeOx at the same dose. The objectives for this series of experiments was to test this hypothesis in vivo to examine whether Fe NPs could a) enable a dose reduction and/or b) improve efficacy at the same dose.

Caution must be exercised in comparing doses of FeOx NPs in rodents versus humans due to the different pharmacokinetics observed across species. Rodents have more active uptake into the liver, with elimination half-life in rats is 2 hours versus 24-36 hours in humans⁵⁰. Therefore a larger dose is used to visualise other compartments in animal experiments. Furthermore, younger rodents have been demonstrated to have up to a 50% decrease in half-life of circulating FeOx NPs indicating enhanced uptake by liver macrophages¹⁷⁶. With these findings in mind, experiments with six week-old mice were performed with doses of Fe and FeOx NPs below the clinical dose used for liver scanning and above the clinical dose used for scanning other compartments.

For imaging the liver, a dose of $3\mu\text{mol Fe kg}^{-1}$ was chosen as this was equivalent to less than a third of the clinical dose of Feridex (a commercial agent used for liver imaging)

at $10\mu\text{mol Fe kg}^{-1}$ ¹⁷⁷. Fe NPs produced a 45% reduction in the T_2 weighted signal intensity in the liver versus 21% for FeOx NPs (Figure 4-1a,b). For imaging the spleen and lymph nodes, the dose was increased above the clinical dose of Ferumoxtran-10 (a commercial agent used for lymph node imaging) of $45\mu\text{mol Fe kg}^{-1}$ ¹⁷⁸. A dose of $160\mu\text{mol kg}^{-1}$ was used which is less than one fifth of the dose that can be used safely in mice ($935\mu\text{mol kg}^{-1}$)¹⁷⁹. At this dose, the T_2 - weighted signal intensity in the liver in both the Fe and FeOx groups was reduced by greater than 75% (see Figure 4-1c, 24 hours). However, in the spleen and lymph nodes, this higher dose of Fe NPs produced a 58 % and 25% reduction in the T_2 -weighted signal versus a corresponding reduction of 29% and 5% with FeOx NPs (Figure 4-2). These findings suggest that at higher doses, the liver uptake of NPs becomes saturated and greater uptake into other organs occurs, as demonstrated in other studies¹⁷⁸. Further evidence of liver saturation was seen in Figure 4-1c where the T_2 weighted signal in the liver was still reduced at 12 weeks compared to control. The important novel finding from these studies is that Fe NPs can produce twice the change in T_2 contrast in the liver, spleen and lymph nodes versus the same dose of FeOx NPs.

4.2.2 Histology of NP uptake into the liver

The working hypothesis was that Fe NPs produced greater changes than FeOx NPs in T_2 contrast due to greater effects on the transverse relaxation of water protons per unit of Fe (T_2 relaxivity) in the tissue of the liver, spleen and lymph nodes. However, a greater change in T_2 contrast could also be explained by an increased quantity in the uptake of Fe NPs over FeOx NPs in the tissues of interest. To test this hypothesis, mice were given a dose of $3\mu\text{mol Fe kg}^{-1}$ of either Fe NPs or FeOx NPs and imaged, as shown in Figure 4-1a. The mice were culled after scanning and their liver tissue was removed, sectioned and examined for the presence of Fe under light microscopy. As seen in Figure 4-3, there is increased Fe (blue stain) seen in the livers of mice that received Fe NPs or FeOx NPs over control mice that received PBS only. There was no qualitative difference in the amount of Fe in mice that received either Fe NPs or FeOx NPs. Quantitative analysis by atomic absorption spectroscopy was not useful in determining the amount of Fe uptake from Fe NPs or FeOx NPs due to the high background content of Fe in the liver (data not shown). The results from light microscopy here suggest that there is no substantial difference in the uptake of either NP in the liver, which supports the

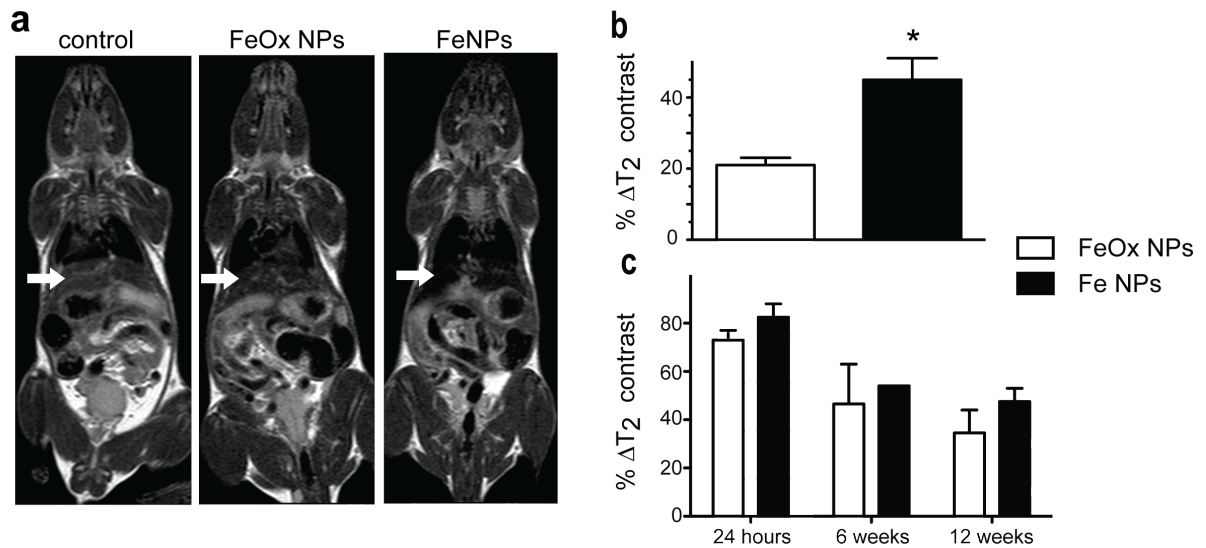


Figure 4.1: Contrast in the liver following intravenous Fe and FeOx NPs. For imaging of liver contrast, mice were given $3\mu\text{mol Fe kg}^{-1}$ (a, b) or $160\mu\text{mol Fe kg}^{-1}$ (c) of Fe NPs or FeOx NPs intravenously and imaged 24 hours later at 1.5T. A control group was imaged which received injections of PBS only. The mice receiving $160\mu\text{mol Fe kg}^{-1}$ NPs were imaged again at 6 weeks and 12 weeks without receiving further contrast agents (c). For all images the signal intensity was measured by first calibrating the signal intensity in the organ of interest with a reference of skeletal muscle in the same image. The values for each organ of each mouse in the Fe NP and FeOx NP groups were then compared with the corresponding mean of the control group and plotted as $\% \Delta T_2$ contrast as follows: (signal intensity mean of all control organs)-(signal intensity in organ of mouse of interest)/ (signal intensity mean of all control organs). ($p < 0.05$ by Mann-Whitney rank-sum test).

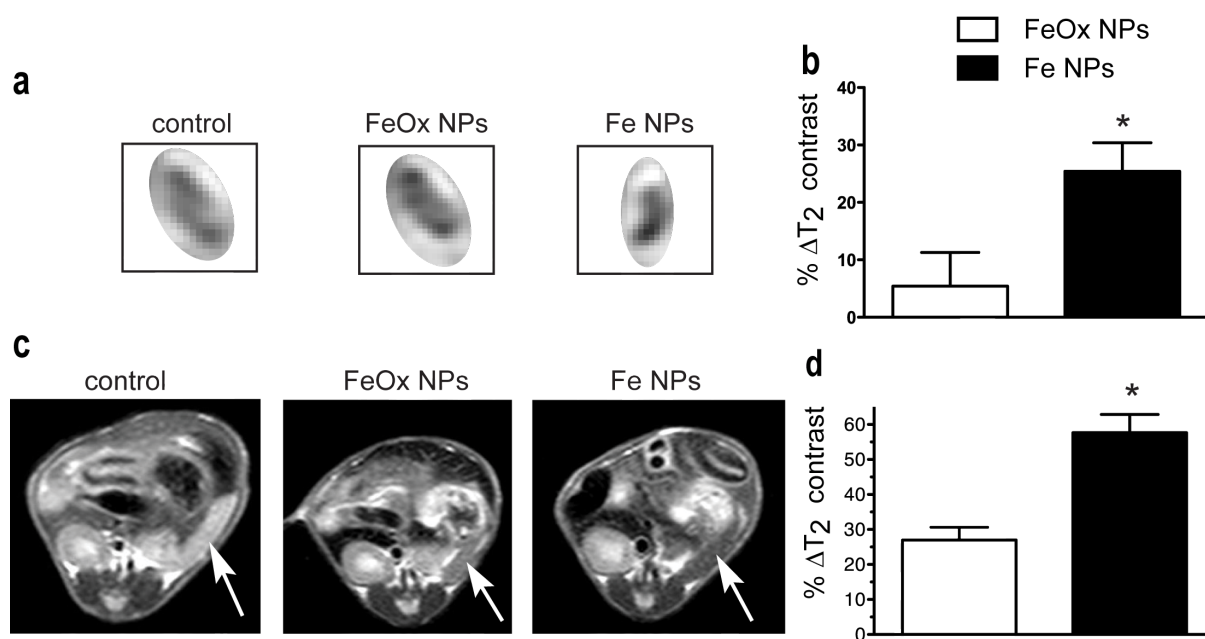


Figure 4.2: Contrast in the spleen and inguinal lymph nodes following intravenous Fe NPs and FeOx NPs. For imaging of contrast in the inguinal lymph nodes (**a,b**) and spleens (**c** (arrow),**d**), a dose of $160\mu\text{mol Fe kg}^{-1}$ was administered intravenously and the mice were imaged 24 hours later at 1.5T. A control group was imaged which received injections of PBS only. The images were analysed and results plotted using the same method as described in the previous figure. ($p < 0.05$ by Mann-Whitney rank-sum test).

hypothesis that the difference in T_2 contrast is produced by the greater T_2 relaxivity of Fe NPs.

4.2.3 Direct tumour imaging in vivo with a subcutaneous melanoma model

The majority of clinical and biomedical studies which employ FeOx NPs as MRI contrast agents to improve tumour detection do not target the tumour directly. Instead, the NPs are taken up by macrophages in the surrounding normal tissue (parenchyma) of the liver or lymph nodes where cancers often metastasize. This limits the use of FeOx NPs to detecting cancers that have spread to (or in some cases, have originated from) these organs. Some studies in the literature report selective tumour targeting in vivo with FeOx NPs that have specialised surface coatings, including the conjugation of antibodies that recognise specific molecules on the surface of a tumour¹⁸⁰. This approach was investigated here to examine whether the uptake of NPs into tumours could be improved by surface conjugation with antibodies and to determine whether Fe NPs could provide enhanced tumour detection. The first step was to examine the uptake of NPs without any antibody conjugation into tumours in vivo. The previous chapter showed that there was effective uptake of Fe NPs and FeOx NPs into a range of cancer cell lines in vitro (Figure 3-10). This was not assured to be the case in vivo due to both the competing uptake of NPs by macrophages in other tissue and the limitations in accessing the tumour microenvironment - parts of which have poor vascular supply, raised interstitial pressure and can be difficult to penetrate by molecules smaller than NPs, such as antibodies¹⁸¹.

To test the non-specific uptake of NPs by tumours in vivo, a subcutaneous melanoma model using B16 cells was employed. Fe NPs were administered at $160\mu\text{mol Fe kg}^{-1}$ intravenously to mice after they had developed significant subcutaneous tumours. As discussed above, this dose of NPs produces a saturation of the liver and enhances uptake into other compartments. Mice were imaged 24 hours later and the T_2 weighted signal in skeletal muscle of each mouse was compared to the signal in its liver, inguinal lymph nodes and tumor. Similar measurements were made for control mice with tumours that received no NPs. These measurements were made to assess the effect of Fe NPs on the T_2 contrast in the tumour compared to other tissues where FeOx NPs have been shown to accumulate and produce effective contrast (liver, lymph nodes) or

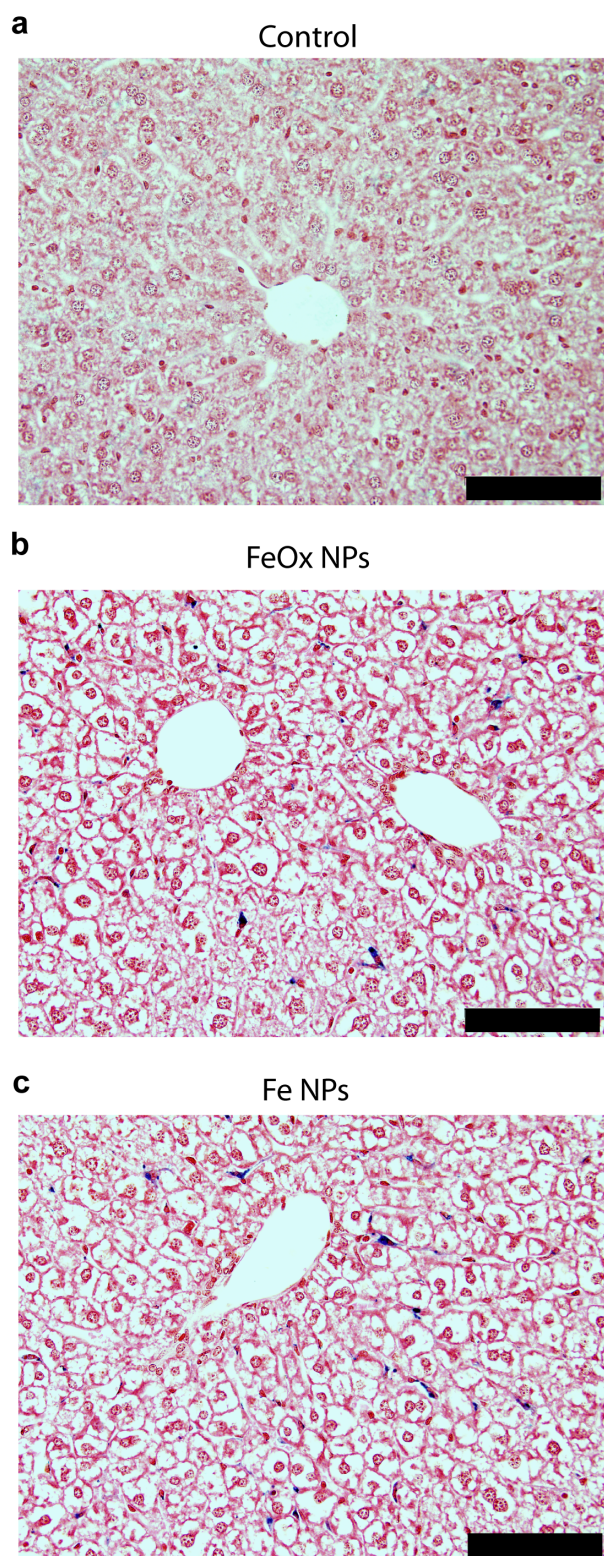


Figure 4.3: The Fe content in liver tissue following administration of Fe NPs and FeOx NPs Mice were given an intravenous dose of $3\mu\text{mol Fe kg}^{-1}$ of Fe NPs or FeOx NPs then culled 14 hours later. The livers were removed, fixed in paraformaldehyde, sectioned and stained with Perl stain. The livers of control mice that received injections of PBS only were used for comparison. (scale bar = $100\mu\text{m}$).

tissues into which they have minimal uptake such as skeletal muscle¹⁶⁴.

The results showed that there was no difference in the muscle:tumour ratio of T_2 contrast between mice that received Fe NPs versus controls (Figure 4-4). In the liver and lymph nodes, the ratio of tissue:muscle T_2 contrast was actually greater in the Fe NP group versus control. These findings suggest that there is no change in tumour T_2 contrast produced by non-specific uptake of Fe NPs in the model studied. Furthermore the presence of a large tumour does not inhibit the contrast enhancement of the liver and the lymph nodes by competitive uptake of Fe NPs. This presents a significant barrier for direct tumour imaging in liver and lymph nodes because for a tumour to be readily visible by direct targeting, it must have less T_2 weighted signal (i.e. appear darker) than surrounding tissue. In this model, the tumours had no change in T_2 contrast whilst there was decreased T_2 contrast intensity observed in both liver and lymph nodes. Therefore, for direct tumour targeting to be effective, a substantial increase in the relative uptake of Fe NPs in the tumour must be achieved.

4.2.4 Investigating the central, hypointense regions of tumours observed in a subset of mice following Fe NP administration

Although the average T_2 weighted signal of tumours were not found to differ in mice that received Fe NPs versus controls, in 2 of the 5 mice that received Fe NPs there was a central, hypointense region of the tumour observed on T_2 weighted MRI (Figure 4-5a). These observations could potentially be explained by uptake of NPs into this region of the tumour due to leakage from abnormal blood vessels or by the presence of macrophages that have taken up NPs and have infiltrated the tumour. Both leaky microvasculature and infiltrating macrophages have been well documented in tumours^{182,183}. If either of these processes were indeed resulting in increased delivery of Fe NPs to the tumour, they could be worth further investigation as a means of increasing the sensitivity and or specificity of direct tumour imaging. To examine this further, the mice from this series were culled after imaging and their tumours were removed for examination for Fe by light microscopy.

The central regions of both tumours with hypointense regions on T_2 weighted images showed extensive necrosis and haemorrhage on Haemotoxylin and Eosin staining

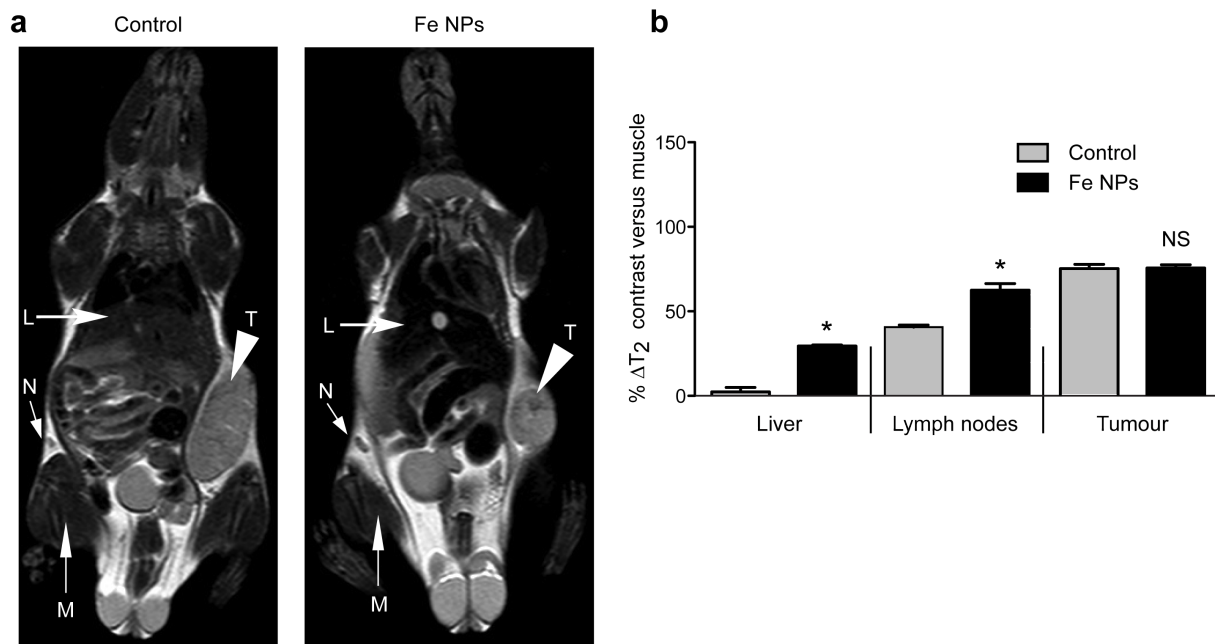


Figure 4.4: T_2 contrast in large tumours versus other tissues following intra-venous Fe NPs. C57BL/6 mice were injected with 10^6 B16 cells in the left flank and imaged by MR one week later. Mice in the Fe NPs group received an intravenous dose of $160\mu\text{mol Fe kg}^{-1}$ of Fe NPs 24 hours prior to MRI, whereas control mice received PBS only. The signal intensity in the tumours (T) were compared within the same mouse to that of the liver (L), contralateral inguinal lymph node (N) and skeletal muscle (M) and plotted as $\% \Delta T_2$ contrast versus tumour as follows: (signal intensity of tumour)-(signal intensity in organ)/ (signal intensity of muscle). ($p < 0.05$ by Mann-Whitney rank-sum test, NS= not statistically significant defined as $p > 0.05$).

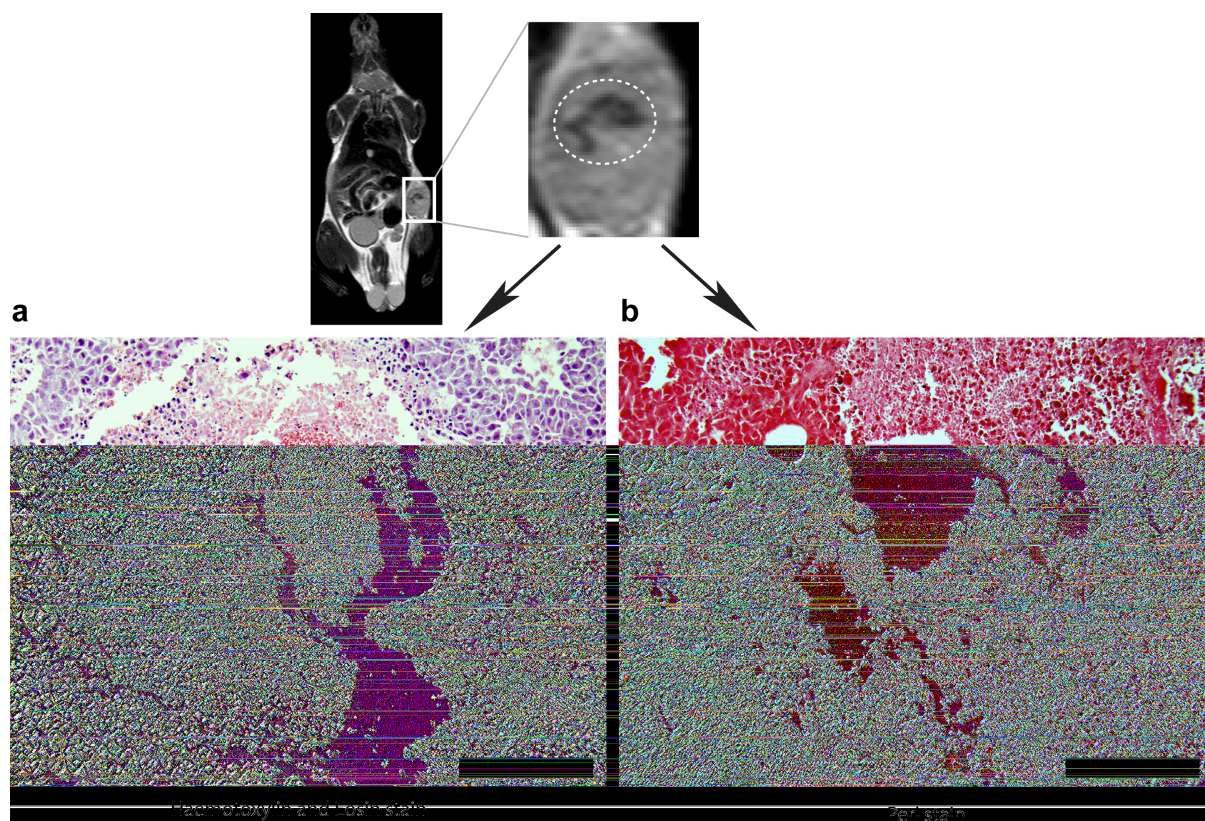


Figure 4.5: Histology of hypointense regions of tumours on T_2 imaging. Mice imaged in Figure 4-4 that had hypointense regions of their tumours on MRI (dashed circle) were euthanized and their tumours were fixed, sectioned and stained with haematoxylin and eosin (**a**) for general histology and Perl stain (**b**) for Fe. (scale bars = $200\mu\text{m}$).

(Figure 4-5a). This is a common process in rapidly growing tumours where the tumour outgrows its own blood supply resulting in the death of poorly perfused tumour cells¹⁸⁴. The Perl stains of this region showed no significant presence of Fe, indicating that the hypointensity on MRI was not likely to be due to the presence of Fe NPs. Central hypointensity on unenhanced T_2 scans has been previously described in several different tumour types, and has also shown to be correlated with necrosis on histology^{185,186}. Here it was not associated with increased uptake of NPs and was therefore independent of T_2 contrast agent administration.

4.2.5 T_2 contrast in smaller tumours after intravenous administration of Fe NPs

An argument could be made that the subcutaneous tumours in Figure 4-4 were so large in comparison with the organism that it is possible that they did uptake the Fe NPs to a significant amount but in a concentration too diffuse to detect by MRI impact T_2 weighted MRI or Perl-stained histological sections. In section 4.2.3, B16 tumours were injected at 10^6 and can double every 12-16 hours in vitro¹⁸⁷. By taking an estimate of doubling time at the shorter end of this range and assuming the B16 could keep up the same rate of growth in vivo, this would present approximately 8×10^9 tumour cells imaged on day 7. Assuming the entire dose of Fe NPs ($200 \mu\text{g}$) was taken up by tumour cells there would be approximately 40pg Fe/cell at the time of imaging. This is more than double the cellular concentration of Fe NPs that produced a 70% reduction in T_2 contrast at 9.4 T in vitro (Figure 3-9). A conservative conclusion could therefore be argued from this series of estimations that the Fe dose administered to image the tumours in Figure 4-4 was of an adequate order of magnitude to produce a detectable change in T_2 contrast if tumour uptake was as low as 50% of the total Fe dose.

However, the percentage of the Fe NPs uptaken by tumours is likely to be much less than 50% because a significant amount of Fe was reaching the liver and the lymph nodes to produce a T_2 contrast change over controls (Figure 4-4) and no significant Fe was seen in the tumours on Perl stain (Figure 4-5). So if the amounts of circulating Fe NPs available to the tumours were reduced due to uptake by macrophage-rich tissues, then an alternative would be to image smaller tumours. Therefore, 1×10^5 B16 cells were injected to produce tumours that were approximately 1/10 to 1/20 of the area on coronal section ($6\text{-}8\text{mm}^3$ versus $80\text{-}100\text{mm}^3$) of the tumours in the previous experiment. Mice were given an intravenous dose of Fe NPs or PBS only (control) and imaged 24 hours later at 1.5T (Figure 4-6a). No difference was seen in the tumour:muscle T_2 contrast ratios between the control and Fe groups. There was a significant change in the tumour:liver and tumour:lymph contrast ratios in the Fe versus control groups. This suggests that there is uptake of Fe NPs into liver and lymph nodes with minimal uptake into the tumour, despite a reduction in tumour size.

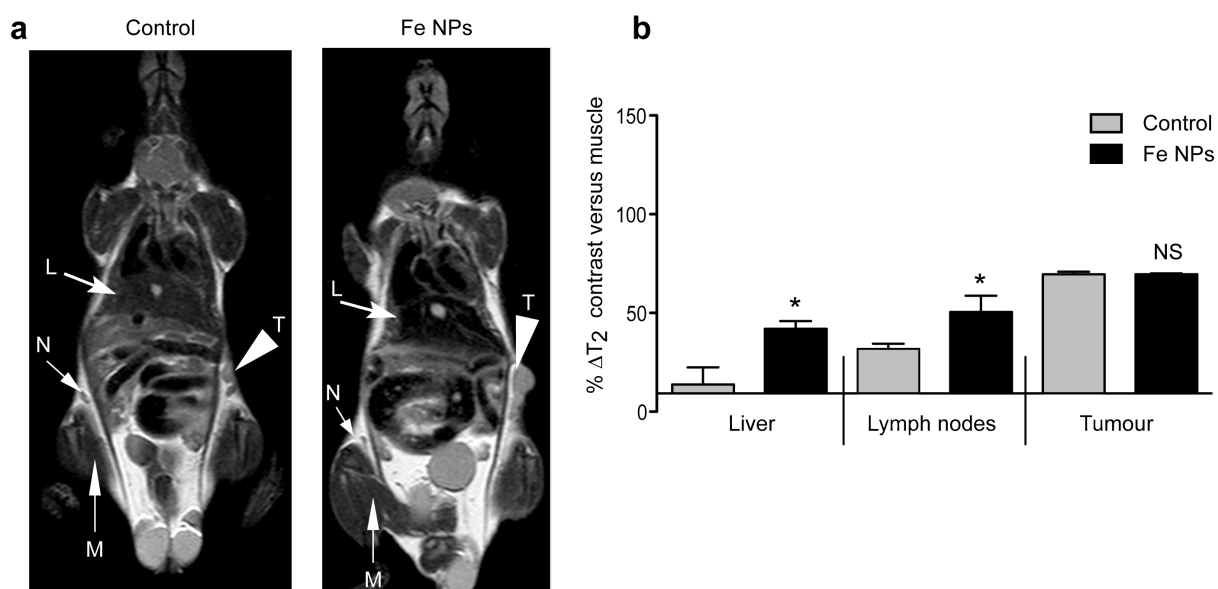


Figure 4.6: T_2 contrast in small tumours versus other tissues following intravenous Fe NPs. C57Bl/6 mice were injected with 10^5 B16 cells in the left flank and imaged by MR one week later. Mice in the Fe NPs group received an intravenous dose of $160\mu\text{mol Fe kg}^{-1}$ of Fe NPs 24 hours prior to MRI, whereas control mice received PBS only. The signal intensity in the tumours (T), liver (L), contralateral inguinal lymph node (L) and skeletal muscle (M) were analysed and plotted as in Figure 4-4. ($p < 0.05$ by Mann-Whitney rank-sum test, NS= not statistically significant defined as $p > 0.05$).

4.2.6 Antibody conjugation of Fe NPs to improve tumour specific uptake

To improve the selective uptake of Fe NPs into tumour cells, tumour selective antibodies can be conjugated to their surface³⁰. The HeLa cervical cancer line is known to overexpress the HER2 receptor on its surface and bind the anti-HER2 antibody, Herceptin¹⁸⁸. Herceptin was conjugated to the outer DMSA shell of the Fe NPs to produce improved uptake into HeLa cells. This reaction involves a linker molecule, 1-Ethyl-3-(3-dimethylaminopropyl) carbodiimide hydrochloride (EDC) that binds a carboxyl group from the DMSA and an amine group on the Herceptin antibody to form an amide linkage. Herceptin-conjugated Fe NPs (Fe-Herceptin) were added to HeLa cell culture at varying concentrations of Fe. For comparison, Fe NPs and unbound Herceptin were added to HeLa cells at the same concentrations. Fe-Herceptin conjugates produced a 39% increase in uptake of the Fe NPs into HeLa cells (Figure 4-7) with a 37% greater change in T_2 weighted contrast. This is of a similar magnitude to other studies where antibody conjugation to FeOx NPs produced a decrease in T_2 contrast of between 30-50% in other tumour models in vitro¹⁸⁹. However, even if it were maintained in vitro, this was not an adequate improvement in Fe uptake to produce effective in vivo contrast, particularly for tumours in organs such as the liver and lymph nodes. As seen in Figure 4-4; liver, lymph nodes and skeletal muscle have a 96, 26 and 71% reduction in T_2 contrast versus tumours following Fe NP administration. Even assuming that the improvement in T_2 contrast of 37% seen in vitro translated fully in vivo, the difference in T_2 contrast between the tumour and these organs would actually reduce in all three cases. In the case of the liver, with untargeted Fe NPs the tumour appears 96% brighter than the liver on T_2 images. If tumour targeting was as effective as in the in vitro HeLa/Herceptin model, the tumour would still be brighter but only by approximately 59%.

The improvement in tumour specific uptake required for effective in vivo contrast is therefore likely to be of a much larger magnitude than the improvement in T_2 contrast of Fe NPs over FeOx NPs. Furthermore, in most clinical tumours there is not consistent expression of tumour specific antigens presenting a further challenge for antibody mediated targeting¹⁹⁰. At this point it was decided not to pursue targeted tumour delivery and to take advantage of the abundant uptake of Fe NPs in the liver, spleen and lymph nodes to improve the detection of tumours in these organs.

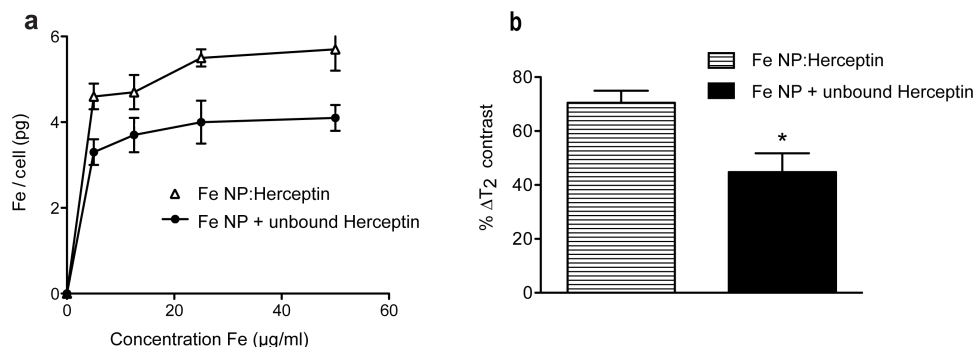


Figure 4.7: Uptake of Herceptin conjugated Fe NPs into HeLa cells Fe NPs conjugated to Herceptin antibodies were added to HeLa cells in culture for 1 hour at varying concentrations (a). The cells were harvested and washed twice before analysis of Fe content by flame atomic absorption spectroscopy (a) or dispersed at 500cells/ μ L in agar and imaged at 9.4 T (b). For comparison Fe NPs with free Herceptin were added at the same concentrations. The HeLa cells imaged in (b) were incubated in 50 μ g Fe ml⁻¹. ($p < 0.05$ with two tailed t test).

4.2.7 Detection of intrasplenic tumours following intravenous Fe NPs

A recent meta-analysis highlights the potential of using FeOx to image lymph node metastases¹⁹¹. Increases in sensitivity and specificity were seen over unenhanced MR scans or computed tomography (CT) across a wide range of cancers¹⁹¹ but this decreases substantially if the size of the lymph node metastasis is less than 5 mm³⁸. The hypothesis that Fe NPs could improve this threshold of detection due to their improved relaxivity was tested in a mouse model. The model involved direct injection of tumour cells into the spleen as a surrogate model of human lymph node metastasis. The spleen in 6 week old C57 mice has a diameter of 2-10mm depending on the axis and orientation, which is of similar size range to the diameter of human lymph nodes, 3-15 mm (if not enlarged)¹⁹². The spleen and lymph nodes are both rich in macrophages and an improvement in both splenic and lymph node contrast can be seen with FeNPs over FeOx (Figure 4-2). Four different cancer cell lines were trialled for experiments to assess tumour detection. Each was injected into the spleen of mice under anaesthesia, and then ex vivo macroscopic examination of the spleen was conducted between 2 and 9 days later (data not shown). The mouse breast cancer line, 4T1 was chosen as it consistently produced tumours (100%) three days after injection into the spleen within a narrow size range (1-3mm).

A series of experiments was set up to determine whether Fe NPs could improve the detection of the intrasplenic tumours when compared to FeOx NPs. Mice were injected with 4T1 cells into the spleen and imaged by MR 2 days later (Figure 4-8 pre-contrast). They then received an intravenous dose of 200 μ g of Fe NPs or FeOx NPs 8 hours before a second scan on day 1 (Figure 4-8 post contrast). As in previous experiments, the mice that received Fe NPs had a greater reduction in T_2 -weighted signal intensity in their splenic tissue which provided clear contrast with the high level of signal intensity maintained in the intrasplenic tumours (Figure 4-8b,d). The tissue to tumour contrast in the spleen was greater in mice that received Fe NPs (60%) versus FeOx NPs (25%, Figure 4-8i). This was a very encouraging result because it demonstrated that the same dose of Fe NPs could produce significantly better tissue:tumour contrast enabling clear discernment of small tumours in vivo.

4.2.8 Histology of spleens and tumours

The hypothesis at this point was that the differences in T_2 signal intensity seen in the contrast-enhanced scans was due to increased uptake of Fe NPs or FeOx NPs in the normal splenic tissue (parenchyma) versus the tumours. This would produce a hypointense (dark) area in the normal splenic tissue on T_2 -weighted MRI scenes due to a higher relative concentration of magnetic NPs. In contrast, tumour tissue has a lower uptake of magnetic NPs and produces a corresponding hyperintense (white) region on MRI. Other processes, such as tumour necrosis (as seen in Figure 4-5), could also cause heterogenous signal intensity within the spleen.

To ensure that the reduction in T_2 -weighted signal intensity seen on the contrast enhanced scans was associated with uptake of NPs, the spleens of mice were removed ex vivo then fixed and sectioned for light microscopy. There was a clear difference between the large, confluent tumour cells and the splenic parenchyma (Figure 4-9). On Perl stain, there was positive staining for Fe throughout the parenchyma and at the parenchyma/tumour boundary in both the Fe NPs and FeOx NPs groups. No Fe was seen in any of the tumours. In the control group there was no Fe seen in either the tumour or the parenchyma. These findings are further evidence of a correlation between Fe NP uptake and increased T_2 contrast with the surrounding tissue on MRI.

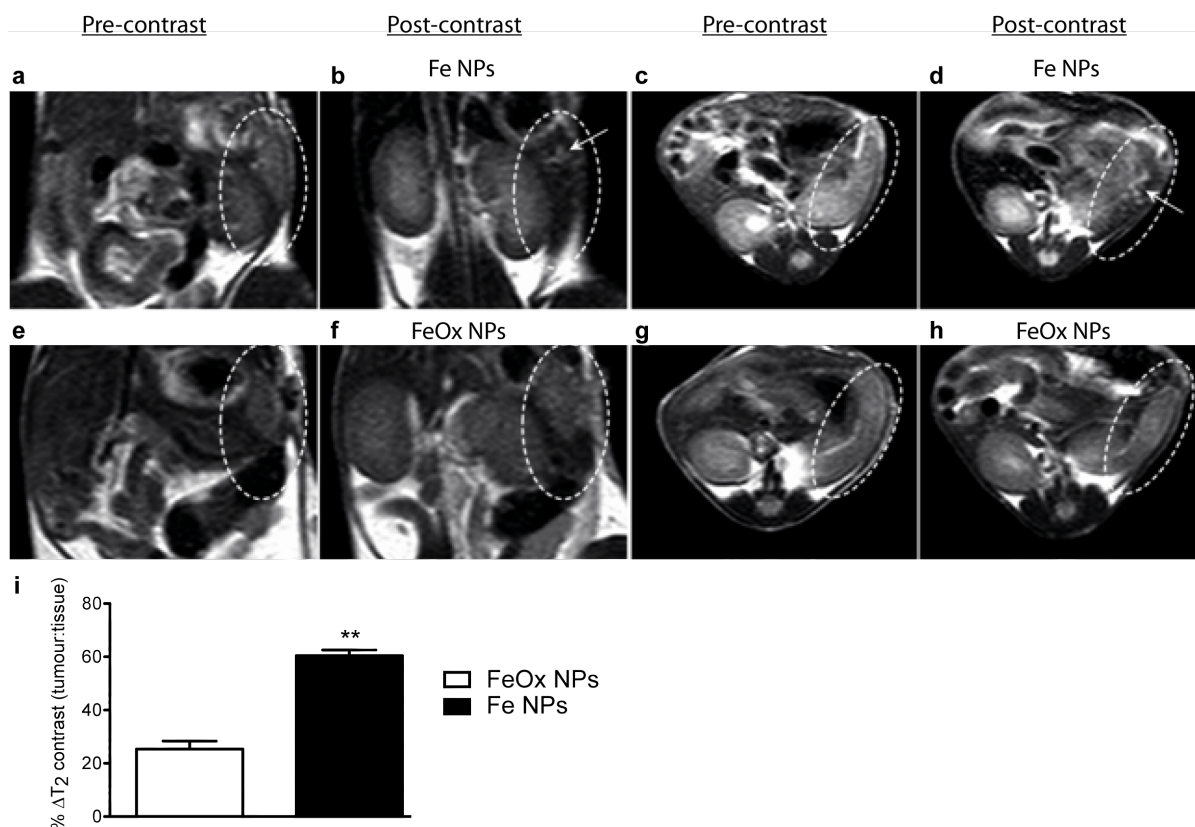


Figure 4.8: Imaging intrasplenic tumours after enhancement with Fe and FeOx NPs. 6 week old Balb/c mice were injected with 10^6 4T1 breast cancer cells into their spleens under anaesthesia and were imaged by MR 48 and 72 hours later, with coronal (a,b,e,f) and axial (c,d,g,h) scans. An intravenous dose of $160\mu\text{mol Fe kg}^{-1}$ of Fe NPs (b,d) or FeOx NPs (f,h) was administered 8 hours before the second scan. The signal intensity in the tumours was compared within the same mouse to that of the spleen and plotted as % ΔT_2 contrast as follows: (signal intensity of tumour)-(signal intensity in spleen)/ (signal intensity of tumour) (* $p < 0.01$ Mann-Whitney rank sum test).

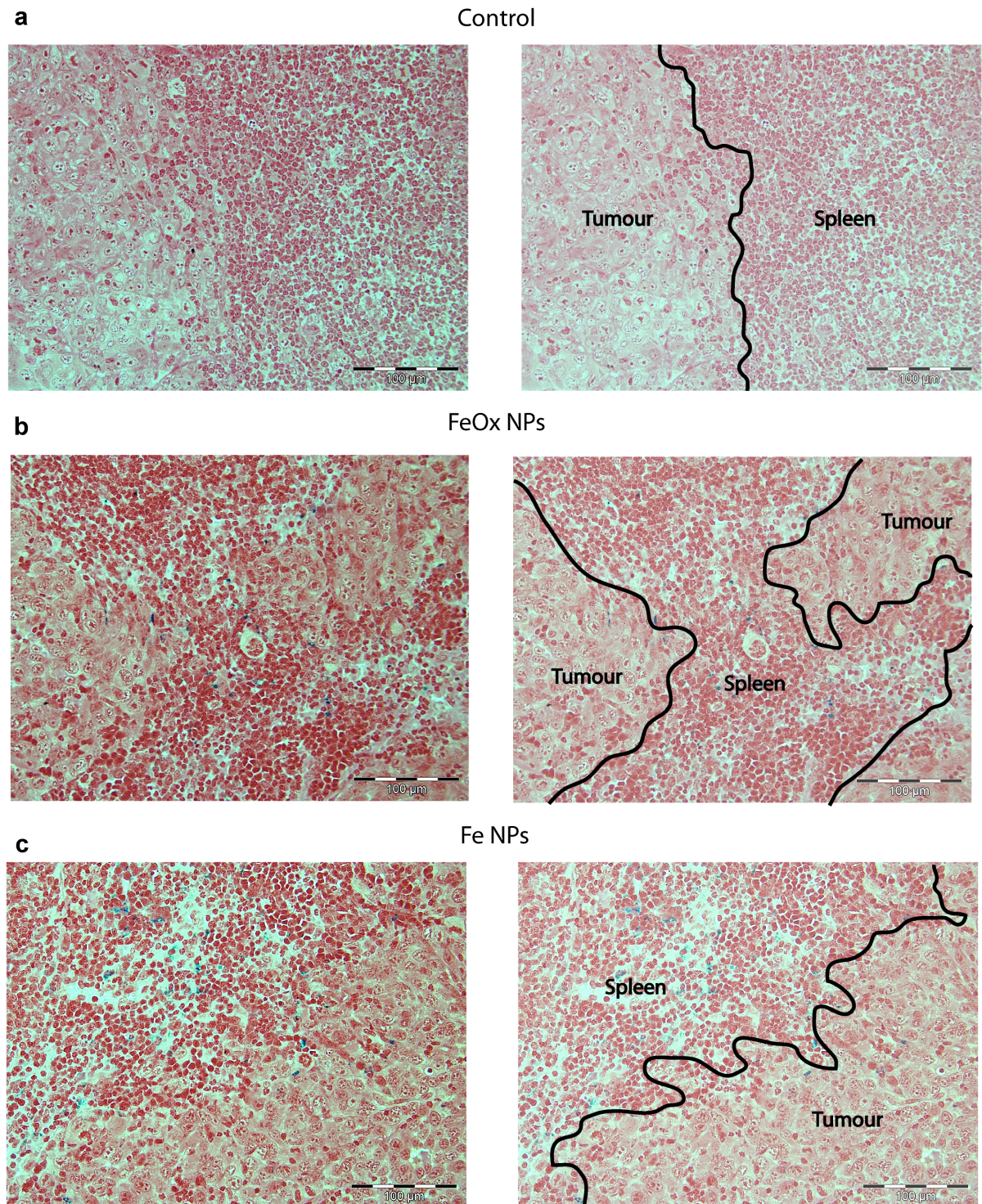


Figure 4.9: Histology of intrasplenic tumours with intravenous Fe NPs or FeOx NPs. Mice from Figure 4-8 were euthanized after the second MR scan, then the spleens were removed, fixed and sectioned for light microscopy. A Perl stain was applied to detect the presence of Fe. (scale bar = 100 μ m).

4.2.9 Effect of Fe NPs on tumour detection by blinded radiologists

To provide robust evidence that Fe NPs could improve the detection of small tumours *in vivo*, a study with analysis by two independent, blinded radiologists was performed. A large series of mice (30 per group) received an intrasplenic injection of either 4T1 tumour cells or PBS only. Three days later, these mice were then randomly assigned to one of three groups corresponding to the contrast agent they were to receive: Fe NPs, FeOx NPs or PBS only (control). The mice were imaged by MR 8 hours after receiving intravenous contrast. The spleens were removed *ex vivo* to confirm the development of intrasplenic tumours measuring 1-3mm (in the tumour group). The images of all 60 mice were sent to two radiologists who had no knowledge of whether the mice had tumours or what type of contrast agent they had received. They were instructed to independently score the spleens on a simple numerical scale as shown in Table 4-2.

Table 4.1: Scoring system for intrasplenic tumours.

Score	Description
1	Confident that no tumour is present
2	Probably no tumour present
3	Equivocal
4	Probably a tumour present
5	Confident that a tumour is present

The scores were sent to an un-blinded investigator and a receiver operator curve was generated (Figure 4-10). Receiver operator curves (ROC) are commonly used to determine a cut-off point for a diagnostic test. The principle behind ROCs is that as a test becomes more sensitive, it usually becomes less specific and ROCs provide visualisation of this relationship so that an appropriate cut-off point can be chosen. ROCs are generated by plotting the sensitivity versus the false positive rate (1-specificity) for each output value of the test. A cut-off point can then be chosen above which all the output values of the test are deemed to be positive for the disease and below which are deemed to be negative. The cut-off point is often made where the slope of the curve begins to level off, indicating that further gains in sensitivity of the test are made only at the expense of increasing losses in specificity. The null hypothesis can be depicted as a line of slope 1 which indicates a test that is 50% specific and 50% sensitive; an improvement in one of these parameters can only be achieved with an

equivalent loss in the other. This represents a test that has only a chance relationship to the disease status of the patient; an example of which could be flipping a coin to determine whether a patient had cancer.

Diagnosis of tumours in the control mice was no more accurate than the null hypothesis for radiologist 1 and only slightly more accurate for radiologist 2 (Figure 4-10c-d, dashed line). This indicates that without contrast enhancement, the tumours were not able to be distinguished easily from the splenic parenchyma. FeOx NPs improved the diagnostic accuracy with a sensitivity and specificity superior to controls at two different cut points for radiologist 1 and three points for radiologist 2. Fe NPs produced a further improvement in both specificity and sensitivity beyond FeOx NPs at four different cut-off points for radiologist 1 and one point for radiologist 2. The specificity of the scans in the Fe NPs group could be increased to 100% whilst maintaining a sensitivity of 70% or 90% (radiologist 1 and 2 respectively). Alternatively, 90% sensitivity was achieved at a cut-point with 80% or 100% specificity (radiologist 1 and 2 respectively). Interestingly, radiologist 2, who scored with overall higher accuracy, achieved a cut-off point where 100% of tumours were detected in the FeOx group, albeit at a low specificity of 40%. This highlights the fact that there was a greater improvement in specificity than sensitivity when comparing Fe to FeOx NPs.

In general, the closer the area under the receiver operator curve (ROC) is to 1, the more accurate the diagnostic test, with 1 representing a perfect test and 0.5 the lowest value possible (i.e. the null hypothesis). In this study, the average area under the curve was 0.92, 0.82 and 0.59 for Fe NPs, FeOx NPs and control groups, respectively. This data set is strong evidence that Fe NPs can produce contrast enhancement that is more effective than FeOx NPs in detecting small tumours in vivo at 1.5T.

4.2.10 Intra-observer accuracy and variability

As FeOx NPs are not marketed in Australia or New Zealand, many radiologists in New Zealand have no experience with using T_2 contrast agents, such as the two in this study. This raises the question of whether a difference in diagnostic consistency and accuracy would be seen between images enhanced with Fe NPs and FeOx NPs. To answer this question, each radiologist's scoring of each mouse was compared and plotted as inter-observer variability (Figure 4-11a). To address intra-observer variability, radiologist 1 was given training with a member of the research team using a random

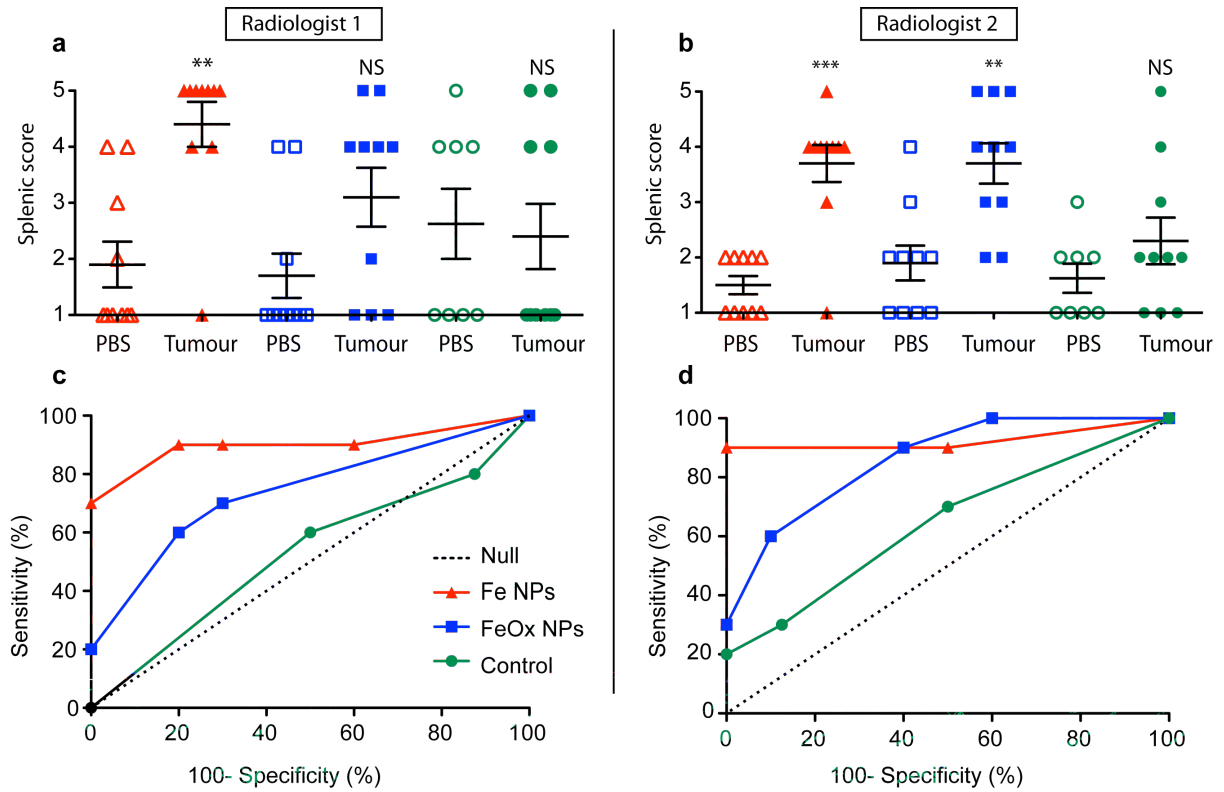


Figure 4.10: Receiver operator curve of in vivo tumour detection with Fe NPs versus FeOx NPs. 60 mice received an intrasplenic injection of either 4T1 cells or PBS. The mice were then randomly assigned to receive one of three intravenous contrast agents; Fe NPs, FeOx NPs, or PBS only (control). MRI scanning was performed 72 hours following tumour inoculation, with contrast administered 8 hours before the scan. The scans were scored by blinded radiologists (**a,c** - radiologist 1, **b,d** - radiologist 2) according to Table 4-1, then analysed and plotted as scatter plots (**a,b**) and receiver operator curves (**c,d**) by an un-blinded investigator. In **a** and **b**, the splenic tumour scores given to the mice that received Fe NPs (red) and FeOx NPs (blue) are shown where PBS and tumour represent mice that received intrasplenic injections of PBS or tumour cells respectively. (NS = $p > 0.05$, * $p < 0.01$, ** $p < 0.001$ by Mann-Whitney rank sum test.)

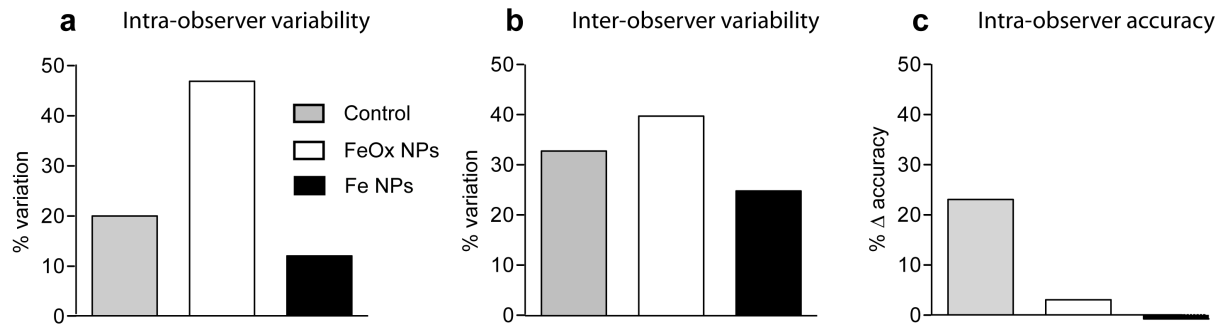


Figure 4.11: Changes in tumour scoring with observer training. The scoring of each mouse was compared between the radiologists (a). After training, radiologist 1 rescored all the mice (b). The variation between the scorings was plotted for each contrast agent group (a,b), with the two scores for each mouse defined as variant if they differed by more than one point. The change in accuracy was determined between the first and second scoring of the data by radiologist 1 (c), with a value of 1-2 considered correct if no tumour was present and 4-5 correct if a tumour was present.

selection of images from the same image set over two thirty minute sessions. One week following training, radiologist 1 was asked to go through and score the image set independently for a second time. The intra-observer variability (Figure 4-11b) of his scoring was plotted for each type of contrast agent. To determine whether accuracy improved with training, the difference in accuracy between the two scorings by radiologist 1 was plotted (Figure 4-11c). When it came to variation both between radiologists (inter-observer) and between different analysis sessions by radiologist 1 (intra-observer), mice in the Fe NP group were scored with the most consistency and those in the FeOx NPs group were scored with the least consistency. The intra-observer variability was not associated with a commensurate change in accuracy meaning that there was no substantial improvement in performance in scoring the FeOx NPs after training. Interestingly, the only change in accuracy of note between scorings was an increase in correct scoring of the control group. This could be due to an improved appreciation for the appearance of non-enhanced images of normal spleen in mice. As analysis of mice in the Fe NP group had the lowest intra-observer and inter-observer variation, this suggested that the images enhanced with Fe NPs were distinct enough to produce consistent scoring and that there was no benefit from radiologist training.

4.3 Discussion

4.3.1 Principle findings

Fe NPs enhanced the in vivo T_2 contrast in the liver, spleen and lymph nodes above that of FeOx NPs. Although specific uptake of Fe NPs into tumour cells was demonstrated in vitro through antibody-conjugated NPs, the in vivo uptake of Fe NPs was predominantly seen in macrophage-rich organs. The preferential in vivo uptake of Fe NPs and FeOx NPs into the spleen over intrasplenic tumours was demonstrated and exploited to improve tumour detection. Fe NPs improved the MRI-based diagnosis of small intrasplenic tumours over FeOx NPs by increasing both the sensitivity and specificity of tumour detection and by decreasing the inter-observer and intra-observer variability.

4.3.2 Mechanism of improved tumour diagnosis

Fe NPs demonstrated a superior T_2 relaxivity over FeOx NPs, which translated into improved specificity and sensitivity of small tumour diagnosis. There is sufficient evidence from this study to consider a mechanism for this observation. It is proposed that there was similar uptake of Fe NPs and FeOx NPs into splenic macrophages in normal spleen parenchyma, with limited uptake into tumours. The larger magnetic moment of Fe NPs produced more efficient transverse relaxation of water protons in the splenic parenchyma versus tumour tissue, resulting in increased tissue:tumour contrast. The improved contrast with Fe NPs produced MR images that were scored with greater accuracy and consistency than those enhanced with FeOx NPs or control.

Fe NPs produce more efficient transverse relaxation than FeOx NPs, as demonstrated in Chapter 3 (324 mM s⁻¹ versus 145 mM s⁻¹, Figure 3-9). When cells were labelled with Fe NPs in vitro, there was at least twice the contrast produced per cell versus those labelled than FeOx NPs (Figure 3-10), with no quantitative difference in the uptake of NPs seen in the cell types tested (Figure 3-11 and 5-2). The in vivo T_2 contrast seen in the liver and spleen after administration of Fe NPs was more than twice that of FeOx NPs with no qualitative differences seen in amount of NP uptake in these organs (Figure 4-3 and 4-9). These findings all suggest that there are no major differences in the cellular uptake in vitro or in vivo between the Fe NPs and FeOx NPs, and that the

improved T_2 contrast seen with Fe NPs is a result of differences in relaxivity relating to the greater magnetic moment of a-Fe versus FeOx.

The same principle could be applied to the imaging of intrasplenic tumours where both types of NP were predominantly taken up by cells in the splenic parenchyma over the introduced tumours, and Fe NPs produced more than twice the tissue to tumour contrast as FeOx NPs (Figure 4-8). The improved contrast with Fe NPs over FeOx NPs produced a clearer distinction between normal and tumour tissue, translating into better overall diagnosis (area of ROC 0.92 versus 0.82 respectively, Figure 4-10) and higher accuracy (mean of 85% versus 55%, Figure 4-10).

It was interesting to note that if a very low specificity (40%) were acceptable, then a higher sensitivity of tumour detection could be achieved with FeOx NPs over Fe NPs by radiologist 2. This was examined further and it was found the difference in sensitivity was due to the misdiagnosis of a single tumour by radiologist 2 (Figure 4-10b).

Interestingly, radiologist 1 misdiagnosed this tumour as well (Figure 4-10a). This tumour measured approximately 1.3mm on gross histology, making it one of the smaller tumours in the study (range 1-3mm). Although this is a single example, tumours of similar size were diagnosed correctly in other groups (1.0mm in FeOx group and 1.2mm in control). This raises the possibility that there may be a size limit at which the gains in accuracy produced by improving relaxivity of a contrast agent is negated by dephasing and partial volume imaging effects caused by the contrast agent around the borders of small tumours.

In this study, a relaxivity ratio between Fe and FeOx NPs of 2.2 translated into an accuracy ratio of 1.5 in diagnosing small intrasplenic tumours. It would be easy to over-interpret this result as there are many factors involved in the diagnostic accuracy of tumours in this study that may vary in other tumour models including tumour size, location and T_2 characteristics. However, this finding does suggest that a large difference in T_2 relaxivity between contrast agents with the same coating and similar uptake characteristics translates to a smaller difference in diagnostic accuracy.

4.3.3 Implications of this study

This study was designed to answer the question of whether Fe NPs can improve the clinical diagnosis of lymph node metastases. The relevance of a mouse model using Fe

NPs to detect intrasplenic tumours needs to be defended with reference to studies with FeOx NPs in rodents and humans.

The spleen was chosen in this study because lymph nodes in mice are too small and the size of a mouse spleen is of similar size to human lymph nodes. Murine lymph nodes, which measure up to 1-2mm in diameter^{193,194} are small enough that tumours between 1-3 mm would produce lymph node enlargement, which has many other causes and is not specific for metastasis. Furthermore, there would not be a significant contrast effect produced with Fe-based NPs as the normal lymph node tissue, which takes up the NPs to produce contrast, would be replaced almost entirely by tumour. The mice used in this study had spleens that were 8-12mm long by 4-5mm wide. This is of a similar magnitude to human lymph nodes with a mean size of 5-13mm^{167,195}, and is of adequate size that tumours can grow up to 3mm without replacing a significant amount of normal tissue, as seen in Figure 4-8.

As shown in many studies, including this one, the spleen and lymph nodes have different amounts of contrast produced after intravenous injection of Fe-based NPs, owing to different uptake between the organs¹⁵⁸. Nanoparticles with a hydrodynamic radius greater than 50nm tend to be taken up by the liver and spleen within minutes, with limited access to lymph nodes³¹. The particles used here had a radius of around 60-80nm, which would favour hepatosplenic uptake and improved T_2 contrast in these organs relative to the lymph nodes as seen in Figures 4-1 and 4-2. This was appropriate in this study as the tumours were in the spleen but to translate these findings into human lymph nodes a different coating strategy could be applied, such as carboxy-dextran, to produce particles with a smaller hydrodynamic radius¹⁰³ which have been shown to be effective in lymph node imaging³⁸. Another coating may affect the relaxivity of the Fe NPs¹⁹⁶, but it is hypothesized that the Fe NPs will still maintain a higher relaxivity than FeOx NPs with the same coating.

To achieve the maximum improvement in small tumour diagnosis, the dose of Fe NPs and FeOx NPs used in this study was chosen to correspond with the clinical dose in humans. A dose of 8 mg/kg was used which is below doses used safely in mice of 30mgkg⁻¹¹⁹⁷ and rats of 10-12 mgkg⁻¹^{44,198}. Rodents have more active uptake into the liver, with elimination half-life in rats is 2 hours versus 24-36 hours in humans. Therefore a larger dose is used to visualise other compartments in animal experiments^{50,178}. Furthermore, younger rodents have been demonstrated to have up to a 50% decrease in half-life indicating enhanced uptake by liver macrophages¹⁷⁶. Feridex

is a commercial Fe Ox NP contrast agent with a similar relaxivity to the Fe Ox NPs used in this study¹⁹⁹. The recommended clinical dose of Feridex is 0.5mg Fekg⁻¹, which reduces T_2 contrast in the liver by 68%¹⁷⁵ compared to a 72% reduction with FeOx NPs at a dose of 8mg Fekg⁻¹ in this study. This suggests that the dose of Fe Ox NPs used in this study for tumour diagnosis was not significantly below the equivalent clinical dose that produces a similar change in T_2 liver contrast in humans. If the dose of Fe Ox NPs used in this study were significantly less than the equivalent clinical dose, it would imply that the increased efficacy in tumour diagnosis seen with Fe NPs could potentially be matched by increasing the dose of Fe Ox NPs to match the clinical dose.

To answer the question of how this study compares with the results of human studies, comparison can be made with a meta-analysis that combined 34 studies using FeOx NPs to diagnose lymph node tumours⁵⁷. The pooled sensitivity of all the studies in this analysis was 0.91 with FeOx NPs compared to 0.39 in unenhanced scans. This compares with results in this chapter of 0.90, 0.70 and 0.30 for Fe NPs, FeOx NPs and unenhanced control, respectively. This implies that the diagnostic task was more challenging in the study performed in mice, which was anticipated as the tumours were smaller. This could also be explained by the fact that the studies compared in the meta-analysis were not all blinded and many of the investigators scoring the tumours had prior research experience with FeOx NPs. The fact that the improvement between FeOx NPs over unenhanced scans was of a similar magnitude to that in the human studies suggests that the mouse model had similar contrast characteristics to that of cancer in human lymph nodes.

4.3.4 Conclusion

The MRI diagnosis of small tumours by radiologists was significantly improved with Fe NPs over FeOx NPs in a blinded study. Although the detection of cancer in human lymph nodes was modeled with an splenic tumours in mice, comparison with other studies suggests that Fe NPs have real potential to deliver more effective diagnosis of early lymph node involvement with cancer.

Chapter 5

MRI tracking of DC/peptide vaccines labelled with Fe NPs to determine antigen-specific responses

5.1 Introduction

Cancer immunotherapy with dendritic cell (DC)-based vaccines has shown promising outcomes in a small subset of patients. One of the difficulties in optimising this therapy has been in assessing the generation of immune responses following vaccination. Most assays of immune responses are performed *ex vivo* and are beset with difficulties in standardisation. This chapter describes a novel *in vivo* strategy using Fe nanoparticles and MRI to detect an induced antigen-specific immune response to a DC-based vaccine combined with a peptide antigen (DC/peptide) in mice.

5.1.1 Mechanisms of tumor suppression and escape from the immune system

In order to design therapies which specifically target cancer cells for removal, it is important to consider what distinguishes cancer cells from the large variety of non-neoplastic tissue present in the body. Weinberg and Hanahan produced a review of the hallmarks of cancer²⁰⁰ which include resisting cell death, sustaining proliferative

signaling, evading growth suppressors, activating invasion and metastasis, enabling replicative immortality and inducing angiogenesis. These were recently updated to include deregulation of cellular energetics and avoiding immune destruction²⁰¹. Whilst all of these processes are important in distinguishing malignant cells, it is the escape from immune control that is of particular interest when designing therapeutic cancer vaccines, for this is the aspect that cancer immunotherapy seeks to remedy in the first instance.

There are multiple lines of evidence from studies of immunosuppressed hosts to suggest that a functioning immune system plays an important role in the prevention of tumor development. Firstly, there is a markedly increased rate of cancers in patients with immunodeficiencies which are uncommon in non-compromised individuals²⁰². Secondly, in mouse knock-out models where selective cells from the innate and adaptive immune system (NK cells and CTLs respectively) are absent, an increased incidence of malignancy was observed^{203,204}. Thirdly, when tumours that have arisen in immune-deficient mice are transplanted to immunocompetent hosts they are rejected, whereas cancer cells that are taken from immunocompetent mice can produce invasive disease in both immunodeficient and immunocompetent recipients²⁰³⁻²⁰⁵. These findings suggest that there is active surveillance by the immune system which can prevent certain instances of malignancy and that tumours that have already developed in an environment of impaired immunity can be eliminated in the presence of a competent immune system.

The list of proposed mechanisms by which tumors evade the immune system has expanded significantly in the last decade²⁰⁶. Three important mechanisms from this list include regulatory T cells, myeloid-derived suppressor cells and T cell exhaustion. The processes by which these entities suppress anti-cancer immunity will be discussed with a view to how they could be overcome by cancer immunotherapy.

Regulatory T cells are T lymphocytes that suppress the activity of other immune cells. They possess a T cell receptor which, like other T cells, can recognize specific antigen presented on an MHC molecule. When regulatory T cells encounter their cognate antigen they secrete immunosuppressive substances such as TGF- β ²⁰⁷. There is evidence that regulatory T cells inhibit anti-tumour responses²⁰⁸ and that blocking regulatory T cells improves the efficacy of cancer immunotherapy²⁰⁹.

Multiple types of cancer have demonstrated the accumulation of myeloid derived

suppressor cells (MDSC) within the tumour²¹⁰⁻²¹². MDSC originate in the bone marrow and are recruited to the tumour by substances such as transforming growth factor (TGF)- β , and IL-10[19]. Note that these substances can be produced by the cancer cells themselves or by other cells such as regulatory T cells. MDSC can suppress anti-tumour immunity by preventing DC maturation²¹³ thus inhibiting their ability to co-stimulate T cells. MDSC also release reactive oxygen species (such as nitric oxide synthetase) which can inhibit and cause programmed cell death (apoptosis) of T cells²¹². There are a number of substances which have proven potential to disrupt the immunosuppressive actions of MDSC including inhibition of nitric oxide synthetase²¹⁴ as well as cytotoxic therapy with 5-Flurouracil²¹⁵. The prevention of DC maturation can be circumvented by vaccination with DC that are exposed to tumor antigen and activating substances ex-vivo before administration in vivo.

As discussed in chapter 1, cytotoxic T lymphocytes (CTL) have proven effectiveness in eliminating cancer cells. Like other T cells, CTL require the expression of co-stimulatory molecules along with the presentation of cognate antigen to become fully activated. If there is prolonged exposure to antigen, particularly in the absence of co-stimulatory molecules, CTL can become "exhausted" and unable to mount a cytotoxic response against tumor cells²¹⁶. This is often the situation in cancers where there is a low level of tumor associated antigens expression combined with the absence of the necessary co-stimulatory molecules of professional antigen presenting cells (like CD86 on DCs). This problem can be addressed with vaccination using autologous DCs which have been manipulated ex-vivo to express both high levels of tumour antigen and co-stimulatory molecules.

5.1.2 DC elimination assay

Dendritic cell (DC)-based vaccines can produce striking remissions of advanced disease, but the clinical response rate in most studies is less than 10%⁹⁰. To improve the response rate to DC-based vaccination, there are numerous parameters yet to optimise such as ex-vivo handling, antigen loading, and finding the ideal subtype and activation of DCs. To investigate the interplay of these factors, it is necessary to monitor the immune responses generated by vaccination. Although several types of assays exist, they have not been applied in a standardised manner and have not been consistently correlated with clinical responses²¹⁷.

The most common clinical assays of immune responses to DC-based vaccination assess the generation and or function of antigen-specific CTLs. These *in vitro* assays are most often performed on peripheral blood taken following vaccination⁸⁹. However, it has been shown that detecting CTLs in peripheral blood, after *in vitro* culture, can introduce artefacts^{218,219} such as detection of naïve, tumour-specific T cells²²⁰. It has been shown that more antigen-specific CTLs can be detected in the draining lymph node than peripheral blood following DC-based vaccination²²¹, which suggests that the draining lymph node may be a more relevant site to measure immune responses. Hermans et al developed an assay²²² which detects the vaccine induced activity of CTLs by measuring the elimination of antigen-loaded DCs in the draining lymph node. This DC elimination assay is performed by *ex vivo* analysis of the draining lymph node by flow cytometry.

The basic principle behind the DC elimination assay is the somewhat paradoxical finding that the antigen-loaded DCs used in a vaccine can ultimately become targets of the cytotoxic immune responses they induce. To elaborate further, a peptide antigen is chosen that binds to MHC I molecules on DCs, and is then presented to CD8⁺ T cells that possess a T cell receptor that recognizes the antigen-MHC class I complex. The DCs have been matured, so they present co-stimulatory signals to CD8⁺ T cells that promote their proliferation and differentiation into CTL, which takes several days. If a sufficiently large population of CTL is generated, the next time the same peptide-loaded DC are administered, the activated CTLs will recognize the peptides the DC present, and rapidly induce cell death. Depending on the strength of the induced response, it is likely that significant numbers of DCs will be eliminated before they can migrate to the draining lymph node. DCs presenting no antigen or a different antigen will not be affected and will migrate to the draining lymph node. Therefore, the degree of DC elimination is much greater in mice that have been vaccinated with the same antigen versus unvaccinated (naïve) mice. If the injected DCs are fluorescently labelled, they can be detected by flow cytometry *ex vivo*, and the degree of DC elimination from the draining lymph node can be quantified.

If this assay could be adapted from an *ex vivo* assay to a non-invasive assay performed *in vivo*, it could provide useful information in clinical studies of DC/peptide vaccines. The work presented in this chapter is concerned with adapting the DC elimination assay to an *in vivo* technique by labelling the DCs with magnetic nanoparticles, as opposed to fluorescent dyes, and by tracking them with MRI. Fe and FeOx NPs are compared with the hypothesis that the improved T₂ contrast seen with Fe NPs in

previous chapters will optimise the MRI sensitivity to labelled DCs.

5.1.3 Aims

The aim of this chapter is to test the hypothesis that the DC elimination assay of antigen-specific CTL function can be adapted to an in vivo assay by labelling DCs with magnetic NPs and imaging the draining lymph node in vivo with MRI. An adjunct to this hypothesis is that Fe NPs will improve the sensitivity of MRI to detect labelled DCs, which will result in improved sensitivity of the assay. The following questions will be addressed in the context of a C57BL/6 mouse model using bone marrow generated DCs labelled with Fe NPs or FeOx NPs, imaged in a clinical MRI scanner in vivo at 1.5T and ex vivo at 9.4T.

1. What is the sensitivity of MRI to detect DCs labelled with Fe or FeOx NPs?
2. Does labelling with Fe NPs affect DC function?
3. Can NP-labelled DCs be tracked in their migration to the draining lymph node at 1.5T?
4. Is there a difference in the contrast of the draining lymph node in naïve versus primed mice?
5. Is there a correlation between the original and the adapted DC elimination assays?
6. Can the assay be applied to DC/tumour lysate vaccines?

5.2 Results

5.2.1 Fe nanoparticles improve sensitivity of dendritic cell detection

The first step in developing an in vivo cell-tracking assay was to determine the sensitivity of MRI to detect DCs labelled with magnetic nanoparticles. Of particular interest was whether this sensitivity could be improved with Fe NPs over that of FeOx NPs.

When $5\mu\text{g Fe ml}^{-1}$ of either contrast agent was added to dendritic cell culture for 48 h, DCs cultured with Fe NPs produced significantly greater change in T_2 relaxation in vitro (Figure 5-1) across a range of cell concentrations. The amount of T_2 reduction/cell was calculated by linear regression of the data shown in Figure 5-1b and found to be 0.1 % per cell for Fe labelled DCs and 0.05% per cell for those labelled with FeOx (95% C.I. 0.08-0.11 and 0.04-0.06 respectively).

To determine the sensitivity of DC detection, a threshold of a certain % change in T_2 relaxation can be applied. If a threshold of 20% change in T_2 relaxation is applied, DCs labelled with Fe NPs were detectable at 200 cells μl^{-1} whereas FeOx were not detected below 500 cells μl^{-1} . A threshold of 50% change in T_2 relaxation could only be reached by DCs cultured in Fe NPs at a concentration of 500 cells μl^{-1} . The visual distinction between these thresholds can be appreciated from Figure 5-1a where the FeOx labelled DCs (middle circle) have produced a greater than 20% reduction in T_2 weighted signal versus the unlabelled control DCs (left circle) and the Fe labelled DCs (right circle) have reduced the T_2 weighted signal by more than 50%. Adjusting the threshold will trade off specificity against sensitivity but it is clear that any threshold set between 20%-50% change in T_2 relaxation would result in a greater sensitivity for detecting DCs labelled with Fe NP versus FeOx NPs.

It was next investigated whether the improved MRI sensitivity to detect DCs labelled with Fe NPs was due to their improved uptake by DCs relative to FeOx NPs. After incubation with the same concentration of Fe NPs or FeOx NPs ($5\mu\text{g Fe ml}^{-1}$) used for MRI detection, DCs were stained with Perl stain to detect the amount of Fe retained in the cells (Figure 5.2a). There was no qualitative difference in the amount of positive Fe stain seen on light microscopy as both Fe and FeOx NPs produced appreciable Fe uptake into DCs. There was no Fe detected in unlabelled controls. Flame atomic absorption spectrometry showed that the quantitative amount of Fe uptake in Fe NP and FeOx NP labelled DCs was similar (Figure 5.2b) at around 10pgFe cell^{-1} . These findings combined with the relaxivity data strongly suggest that there remains a qualitative rather than quantitative difference in the iron present within DCs labelled with the two different NPs, most likely due to the retained α -Fe core of the Fe NPs with its superior magnetic properties.

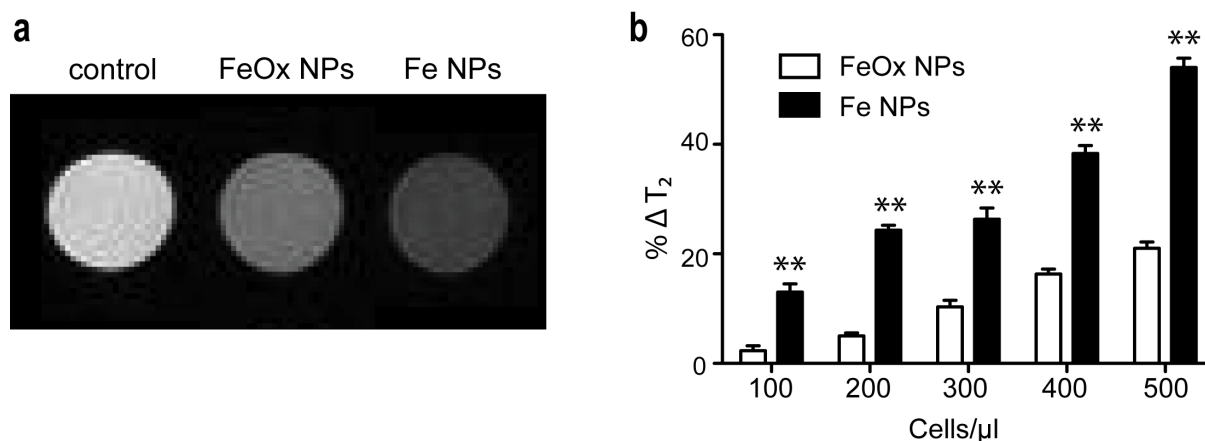


Figure 5.1: Detection of DCs labelled with Fe NPs and FeOx NPs at 9.4T. DCs were cultured in $5\mu\text{g Fe ml}^{-1}$ of Fe NPs or FeOx NPs and dispersed in 1% agar at concentrations ranging from 100-500 cells μl^{-1} . Unlabelled DCs were used as a control. The DC dispersions were imaged at 9.4T using a multi-slice spin echo sequence with an echo time of 8ms. The T_2 times of the cell dispersions were determined by manually selecting a region of interest within the cell dispersion then plotting the T_2 relaxation as in Figure 3-6. (a) MR images of DC cell dispersions at 500 cells μl^{-1} labelled with Fe NPs, FeOx NPs or PBS control. (b) The T_2 times of the DC dispersions were compared to that of the control cell layer and plotted as $\% \Delta T_2 = (T_2 \text{ control} - T_2 \text{ interest}) / T_2 \text{ control}$. (**p < 0.01 by two tailed t test)

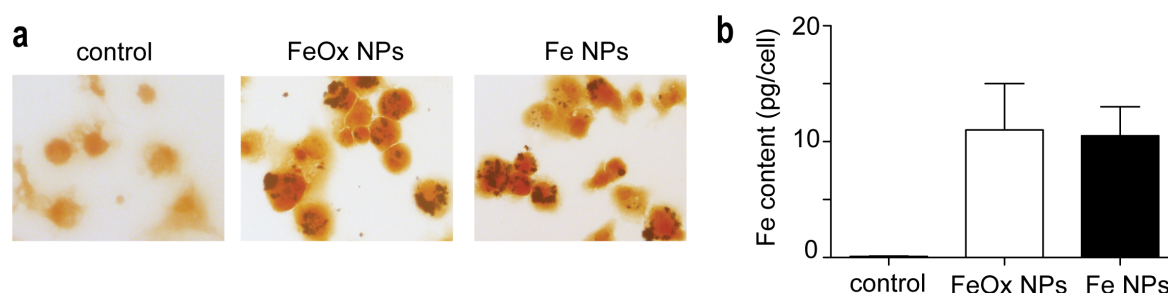


Figure 5.2: Fe NP and FeOx NP uptake into DCs. DCs incubated with $5\mu\text{g Fe ml}^{-1}$ of Fe NPs or FeOx NPs were washed, harvested, fixed and stained with Perl's stain for Fe. A group incubated with PBS only was used as a control (a). Atomic absorption spectroscopy was performed on the three groups of cells to determine the quantitative Fe content per cell (b).

5.2.2 Fe NPs and FeOx NPs do not effect DC viability, metabolism or activation at the dose used for MRI labelling

After establishing the sensitivity and Fe uptake characteristics of labelled DCs, it was important to determine whether labelling the different NPs produced measurable differences in cell viability, metabolism or activation. The viability and metabolism of Fe NPs was examined in DCs in vitro and compared to that of FeOx NPs (Figure 5-3). The viability assay (Figure 5.3a) distinguishes live cells with intact membranes by their ability to exclude the dye trypan blue. There was no significant difference in viability of DCs cultured with either type of NP. No significant effects on viability were evident compared to unlabelled controls until the concentration of NPs exceeded 20 times that used for MRI detection.

Cell metabolism was measured by the 3-(4,5-Dimethylthiazol-2-yl)-2,5-diphenyltetrazolium bromide (MTT) assay, a colorimetric assay where metabolically active cells reduce MTT to formazan dye, producing a purple colour that can be measured by spectrophotometry. There was no significant difference seen in the metabolism of DCs cultured in Fe NPs versus FeOx NPs but there was a sharp decline in both groups versus unlabelled controls once the Fe concentration exceeded $160\mu\text{g/mL}$. This assay is a more sensitive measure of viability than trypan blue exclusion and indicates that the dose at which the DC viability declines below 50% (LC_{50}), is between $160\text{--}180\mu\text{g Fe mL}^{-1}$ for both Fe and FeOx labelled cells.

For DCs to efficiently migrate to the draining lymph node after subcutaneous injection, they have to be activated by stimulatory molecules such as bacterial lipopolysaccharide²²³ (LPS). If Fe NPs interfered with this activation it would render them inappropriate as labels for tracking DC migration. DC activation is associated with the increased expression of surface molecules involved in T cell stimulation, including the co-stimulatory molecule CD86. This is particularly important in the context of DC vaccines as immature DCs are not good at stimulating T cell responses and can induce tolerance²²⁴.

The expression of CD86 can be determined by the addition of CD86 specific antibodies conjugated to fluorescent dyes, and then examining the cells by flow cytometry. Flow

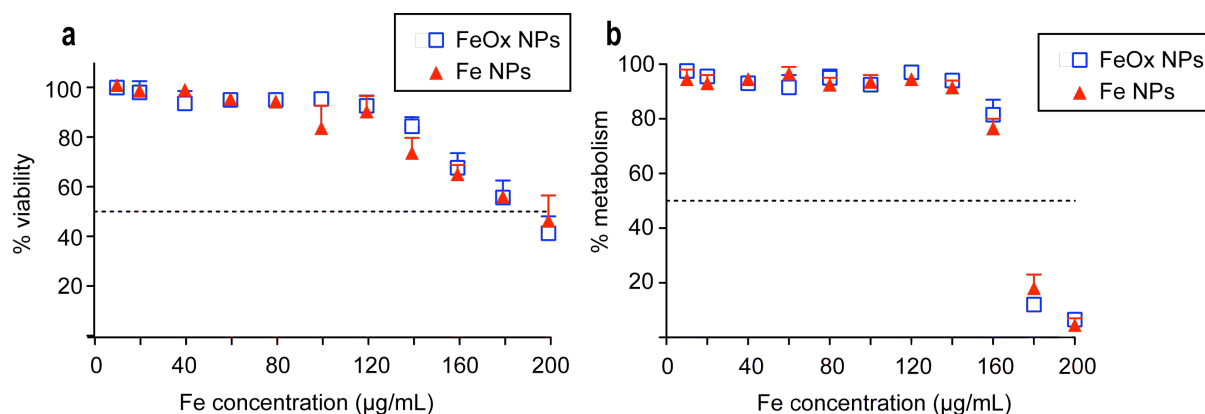


Figure 5.3: Cytotoxicity of Fe NPs versus FeOx NPs in DCs. DCs were transferred to a 96 well plate at 5000 cells/well in complete medium on Day 5 of culture. Fe NPs and FeOx NPs were added at concentrations ranging from 0-200 $\mu\text{g Fe ml}^{-1}$ in triplicate wells. As a control, wells with media only (no cells) were set up for every concentration of NPs. On Day 7, live cells were distinguished by the exclusion of trypan blue dye (a) and an MTT assay was performed to assess cellular metabolism (b). The dashed line represents a decline of 50% relative to control. These experiments were repeated five times with representative examples shown.

cytometry works by directing a beam of laser light onto a stream of fluid containing a column of cells in single file. Each cell scatters the laser beam according to its size and granularity and fluorescent molecules attached to the cell can be detected by their excitation and emission of light of a lower wavelength than the laser beam.

The DCs were incubated with Fe or FeOx NPs for 48 hours, stimulated with LPS for the final 24 hours, and then analysed by flow cytometry for the expression of CD86 (Figure 5-4). At the doses used for MR detection ($5 \mu\text{g Fe ml}^{-1}$), there was no appreciable change in LPS-mediated up-regulation of CD86 expression in DCs cultured with either type of NP versus unlabelled control (Figure 5-4a-c). However, when DCs were labelled with a higher concentration of NPs ($50 \mu\text{g Fe ml}^{-1}$) there was an increased proportion of CD86⁺ cells when no LPS added and conversely a decrease in the proportion of CD86⁺ when LPS was added (Figure 5-4d,e). These results suggest that Fe and FeOx NPs may interfere with DC activation at a dose that is significantly lower ($50 \mu\text{g Fe ml}^{-1}$) than the lowest dose at which cytotoxic effects are seen ($160 \mu\text{g Fe ml}^{-1}$).

The expression of CD86 was also examined on DCs that had been exposed to $5 \mu\text{g/ml}$ of the different NPs in vitro, and then labelled with CFSE before injection into naïve mice. All injected DCs recovered from the draining lymph node 48 hours later had

become further activated in vivo, expressing similarly high levels of CD86 regardless of the type of NP they had been labelled with (Figure 5-4c).

5.2.3 VITAL assay demonstrates antigen-specific cell elimination in vaccinated mice

Before applying Fe NP labelling to DC-based vaccines, it was important to first check that the DC/peptide vaccine was producing antigen specific killing by CTLs by performing an in vivo cytotoxicity assay. The key concept of this assay is that in a vaccinated mouse there will be preferential removal of cells that are expressing a greater concentration of the vaccine antigen. This is measured by assessing the elimination of fluorescent "target" cells (typically syngeneic splenocytes) that have been loaded with specific antigen before injection^{225,226}. The VITAL assay⁹⁹ is a variation on this assay in which three groups of target cells with three different concentrations of antigen are injected. The fluorescent dye CFSE is used at a different concentration on each group to allow discrimination by flow cytometry. As a control, a fourth group of cells that has not been loaded with antigen is labelled with a different dye, cell tracker orange (CTO). The four populations of cells are administered together intravenously in equal number. In mice that have received an effective vaccination with DCs loaded with the same antigen, selective elimination of target cells will result in an increasing ratio between the cells without antigen (CTO labelled "control cells") and those that were labelled at increasing concentrations (CFSE labelled "target cells").

The results of the VITAL assay are shown in Figure 5-5. The peptide antigen used in the vaccine was SIINFEKL, a well-studied derivative of the chicken ovalbumin protein which is known to be presented by the MHC molecule H-2Kb²²⁷, and can therefore induce strong immunity in the C57BL/6 strain of mice. As expected, in the naïve mice there was no significant difference in the ratio of control cells to any of the target cell populations. In primed mice there was an increase in the ratio of control to target cells, which increased with increasing SIINFEKL concentration of the target cells. The difference between the control to target cell ratios was significantly different between naïve and primed mice at all three concentrations of SIINFEKL (Figure 5-5b). This indicates that the DC/peptide vaccine assayed in this study did induce a CTL response that resulted in measurable antigen-specific cell lysis, providing a useful model for analysing vaccine-induced responses by MRI.

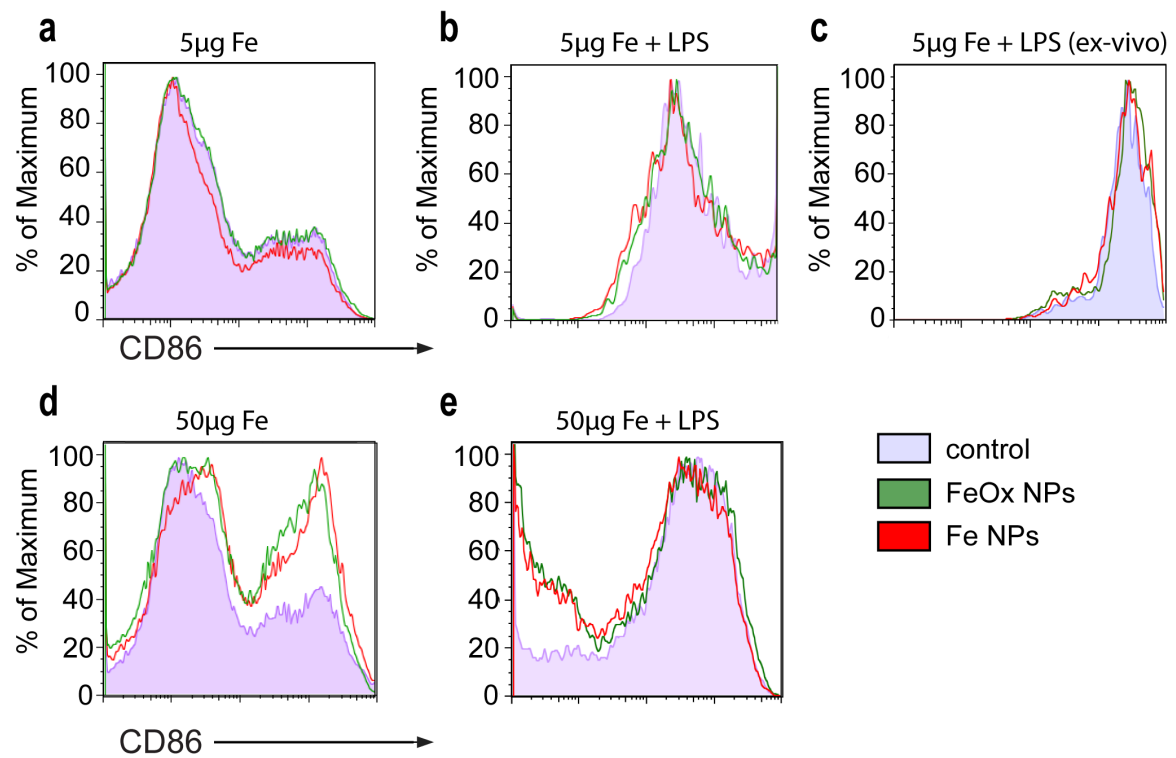


Figure 5.4: DC maturation after incubation with Fe NPs and FeOx NPs. DCs were cultured with $5\mu\text{g Fe ml}^{-1}$ (a,b,c) or $50\mu\text{g Fe ml}^{-1}$ (d,e) of Fe NPs, FeOx NPs or PBS only (control) from Day 5. LPS was added to DCs (b,e) 24 hours later. Cells were harvested from culture (a,b,d,e) or from the draining lymph nodes after injection into mice (c) and analysed by flow cytometry for the expression of CD86 after passing through gates to exclude debris and dead cells (Figure 2-2).

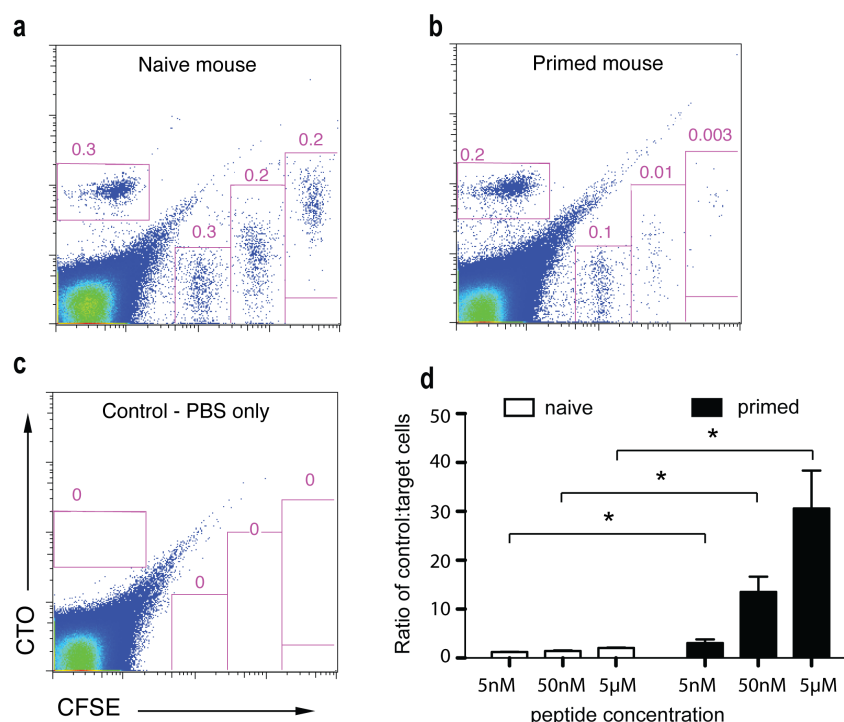


Figure 5.5: VITAL assay demonstrates antigen-specific cell lysis in vaccinated mice. Splenocytes were loaded with 50nM, 5 nM, and 0.5 nM of SIINFEKL peptide and labelled with increasing amounts of CFSE, respectively. Splenocytes not loaded with peptide were labelled with CTO as a control. Equal proportions of all cell populations were injected intravenously into groups of immunized ("primed") and naïve mice. Naïve mice that received injections of PBS only were used as a further control (c). Lymph nodes were removed from mice 24 hours later and analysed by flow cytometry. Representative flow plots of naïve (a), primed (b) and control mice are shown. The ratio of CTO labelled control cells to CFSE labelled target cells is shown for naïve and primed mice (d). (*p<0.05 by unpaired t-test)

5.2.4 Fe NPs and FeOx NPs do not affect DC migration or antigen presentation to cytotoxic T cells

After demonstrating that the DC/peptide vaccine induced antigen-specific killing, it was important to ensure that loading DCs with NPs did not affect their ability to migrate to the draining lymph node or to present the SIINFEKL antigen to T-cells, both of which could interfere with the proposed MRI-based assay of CTL induction. Three groups of DC/peptide vaccines were set up on the basis of the contrast agent they were cultured with: Fe NPs, or FeOx NPs or PBS control. All groups were activated with LPS, loaded with SIINFEKL and labelled with CFSE before subcutaneous injection. A similar number of CFSE positive cells were recovered at 48 hours from the draining lymph nodes of naïve mice from all three groups (Figure 5.6 a), indicating that the NPs did not affect in vivo migration of the DCs.

When the same DC/peptide vaccines were given to mice primed one week earlier with DCs loaded with SIINFEKL, almost no labelled cells were recovered from the draining lymph nodes of any of the three vaccine groups (Figure 5-5b). The abrogation of DC migration to the lymph node in primed mice is consistent with the induction of a cytotoxic T cell response against the SIINFEKL peptide causing elimination of the cells before from the nodes²²⁸. This indicates that loading DCs with Fe NPs or FeOx NPs does not interfere with either their migration to the draining lymph nodes or their presentation of antigen to cytotoxic T cells.

5.2.5 DC migration can be detected ex vivo by MRI at 9.4 T

Before performing experiments to track migration of NP-loaded DC in a clinical scanner at 1.5 T, an ex vivo trial of tracking labelled DCs was performed at 9.4 T. Naïve mice and mice primed with a DC/peptide (SIINFEKL) vaccine received a subcutaneous injection of DCs labelled with Fe NPs and loaded with SIINFEKL into the upper hindlimb. After 48 hours the draining inguinal lymph nodes were removed and examined at 9.4 T (Figure 5.7). There was a significant decrease in the T_2 relaxation time of the nodes removed from naïve versus either primed mice or controls (no vaccination). This indicated that in the naïve mice there was a significant amount of Fe NPs in the draining lymph node resulting from migration of peptide-loaded DCs, whereas in primed mice the induced CTL effectively eliminated the peptide-loaded cells

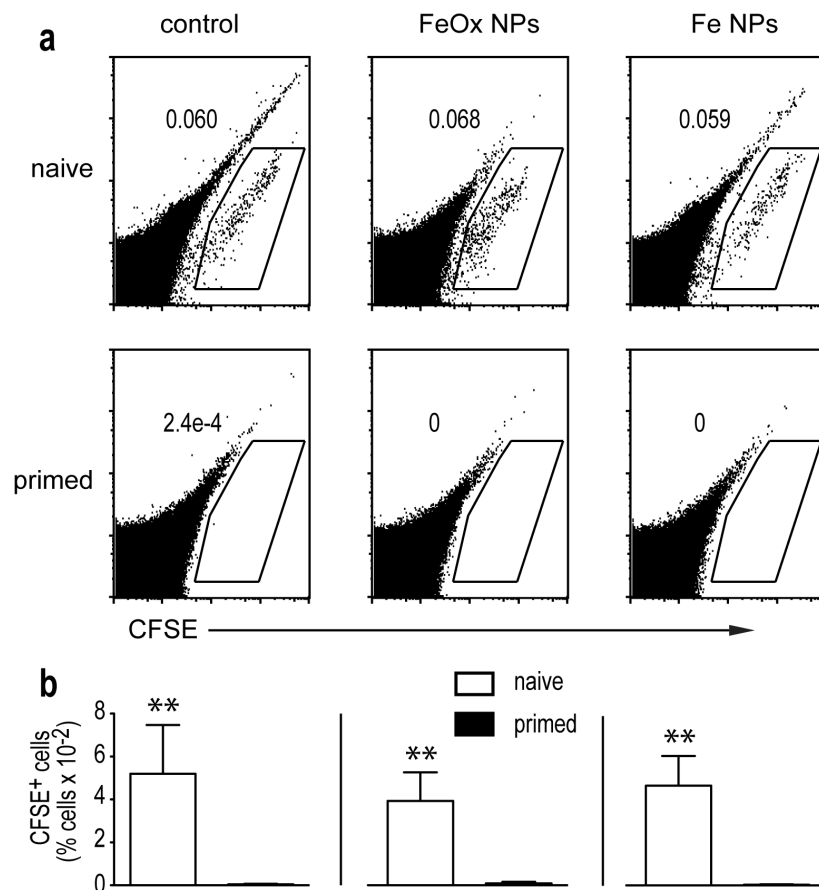


Figure 5.6: Migration of DC/peptide vaccines labelled with Fe NPs or FeOx NPs to the draining lymph node by ex vivo flow cytometry. DCs were incubated with Fe NPs, FeOx NPs or PBS only (control), loaded with peptide, matured with LPS, labelled with CFSE and injected subcutaneously into naïve and vaccinated ("primed") mice. Lymph nodes were removed from mice 48 hours later and analysed by flow cytometry. **(a)** Representative flow plots of control (left column), DCs labelled with FeOx NPs (middle column) or Fe NPs (right column). **(b)** Histogram plots of the number of CFSE⁺ cells recovered from the lymph nodes are shown beneath their respective groups from left: control, FeOx NPs and Fe NPs. (**p<0.01 by unpaired t-test)

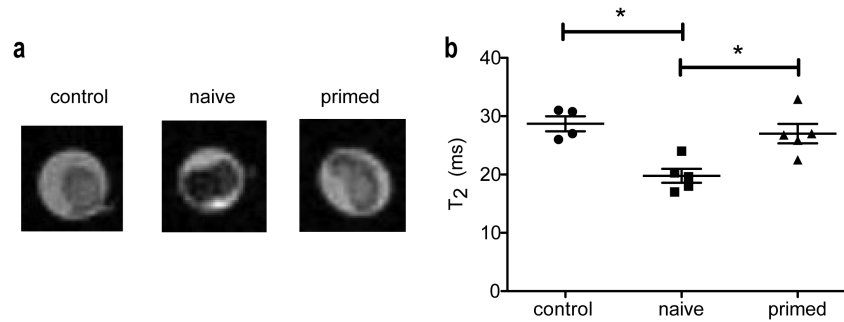


Figure 5.7: MRI of draining lymph nodes ex vivo at 9.4T. DCs labelled with Fe NPs, loaded with peptide and matured with LPS were injected into the upper hind limb of naïve and vaccinated ("primed") mice. Mice injected with DCs unlabelled with NPs were injected as a control. The draining lymph nodes were harvested 48 hours later and dispersed intact into a 1% agar gel matrix and the T_2 relaxation time was determined at 9.4T (b). MR images were acquired (a) using a 2D multi-slice spin-echo sequence, with the following parameters: echo time (TE) = 8 ms, repetition time (TR) = 2000ms, pixel size = $100\mu\text{m} \times 100\mu\text{m}$, slice thickness = 0.5mm. (* $p < 0.05$ by ANOVA with Bonferroni post test)

and few NPs reached the node.

5.2.6 Only Fe NPs are effective for tracking DC migration in naïve versus primed mice

The proof of principle had been demonstrated: Fe NP labelling could enable the different degree of DC migration in naïve versus primed mice to be distinguished by MRI. The task remained to test the system in vivo at 1.5 T and compare the performance of Fe NPs with FeOx NPs.

Three groups of DC vaccines were set up on the basis of the contrast agent applied: Fe NPs, or FeOx NPs or control (PBS). The three different vaccines were each injected into the upper hindlimb of both naïve and primed mice. The MRI appearance of the draining lymph nodes 30 hours after injection are shown in Figure 5-8. The contralateral (non-draining) lymph nodes are also shown and were used as an internal control (Figure 5-8b, right column). Naïve mice that were injected with DCs labelled with either contrast agent tended to show a reduction in T_2 weighted signal in the draining lymph node versus the contralateral lymph node (Figure 5-8c) indicating migration to the draining node. In primed mice, there was no difference detected

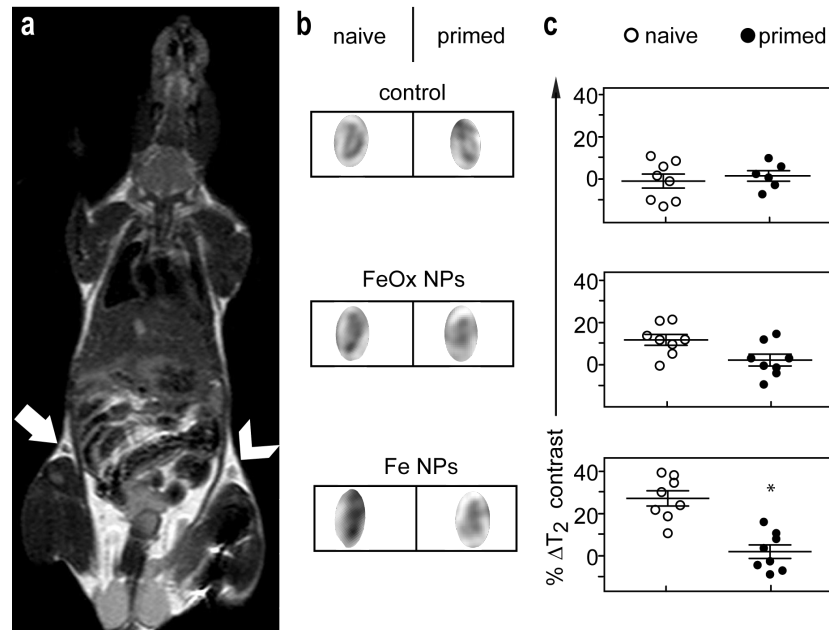


Figure 5.8: MRI of draining lymph nodes in vivo at 1.5T following DC/peptide vaccine labelled with Fe NPs or FeOX NPs. DCs were labelled with Fe NPs, FeOx NPs or PBS only (control), loaded with peptide, matured with LPS and injected into the upper hind limb of naïve and vaccinated ("primed") mice. MRI was performed 48 hours later in vivo at 1.5T, with a representative image from the Fe NP group shown (a). For all images the signal intensity was measured by comparing the signal intensity in the draining inguinal lymph node (a-arrow, b) with a reference of skeletal muscle in the same image. The values for each draining lymph node of each mouse in the Fe NP and FeOx NP groups were then compared with the contralateral node (a-arrowhead) and plotted (c) as %ΔT₂ contrast as follows: (signal intensity of contralateral node)-(signal intensity in draining lymph node)/ (signal intensity of contralateral node). (*p<0.05 by Mann-Whitney rank-sum test)

between draining and contralateral lymph nodes in any of the groups, indicating CTL-mediated elimination of migrating cells. However, only the mice injected with Fe NP labelled DC did the difference between naïve and primed mice show statistical significance. This indicates that although cells labelled with either NP migrated to the draining lymph node in a similar numbers (as seen in Figure 5-6), Fe NPs produced more effective contrast. This was an important distinction as if this test were applied as a marker of an antigen-specific CTL mediated immune response, only Fe NPs would have enabled enough MRI sensitivity to distinguish when DCs migrate or are eliminated before reaching the lymph nodes.

5.2.7 Dose of Fe NPs injected without cells detectable at inguinal lymph node

Despite the different MRI contrast in naïve and primed mice displayed in Figure 5-8, it remained important to investigate whether the Fe NPs were transported to the draining lymph node by DCs and thus a true measure of DC migration. Another explanation could be that the Fe was released from the vast majority of DCs that accumulate at the injection site, and do not migrate to the draining lymph node.

To examine this, the total amount of Fe NPs or FeOx NPs that would normally be added to 10^6 DCs before injection (10^6 cells \times 10 pg Fe/cell = $10\mu\text{g}$) was injected without DCs subcutaneously in the upper hind limb and the draining lymph nodes were imaged. As shown in Figure 5-9b, there was no significant change in contrast with either Fe NPs or FeOx NPs at this dose. When a $200\mu\text{g}$ dose of Fe was injected in the same manner, there was a difference in T_2 contrast seen in both groups with Fe NPs producing significantly better contrast than FeOx NPs (Figure 5-9a,b). However, there was no significant difference in the contrast between a $200\mu\text{g}$ dose given subcutaneously and a $10\mu\text{g}$ dose loaded onto DCs within either NP group (see Figure 5-8). This suggests that the transport of Fe to the draining lymph node is much more efficient by loading in DCs, and that changes in the T_2 contrast in the draining lymph node are related to migration of NP-labelled DCs and not Fe NPs released at the injection site.

5.2.8 DC/lysate vaccines fail to induce DC elimination

The next series of experiments addressed the question of whether this cell tracking assay could be applied to a tumour lysate-based vaccine where the vaccination consists of multiple unknown tumour antigens. These vaccines are thought to generate immune responses to multiple antigens, but because the density of each antigen on the injected DCs is low, the cytolytic responses to each individual antigen may be low. When DCs were loaded with lysate from tumour cells killed by freeze-thawing, they failed to generate a cytotoxic lymphocyte response powerful enough to abrogate DC migration. Even with the addition of a powerful adjuvant⁹⁸ (the iNKT cell ligand α -GalCer) to enhance the response, or when increasing doses of tumour lysate were employed, there was no reduction in the number of DCs recovered in the draining lymph nodes in primed mice (Figure 5-10). In this context, mice vaccinated with DCs loaded with Fe

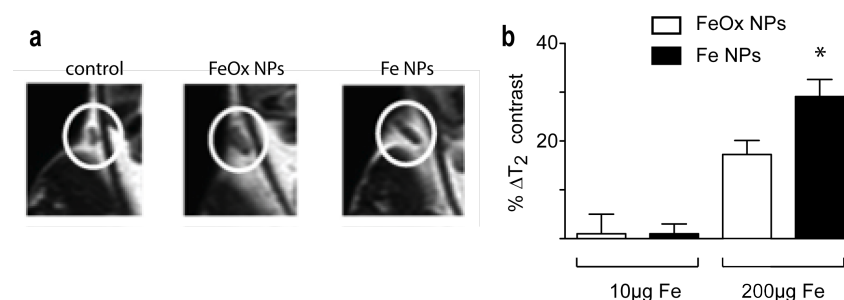


Figure 5.9: Inguinal nodes after s.c. injection of 10µg and 200µg of Fe. Mice were injected subcutaneously in the upper hind limb with a dose of 10 or 200µg Fe ml⁻¹ of either Fe NPs or FeOx NPs, or PBS only (control). MRI was performed 48 hours later in vivo at 1.5T, with a representative draining lymph node from each group shown at a dose of 200µg Fe (**a**-circles). For all images the T_2 contrast was measured by comparing the signal intensity in the draining lymph node with a reference of skeletal muscle in the same image. The values for each draining lymph node of each mouse in the Fe NP and FeOx NP groups were then compared with the contralateral node and plotted (**b**) as % ΔT_2 contrast as follows: (signal intensity of contralateral node)-(signal intensity in draining lymph node)/ (signal intensity of contralateral node). (* $p < 0.05$ by Mann-Whitney rank-sum test)

NPs produced significant contrast changes in the draining lymph node in both naïve and primed mice (Figure 5-11). Did the DC/lysate vaccine fail to induce an antigen-specific immune response? This was shown not to be the case in Chapter 6, where experiments showed that DC/lysate vaccines were able to protect mice against tumours from the same cell tumour line as the lysate (Figure 6-6). The results here showed the assay to be ineffective for assessing the broad, but potentially weaker cytotoxic immune responses induced to this DC/lysate vaccine.

5.3 Discussion

5.3.1 Principle findings

Labelling DCs with Fe NPs was shown to improve the MR sensitivity to twice the level of DCs labelled with FeOx NPs, without altering the maturation, migration or viability of the DCs. The increased sensitivity of DCs labelled with Fe NPs enabled the translation of the ex-vivo DC elimination assay to be performed in vivo with MRI. The adapted version of the DC elimination assay was able to detect an antigen-specific CTL

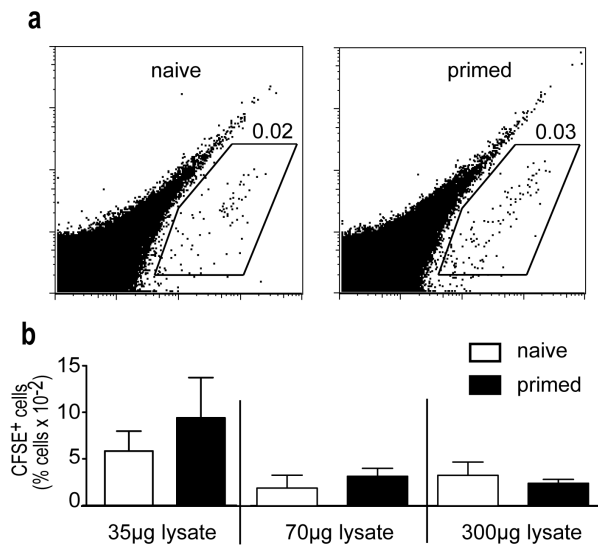


Figure 5.10: Migration of DC/lysate vaccines to the draining lymph node by ex vivo flow cytometry. DCs were loaded with varying concentrations of GL-261 tumour lysate, matured with LPS, labelled with CFSE and injected subcutaneously into naïve and vaccinated ("primed") mice. Lymph nodes were removed from mice 48 hours later and analysed by flow cytometry. (a) Representative flow plots are shown of naïve (a-left plot) and primed (a-right plot) mice injected with DCs cultured with 35µg of tumour lysate/10⁶ cells. (b) Histogram plots of the number of CFSE⁺ cells recovered from the lymph nodes are shown for different groups based on the amount of tumour lysate added to DC culture.

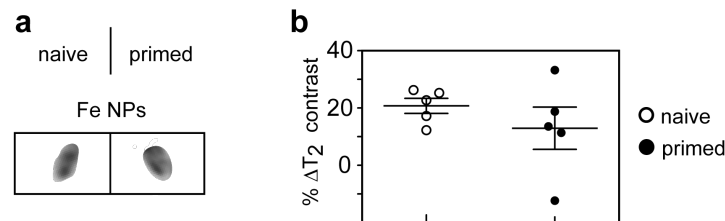


Figure 5.11: MRI of draining lymph nodes in vivo at 1.5T following DC/lysate vaccine labelled with Fe NPs or FeOX NPs. DCs were labelled with Fe NPs, loaded with 35µg of tumour lysate, matured with LPS and injected into the upper hind limb of naïve and vaccinated ("primed") mice. MRI was performed 48 hours later in vivo at 1.5T. For all images the contrast was measured by comparing the signal intensity in the draining inguinal lymph node (a) with a reference of skeletal muscle in the same image. The values for each draining lymph node of each mouse in the Fe NP and FeOx NP groups were then compared with the contralateral node and plotted (a) as %ΔT₂ contrast as follows: (signal intensity of contralateral node)-(signal intensity in draining lymph node)/ (signal intensity of contralateral node)

driven immune response to DC/peptide but not DC/lysate vaccination, with the MRI measurement of DC migration correlating in all instances with the ex vivo flow cytometry measurements.

5.3.2 Mechanism of DC elimination

The phenomenon of antigen-specific elimination of DCs from the draining lymph node was first described in 2000 by Hermans et al²²⁹, who demonstrated that DCs loaded with a peptide antigen are eliminated in a CD8⁺ T cell dependent manner from the draining lymph nodes in mice vaccinated with the same DC/peptide preparation. The same phenomenon was observed when mice were infected with influenza virus, with DCs loaded with an influenza peptide antigen eliminated from the draining lymph node²²². Furthermore, it was suggested that measuring the elimination of CFSE labelled DCs by ex vivo flow cytometry could be used as the basis of an assay of in vivo CTL responses²²². These findings were followed up by a series of studies examining the mechanism and the importance of this phenomenon.

The mechanism of antigen specific elimination of DCs was shown to be dependent on CTLs^{229,230}. These cells recognise antigen presented on MHC class I molecules through direct contact with their T-cell receptor. CTLs possess the ability to rapidly induce apoptosis mediated cell death of the antigen presenting "target" cells through two main mechanisms. CTLs can release cytoplasmic granule toxins including perforin, a membrane disrupting protein²³¹ and granzyme B, a serine protease that activates apoptosis pathways directly (Bcl-2 pathways)²³² and indirectly(caspase pathways)^{233,234}. CTLs can also promote apoptosis of target cells by the ligation of their Fas ligand, FasL, with Fas receptors on the target cell²³⁵.

The relative importance of perforin, granzyme B and FasL ligand pathways in CTL mediated elimination of target cells has been investigated. The FasL has been shown to be inessential for target cell killing as demonstrated through models of genetic knockdown of FasL²³⁰ and FasL antagonism²³⁶. This is combined with some evidence that DCs are resistant to FasL mediated killing²³⁷. In contrast, both perforin^{228,236} and granzyme B²³⁶ have been shown to play critical roles such that if either pathway is inhibited, reduced or absent killing of target cells result.

The physiological role of CTL mediated elimination of DCs is considered to be

important in immune regulation and the prevention of autoimmunity, with evidence for this is seen in both humans and mice. CTL mediated DC elimination has been shown to reduce CD8⁺ T cell proliferation²²⁸, and in mice the inability of perforin-deficient T cells to eliminate DCs and control T cell proliferation leads to autoimmune damage in mice infected with lymphocytic choriomeningitis virus²³⁸. This was also seen in infections with *Listeria monocytogenes*. In humans, uncontrolled lymphoproliferation is seen in viral infections in patients with perforin mutations²³⁹ or increased resistance of DCs to apoptosis²⁴⁰. These findings suggest that mechanisms such as CTL-mediated DC elimination are important in preventing autoimmune damage and pathogenic lymphoproliferation by regulating CD8⁺ T cell proliferation.

The process of CTL mediated killing of target cells is itself regulated by at least two mechanisms that can protect the antigen-presenting target cells from elimination. Meuller et al demonstrated that antigen-specific CD4⁺ T cells can protect DCs from CTL elimination through binding to CD40 on DCs²⁴¹. Watchmaker et al showed that CD8⁺ memory cells can provide similar protection through secretion of TNF- α ²³⁶. Interestingly, both mechanisms were shown to involve upregulation of a granzyme B inhibitor in DCs²³⁶. However, studies by Ronchese and colleagues suggest that the upregulation of granzyme B inhibition is not enough to protect DCs from CTL elimination²⁴², which suggests that CD4⁺ T cells and CD8⁺ memory T cells may bestow protection to DCs by other undiscovered mechanisms as well.

From these findings, which elucidate some of the mechanisms involved in CTL mediated elimination of target cells, can the failure of CTL-mediated elimination of DCs loaded with tumour lysate be explained? The hypothesis generated was that the DCs in DC/lysate vaccines are protected from CTL-mediated lysis by increased numbers of antigen-specific CD4⁺ T cells and CD8⁺ memory T cells. DC/lysate vaccines present antigens to both CD4⁺ and CD8⁺ T cells and can produce proliferation in both cell types²⁴³. This is in contrast to DC/peptide vaccines made with MHC I restricted peptides (such as SIINFEKL in C57Bl/6 mice) that are presented only to CD8⁺ T cells²⁴⁴ (although MHC II peptides could be also present in DC/lysate cultures - from proteins in foetal calf serum). CD4⁺ T cells are important (but not essential) in the generation of CD8⁺ memory T cells²⁴⁵. In Chapter 6 (Figure 6-5), it is shown that DC/lysate vaccines cause a marked increase in memory CD8⁺ T cells in the draining lymph node. It is hypothesized that DC/lysate vaccination induced proliferation of CD4⁺ T cells and CD8⁺ memory T cells, which were of a quality and/or quantity that

differed from those generated by the DC/peptide vaccine, such that they were able to protect the injected DCs loaded with tumour lysate from CTL mediated killing.

This hypothesis would take further studies to test but what can be argued with the available data is that the DC/lysate vaccine could have generated an antigen-specific immune response that did not result in CTL mediated elimination of DCs loaded with tumour lysate. Further evidence of this is seen in Figure 6-6 where DC/lysate vaccines provide antigen-specific tumour protection. In summary, mechanistic studies suggest that a vaccine could induce an antigen-specific immune response that does not necessarily result in CTL mediated elimination of DCs arriving in the draining lymph node. An assay based on DC elimination would therefore detect a subtype of antigen-specific immune responses, producing a loss in sensitivity and a gain in specificity.

5.3.3 Implications of the study

DCs play an important role in regulating adaptive immune responses²⁴⁶, highlighted by their use in cancer immunotherapy⁸⁷. Crucial to this role is the transport of antigen by DCs to secondary lymphoid tissue where it is recognised by T cells. Accordingly, there has been a wide range of imaging modalities applied to tracking DCs after their administration in vivo. These include gamma scintigraphy²⁴⁷, positron emission tomography²⁴⁸, two-photon intravital microscopy²⁴⁹, bioluminescence²⁵⁰ and MRI²⁵¹. MRI has the advantage of producing the best spatial resolution of all the non-invasive imaging modalities³⁹ and does not involve exposure to ionising radiation.

In order to distinguish DCs from surrounding tissue by MRI, they need to be labelled with a contrast agent. FeOx NPs have been employed for this task in both humans²⁵² and mice²⁵¹. Ahrens et al. were the first to load DCs with FeOx NPs and track their migration in vivo at 11.7T²⁵³. No DCs were detected by MRI in the draining lymph nodes over four days, which was attributed to the source of the DCs, which were from an immortalized cell line as opposed to bone marrow derived DCs used in this thesis. De Vries et al. demonstrated that MRI of DCs labelled with FeOx NPs can be used for tracking DC-based vaccines in humans at 4.7T²⁵². Baumjohann and colleagues found that there was correlation of FeOx NP labelled DC migration by histology, flow cytometry and MRI at 4.7T²⁵¹. All three studies found that labelling with FeOx NPs did not result in changes in DC surface marker expression, induction of apoptosis,

migration or T cell priming in vivo.

The findings reported in this chapter present several advances to the application of MRI to DC cell tracking. Whilst this study was not the first to show that DC migration to the draining lymph node can be effectively tracked at 1.5T²⁵⁴, it adds further support to the concept and remains one of the few studies carried out at 1.5T. Clinical MRI scanners with a field strength greater than 1.5T are not widely available in New Zealand, so being able to track DC migration at 1.5T greatly improves the feasibility of including such technology in a clinical trial.

This study was the first to apply MRI tracking of DCs to measure DC elimination in vivo, measuring the CTL mediated DC elimination assay described by Hermans et al²²² with in vivo MRI correlated with ex vivo flow cytometry. The use of Fe NPs to label DCs was essential for this advance as performing the elimination assay with MRI was not effective with the use of FeOx NPs at 1.5T. This was assisted by the use of Fe NPs that increased the sensitivity of MRI to detect loaded DCs to twice the level of FeOx NPs in this study and reported elsewhere²⁵⁵, whilst loading a similar amount of Fe/cell^{252,255}. The adaptation of this assay to a non-invasive technique performed in vivo means that it could be applied to clinical immunotherapy trials.

The DC elimination assay has potential advantages over other assays used to assess the generation of an antigen-specific immune response. Although the DC elimination assay is not sensitive enough to assess DC/lysate vaccines, it has been shown to be more sensitive than the detection of CTL cytotoxicity in vitro following DC/peptide vaccination²²². It can provide information about in vivo function of CTL activity that is not available with other assays used in clinical trials²⁵⁶. Furthermore, the DC elimination assay may prove to have a greater sensitivity than blood based assays in clinical trials based on the clinical findings that antigen-specific CD8⁺ T cells can be detected in the biopsies of the draining lymph node²²¹ or the vaccine injection site²⁵², whereas at the same time, these T cells were largely undetectable in blood. These factors, combined with the non-invasive nature of the assay, warrant consideration of the DC elimination assay with Fe NP enhanced MRI, to be applied to DC/peptide clinical vaccine trials.

5.3.4 Remaining questions

One of the most vital questions that this study raises is whether the DC/elimination assay, performed in vivo with Fe NP labelled DC/peptide vaccines, would detect antigen-specific immune responses in a human clinical vaccine trial, and whether such immune responses would be associated with improved clinical outcomes.

It has been shown that MRI tracking of DCs labelled with FeOx NPs can be applied safely and effectively to a clinical vaccine trial, and is more accurate than scintigraphy for detecting DC positive lymph nodes²⁵². This clinical study by de Vries et al. was performed at 4.7T where there is approximately three times the signal to noise ratio compared with imaging at a field strength of 1.5T. There are some advantages in moving from the imaging lymph nodes in mice to humans. The volume of lymph nodes in humans is approximately 100-200 times that of the murine lymph nodes imaged in this study²²¹. This would enable multiple slices of 1mm thickness (used in this study) to be imaged through the node, thereby reducing the partial volume imaging seen in this study. Since clinical studies typically involve injection of around $5 - 10 \times 10^6$ DCs²⁵⁶, which is more than the number used in this study (1×10^6), the DC/lymph node volume ratio would be reduced by a factor of 10-40 in depending upon the volume of the draining lymph node in the patient. This may not prove to be a severe limitation as the identification of regions of DC migration within the lymph node may be visible in larger lymph nodes²⁵².

The biggest factor in whether the in vivo DC elimination assay will be of ultimate benefit is whether it correlates with positive clinical outcomes. An argument could be made that by elimination of DCs loaded with peptide, administered in successive booster vaccinations, that T cell proliferation is being limited and this may negatively impact on the anti-tumour activity. There is evidence that DC elimination does reduce T cell proliferation^{228,230}, but the effect of this on anti-tumour immune activity has not been determined. Conversely, it could be argued that if DC elimination is shown to have a negative association with clinical outcome then it could be just as useful an assay to perform. As the timing of booster vaccinations has been shown to influence T-cell proliferation through varying the amount of DC elimination²³⁶, the DC elimination assay could provide valuable information about the optimum timing of specific DC/peptide vaccines.

In summary, the most important outstanding question is: what is the relationship

between DC elimination and clinical outcomes in response to a DC/peptide vaccine? Future studies addressing this relationship could have more than one potential outcome in which the DC elimination assay could provide information of benefit.

5.3.5 Conclusion

The use of Fe NPs has distinct advantages over FeOx NPs for tracking DCs in vivo with MRI. The successful adaptation of the DC elimination assay to a non-invasive procedure, using the MRI detection of DCs labelled with Fe NPs, makes it a strong candidate for inclusion in future clinical studies of DC/peptide vaccines.

Chapter 6

Assessing antigen-specific responses to vaccination by monitoring enlargement of draining lymph nodes by MRI

6.1 Introduction

DC vaccines prepared with exogenously administered peptide tumour antigens have traditionally been the most common method of DC-based cancer immunotherapy²⁴⁴. However, DC vaccines prepared with tumour cell lysate have several advantages over DC/peptide vaccines and have produced better results in clinical studies^{257–259}. One of the disadvantages of DC/lysate vaccines is the difficulty in assessing antigen-specific responses to the ill-defined tumour antigens in the tumour lysate. DC/lysate vaccines were observed to produce enlargement of the draining lymph node on MRI during experimental work performed in the last chapter. Based on this response, this chapter introduces a novel assay to determine the presence of an antigen-specific response following DC/lysate vaccination by measuring the area of the draining lymph node (DLN) with MRI.

6.1.1 The advantages of lysate-based vaccines

DC/lysate vaccines have been shown to be more effective than DC/peptide vaccines for producing clinical responses in cancer immunotherapy, with a review of clinical trials finding more than twice the objective response rate with DC/lysate based vaccines²⁵⁸. The relative limitations of DC/peptide vaccines have been well documented and recent years have seen the increasing use of alternative vaccine strategies⁸⁸. The three main restrictions to peptide vaccination include restricted patient selection on the basis of HLA alleles expressed, limited activation of CD4⁺ T cells due to the size constraints of the peptide (MHC class II molecules requiring longer peptides), and a limited repertoire of known tumour antigens that can be targeted by the vaccine-induced response. These restrictions limit the clinical application and effectiveness of peptide vaccines and are explored in further detail below.

One of the main deficiencies of peptide vaccination is that patients with different human leukocyte antigen (HLA) subtypes have different MHC molecules that bind different peptide antigens. Therefore the peptides used in vaccines have to be especially chosen so that they bind MHC class I and/or II molecules in a given patient's HLA-subtype. This restricts the number of candidate peptides, the number of patients in which they can be effectively deployed and potentially the type of immune cells that they can activate. For example, if a peptide is used that contains an epitope that binds MHC class I but not class II, it may successfully produce large numbers of CTLs, but it will be ineffective at CD4⁺ T cell stimulation. Lack of CD4⁺ T cell-stimulation by peptide vaccines could explain lack of long-lived immunity as it has now been well established that antigen-specific CD4⁺ T cells are crucial for the priming of long lived memory CD8⁺ T cells^{245,260}. Furthermore, vaccinating with a single peptide antigen generates only a restricted repertoire of tumour antigen-specific T cells²²⁴. Tumours possess antigenic variation²⁶¹ and could escape the immune response induced by DC/peptide vaccination through reduced levels of expression²⁶² or a mutation in a single targeted antigen²⁶³.

An alternative to DC/peptide vaccines is DC/tumour lysate vaccines where cells from a patient's tumour are lysed and loaded onto the patient's DCs ex vivo. This has several advantages over DC/peptide vaccines in that it provides patient and tumour specific therapy with a relevant array of tumour antigens loaded onto a patients MHC molecules, regardless of their HLA type. DCs loaded with killed tumour cells ex vivo have been shown to present antigen to both CD4⁺ and CD8⁺ T cells^{264,265} and produce

long lived memory⁸⁶ and protection against tumours²⁶⁶. However, the development of DC/lysate vaccines has been limited by difficulty in assessing their generation of tumour antigen-specific immunity, the induction of which has been correlated with positive clinical outcome in two thirds of DC/peptide clinical trials²⁵⁶.

6.1.2 The need for an assay to detect an immune response to multiple (unknown) antigens

The main goal of monitoring antigen-specific T cell responses in immunotherapy trials is to determine whether a treated patient has developed an immune response following vaccination and if the detected response is associated with a clinical outcome. This assists in future vaccine development by determining whether the current vaccine is potent enough to produce a detectable immune response and, if an immune response is generated, whether it is capable of improving clinical outcomes.

The previous chapter discussed a novel *in vivo* strategy for detecting an antigen-specific immune response generated by DC/peptide vaccines. It was not sensitive enough to detect the immune response generated by DC/lysate vaccines. This is a common problem with the variety of *in vitro* assays that can detect the generation of antigen-specific CD8⁺ T cells by DC/peptide vaccines. Antigen-specific immune responses generated by DC/lysate vaccines are more difficult to detect with these assays due to the multiple, poorly defined antigens in the tumour lysate.

As an example to illustrate this point, consider the tetramer assay used to quantify antigen-specific CD8⁺ T cells²⁶⁷. In this assay, T cells from the patient are taken from peripheral blood and exposed to fluorescent multimeric MHC I molecules loaded with peptide antigen for analysis of binding by flow cytometry. Any CD8⁺ T cells with antigen receptors that recognise the peptide presented on the MHC tetramer will stain positive. If this number increases after DC/peptide vaccination it indicates expansion of antigen-specific T cells and is considered a positive response. This assay is not able to quantify antigen-specific T cells induced by a DC/lysate vaccine unless all of the antigens in the tumour lysate were known and were able to be loaded onto MHC Class I and Class II tetramers, which is not feasible. A compromise is to load tetramers with generic tumour antigens that the tumour type has been shown to express²⁶⁸. This approach is severely limited in the information it provides as patients may develop

effective immune responses against other undefined tumour antigens and therefore be regarded as tetramer negative. Another commonly used assay to measure antigen-specific immune responses, Elispot, may also fail to identify responses to relevant antigens with tumour lysate vaccines²⁶⁹. Therefore, a more effective assay of immune responses to DC/lysate vaccination is required.

6.1.3 Enlargement of the draining lymph node following DC/lysate vaccination

During the DC tracking experiments in the previous chapter, it was noted that the draining lymph nodes were enlarged in mice that received both priming and secondary vaccination with the same DC/lysate vaccine. This was observed on MRI 30 hours following subcutaneous secondary vaccination and was not observed in mice that did not receive a priming vaccine. The phenomenon of sequestration of antigen-specific lymphocytes from the peripheral blood into lymphoid tissues, peaking at 24-48 hours after antigen exposure, was first described over 30 years ago²⁷⁰. Draining lymph node enlargement has been shown to be due to an antigen-specific reaction where challenged nodes can weigh up to three times the contralateral node at 48 h²⁷¹.

The work in this chapter investigates whether the observations of early draining lymph node enlargement by MRI is related to the described phenomenon by the antigen-specific recruitment of lymphocytes. The selective enlargement in the mice that received priming vaccinations could be explained by the generation of increased numbers of tumour lysate antigen-specific lymphocytes, which were then recruited to the draining lymph on secondary vaccination. More importantly, could MRI of the draining lymph nodes be used as the basis for a non-invasive in vivo assay to assess the generation of an antigen-specific immune response following DC/lysate vaccination?

6.1.4 Aims

The aim of this chapter is to test the hypothesis that the MRI measurement of early draining lymph node enlargement can be used as a marker of an antigen-specific immune response generated by DC-based vaccination. The following questions will be addressed in the context of a C57BL/6 mouse model using bone marrow generated DCs,

established mouse tumour cell lines and MRI in a clinical scanner at 1.5T.

1. Is early lymph node enlargement an antigen-specific response to vaccination?
2. Is early lymph node enlargement seen following challenge with DC/lysate and DC/peptide vaccines?
3. What is the time course of the enlargement?
4. Does re-enlargement occur after a third vaccination?
5. What are the cell types involved in the enlargement?
6. Does early lymph node enlargement correlate with tumour protection?

6.2 Results

6.2.1 Lymph node enlargement is an antigen-specific response to vaccination

Based on the knowledge that induction of immune responses is associated with trapping of lymphocytes in lymphoid tissue, it was speculated that an MRI-based assay of lymph node size could be used to assess vaccine-induced responses. It was hypothesized that measurable increases in lymph node size would be observed shortly after a second round of vaccination, as the response induced by the primary vaccination would orchestrate rapid lymphocyte trapping upon re-exposure to vaccine-associated antigens. In contrast, where primary vaccination has failed to elicit an immune response, no such increase would be observed. The first step in developing such an assay was to show that MRI could detect post-vaccination changes in lymph size in vaccinated animals relative to naïve controls. Vaccines comprising DCs loaded with tumour lysate were used for this analysis. These were prepared by first harvesting 10^6 glioma cancer cells in culture and lysing them by rapid freezing in liquid nitrogen and thawing to 37°C three times. The glioma cell lysate was then added to 10^6 DCs on day 5 of their culture in vitro. The adjuvant, a-GalCer, was added on day 6 to enhance vaccine potency. On day 7, DCs were harvested and 10^6 were injected intravenously into each mouse in the "primed" group only. The secondary (or "challenge") vaccine, injected 7 days later, was prepared in same way except that LPS was added on day 6, instead of a-GalCer, to

improve DC migration to the draining lymph node²²³. The DCs were injected subcutaneously, 10^6 cells/mouse in the upper hind-limb of mice, in the primed animals, and also a group of naïve controls. The draining and contralateral inguinal lymph nodes were imaged by MR 30 hours later with the results shown in Figure 6-1.

In primed mice, there was a significant increase in the mean area of the draining lymph nodes compared with the contralateral lymph nodes; no such difference was observed in naïve mice. This response was reproducible, with all of the draining lymph nodes in the primed group being larger than the opposite nodes in the same mouse (Figure 6-1c). The areas of the lymph nodes can be expressed by plotting the area of each lymph node (as in Figure 6-1b and c) or by taking the difference (area of draining lymph node) - (area of contralateral lymph node) and expressing this as a percentage of the area of the contralateral lymph node for each mouse (Figure 6.1d). The latter method is employed for the rest of this chapter as it removes some of the background statistical noise produced by comparing mice of different sizes (up to a 10% difference in mass was observed in 6 week old syngeneic littermates) and obviates the need to use paired statistical tests when comparing groups of mice.

These initial results were promising but not altogether convincing as the primed mice had received a powerful adjuvant, (a-GalCer), that the naïve mice had not. Furthermore, it remained to be proven that the enlargement was related to any mechanism specific to the tumour antigen in the DC/lysate vaccine. It could perhaps be a marker of an induced immune response to a non-tumour constituent of the vaccine, such as to foetal calf serum in which the DCs are cultured. Therefore, a further series of experiments was performed to tease out whether the enlargement of the draining lymph node was indeed a marker of a tumour antigen-specific response following DC/lysate challenge. For these experiments, all mice were primed with DCs loaded with glioma cell lysate, then challenged with a DC/lysate vaccine made from either glioma cells ("G:G" group) or from an unrelated thymoma cancer cell line ("G:T" group). Analysis 30 hours after vaccine challenge showed that the G:G group had more than three times the increase in the size of their draining lymph nodes versus the G:T group (Figure 6-2b, mean 95% versus 31% respectively). This finding indicates that the major contribution to enlargement of the draining lymph nodes was a specific immune response to the glioma cell lysate constituent of the DC/lysate vaccine.

As the glioma cell line originates from neuroglial cells that express antigens that are immunoprivileged²⁷² (not normally accessed by the immune system), the results in

Figure 6-1e may be unique to the glioma cell line and not applicable to other types of cancer. To test this, a similar experiment was performed with a crucial difference: all mice were primed with the thymoma cell line and then challenged with a DC/lysate vaccine containing either glioma ("T:G" group) or thymoma ("T:T" group) cell lysates. Enlargement of the draining lymph nodes was observed only in mice that received the same priming and challenging DC/lysate vaccine (Figure 6-1f, T:T group). Therefore, it can be concluded from these experiments that significant lymph node enlargement is attributable to antigen-specific responses to the lysate constituents of the vaccine; hence the same antigens must be present in priming and challenging vaccines.

Was the observed phenomenon of antigen-specific enlargement of the draining lymph node particular to DC-based vaccines with the incorporation of tumour lysate? To answer this question the same DC/peptide vaccine described in Chapter 5 was employed. Lymph node enlargement was seen following DC/peptide vaccination in primed mice but not in naïve mice (Figure 6-2). This implies that enlargement of the draining lymph node can be induced with single or multiple antigens incorporated into a DC-based vaccine.

6.2.2 Time course of the draining lymph node enlargement

For the examined phenomenon of draining lymph node enlargement to become the basis of an assay to measure antigen-specific responses to DC-based vaccines, it was important to determine the time course of the enlargement. Of particular importance was to determine the window of time in which significant antigen-specific enlargement of the draining lymph node was observed.

An important factor in the size of a lymph node is the network of blood vessels within the lymph node, which are lined by endothelial cells. Mature DCs can induce proliferation of endothelial cells, which in turn increase the cellularity and size of a lymph node by expanding the network of blood vessels and increasing the supply of cells entering the node²⁷³. DCs in all of the DC-based vaccines examined here could induce this process after migrating to the DLN following subcutaneous injection. This process is not antigen-specific and will therefore produce lymph node enlargement in the DLN in naïve mice as well as primed mice - potentially interfering with the proposed antigen-specific assay. Endothelial cell proliferation peaks at 7 days but can be seen as early as 48 hours post injection of DCs²⁷³. Therefore the time course of

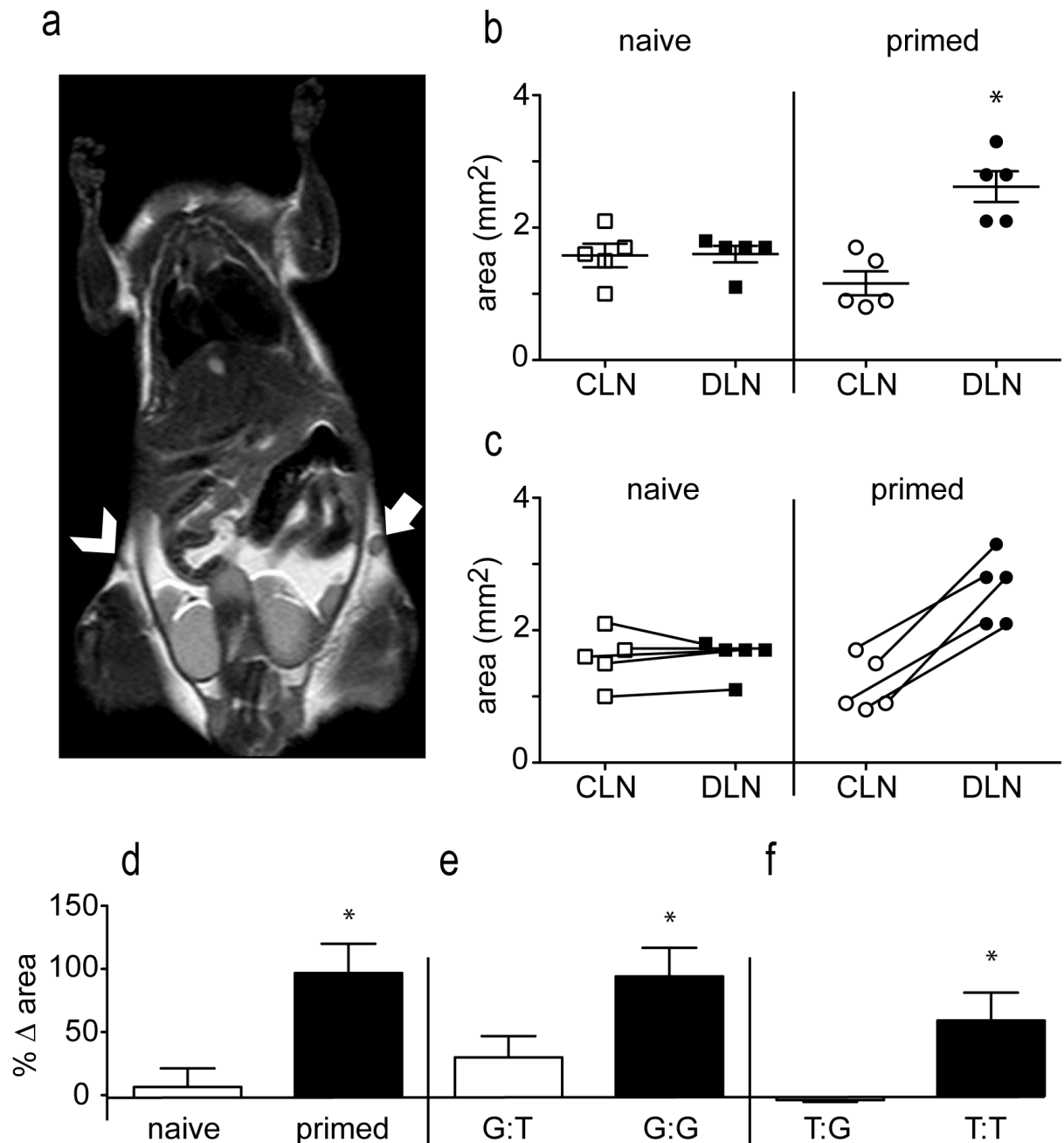


Figure 6.1: Area of draining and contralateral lymph nodes following DC/lysate vaccination. Mice were scanned at 1.5T with a T_2 -weighted spin echo sequence 30 hours after receiving subcutaneous vaccination into the upper hindlimb. The area of the draining (a, solid arrow and b, DLN) and contralateral (a, arrowhead and b, CLN) inguinal lymph nodes were measured with the areas plotted in (b). The pairing of the draining and contralateral lymph nodes in the same mice are shown in (c). The percentage difference in the area of the draining versus the contralateral lymph nodes was calculated for each mouse and plotted d as follows: (area of draining lymph node) - (area of contralateral lymph node) / (area of contralateral lymph node). In (e), all mice were primed with the same glioma cell-based DC/lysate vaccine, then challenged with a DC/lysate vaccine made from either glioma cells (G:G) or from thymoma cells (G:T). In (f), both groups were primed with thymoma based DC/lysate vaccines and challenged with either glioma (T:G) or thymoma based (T:T). (* $p < 0.05$ by two-tailed t test)

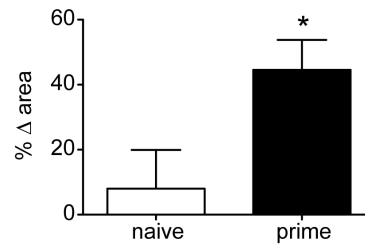


Figure 6.2: Difference in the area between draining and contralateral lymph nodes following DC/peptide vaccination. Mice primed with a DC/peptide vaccine (primed) and naïve mice were imaged 30 hours after DC/peptide vaccination. The results are plotted as the difference in the area between the draining and contralateral lymph nodes for each mouse as in Figure 6-1. (* $p < 0.05$ by two-tailed t test)

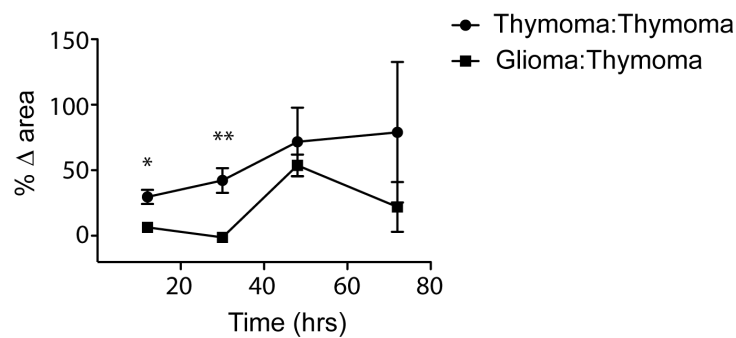


Figure 6.3: Time course of draining lymph node enlargement following DC/lysate vaccination. All mice were primed with the same thymoma cell-based DC/lysate vaccine, then challenged with a DC/lysate vaccine made from either glioma cells (Thymoma:Glioma) or from thymoma cells (Thymoma:Thymoma). The mice were scanned in groups at 12, 30, 48 or 72 hours following vaccination. (* $p < 0.05$, ** $p < 0.01$ by two-tailed t test)

lymph node enlargement was examined around this point at 12, 30, 48 and 72 hours post administration of DC/lysate vaccine (Figure 6-3).

Only at the time points prior to 48 hours was there a difference in DLN enlargement between the two vaccine groups that reached statistical significance. For this reason, measuring DLN enlargement is no longer a marker of an antigen-specific response from 48 hours post-vaccination and the assay must be applied before this time point.

6.2.3 Re-challenge vaccination produces re-enlargement

Cancer immunotherapy with DC-based vaccines usually involves multiple vaccinations separated by one to four weeks⁸⁷ to improve the memory response²⁷⁴. Therefore it was investigated whether DLN enlargement was seen after multiple vaccinations.

Experiments were set up to distinguish the difference in the size of the DLN between mice that received two versus three of the same DC-lysate vaccines. All mice received two vaccines, 1 week apart. Two weeks later, only mice in the "re-challenge" group received a third vaccine; all mice were then imaged 30 hours later.

The results showed that all mice had a similar degree of DLN enlargement 30 hours following the second vaccination (Figure 6-4). However, the mice in the re-challenge group developed further DLN enlargement after a third vaccine. In contrast, over the same timeframe, the DLN of the mice that did not receive this last boost were reduced in size to the point that they were no longer significantly larger than the contralateral nodes. These findings are evidence that it would be appropriate to use MR imaging of the DLN, as a marker of an antigen-specific response, when vaccines are as close as 2 weeks apart. This would not have been the case if either the DLN had remained enlarged 2 weeks following the second vaccine, or if there had not been a repeat in DLN enlargement following the third vaccine.

6.2.4 Cell types involved in lymph node infiltration

After investigating the antigen-specificity and timing of DLN enlargement, it was important to look at the nature of the enlargement. Could the enlargement of the DLN be explained by cellular infiltration and if so what were the types of cells involved in the response?

To answer this question, the DLN and contralateral lymph nodes were removed and processed into single cell suspensions for analysis by flow cytometry (Figure 6-5). All mice were vaccinated with a thymoma cell based DC/lysate vaccine then a week later were challenged with either DCs only (T:DC), a glioma based DC/lysate vaccine (T:G) or the original thymoma based DC/lysate vaccine (T:T).

The total cells recovered from the DLN versus the contralateral lymph nodes was increased by almost 400% in the T:T group. The increase in cell numbers alone was of

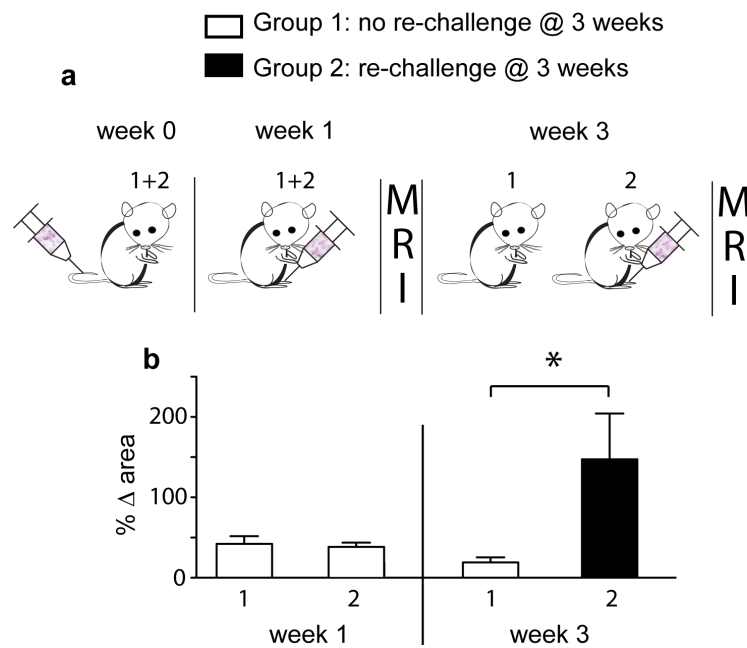


Figure 6.4: Area of draining lymph nodes following re-challenge with DC/lysate vaccine. A schematic shows the vaccine administration and MRI schedule in the two groups (**a**). All mice received two doses of the same thymoma cell based DC/lysate vaccine one week apart. MRI of all mice was performed 30 hours following the second vaccination (**b**, week 1). Two weeks later, only the mice in the "re-challenge" group received a third vaccine. MRI of all mice was performed 30 hours later (**b**, week 3). (* $p < 0.05$)

sufficient magnitude to explain the DLN enlargement observed on MRI without involving other mechanisms such as oedema or an increase in vascularity of the lymph node, although these other mechanisms could not be ruled out.

The increase in cell numbers was made up of a broad variety of cell types including all lymphocytes: CD4⁺ (B220-/CD4⁺) and CD8⁺ (B220-/CD4⁺) T cells, B cells (B220⁺), NK (B220-/CD4-/CD3-/NK1.1⁺) and NKT cells (B220-/CD3⁺/NK1.1⁺) as well as myeloid cell types such as DCs (B220-/CD11c⁺), monocytes (B220-/CD11c-/Ly6CHi) and macrophages (B220-/CD11c-/F480⁺). In all cell types examined there was an increase in the mean cell number in the DLN of the repeated thymoma-based DC/lysate vaccination (T:T group) relative to other challenge groups, although this trend did not reach statistical significance for myeloid cells. Challenge with DC only, or the glioma-based DC/lysate vaccine (T:G) showed a trend to increased myeloid cell numbers in the DLN (Figure 6-5c) although these increases did not reach statistical significance.

The T cells were further separated into naïve, central memory and effector memory cells. naïve cells are those that have not been activated through their T-cell receptor coming into contact with antigen presented on an antigen presenting cell. Central and effector memory T cells are both important for anti-tumour activity and prevention of relapse⁸⁸, and they possess distinct phenotypes and functions²⁷⁵.

Central memory T cells (Tcm) circulate through secondary lymphoid tissues and have little effector function²⁷⁶. They can respond to antigen rapidly and dividing and differentiating into effector T cells. In contrast, effector memory T cells (Tem) can migrate to peripheral tissues and mount an immediate cytolytic response with Tcm cells²⁷⁷. Effector memory cells undergo modest proliferation upon antigenic stimulation, at lower levels than central memory cells²⁷⁸.

Tcm were defined in this study as CD62L⁺CD44⁺ cells and effector memory cells as CD62L⁻CD44⁺ cells^{279,280}. The number of CD4⁺ and CD8⁺ naïve and Tem cells were increased in the DLN of the T:T group but not to a greater extent than the overall CD4⁺ or CD8⁺ T cells. However, both CD4⁺ and CD8⁺ Tcm were markedly increased in the T:T group over the other two vaccine groups. This increase was approximately twice the magnitude of the total cell increase, suggesting a selective recruitment. This indicates that all subsets of T cells were being recruited, with a specific excess in one of the subtypes associated with tumour protection. Caution must be taken not to over interpret the relationship between the number of different cells recruited and the

effectiveness of the vaccine as the number of T cells specific for tumour antigens can not be determined or even estimated from this method of analysis. In summary, the results show that there is a broad-spectrum recruitment of lymphocytes, dominated by central memory cells, to the DLN of mice primed and boosted with the same DC/lysate vaccine and that this process is antigen-specific.

6.2.5 Lymph node enlargement correlates with tumour protection

The final step in testing the DLN enlargement phenomenon was to examine whether a DC/lysate vaccine, which had been shown to produce antigen-specific DLN enlargement, could also provide antigen-specific protection against tumour challenge. The same glioma- and thymoma-based DC/lysate vaccines that were examined earlier in this chapter, were administered to mice for tumour challenge experiments. Two control groups were also set up, one which received a DC-only vaccine (DC only) and a group which received no vaccination at all (no vaccine). One week later all mice received a subcutaneous challenge with thymoma cells. It was shown that the mice that received the thymoma vaccine had significantly better protection from developing tumours within 60 days (Figure 6-6). All of the mice within the other three groups developed tumours within 20 days, whereas in the thymoma vaccine group fewer than 50% developed tumours within 60 days. The experiment was repeated three times with a representative experiment (Figure 6-6a) and the pooled data shown (Figure 6-6b). These results demonstrate that for the DC/lysate vaccine tested, there was antigen-specific tumour protection.

6.3 Discussion

6.3.1 Principle findings

The enlargement of draining lymph nodes as measured by MRI was found to be an antigen-specific response to DC/lysate and DC/peptide vaccines occurring within 48 hours of secondary vaccination. When the draining lymph nodes were imaged 2 weeks after secondary vaccination, they were no longer enlarged, unless a third vaccine was

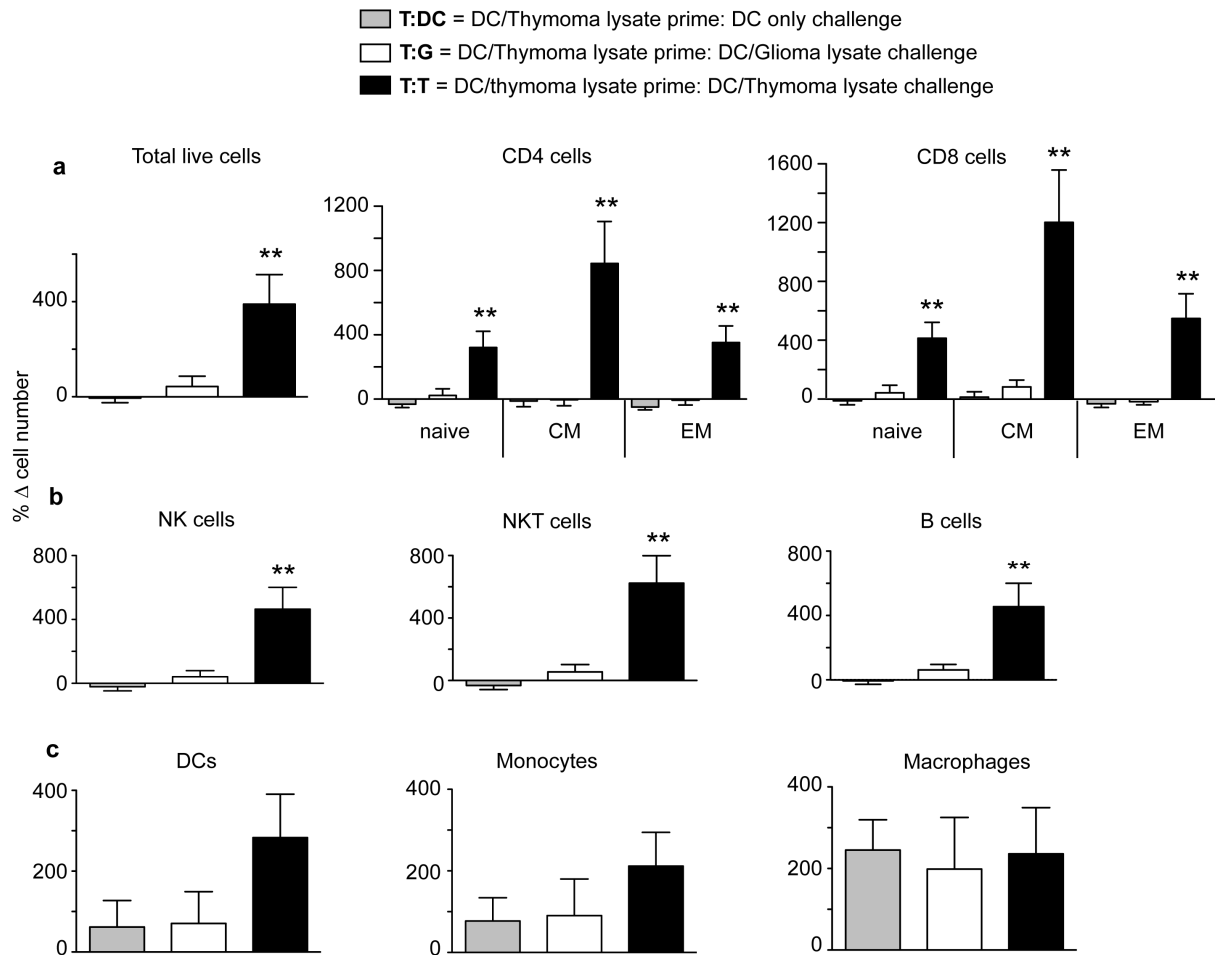


Figure 6.5: Cell types involved in lymph node infiltration. The draining and inguinal lymph nodes were removed 30 hours post-vaccination in mice that were primed with a thymoma based DC/lysate vaccine and boosted with either DCs only (T:DC), a glioma based DC/lysate vaccine (T:G) or the original thymoma based DC/lysate vaccine (T:T). The gating strategies of different cell types were as follows: CD4⁺ (B220-/CD4⁺) and CD8⁺ (B220-/CD4⁺) T cells, B cells (B220⁺), NK (B220-/CD4-/CD3-/NK1.1⁺), NKT cells (B220-/CD3⁺/NK1.1⁺), DCs (B220-/CD11c⁺), monocytes (B220-/CD11c-/Ly6Chi) and macrophages (B220-/CD11c-/F480⁺). The antibodies, fluorophores and flow cytometry plots are detailed in Chapter 2-6. The increase in the number of cells was plotted as percentage difference as follows: (number of cells in DLN) - (number of cells in the contralateral lymph node) / (number of cells in the contralateral lymph node). (*p<0.05, **p<0.01 by ANOVA with Bonferonni multiple comparison test)

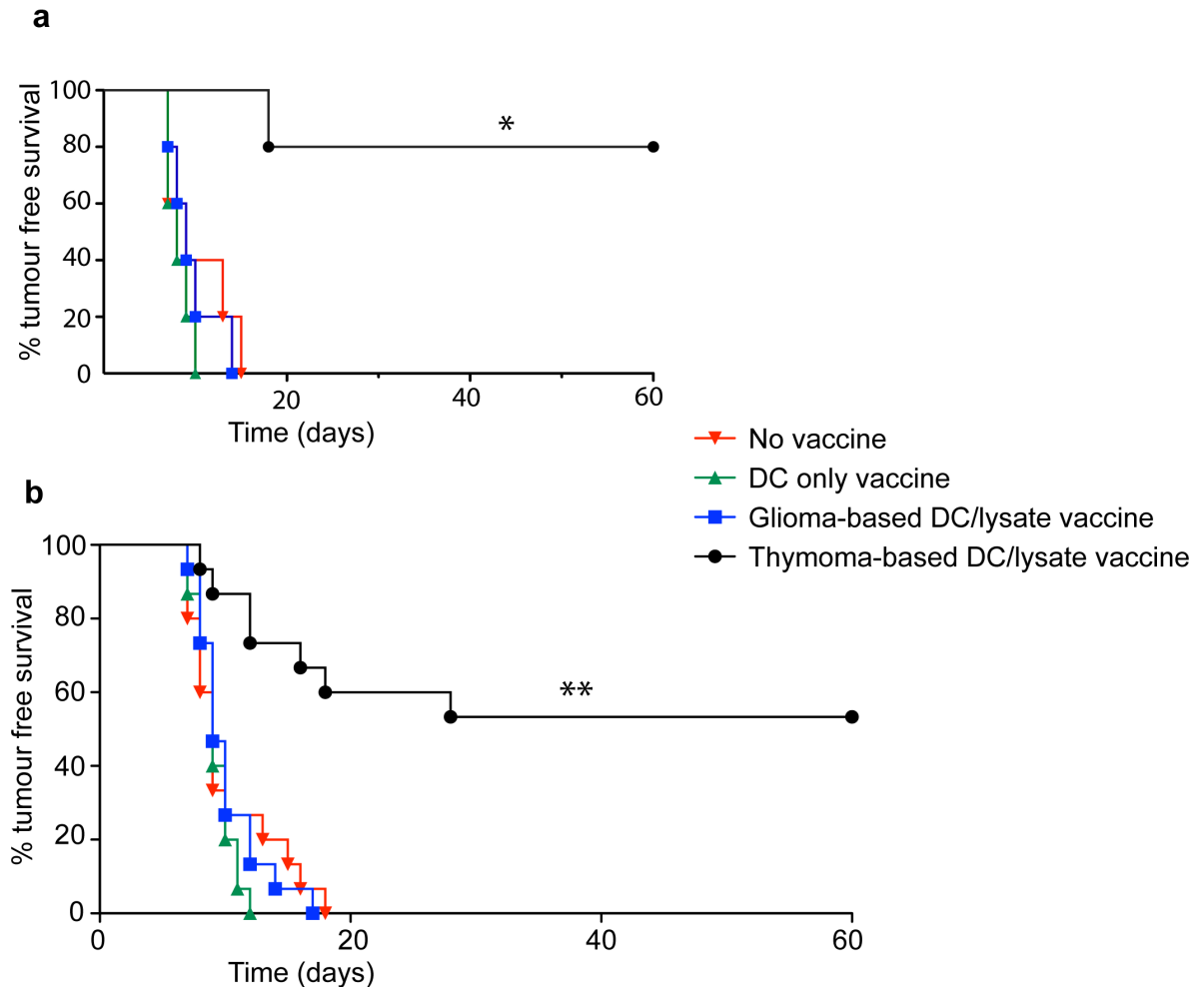


Figure 6.6: Subcutaneous thymoma tumour challenge in mice following vaccination. Mice were vaccinated with a DC/lysate vaccine based on either glioma or thymoma cell lysate. A DC-only and a no vaccine group were used as controls. A subcutaneous injection containing 10^6 thymoma cells was administered to all mice one week following vaccination. Mice were examined daily from day 6 and deemed to be positive for tumours when they developed a mass measuring greater than 4mm^2 by external calliper measurements. The survival curve of a representative experiment with 5 mice per group is shown (a) along with a pooled sample of three individual experiments (b). (* $p < 0.05$, ** $p < 0.001$ by log rank test)

administered, in which case there was further enlargement. The lymph node enlargement was associated with an increase in all lymphocyte populations with the largest increase seen in CD4⁺ and CD8⁺ central memory T cells. Mice that received DC/lysate vaccines were protected from tumour challenge with the same tumour used in the lysate. This protection was not seen with DC/lysate vaccines made from another tumour cell type. Therefore, a correlation was observed between the induction of an antigen-specific immune response by DC/lysate vaccination, as measured by early draining lymph node enlargement, and tumour protection.

6.3.2 Mechanism of the draining lymph node enlargement

Although the mechanism of cell recruitment into the draining lymph node following DC/lysate vaccination was not investigated in this study, a hypothesis can be generated by comparison with similar studies in the literature. Since lymphocyte migration into a lymph node was shown to markedly increase in the presence of antigen over 45 years ago²⁸¹, there have been many studies investigating the importance and the mechanisms of lymphocyte trafficking into lymph nodes in response to antigen-specific interactions.

This process of early lymphocyte recruitment to the draining lymph node is conserved across multiple species^{282–284} indicating a fundamental role in adaptive immunity. What is the functional significance of lymphocyte accumulation in antigen-challenged lymph nodes? The increased lymphocyte traffic through an antigen challenged lymph node can improve the probability that lymphocytes will come into contact with their cognate antigen²⁸¹. Furthermore, the specific migration of clonally expanded memory T cells to sites of antigen deposition enables a rapid functional response if they encounter their cognate antigen²⁸⁵ which could be applied to antigen-challenged lymph nodes²⁸⁶. Strong evidence of the importance of this phenomenon is seen when the cells are removed from an antigen challenged lymph node resulting in the failure to develop systemic immune memory to that antigen²⁸⁷.

Hall and Morris performed one of the earliest studies looking at the mechanism of lymph node recruitment to antigen challenged lymph nodes. They showed that the increase in lymphocytes within an antigen stimulated lymph node is not caused by lymphocyte proliferation within the node, or by increased migration into the node through the afferent lymphatics, but is due to traffic of cells from the blood²⁸¹. Lymphocyte entry into the lymph node from the blood is further supported by the

finding that there is a four fold increase in blood supply to the lymph node following antigen challenge²⁸⁸. Mackay et al showed that, in addition to the general increase in cell traffic through an antigen challenged lymph node, there are also specific increases in the ratio of central memory to other T cell subsets²⁸⁶.

Cahill et al. showed that a "cell shutdown" occurs in lymph nodes when challenged with antigen²⁸². This cell shutdown causes reduced efferent outflow and accumulation of all lymphocytes within the lymph node, including B cells, within 12 hours. This response was markedly increased in animals that had been primed to the antigen.

These early studies describe a similar phenomenon to what was observed in this study, namely the accumulation of lymphocytes into the antigen challenged nodes of primed mice within 48 hours and the preferential recruitment of central memory cells. Furthermore, these studies show that the increase in cell numbers into the antigen challenged lymph node is due to lymphocyte influx from the blood and not cell proliferation within the node. They do not answer the question of how the response is antigen-specific or its molecular mechanism.

McConnell and Hopkins examined the mechanism by which cell shutdown occurs in lymph nodes only on secondary challenge with antigen. They showed that complement activation can cause cell shutdown with similar kinetics to antigen mediated cell shutdown²⁸⁹. Complement can be activated by antibody bound to antigen and could therefore be a result of an antigen-specific response by B cells (a subtype of which, plasma cells, secrete antibody). Complement activation causes release of PGE₂ and by inhibiting PGE₂ cell shutdown was abrogated²⁹⁰.

There is evidence that T cells also play a key role in shutdown of cell egress from antigen challenged lymph nodes. Lymphocyte retention can be induced by the intra-lymphatic infusion of primed T cell supernatant²⁸⁹. Cytokine production is rapid after antigen re-exposure in memory T cells (2 hours) versus naïve T cells (6-20 hours)²⁹¹. If the DC/lysate vaccine produced an increased memory T cell population, specific for tumour antigens in the lysate, this could explain why the cell accumulation was seen within 12 hours. It is not unlikely that an expanded pool of memory T cells specific for tumour antigens would soon come into contact with antigen in the draining lymph node as $\approx 2\%$ of the recirculating lymphocyte pool transits through a single inguinal lymph node in a mouse per day²⁹². Central memory cells are known to recirculate through lymph nodes until they come into contact with antigen, at which

point they mount strong recall responses whenever the antigen returns^{277,293}.

These findings suggest antigen-specific mechanisms of lymphocyte accumulation in lymph nodes that could well be at play in the DC vaccine model described in this chapter. They are somewhat lacking in molecular detail, as the mechanisms of antigen-specific inhibition of egress are still yet to be determined^{294,295}. Promising candidates, such as the secretion of T-cell chemokines by DCs, including CCL22, CXCL10 and CXCL13, were shown not to mediate the early sequestration of T cells into the lymph node within 48 hours of vaccination²⁹⁶.

There exists a powerful molecular mechanism of inhibiting lymphocyte egress from lymph nodes that has been actively researched in the last decade. FTY-720 is a sphingosine 1-phosphate (S1P) receptor agonist that inhibits the egress of lymphocytes from thymus, lymph node and Peyer's patches (but not from the spleen), thereby depleting lymphocytes from the circulation, resulting in an immunosuppressive effect²⁹⁷. S1P1 receptors are present on T and B lymphocytes and when S1P is present at low levels it promotes chemotaxis²⁹⁸. There is debate in the literature about how S1P acts within a lymph node to inhibit lymphocyte egress²⁴⁹. One hypothesis proposes that a concentration gradient of S1P exists in lymph nodes, with a low concentration within the node except near exit sites. S1P is secreted by cells near the exit site to the lymph nodes and by acting on S1P1 receptors on lymphocytes, it drives their egress and re-circulation. When S1P is present in high concentrations (i.e. with exogenous administration of FTY720) it binds to S1P1 receptors on lymphocytes, promoting receptor down-regulation and preventing chemotaxis toward the exit sites²⁹⁹. A second hypothesis proposes instead that S1P1 agonists act on endothelial cells to block lymphocyte egress³⁰⁰ through the sinus endothelium of the lymph node. Although the connection between S1P1 and early antigen-specific lymph node accumulation of lymphocytes has not been determined²⁹⁴, it is a credible candidate pathway that restricts lymphocyte egress from lymph nodes.

The mechanism of early lymphocyte accumulation in antigen challenged lymph nodes remains to be clearly elucidated. It is hypothesized from the studies above that it is both an important process in producing memory responses, and that it is likely to involve several different cell types and pathways. When antigen-specific memory T cells which come into contact with antigen presented on DCs in the lymph node, cytokines are released that can induce cell accumulation. Complement activation, presumably from antibody-antigen complexes, can produce PGE₂ mediated shutdown of cell egress

from lymph nodes and this is reversible by inhibition of PGE₂. No involvement in this process has been proven for the S1P pathway as yet, but it is likely that future studies will reveal how its potent ability to prevent lymphocyte egress from lymph nodes could be related to early antigen-specific accumulation in antigen challenged lymph nodes.

6.3.3 Implications of the study

The assay introduced in this chapter was sensitive enough to detect an antigen-specific immune response generated by DC/lysate vaccines, whereas the assay discussed in the last chapter, based on elimination of migrating antigen-loaded DCs, was not. It is worth examining why the lymph node enlargement assay is more sensitive than the DC migration assay. The DC migration assay depends on the CTL dependent elimination of DCs before they reach the draining lymph node. As hypothesized in Chapter 5, this could be prevented by the production of a CD4⁺ T cell and CD8⁺ memory cells that protect the DCs from CTL mediated killing. Whatever the mechanism, it was shown (in Figure 5-10,11) that the DC/lysate vaccine did not prevent DCs migrating to the draining lymph node.

In contrast, the draining lymph node enlargement assay potentially depends on three different steps: i) the stimulation of an antigen-specific immune response that is not necessarily CTL predominant, ii) the recognition of the tumour antigens presented on DCs by specific lymphocytes that then release cytokines but do not need to induce apoptosis in the antigen presenting DC, iii) recruitment of cells to the draining lymph node on an order that can produce enlargement detectable by MRI. Step ii) requires further dissection (see section 6.3.2) but assuming that these general principles are correct, it can be seen why the draining lymph node assay was able to detect antigen-specific responses from both DC/lysate and DC/peptide vaccines, whereas the DC migration assay from Chapter 5 was sensitive enough only for responses to DC/peptide vaccines.

Another advantage of the draining lymph node enlargement assay was that it is very simple to measure the size of lymph nodes with MRI. Measuring contrast in murine lymph nodes was prone to volume averaging effects due to the presence of adjacent fat along the slice selection axis (which was three times as thick as the other two dimensions in order to increase signal to noise ratio). This did not affect the measurement of the lymph node area because the distinction between the border of the

lymph node and the fat was very clear in plane of the image (see Figure 6-1a).

Comparing the area of the draining with the contralateral lymph node was a very straightforward method to standardise the degree of enlargement, which minimised the error of group comparisons. Furthermore, the assay does not require the use of high field ($>1.5\text{T}$) MRI nor does it require the use of contrast agents. The measurements of lymph node area can be made within minutes without requiring specialist radiologist interpretation. This is in contrast to two of the major assays used in clinical vaccine trials tetramer and ELISPOT, which remain labour intensive and are difficult to standardize⁸⁸. A standardisation study of the tetramer assay performed across 27 laboratories showed a wide variation in the frequencies of antigen-specific T cells reported²⁶⁷. Similar discrepancies have been reported for ELISPOT³⁰¹. Although the lymph node enlargement assay does not quantify the production of antigen-specific T cells, nor does it assess their function such as cytokine release on re-exposure to antigen, the tetramer and ELISPOT assays have limited utility to detect these immune responses in the context of DC/lysate vaccines (refer Section 6.1.2).

The requirement for an MRI scan could be seen as a limitation of the lymph node enlargement assay, but arguably not a major one. All tertiary hospitals in New Zealand now have access to at least one 1.5T MRI scanner and it is unlikely a clinical vaccine trial, with its stringent requirements for good medical practice standards (GMP), would be performed outside a tertiary centre. In fact, maintaining a licensed GMP laboratory to prepare the vaccines in a clinical trial is a far more limiting factor than the availability of MRI, with only 2 such laboratories registered in Auckland and Wellington in 2008³⁰².

The requirement for an MRI scan to be timed within 48 hours of vaccination is perhaps more of a constraint. If the human kinetics of early draining lymph node enlargement resemble that of the mouse (Figure 6-3), then enlargement will be associated with an antigen-specific response from 12-30 hours following vaccination. This window is large enough to allow a clinic visit to perform vaccination with an MRI the following day, with either procedure able to be performed in the morning or afternoon.

The use of MRI highlights some of the clear advantages of the lymph node enlargement assay over peripheral blood based assays in that it is performed non-invasively, in vivo and at a site that it is immunologically relevant. Most other assays sample the circulating lymphocyte pool to monitor specific T-cell responses, although it may not be

the most relevant in terms of establishing correlations with clinical tumour response²¹⁷. Antigen-specific T cells were readily detected in the biopsies of the draining lymph node²²¹ or the vaccine injection site³⁰³, whereas at the same time, these T cells were largely undetectable in blood. Responses in the draining lymph node are known to be specifically relevant. When T cells harvested from the draining lymph node are adoptively transferred, they can protect against tumours, which is not seen if T cells from non draining nodes, or peripheral blood are used³⁰⁴. This could explain why the lymph node enlargement assay has increased sensitivity to detect antigen-specific immune responses generated by DC/lysate vaccines.

The identification of the draining lymph node(s) from the site of vaccination is an issue that will need to be addressed in humans. The draining lymph node(s) can be identified using transcutaneous evaluation of gamma counts using a standard handheld gamma probe following technetium-99 administration around the site of vaccination²²¹. This has the undesirable requirement of further hardware and the administration of radioactive substances. An alternative method would be to take measurements of a cluster of lymph nodes associated with drainage of the vaccination site and compare them to the contralateral side. The larger the cluster of lymph nodes analysed the larger the noise in the measurement. The upper extremity, which is the most common site of vaccine administration⁸⁹, has one of the most consistent lymphatic drainage patterns in the body³⁰⁵. Therefore it may be possible to identify a typical pattern of drainage to a restricted number of lymph nodes using a consistent vaccination site. This will require further research to address, the burden of which is lessened by the simplicity and non-invasive nature of the early draining lymph node assay.

There is a general limitation in translating studies performed by measuring tumour protection by prophylactic vaccination in healthy mice. Restraint is required in the degree of comparison that can be made to clinical vaccine trials conducted in patients with compromised immune systems³⁰⁶. The tumour studies were performed here to test the proof of principle that early draining lymph node enlargement could be associated with some measure of tumour protection.

6.3.4 Remaining questions

This study raises some questions pertaining to its potential application in clinical cancer vaccine trials. The unresolved issues surround the mechanism of early lymph

node enlargement, whether the same result can be achieved in humans and whether the magnitude of the enlargement would be associated with clinical benefit.

In the absence of an identified mechanism of early lymph node enlargement, no correlations can be drawn between the magnitude of the lymph node enlargement and the number and function of antigen-specific cells. The mechanism of early lymph node enlargement could be further elucidated by measuring the cytokines in the supernatant of draining versus contralateral lymph nodes in primed and naïve mice at various time points following vaccination. If a difference were found in the secretion of certain cytokines, these cytokines could then be inhibited by blocking antibodies in a further experiment, and observing whether this abrogated lymph node enlargement and/or tumour protection. In addition, the implicated cytokines could be added to lymph nodes in naïve mice to see if they produce lymphocyte accumulation. If the cytokine milieu were found to be more typical of an immunoregulatory (suppressive) process, with increased levels of IL-10, TGF- α or interferon- γ ^{307–309}, then the association between early draining lymph node enlargement and tumour protection in this study may not be closely related or reproducible in other studies.

One of the main reasons for establishing the mechanism of early lymph node enlargement is associated with the type of immune response that is associated with tumour protection. A more direct approach would be to address this in a clinical trial. The question remains as to whether lymph node enlargement following DC/lysate vaccine will be seen in humans and whether it will be associated with an antigen-specific immune response. Sequestration of lymphocytes in antigen-challenged lymph nodes is known to occur in humans¹⁹⁵. It would also be interesting to determine if the magnitude of the draining lymph node enlargement was associated with positive clinical outcomes. Due to the simplicity and non-invasiveness of the lymph node enlargement assay, the next step could be to examine these questions in a clinical trial before investing further resources into solving its mechanism in mice. This would assess the utility of the lymph node enlargement assay in the most relevant context: the patient with cancer undergoing immunotherapy.

A final question is whether the assessment of early lymph node enlargement could be performed with ultrasound. Ultrasound is effective at assessment of peripheral lymph nodes³¹⁰ and is cheaper and generally more available than MRI. The downsides of ultrasound are that it has poor spatial resolution and its signal is attenuated in obese individuals³¹¹. Furthermore, reproducibility of ultrasound in repeat measurements of

the same lymph node can be difficult due to the lack of external landmarks. Despite these shortcomings it could well prove adequate for this assay, which only requires a simple series of measurements to be performed in peripheral lymph nodes.

6.3.5 Conclusion

This chapter introduces a novel assay to assess the generation of an antigen-specific response to DC-based vaccination by measuring the area of the draining and contralateral lymph nodes with MRI. Enlargement of the draining lymph node within 48 hours of vaccination was found to be associated with an antigen-specific immune response and tumour protection in the mouse model studied. This novel assay, based on a well-described phenomenon, is easy to perform and standardise, is applicable to both DC/peptide and DC/lysate vaccines and it could be readily applied in clinical vaccine trials to examine the generation of an antigen-specific immune response following vaccination.

Chapter 7

General discussion

This thesis argues that Fe NPs produce more effective MRI contrast on T_2 weighted sequences than FeOx NPs. It has been shown that the enhanced contrast with Fe NPs translated into improved MRI-based applications, including increased sensitivity of cellular detection (Chapter 3), improved diagnosis of small tumours (Chapter 4) and increased accuracy of cell tracking enabling assessment of antigen-specific immune responses following DC/peptide vaccines (Chapter 5). Observations from this research led to the development of an MRI-based assay that can detect antigen-specific immune responses induced by DC/lysate based vaccination (Chapter 6). In this chapter, the limitations and broader implications of these findings are explored with reference to replacing FeOx NPs and gadolinium-based contrast agents with Fe NPs.

Limitations of this study

This study has several limitations worth noting. Such limitations are related to the methods by which the central hypothesis was tested. They concern the FeOx NPs which were used for comparison with the Fe NPs, the type of MRI techniques employed and the use of animal models.

Instead of purchasing clinically approved FeOx NPs, the decision was made to synthesize FeOx NPs following a well known synthetic method (see Chapter 2). A direct comparison between commercial FeOx NPs (such as Sinerem) and Fe NPs would have the advantage of establishing whether Fe NPs outperform a type of FeOx NP with proven clinical efficacy. This course was not taken because there are no commercially

available FeOx NPs which have a DMSA coating. As discussed in Chapter 3, the coating of a NP has a significant effect on its magnetic properties and pharmacokinetics. The central question of this thesis was whether the presence of a highly magnetic iron core could improve the biomedical applications of FeOx NPs, and this was best addressed by comparing NPs with the same coating molecules. Determining the optimal coating strategy to improve the performance of magnetic NPs is important but has been extensively investigated by others^{168–171}.

The MR imaging in this thesis relied exclusively upon T_2 weighted spin echo imaging. This is not the most sensitive method to detect the magnetic field distortions produced by magnetic NPs. Gradient echo techniques which can detect changes in T_2^* are known to be more sensitive to detect the presence of FeOx NPs⁵². However, the image distortion produced by Fe NPs was found to compromise image quality significantly using gradient echo techniques in our in vivo mouse imaging experiments, such that any gains in sensitivity were not appreciable. A further potential limitation with this study was that T_2 mapping of images was not performed in any of the in-vivo imaging at 1.5 T. This technique has the advantage of potentially greater sensitivity and specificity compared to single T_2 weighted images. For example, T_2 mapping can better distinguish areas of signal void due to low proton content, such as in lung tissue, versus rapid T_2 decay, such as in an area of high Fe NP concentration. T_2 mapping was not available for experiments in this thesis due to software restrictions in operating the clinical MRI scanner. There was certainly an advantage in not using T_2 mapping in that it is not used in routine clinical practice and would have presented a potential hurdle in translating this research into the clinic.

This study used models which were used cells (surgically administered immortalized cancer cells), organs (spleen) and organisms (mouse) different to those of which it is ultimately concerned with (native metastatic tumours, lymph nodes and humans respectively). This was a necessary step because the use of non-human organisms are currently necessary to establish proof of principle and general toxicity before phase 1 human trials can be commenced. As discussed in Chapter 4, the use of a mouse model involving implanted intrasplenic tumors as a surrogate for lymph node metastases was necessary due to the difference in size between the lymph nodes of mice and men. All three of these factors will require future verification in clinical studies before conclusions about the clinical effectiveness of Fe NPs can be ultimately determined.

Could Fe NPs supplant GBCA?

Gadolinium-based contrast agents (GBCA) were first approved by the United States Food and Drug Administration (FDA) in 1988, as MRI scanners were becoming more widely available³¹². Since then, the number of FDA-approved GBCAs³¹³ has grown to seven and these have been administered with over 100 million MRI scans worldwide²². GBCAs are the only MRI contrast agent available in Australia and New Zealand.

The longstanding use and popularity of GBCAs presents a barrier to their substitution with another type of MRI contrast agent. There are many well described pathological lesions that can be diagnosed with GBCA-enhanced MRI (as discussed in Chapter 1) and familiarity with the interpretation of GBCA-enhanced scans is part of not only specialist radiology training but also the standard medical curriculum in Australasia and elsewhere. It could be argued that a new contrast agent with similar effectiveness to GBCAs would face a significant hurdle to gain market share. The best strategy might be to target the areas where GBCAs are contraindicated or where they do not perform particularly well.

Until recently, MRI with GBCAs had few contraindications and was used preferentially in patients with renal impairment over CT using iodine based contrast agents³¹⁴. A concern was first raised in 2006 that GBCAs may be associated with a fibrosing skin disorder with multiorgan involvement called nephrogenic systemic fibrosis (NSF)³¹⁵. A meta-analysis performed in 2009 reported a significant association between all GBCAs and the development of NSF, with an odds ratio of 26.7 (95% confidence interval 10.3-69.4). This means that patients who were administered GBCAs were 27 times more likely to develop NSF than those who had no exposure. NSF was seen almost exclusively in patients with advanced renal disease³¹⁶ where the combination of metabolic acidosis³¹⁷, high concentrations of competing metal ions³¹⁸ and inadequate clearance of GBCA³¹⁷ leads to gadolinium ion dissociation. The gadolinium ion can form salts with phosphate³¹⁷ and other anions that are elevated in renal failure, with the salts then being potentially deposited in many organs including muscle, bone, liver and skin. A study examining the skin biopsies of patients with NSF found gadolinium in six out of seven samples examined³¹⁹. Although there is a suggestion that some GBCAs carry a greater risk than others in inducing NSF³²⁰, all GBCAs may best be avoided in renal failure, as the gadolinium is toxic to the kidneys in renal impairment, even at the recommended reduced doses³²¹ and there is no effective treatment of NSF³²².

The total number of reported cases of NSF, since the original description in 2006, is 350 as of June 2011³²³. Despite the incidence of NSF being estimated at a very modest 4 for 1000 patient-years with end-stage renal failure³²⁴, the relationship between GBCAs and NSF has generated a lot of publicity. It is important to emphasize that NSF has only been reported in patients with end-stage renal failure³²¹. Nevertheless, an internet search for "gadolinium MRI" performed in June 2011 with the Google search engine returned 13 of the first 20 hits involving NSF (including advertisements from American legal firms specialising in malpractice). Combine this with the observation that FeOx NPs have been administered clinically with an excellent safety profile for over 50 years (initially for the treatment of anemia)³²⁵ and patients with hepatic and renal failure were included in a large FeOx NP trial⁵¹, and it seems that a solid opportunity exists to develop Fe NPs to be marketed in patients with renal failure.

The main limitation to this hypothesis is that FeOx NPs (and by extension Fe NPs) provide different information to GBCAs. For example, in stroke imaging, GBCAs and FeOx NPs can provide different results since breakdown of the bloodbrain barrier (as detected by GBCAs) and cellular infiltration of the brain by macrophages (as detected by FeOx NPs) are not closely linked³²⁶. Interpretation of FeOx NP enhanced scans requires radiologist training because the resulting hypo intense (dark) areas on T_2 - weighted images can be confused with the signals from bleeding, calcification, or metal deposits³²⁷. The interpretation of MRI with FeOx NPs has proven difficult in cancer trials with untrained radiologists³²⁸. A path of least resistance for radiologists wanting to image patients with renal failure may be the development of GBCAs with more stable chelating agents that are able to retain the gadolinium ions and prevent NSF.

Promising biomedical applications of Fe NPs

Although FeOx NPs may not be the panacea to replace GBCAs in patients with renal failure, there are two areas where FeOx NPs have shown clear benefits in over GBCAs, and that is in the imaging of lymph node metastases and cell tracking. Two recent meta-analyses looking at the performance of GBCAs³²⁹ and FeOx NPs⁵⁷ in diagnosing malignancy in lymph nodes suggest that FeOx NPs have better sensitivity and specificity in this application. The sensitivity of FeOx NPs enhanced MRI was 0.90 (95% confidence interval: 0.88-0.91) versus 0.84 (0.70 to 0.92) for GBCAs, with specificities of 0.96 (0.95-0.97) versus 0.82 (0.72 to 0.89) respectively. The meta-analysis

of FeOx NPs⁵⁷ addressed a valid criticism of their use, which is that it takes 24 hours after administration of FeOx NPs before an optimal MRI scan of the lymph nodes can be made. It was found that there was no decrease in diagnostic accuracy when a pre-contrast scan was omitted with FeOx NPs.

Although the reported values of sensitivity for the two types of contrast agent had overlapping confidence intervals, MRI enhanced with FeOx NPs produced an improvement in sensitivity over unenhanced scans that reached statistical significance whereas GBCAs enhanced scans did not. An earlier meta-analysis examining FeOx NPs in the diagnosis of lymph node metastases³³⁰ reported similar values of sensitivity (0.88) and specificity (0.96). The most remarkable finding from comparison of the three studies is the improvement in specificity in images enhanced with FeOx NPs compared to GBCAs. These differences can be partially explained by the different mechanisms of contrast produced by FeOx NPs and GBCAs.

A side effect which has been commonly encountered with large FeOx NPs (> 100nm such as Feridex) is the onset of severe back pain with administration. The mechanism of the pain is unclear but was severe enough to warrant interruption or discontinuation of the infusion in 2.5% of patients¹⁷⁷. This problem can be ameliorated by administering Feridex by slow infusion. Fe NPs, with their improved T_2 relaxivity, could be administered at lower doses than FeOx NPs thus decreasing the time of infusion and/or reducing the risk of side effects.

FeOx NPs are taken up by phagocytic cells, particularly macrophages, that are abundant in lymph nodes. As discussed in Chapter 4, normal lymph node tissue is rich in macrophages, whereas tumour tissue has relatively fewer macrophages and decreased relative uptake of FeOx NPs³³¹. In contrast, GBCAs, which remain extracellular, can detect the new blood vessels that develop within and around lymph nodes following implantation of metastatic cells³³² and demonstrate some of the abnormal morphological characteristics of tumor tissue within the node^{333,334}. Lymph node enlargement associated with inflammation can also result in new blood vessel formation³³⁵ and is in general associated with an increased infiltration of macrophages³²⁶. Therefore, in an inflamed, non-cancerous lymph node, GBCAs could give a false positive result by highlighting new blood vessels whilst FeOx NPs would be taken up actively across the node and give a true negative result for cancer infiltration.

Despite these advantages of FeOx NPs over GBCAs, there are still drawbacks to FeOx

NPs which have prevented their licensure for imaging lymph nodes by the European Medicine Agency (EMA) or the US FDA. These were summarised in a licensing withdrawal report of an FeOx NP agent, Sinerem, that failed to gain approval by the EMA⁵¹. The report was based primarily on a multi-centre clinical trial which enrolled 1,777 patients. The report states that:

1. "The pivotal study failed to demonstrate a consistent and statistically significant benefit for Sinerem in sensitivity and failed to confirm non-inferiority with regards to specificity."
2. "The lack of consistency between the three readers, both with regards to initial assessment and post-Sinerem assessments is worrisome."

Both of these issues could be potentially ameliorated with the use of Fe NPs instead of FeOx NPs. In chapter 4 it was demonstrated that Fe NPs can improve both the sensitivity and specificity of tumour diagnosis in macrophage rich organs (Figure 4-10) and that Fe NPs can reduce the intra- and inter-observer variability of diagnosis relative to FeOx NPs (Figure 4-11). Furthermore, the clinical need for such a contrast agent in prostatic cancer was reported by Arnon Krongrad, one of the pioneers of minimally-invasive prostatic surgery³³⁶, who commented in response to the Sinerem ruling³³⁷:

"We [the industry] desperately need better tests that can be used to accurately detect the presence of prostate cancer once it has escaped from the prostate into other organs. It would seem all too sad if the research on (Sinerem) cannot be used as the basis for another attempt to develop a new imaging agent with a comparable safety profile and a slightly better effectiveness profile."

The findings in this thesis give weight to the argument that Fe NPs could meet this demand with their improved efficacy and similar safety profile.

One application in which the effectiveness of FeOx NPs is unrivalled by GBCAs is in the labelling of cells for tracking with MRI. Due to the relatively low T_1 contrast effects per unit concentration (relaxivity) of GBCAs, which is reduced within cells³³⁸ and at higher magnetic fields used for cell tracking³³⁹, combined with poor intracellular biocompatibility³⁴⁰, there are relatively few examples of cell labeling applications using Gd in the scientific literature^{341,342}. FeOx NPs do not suffer from any of these drawbacks and are currently the most widely used contrast agent for MRI cell tracking

studies³⁴³. Fe NPs can improve the sensitivity of cell tracking studies beyond that of FeOx NPs by lowering the threshold of labelled cell detection, as demonstrated in Chapters 3 and 5. This is particularly important when sensitivity is the limiting factor of a cell tracking application, which is often the case with 1.5 T scanners³⁴⁴.

In some cell tracking applications, the dose of Fe used to label cells can be the limiting factor. Although there is evidence that FeOx NPs can be used to track stem cells without affecting their phenotype^{345,346}, some studies have shown that FeOx NPs can interfere with chondrogenesis of mesenchymal stem cells³⁴⁷, microglial cell implantation in the spinal cord³⁴⁸ and macrophage-T cell interactions³⁴⁹. It was also shown in Chapter 5 that at higher doses, Fe NPs and FeOx NPs can interfere with dendritic cell maturation (Figure 5.4). Therefore there is scope for Fe NPs to be applied at the same doses as FeOx NPs to improve sensitivity or at reduced doses to reduce effects without compromising sensitivity. Although cell tracking applications currently exist exclusively in the research realm (no agents have been approved for cell tracking in the clinic), the use of magnetic NPs for MRI cell tracking is likely to increase alongside the expanding funding research in stem cell therapies³⁵⁰ and with the FDA approval of the first cell-based vaccine³⁵¹.

Beyond lymph node imaging and cell tracking, there are a multitude of clinical applications of FeOx NPs that are being researched. These include in vivo drug-delivery³⁵² and drug release³⁵³, gene therapy³⁵⁴, molecular sensors³⁵⁵, cellular mechanical manipulation³⁵⁶, MRI reporter genes³⁵⁷ and magnetic hyperthermia³⁵⁸. Although these applications are beyond the scope of this thesis, it is worth noting that Fe NPs, with their superior magnetic properties, could potentially improve many if not all of these applications. Investigating this hypothesis would require comparative studies with FeOx NPs, such as those performed in this thesis. A promising candidate would be the use of Fe NPs to improve magnetic hyperthermia, and it has been shown that NPs with increased magnetisation can improve the hyperthermic effect³⁵⁹. Fe NPs offer the additional benefit of improved MRI sensitivity which could result in better cancer identification combined with MRI and treatment with magnetic hyperthermia.

The development of a non-invasive assay to detect the presence of antigen-specific immune responses following DC/lysate vaccination is a significant contribution made by this thesis research to the field of cancer immunotherapy. Although Fe NPs are not strictly required for this assay, they could be administered to identify the draining lymph node of a vaccination site in which to observe the enlargement. The

identification of draining lymph nodes has been successfully demonstrated using FeOx NPs^{360,361}. Although it is more readily accessible and easier to operate, it is unlikely that ultrasound would be used instead of MRI for conducting repeated measurements of lymph nodes, as discussed in chapter 6. Therefore a preliminary MRI scan with Fe NPs could be used to assess the draining lymph node and measure its baseline size, followed by a second scan, 12-30 hours after DC vaccination.

A final aspect worth considering regards the cost of manufacturing MRI contrast agents. Despite the fact that gadolinium is a rare-earth mineral that is substantially more expensive as a bulk material than Fe (USD \$120/kg versus 0.20/kg, respectively), the marketed price of FeOx NPs is greater than GBCAs³⁶². This is due in part to difficulties in translating the synthesis of FeOx NPs to industrial scale processes able that are able to produce large quantities of consistent quality NPs⁴⁹. The patented synthetic method of producing Fe NPs presented in this thesis requires an approximate cost of NZD \$1,382/g including labour costs³⁶³. This compares with similar size (20nm) FeOx NPs of chemical grade that are sold for NZD \$33,516/g (Sigma Aldrich). Although challenges still remain in upscaling the synthetic method, there is a very large margin between the current cost of manufacturing Fe NPs and the listed price of FeOx NPs. Reduced cost could prove to be another advantage of the commercial application of Fe NPs over FeOx NPs.

In conclusion, this thesis has argued that Fe NPs can produce more effective MRI contrast than FeOx NPs to enhance cell detection, increase the accuracy in detecting small tumours and improve cell tracking. The resulting improvement in MRI contrast with Fe NPs led to the development of novel techniques that can be readily applied in clinical vaccine trials to measure the antigen specific immune response following DC-based vaccines. Fe NPs hold excellent potential to improve the MRI diagnosis of lymph node metastases where FeOx NPs have failed to cross the threshold for clinical approval. Further clinical applications of FeOx NPs, specifically stem cell tracking and magnetic hyperthermia of cancer tissue, warrant investigation with Fe NPs to improve their effectiveness.

Publications arising from this thesis

Accepted

Peter Ferguson*, Soshan Cheong*, Kirk W. Feindel, Ian F. Hermans, Paul T. Callaghan, Claire Meyer, Angela Slocombe, Chia-Hao Su, Fong-Yu Cheng, Chen-Sheng Yeh, Bridget Ingham, Michael F. Toney, and Richard D. Tilley (*= co-first authors). *"Simple Synthesis and Functionalization of Iron Nanoparticles for Magnetic Resonance Imaging"* in *Angewandte Chemie International Edition* 2011 vol. 50 (18) pp. 4206-4209, VIP paper. Featured on the back cover.

David A. J. Herman, Peter Ferguson, Soshan Cheong, Ian F. Hermans, Ben J. Ruck, Kathryn M. Allan, Sujay Prabakar, John L. Spencer, Conrad D. Lendrum and Richard D. Tilley. *"Synthesis and Functionalization of Iron/Iron Oxide Core/Shell Nanoparticles for T₂ Contrast Enhancement in Magnetic Resonance Imaging"* in *Chemical Communications* 2011 vol. 47 (32) pp. 9221-9223 .

Submitted

Peter Ferguson, Kirk W. Feindel, Angela Slocombe, Matthew MacKay, Trudy Wignall, Richard Tilley and Ian F. Hermans. *"Strongly magnetic iron/iron oxide core/shell nanoparticles improve magnetic resonance imaging of tumors in lymphoid tissue"* - submitted to *Cancer Research*.

Soshan Cheong, P. Ferguson, I. F. Hermans, Sujay Prabakar, David Herman, Guy N. L. Jameson and Richard D. Tilley. *"Synthesis of Highly Crystalline and Stable Iron/Iron Oxide Core/Shell Nanoparticles For Cell Studies"* - submitted to *Chempluschem*.

In preparation

Peter Ferguson, Angela Slocombe and Ian F. Hermans. *"Non-invasive monitoring of dendritic cell-based vaccines with MRI"* - to be submitted to the *Journal of Clinical Investigation*.

A Journal of the Gesellschaft Deutscher Chemiker

50
YEARS

Angewandte

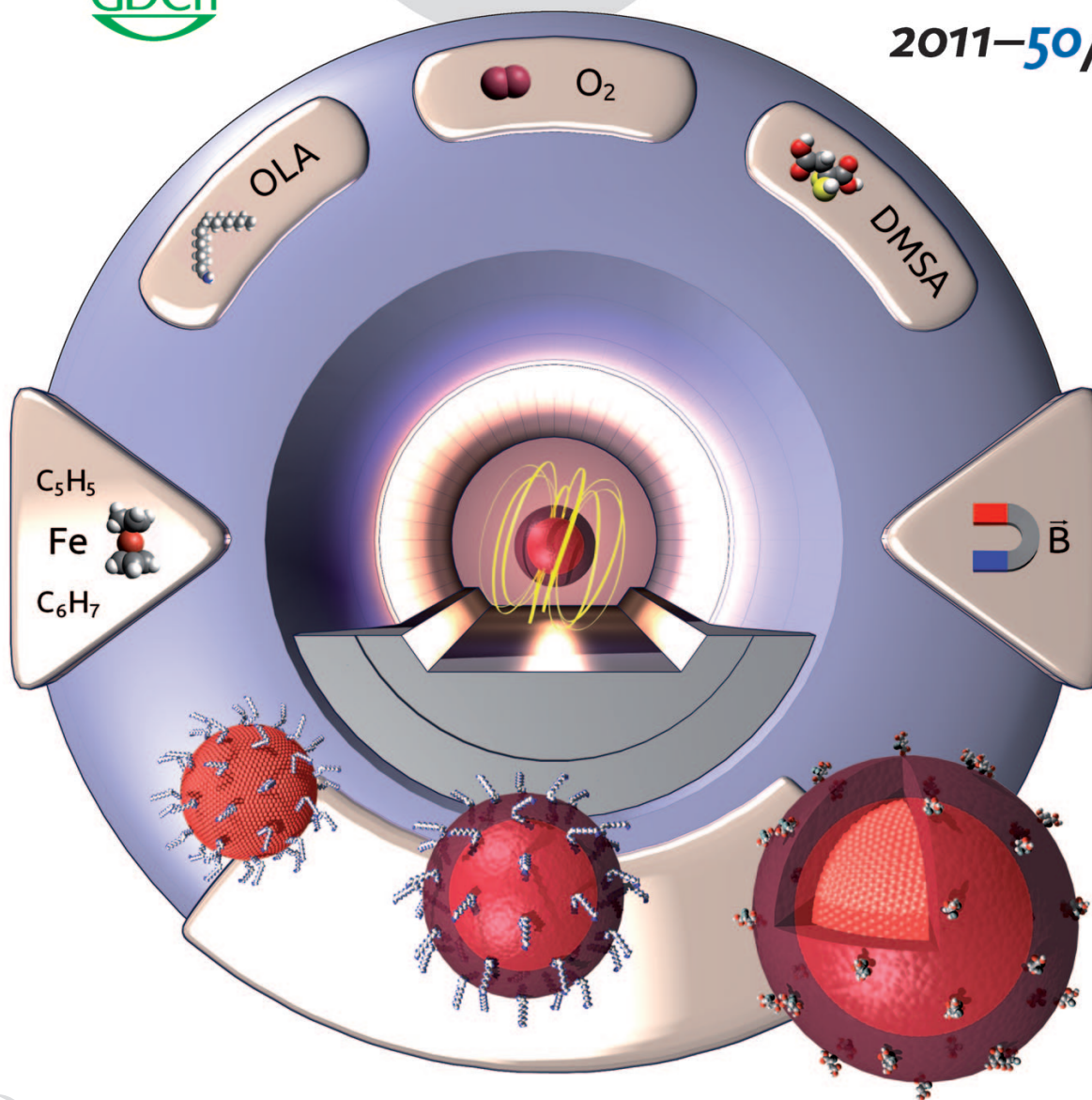
International Edition

Chemie

GDCh

www.angewandte.org

2011–50/18



Strongly magnetic single-crystal ...

... iron core/iron oxide shell nanoparticles have been synthesized in a facile manner without the need for highly toxic precursors (DMSA = dimercaptosuccinic acid, OLA = oleylamine). R. D. Tilley et al. describe in their Communication on page 4206 ff., how the nanoparticles are highly effective as negative contrast agents for magnetic resonance imaging. In vivo studies show that the core/shell nanoparticles enable the successful detection of tumors as small as 1–3 nm.

 WILEY-VCH

Back Cover

Soshan Cheong, Peter Ferguson, Kirk W. Feindel, Ian F. Hermans, Paul T. Callaghan, Claire Meyer, Angela Slocombe, Chia-Hao Su, Fong-Yu Cheng, Chen-Sheng Yeh, Bridget Ingham, Michael F. Toney, and Richard D. Tilley*

Strongly magnetic single-crystal iron core/iron oxide shell nanoparticles have been synthesized in a facile manner without the need for highly toxic precursors (DMSA = dimercaptosuccinic acid, OLA = oleylamine). R. D. Tilley et al. describe in their Communication on page 4206 ff., how the nanoparticles are highly effective as negative contrast agents for magnetic resonance imaging. In vivo studies show that the core/shell nanoparticles enable the successful detection of tumors as small as 1–3 nm.



Simple Synthesis and Functionalization of Iron Nanoparticles for Magnetic Resonance Imaging**

Soshan Cheong, Peter Ferguson, Kirk W. Feindel, Ian F. Hermans, Paul T. Callaghan, Claire Meyer, Angela Slocombe, Chia-Hao Su, Fong-Yu Cheng, Chen-Sheng Yeh, Bridget Ingham, Michael F. Toney, and Richard D. Tilley*

Magnetic nanoparticles (NPs) are increasingly important in many biomedical applications, such as drug delivery, hyperthermia, and magnetic resonance imaging (MRI) contrast enhancement.^[1] For MRI, iron oxide NPs are the only commercial T_2 or negative contrast agents, due to their biocompatibility and ease of synthesis^[2] and research in the area is highly active.^[3] The efficacy of these contrast agents depends mainly on the surface chemistry and magnetic properties of the NPs.^[1] Materials with larger magnetization

could induce more efficient transverse (T_2) relaxation of protons and result in greater contrast enhancement.^[4] As iron has the highest saturation magnetization at room temperature among all elements,^[5] and is biocompatible, it is an ideal candidate for MRI contrast enhancement. Nevertheless, the development of using iron NPs for magnetic applications has been challenging and limited compared to those of its oxides, due to the difficulty in preparing stable iron NPs with simple synthesis methods and precursors.^[5,6]

Under ambient conditions, iron NPs of 8 nm or smaller oxidize completely upon exposure to air.^[7] For larger NPs, an oxide shell of 3–4 nm forms instantly on the surface, forming iron/iron oxide core/shell NPs. Groundbreaking studies for the synthesis of iron NPs of larger than 8 nm has largely been achieved by decomposition of iron pentacarbonyl, $[\text{Fe}(\text{CO})_5]$.^[6,8] Additional reports include the use of other precursors in forming iron nanocubes.^[9] However, all of these processes are limited in terms of ease of synthesis and scalability; $[\text{Fe}(\text{CO})_5]$ is volatile and highly toxic,^[5] and other processes involve precursors that are expensive and air-sensitive,^[9a] or require high decomposition temperatures.^[9b]

Here, we chose an easy to handle iron organometallic sandwich compound as the precursor and prepared single-crystal iron NPs using a simple, low-temperature synthesis method. The iron nanocrystals oxidized naturally to form highly crystalline iron/iron oxide core/shell NPs. The ease of this synthesis facilitates the larger-scale application of stabilized iron NPs. To enable the use of these NPs in biological applications, the NP surface was modified to make the NPs water soluble. The strongly magnetic core/shell NPs are shown to be more effective T_2 contrast agents for in vivo MRI and small tumor detection, compared to pure iron oxides. The successful detection of small tumors in vivo demonstrated here holds a great promise for accurate detection of early metastases in human lymph nodes, which has a large impact on the treatment and prognosis of a range of cancers.

The iron/iron oxide core/shell NPs were prepared by first synthesizing iron nanocrystals by decomposition of the iron precursor $[\text{Fe}(\text{C}_5\text{H}_5)(\text{C}_6\text{H}_7)]$, in the presence of oleylamine (OLA) stabilizing molecules. The non-carbonyl, sandwich compound was chosen for its simple preparation and ease of decomposition compared to other more stable sandwich compounds such as ferrocene.^[10] The synthesis was carried out in a closed reaction vessel^[11] under a mild hydrogen atmosphere, at 130 °C. The temperature required was lower than the usual temperature range (150–300 °C) needed for decomposition of other iron precursors in previous studies. Once

- [*] Dr. K. W. Feindel, Prof. P. T. Callaghan, Prof. R. D. Tilley
School of Chemical and Physical Sciences and The MacDiarmid
Institute for Advanced Materials and Nanotechnology, Victoria
University of Wellington, Wellington 6012 (New Zealand)
Fax: (+64) 4-463-5237
E-mail: richard.tilley@vuw.ac.nz
- Dr. S. Cheong,^[‡] Dr. B. Ingham
Industrial Research Limited and The MacDiarmid Institute for
Advanced Materials and Nanotechnology
P. O. Box 31-310, Lower Hutt 5040 (New Zealand)
- Dr. P. Ferguson,^[‡] Dr. I. F. Hermans
Malaghan Institute of Medical Research
P. O. Box 7060, Wellington 6012 (New Zealand)
- Dr. C. Meyer
Institut Néel (CNRS and UJF), Grenoble (France)
- A. Slocombe
Department of Radiology, Wellington Hospital
Wellington 6021 (New Zealand)
- Dr. C.-H. Su
Center for Translational Research in Biomedical Science, Chang
Gung Memorial Hospital-Kaohsiung Medical Center
Kaohsiung 833 (Taiwan)
- Prof. F.-Y. Cheng, Prof. C.-S. Yeh
Department of Chemistry and Center for Micro/Nano Technology
Research, National Cheng Kung University, Tainan 701 (Taiwan)
- Dr. M. F. Toney
Stanford Synchrotron Radiation Lightsource, SLAC National Accelerator
Laboratory, Menlo Park, CA 94025 (USA)

[‡] These authors contributed equally to this work.

- [**] This research was supported by the Foundation for Science, Research and Technology through grant PROJ-13733-NMTS. P.F. thanks the Health Research Council and the Wellington Medical Research Foundation for funding. K.W.F. thanks the Natural Sciences and Engineering Research Council of Canada (NSERC) for funding. Portions of this research were carried out at the Stanford Synchrotron Radiation Lightsource, a national user facility operated by Stanford University on behalf of the U.S. Department of Energy, Office of Basic Energy Sciences.

Supporting information for this article is available on the WWW under <http://dx.doi.org/10.1002/anie.201100562>.

synthesized, the iron nanocrystals were exposed to air to allow oxidation of the surface, forming iron/iron oxide core/shell NPs.

From an application point of view, the oxide layer can be exploited for two purposes: 1) to act as a passivation shell that prevents further oxidation,^[7] and 2) to be readily functionalized for various biomedical applications using protocols established for iron oxides.^[2b] The stabilizing agent OLA was exchanged with dimercaptosuccinic acid (DMSA) as a capping agent to achieve a stable dispersion in water. DMSA was chosen for its excellent safety profile.^[12] Besides, its strong binding of the oxygen-containing acid groups to the iron atoms on the NP surface^[13] means the OLA is easily replaced. Upon ligand exchange, the DMSA-coated NPs were readily dispersible in water, and the core/shell structures were stable for at least six months (Supporting Information, Figure S1).

Figure 1a shows a transmission electron microscopy (TEM) image of the spherical, core/shell NPs obtained. The NPs were relatively monodisperse, with an average size of (16 ± 1.5) nm (calculated from 450 NPs). The contrast of the NPs in the image shows a darker core and a lighter shell that reveals a core/shell structure. In high-resolution TEM (HRTEM) images, uniform lattice fringes were observed across the entire NP core, with spacings corresponding to α -Fe(110). For the shell, multiple crystalline domains with

lattice spacings matching those of iron oxide were observed (Figure 1b). The X-ray diffraction (XRD) pattern of the sample (Figure 1c) shows diffraction peaks of bulk body-centered cubic iron or α -Fe, and iron oxide of spinel structure, that is, magnetite (Fe_3O_4) or maghemite ($\gamma\text{-Fe}_2\text{O}_3$). The latter is consistent with the native iron oxide film structure previously reported.^[14] Using the Scherrer equation,^[15] the average crystallite size of α -Fe was estimated from the peak width of Fe(110) and Fe(211), to be (8.9 ± 0.7) nm. This value is close to the average iron core size of (9.0 ± 1.0) nm measured on TEM images. The much broader peaks of iron oxide shows a much smaller average crystallite size, and agree with TEM observation of a 3.2 nm, polycrystalline shell layer of the NPs.

The magnetic hysteresis loop of the sample measured at 300 K (Figure 1d) shows that the iron/iron oxide core/shell NPs exhibit a soft ferromagnetic behavior, with a remnant magnetization of ca. $19 \text{ emu g}^{-1}(\text{Fe})$, and a coercivity of ca. 370 Oe. The magnetization values were 140 and $150 \text{ emu g}^{-1}(\text{Fe})$ at low (2 T) and high (6 T) fields, respectively ($1 \text{ T} = 10 \text{ kOe}$). This magnetization value is in agreement with other reports of NPs comprising iron core and iron oxide shell of similar size range.^[16] The presence of a single-crystal iron core in the sample induces a far higher magnetization compared to iron oxide NPs that typically range from 40– $70 \text{ emu g}^{-1}(\text{Fe})$.^[2]

To compare the properties of the core/shell NPs, DMSA-coated iron oxide NPs of similar size, of average diameter (15 ± 2) nm, were prepared using standard methods.^[17] The effectiveness of the NPs as contrast agents was first assessed by measuring T_2 -weighted MR images of the NPs at 9.4 T. The NPs were dispersed in agar at different concentrations of iron (in $\mu\text{g}(\text{iron})\text{mL}^{-1}$). As shown in Figure 2a, the core/shell NPs produced much improved negative contrast compared to the oxide NPs at a range of iron concentrations, from 0.5 to $10 \mu\text{g}(\text{Fe})\text{mL}^{-1}$. In addition, contrast enhancement produced by the core/shell NPs can be detected down to a concentration of $0.5 \mu\text{g}(\text{Fe})\text{mL}^{-1}$, at which the oxide NPs showed no noticeable difference in the contrast compared the control.

The transverse relaxivity (r_2) of the core/shell NPs was determined for the samples and compared with that of the oxide NPs. (See Figure S2 for a representative plot of T_2 vs. $[\text{Fe}]$.) The core/shell NPs had an r_2 of $324 \text{ mM}^{-1}\text{s}^{-1}$, more than twice that of the oxide NPs, of $145 \text{ mM}^{-1}\text{s}^{-1}$, as shown in Figure 2b. Contrast improvement relative to that of iron oxide NPs has been reported for amorphous, iron-based core/shell NPs of similar sizes.^[18] However, little improvement was observed for the r_2 value indicating the importance of the single-crystal α -Fe core in our samples. This increase in r_2 indicates a significantly improved sensitivity of the MR signal for iron that will enable applications of much lower doses and produce far greater detection.

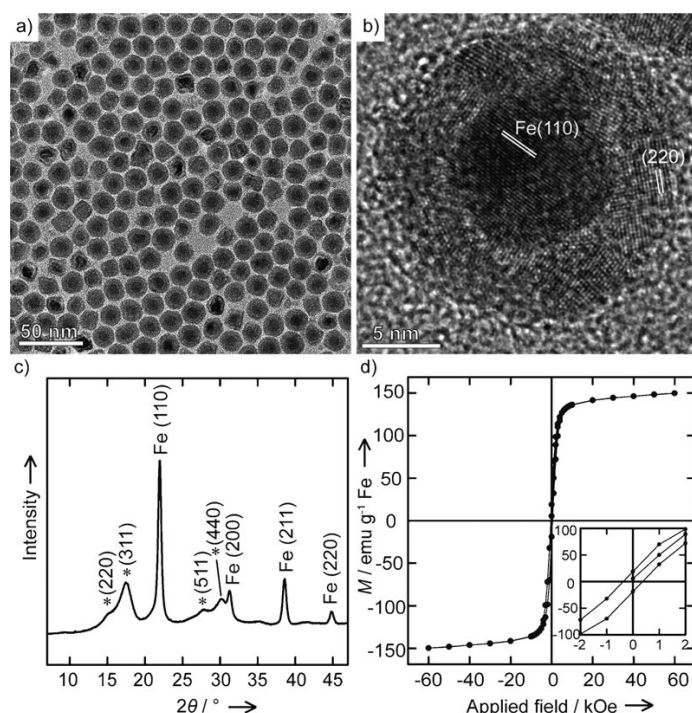


Figure 1. a) TEM image of 16 nm iron/iron oxide core/shell nanoparticles. b) HRTEM image showing a core of single-crystal α -Fe, with {110} planes observed across the core area, and a shell consisting of multiple domains of iron oxide, with {220} planes observed on sections of the shell. c) XRD pattern of the nanoparticles obtained using synchrotron radiation ($\lambda = 0.775 \text{ \AA}$), with diffraction peaks indexed to α -Fe and iron oxide of the spinel phase (*). d) Magnetization (M) of the core/shell nanoparticles at 300 K, with inset showing the low-field region.

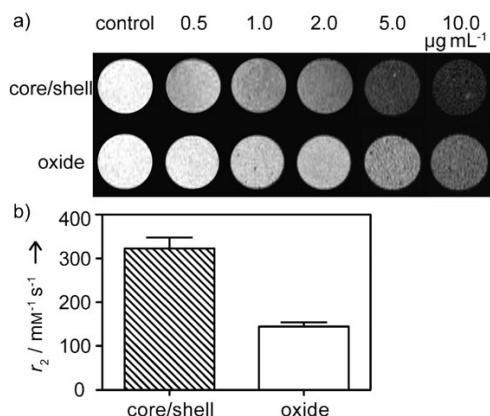


Figure 2. a) T_2 -weighted MR images at 9.4 T comparing the T_2 contrast (darkening effect) from the iron/iron oxide core/shell nanoparticles and iron oxide nanoparticles in agar with Fe concentration of 0 (control), 0.5, 1.0, 2.0, 5.0, and 10.0 µg(Fe) mL⁻¹. b) Relaxivity (r_2) of the core/shell and oxide nanoparticles determined from the same samples.

To assess the clinical applicability of the NPs in vivo, the iron/iron oxide core/shell and iron oxide NPs were administered to mice and MRI experiments were performed at 1.5 T. Contrast effects of the NPs were examined at the liver, spleen, and lymph nodes. Tissues in these organs are rich in phagocytic cells and have a strong tendency to uptake circulating iron and iron oxide NPs.^[19]

As shown in Figure 3a–c, the core/shell NPs produced noticeably darker contrast than the oxide NPs for all three organs (regions indicated by arrows). The contrast effects were statistically analyzed by comparing the % reduction in the T_2 signal produced by the NPs relative to that observed for the control mice (Figure 3d). When the core/shell NPs were used as the contrast agents, typically twice the contrast improvement was observed over the use of oxide NPs. With core/shell NPs, 45, 58 and 29 % reduction in the T_2 -weighted signal were seen in the liver, spleen and lymph nodes, respectively. The corresponding signal reduction with the use of oxide NPs were 21, 29 and 17 %, respectively. The fact that contrast is improved for the mouse lymph nodes that have an average size of 1.5 mm, is particularly significant and indicates that the core/shell NPs could improve the detection of small tumors.

To investigate small tumor detection in vivo, mice bearing breast cancer cells were administered with the core/shell and oxide NPs and T_2 -weighted MR images were obtained. In the MR images of the mouse that received the core/shell NPs, tumor of 1–3 mm could be unambiguously detected (Figure S3). In comparison, the contrast enhancement achieved by the oxide NPs was relatively insignificant and the tumor could not be visibly distinguished. It has been shown that the sensitivity for detecting cancerous nodes in vivo decreases to below 50 % when the tumor is smaller than 5 mm.^[20] The improved tumor detection demonstrated here by the core/shell NPs holds the potential to a more effective detection of

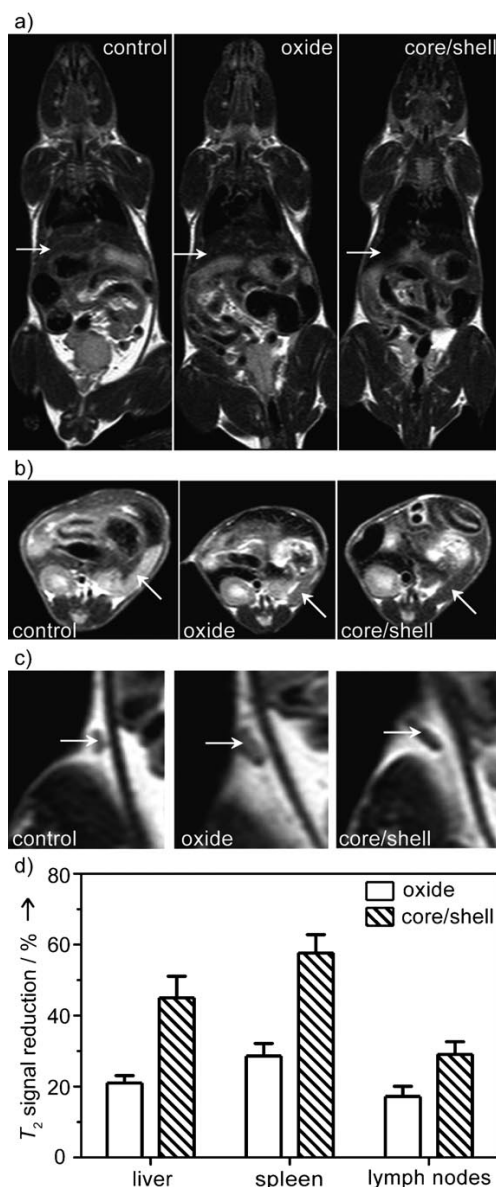


Figure 3. T_2 -weighted MR images of a control mouse and mice 24 h after injection of iron oxide and iron/iron oxide core/shell nanoparticles; arrows indicate the regions of interest, where T_2 contrast was analyzed: a) coronal images with arrows indicating the liver; b) axial images at the level of spleen; c) coronal images enlarged at the left inguinal region. d) Bar graph comparing the % reduction of T_2 relative to that of control caused by the presence of oxide and core/shell nanoparticles in the liver (a), spleen (b), and lymph nodes (c).

early lymph node metastases, which has a large impact on the treatment of a range of cancers.

In this study, the doses of contrast agents used are much lower than the maximum safe limit reported for mice,^[21] and we found no evidence of overt toxicity or failure to thrive in any mice for up to three months after nanoparticle administration.

In summary, single-crystal iron NPs were synthesized through a straightforward solution-phase route, which involved low temperatures and without the use of highly toxic chemicals. Natural oxidation of the iron nanocrystals subsequently yielded highly crystalline iron/iron oxide core/shell NPs. These NPs are demonstrated to exhibit highly effective MR contrast enhancement in multiple organs, and to enable unambiguous detection of small tumors of 1–3 mm in vivo at 1.5 T. The improvements in MR contrast will contribute to further development and advancement of various diagnostic and therapeutic medical applications.

Experimental Section

The iron precursor $[\text{Fe}(\text{C}_5\text{H}_5)(\text{C}_6\text{H}_7)]$ was prepared according to a previously described method.^[22] For the synthesis of iron nanocrystals, the iron precursor (0.4 g), OLA (2 mL, Aldrich, 98%), and mesitylene (8 mL, Aldrich, 98%) were added to a closed reaction vessel, which was then flushed three times with hydrogen gas (H_2) before being filled with 100 kPa H_2 , and sealed. The bottle was placed into an oven heated at 130 °C and remained for 2 days. The reaction was allowed to cool to room temperature naturally before the reaction vessel was opened to air. Ligand exchange to replace OLA with DMSA was carried out based on known methods.^[23] Each synthesis typically produced 60 mg Fe, which gave approximately 50% yield.

The TEM images were taken on a JEOL 2010, operated at an acceleration voltage of 200 keV. Powder XRD measurements were conducted at the Stanford Synchrotron Radiation Lightsource at beam line 7–2, using radiation of $\lambda = 0.775 \text{ \AA}$. Magnetization measurements were performed on a Quantum Design SQUID magnetometer, of model MPMS-XL. MRI of NPs was performed at 9.4 T, using a Bruker Instruments AVANCE400 NMR spectrometer, equipped with a Bruker Micro 2.5 imaging module. In vivo MRI of mice was performed using a clinical 1.5-T MR scanner (Philips Medical Systems), equipped with a wrist solenoid coil.

Received: January 22, 2011

Published online: April 6, 2011

Keywords: imaging agents · iron oxide · magnetic resonance imaging · nanoparticles

- [1] Q. A. Pankhurst, N. K. T. Thanh, S. K. Jones, J. Dobson, *J. Phys. D* **2009**, 42, 224001.
- [2] a) H. B. Na, I. C. Song, T. Hyeon, *Adv. Mater.* **2009**, 21, 2133–2148; b) A. K. Gupta, M. Gupta, *Biomaterials* **2005**, 26, 3995–4021.
- [3] a) C. Corot, P. Robert, J.-M. Idee, M. Port, *Adv. Drug Delivery Rev.* **2006**, 58, 1471–1504; b) S. Laurent, D. Forge, M. Port, A. Roch, C. Robic, L. V. Elst, R. N. Muller, *Chem. Rev.* **2008**, 108, 2064–2110.
- [4] a) Y.-w. Jun, Y.-M. Huh, J.-s. Choi, J.-H. Lee, H.-T. Song, S. Kim, S. Kim, S. Yoon, K.-S. Kim, J.-S. Shin, J.-S. Suh, J. Cheon, *J. Am. Chem. Soc.* **2005**, 127, 5732–5733; b) J.-H. Lee, Y.-M. Huh, Y.-w. Jun, J.-w. Seo, J.-t. Jang, H.-T. Song, S. Kim, E.-J. Cho, H.-G. Yoon, J.-S. Suh, J. Cheon, *Nat. Med.* **2007**, 13, 95–99.
- [5] D. L. Huber, *Small* **2005**, 1, 482–501.
- [6] S. Peng, C. Wang, J. Xie, S. Sun, *J. Am. Chem. Soc.* **2006**, 128, 10676.
- [7] C. M. Wang, D. R. Baer, L. E. Thomas, J. E. Amonette, J. Antony, Y. Qiang, G. Duscher, *J. Appl. Phys.* **2005**, 98, 094308.
- [8] a) A. Cabot, V. F. Puentes, E. Shevchenko, Y. Yin, L. Balcells, M. A. Marcus, S. M. Hughes, A. P. Alivisatos, *J. Am. Chem. Soc.* **2007**, 129, 10358–10360; b) H. Lee, T.-J. Yoon, R. Weissleder, *Angew. Chem.* **2009**, 121, 5767–5770; *Angew. Chem. Int. Ed.* **2009**, 48, 5657–5660.
- [9] a) F. Dumestre, B. Chaudret, C. Amiens, P. Renaud, P. Fejes, *Science* **2004**, 303, 821–823; b) A. Shavel, B. Rodríguez-González, M. Spasova, M. Farle, L. M. Liz-Marzán, *Adv. Funct. Mater.* **2007**, 17, 3870–3876.
- [10] D. Astruc, *Tetrahedron* **1983**, 39, 4027–4095.
- [11] a) J. Watt, N. Young, S. Haigh, A. Kirkland, R. D. Tilley, *Adv. Mater.* **2009**, 21, 2288–2293; b) S. Cheong, J. Watt, B. Ingham, M. F. Toney, R. D. Tilley, *J. Am. Chem. Soc.* **2009**, 131, 14590–14595.
- [12] J. J. Chisolm, Jr., *Clin. Toxicol.* **2000**, 38, 365–375.
- [13] A. L. Miller, *Altern. Med. Rev.* **1998**, 3, 199–207.
- [14] M. F. Toney, A. J. Davenport, L. J. Oblonsky, M. P. Ryan, C. M. Vitus, *Phys. Rev. Lett.* **1997**, 79, 4282–4285.
- [15] H. P. Klug, L. E. Alexander, *X-ray Diffraction Procedures for Polycrystalline and Amorphous Materials*, Wiley, New York, **1974**.
- [16] S. Gangopadhyay, C. G. Hadjipanayis, B. Dale, C. M. Sorensen, K. J. Klabunde, V. Papaefthymiou, A. Kostikas, *Phys. Rev. B* **1992**, 45, 9778–9787.
- [17] a) T. R. Pisanic II, J. D. Blackwell, V. I. Shubayev, R. R. Finones, S. Jin, *Biomaterials* **2007**, 28, 2572–2581; b) H. Zhao, K. Saatchi, U. O. Hafeli, *J. Magn. Magn. Mater.* **2009**, 321, 1356–1363.
- [18] C. G. Hadjipanayis, M. J. Bonder, S. Balakrishnan, X. Wang, H. Mao, G. C. Hadjipanayis, *Small* **2008**, 4, 1925–1929.
- [19] T. K. Jain, M. K. Reddy, M. A. Morales, D. L. Leslie-Pelecky, V. Labhasetwar, *Mol. Pharm.* **2008**, 5, 316–327.
- [20] M. G. Harisinghani, J. O. Barentsz, P. F. Hahn, W. M. Deserno, S. Tabatabaei, C. H. van de Kaa, J. de La Rosette, R. Weissleder, *N. Engl. J. Med.* **2003**, 348, 2491–2499.
- [21] a) M. K. Yu, Y. Y. Jeong, J. Park, S. Park, J. W. Kim, J. J. Min, K. Kim, S. Jon, *Angew. Chem.* **2008**, 120, 5442–5445; *Angew. Chem. Int. Ed.* **2008**, 47, 5362–5365; b) C. Bárcena, A. K. Sra, G. S. Chaubey, C. Khemtong, J. P. Liu, J. Gao, *Chem. Commun.* **2008**, 2224–2226.
- [22] M. L. H. Green, L. Pratt, G. Wilkinson, *J. Chem. Soc.* **1960**, 989–997.
- [23] N. Fauconnier, J. N. Pons, J. Roger, A. Bee, *J. Colloid Interface Sci.* **1997**, 194, 427–433.

Supporting Information

© Wiley-VCH 2011

69451 Weinheim, Germany

**Simple Synthesis and Functionalization of Iron Nanoparticles for
Magnetic Resonance Imaging****

*Soshan Cheong, Peter Ferguson, Kirk W. Feindel, Ian F. Hermans, Paul T. Callaghan,
Claire Meyer, Angela Slocombe, Chia-Hao Su, Fong-Yu Cheng, Chen-Sheng Yeh,
Bridget Ingham, Michael F. Toney, and Richard D. Tilley**

anie_201100562_sm_miscellaneous_information.pdf

Supporting Information

Experimental Section

Preparation of water dispersible iron/iron oxide core/shell nanoparticles: All reagents were used as received without further purification. The iron precursor $\text{Fe}(\text{C}_5\text{H}_5)(\text{C}_6\text{H}_7)$ was prepared according to a previously described method.^[1] For the synthesis of iron nanocrystals, the iron precursor (0.4 g, ~2 mmol), oleylamine (2 mL, ~6 mmol, Aldrich, 98%) and mesitylene (8 mL, Aldrich, 98%) were added to a closed reaction vessel (Fischer-Porter bottle), which was then flushed three times with hydrogen gas (H_2) before being filled with 100 kPa H_2 , and sealed. The bottle was placed into an oven heated at 130 °C and remained for 2 days. The reaction was allowed to cool to room temperature naturally before the reaction vessel was opened to air. Ligand exchange to replace oleylamine (OLA) with *meso*-2,3-dimercaptosuccinic acid (DMSA) was carried out based on known methods.^[2] The as-synthesized nanoparticle solution was sonicated briefly and divided into four equal portions. For each aliquot, the solution was dried in vacuum overnight to leave a powder, which was then dispersed in 20 mL of degassed and deionized (DDI) water. Separately, DMSA (20 mg, Aldrich, 98%) was added to 20 mL of DDI water. The pH of both solutions was adjusted to 3.0 with HCl, prior to mixing the solutions. After adding the DMSA solution to the nanoparticle solution the pH was again adjusted to 3.0 with HCl under vigorous stirring and constant nitrogen bubbling, and remained for 30 minutes. The resulting mixture was centrifuged at 3500 rpm for 10 minutes, to give a black precipitate, which was redispersed in 20 mL DI water. The supernatant, comprising aqueous and oil (OLA) layers, was discarded. The pH of the product dispersion was adjusted with NaOH to 9.25-9.5 under constant stirring and was maintained for 30 minutes before lowering the pH to 7.4 with HCl. The resulting solution was centrifuged at 3500 rpm for 10 minutes. The supernatant was discarded, and the nanoparticles were dispersed in water or sterile phosphate-buffered saline (PBS), which was sterile filtered. The dispersion in PBS was used as stock solution and was stored at 4 °C. The iron content of each stock solution was determined by atomic absorption spectrometry. Each synthesis typically produced 60 mg Fe, which gave ~50% yield.

Preparation of iron oxide nanoparticles: The nanoparticles were synthesized following a commonly adopted method.^[3,4] Briefly, under vigorous stirring, two solutions, (i) FeCl_3 (5.406 g, Aldrich, 99%) in 20 mL deionized (DI) water, and (ii) FeCl_2 (1.988 g, Aldrich, 98%) in 5 mL of HCl (2 M), were added to 100 mL DI water, to which 120 mL of ammonia solution (2 M) was added, and remained under stirring for 5 minutes. Black precipitate was purified by centrifugation at 3500 rpm for 20 minutes, and redispersed in DI water. The same purification process was repeated 4 additional times and the resulting precipitate was redispersed in 35 mL DI water. DMSA coating was applied using the same ligand exchange procedure for the core/shell nanoparticles.

Physical measurements: The TEM images and electron diffraction patterns were taken on a JEOL 2010, operated at an acceleration voltage of 200 keV. TEM samples were prepared by dipping a carbon-coated TEM grid into the nanoparticle dispersion and allowing the solvent to evaporate under ambient conditions. Powder XRD measurements were conducted at the Stanford Synchrotron Radiation Lightsource at beam line 7-2, using radiation of $\lambda = 0.775 \text{ \AA}$ with a point detector geometry using 1 mrad ($\approx 0.057^\circ$) Soller slits. Diffractogram was recorded between 2θ values of 7° and 47° . The sample was prepared by placing the nanoparticle dispersion on a silicon wafer and was allowed to evaporate under ambient conditions. Magnetization measurements were carried out on a dried powder, pressed and secured in a cylindrical

gelatin holder. The measurements were performed at 300 K, on a Quantum Design SQUID magnetometer, of model MPMS-XL.

Preparation of nanoparticle dispersion in agar: 2% agar was used. A stock solution was diluted with PBS to give concentrations of 1, 2, 3, 4, 10 and 20 $\mu\text{g mL}^{-1}$ of Fe in PBS. To 100 μL of each of the dilutions, 100 μL of 2% agar was added to give concentrations of 0.5, 1.0, 1.5, 2.0, 5.0 and 10.0 $\mu\text{gFe mL}^{-1}$ in 1% agar. The control was prepared by adding 100 μL of 2% agar to 100 μL PBS.

MRI of nanoparticles: MRI was performed using a Bruker Instruments AVANCE400 nuclear magnetic resonance (NMR) spectrometer, equipped with a Bruker Micro 2.5 imaging module. MR images were acquired at 9.4 T using a 2D multi-slice spin-echo sequence, at room temperature, with the following parameters: echo time (TE) = 8 ms, repetition time (TR) = 2000 ms, pixel size = 100 μm x 100 μm , slice thickness = 0.5 mm, number of echoes = 64, 4 averages, total experiment time = 16 min. Measurements were repeated on four separate samples for each iron concentration for consistency.

Determination of transverse relaxivity (r_2): Paravision software (Bruker) was used for MR image reconstruction and analysis. A region of interest was manually selected within the axial image of each nanoparticle dispersion in agar. A plot of the signal intensity against the echo time was fitted with an exponential function: $I(t) = I_0 \exp(-t/T_2)$; where $I(t)$ = signal intensity at time t , I_0 = signal intensity at 0 s, and the transverse time T_2 was then calculated. The plot of $1/T_2(\text{sample}) - 1/T_2(\text{control})$ against iron concentration ([Fe], in mM) (see Supplementary Figure S3) was fitted with a linear function: $1/T_2(\text{sample}) - 1/T_2(\text{control}) = r_2 \times [\text{Fe}]$; where the relaxivity r_2 was determined as the slope of the fit. This procedure was repeated four times for the core/shell and the oxide nanoparticle dispersions to determine the average and the standard error of the mean (s.e.m.).

In vivo studies: All mice were handled in accordance with the Animal Ethics Policy approved by the Animal Ethics Committee of Victoria University of Wellington. Nanoparticles dispersed in PBS (200 μL) were administered either intravenously through the tail vein or subcutaneously into the hind limb of 6 week-old C57BL/6 mice. A control mouse was injected with the same volume of PBS, without the presence of nanoparticles. 24 hours after injection the mice were anaesthetized by intraperitoneal (IP) injection of a ketamine/xylazine mixture in PBS (100/10 mg/kg) and MRI was performed. For the tumor studies, 6 week-old BALB/c mice were anaesthetized by IP injection as described above. 10 and 5 mm incisions were made through the skin in the left hypochondrium and the peritoneum, respectively. The spleen was exposed and injected with 1 million 4T1 breast cancer cells. The peritoneum and skin were closed with sutures and the mice were given buprenorphine (0.1 mg/kg single dose) and carprofen (5 mg/kg, 2 doses 12 hours apart) subcutaneously for analgesia. 72 hours after the cancer cell implantation the mice were anaesthetized by IP injection and MRI was performed. Nanoparticles dispersed in PBS were then administered intravenously and MRI was performed 8 hours after injection. Doses of 3 $\mu\text{mol Fe kg}^{-1}$ were employed for imaging the liver and 120 $\mu\text{mol Fe kg}^{-1}$ for the spleen and lymph nodes. In vivo MRI was performed using a clinical 1.5-T MR scanner (Philips Medical Systems), equipped with a wrist solenoid coil. The mice were positioned in the centre of the wrist coil and the same protocols were used for all images. T_2 -weighted spin-echo images were acquired with the following parameters: TE = 54 ms, TR = 2000 ms, pixel size = 300 μm x 300 μm , thickness = 1 mm, number of echoes = 8, 3 averages, total experiment time = 4 min. 24 s. Images were analyzed with ImageJ (National Institutes of Health) by manually selecting regions of interest (ROIs) corresponding to the liver, spleen or inguinal lymph nodes and integrating the signal intensity of each ROI.

Supplementary Figures

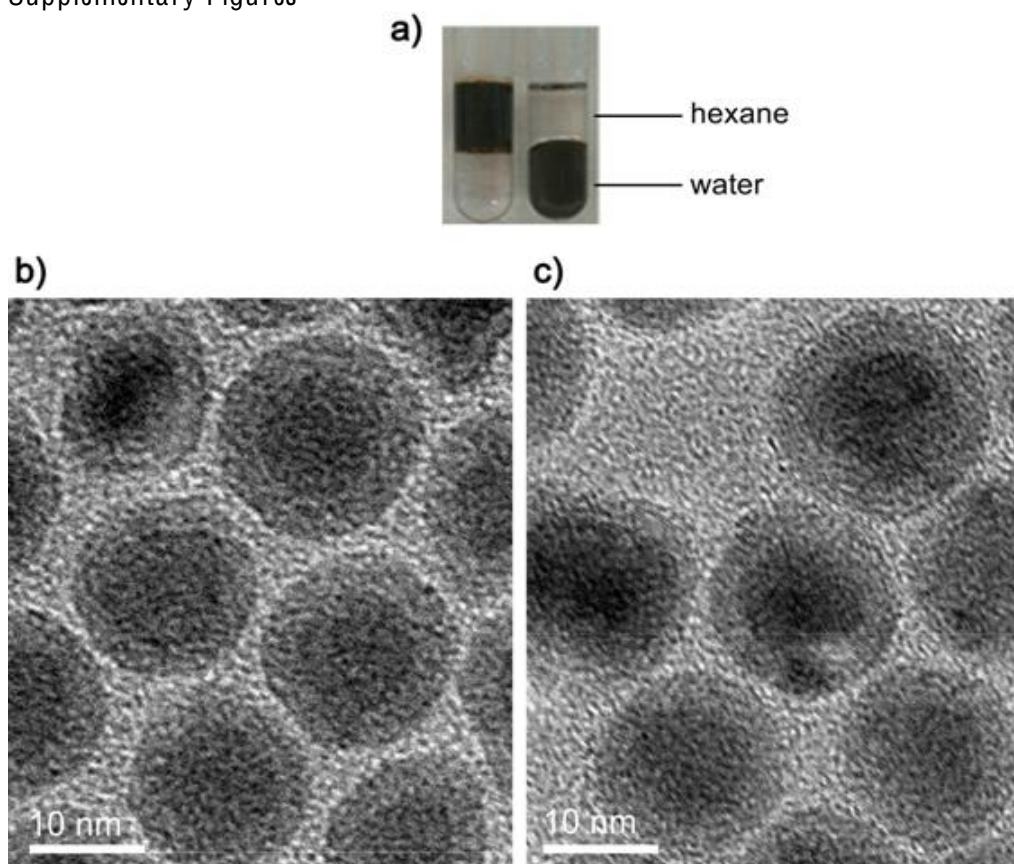


Figure S1. a) Photo shows dispersion of nanoparticles in hexane and in water, before and after ligand exchange, respectively. TEM images of iron/iron oxide core/shell nanoparticles dispersed in a) hexane and in b) water, six months after synthesis, showing the stability of the core/shell structures over time.

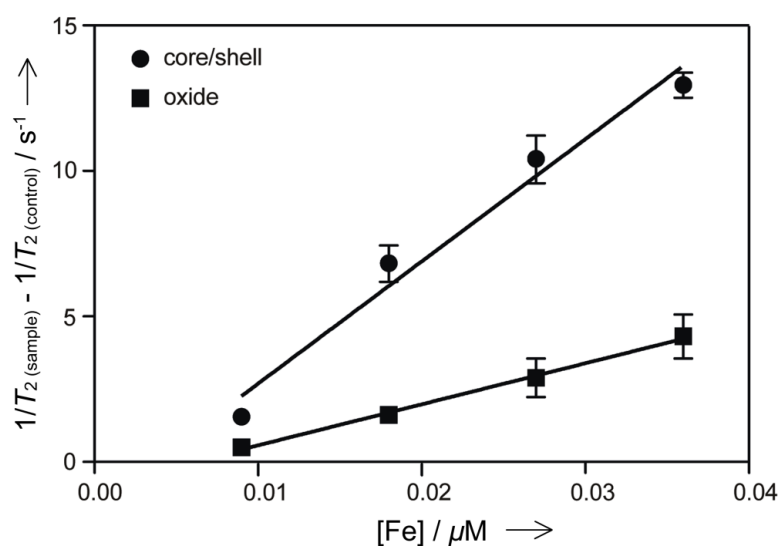


Figure S2. Sample plot using T_2 measurements of nanoparticles at varying iron concentrations to determine relaxivity.

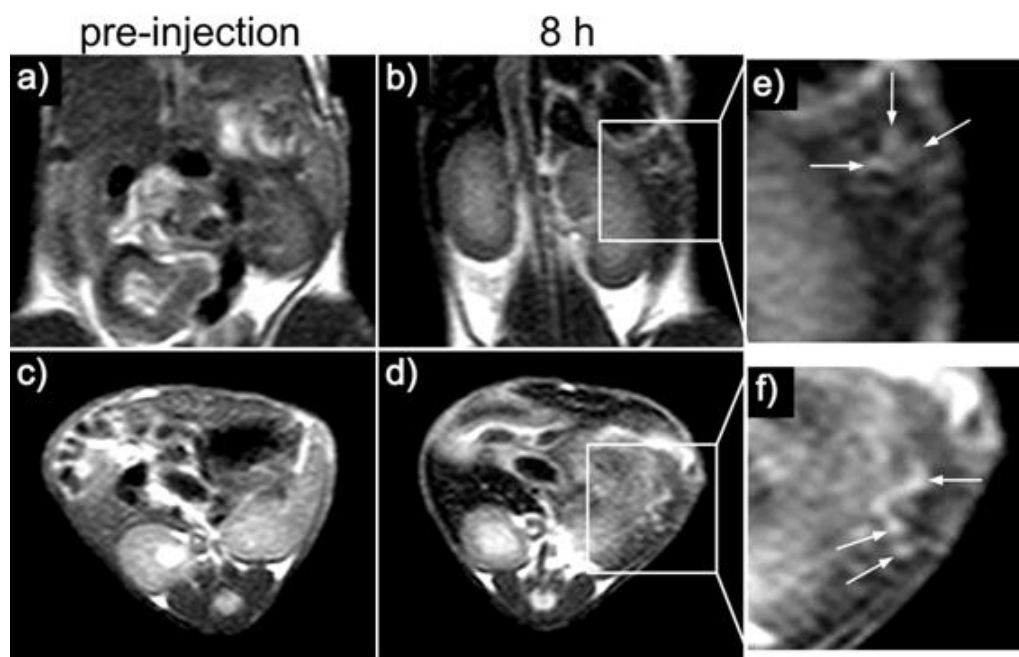


Figure S3. T_2 -weighted MR images of a mouse implanted with 4T1 breast cancer cells a,c) pre-injection and b,d) 8 hours post-injection of iron/iron oxide core/shell nanoparticles. (a) and (b) are the coronal images, whereas (c) and (d) show the axial images at the level of spleen. e,f) Enlargements at the spleen region, as boxed in (b) and (d), respectively. After injection of the core/shell nanoparticles, dark contrast is observed at the spleen region and the tumors appear relatively bright and can be readily identified (arrows).

The mice were sacrificed after post-injection imaging and the spleens were examined. 1-3 mm tumors were present in all mice, although only the tumors in the mice that had received the core/shell nanoparticles were detected using MRI in vivo.

References

- [1] M. L. H. Green, L. Pratt, G. Wilkinson, *J. Chem. Soc.* 1960, 989.
- [2] N. Fauconnier, J. N. Pons, J. Roger, A. Bee, *J. Colloid Interface Sci.* 1997, *194*, 427.
- [3] T. R. Pisanic II, J. D. Blackwell, V. I. Shubayev, R. R. Finones, S. Jin, *Biomater.* 2007, *28*, 2572.
- [4] H. Zhao, K. Saatchi, U. O. Hafeli, *J. Magn. Magn. Mater.* 2009, *321*, 1356.

Complete reference

- [4a] Y.-w. Jun, Y.-M. Huh, J.-s. Choi, J.-H. Lee, H.-T. Song, S. Kim, S. Yoon, K.-S. Kim, J.-S. Shin, J.-S. Suh, J. Cheon, *J. Am. Chem. Soc.* 2005, *127*, 5732-5733.
- [4b] J.-H. Lee, Y.-M. Huh, Y.-w. Jun, J.-w. Seo, J.-t. Jang, H.-T. Song, S. Kim, E.-J. Cho, H.-G. Yoon, J.-S. Suh, J. Cheon, *Nat. Med.* 2007, *13*, 95-99.

Hot-injection synthesis of iron/iron oxide core/shell nanoparticles for T_2 contrast enhancement in magnetic resonance imaging†

David A. J. Herman,^a Peter Ferguson,^b Soshan Cheong,^{ac} Ian F. Hermans,^b Ben J. Ruck,^a Kathryn M. Allan,^a Sujay Prabakar,^a John L. Spencer,^a Conrad D. Lendrum^c and Richard D. Tilley^{*a}

Received 9th June 2011, Accepted 29th June 2011

DOI: 10.1039/c1cc13416g

Here we report a new, bench-top synthesis for iron/iron oxide core/shell nanoparticles *via* the thermal decomposition of $\text{Fe}(\eta^5\text{-C}_6\text{H}_3\text{Me}_4)_2$. The iron/iron oxide core/shell nanoparticles are superparamagnetic at room temperature and show improved negative contrast in T_2 -weighted MR imaging compared to pure iron oxides nanoparticles, and have a transverse relaxivity (r_2) of $332 \text{ mM}^{-1} \text{ s}^{-1}$.

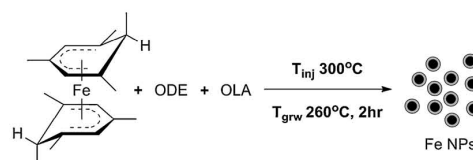
Magnetic nanoparticles are an attractive area of research due to their size dependent magnetism and biomedical applications, such as magnetic hyperthermia, bioseparation and magnetic resonance imaging (MRI) contrast agents.¹ For MRI contrast agents, superparamagnetic nanoparticles are desired, to prevent aggregation occurring in the body when the applied magnetic field is removed.² Currently, superparamagnetic iron oxide nanoparticles (SPIOs) are the only commercially available negative contrast agents^{2b} and are able to shorten T_2 relaxation times.^{3,4} Reports show that materials with larger magnetizations, can induce further shortening of T_2 relaxation times resulting in greater MRI contrast enhancement.⁵ Iron is ferromagnetic and has the highest saturation magnetization (218 emu g^{-1}) of the elements. Iron nanoparticles smaller than 15 nm are expected to be superparamagnetic.⁶ The magnetic properties when coupled with the biocompatibility, make iron based nanoparticles ideal candidates for MRI contrast agents.^{6,7} Development in this area remains challenging due to difficulty in obtaining stable iron nanoparticles from simple synthetic procedures and precursors.^{7,8}

Under ambient conditions, iron nanoparticles smaller than 8 nm in size fully oxidize upon exposure to air.⁹ Larger iron nanoparticles upon exposure to air form a 2–3 nm iron oxide shell on the surface, yielding iron/iron oxide core/shell nanoparticles.

Successful studies for the synthesis of iron nanoparticles of sizes greater than 8 nm has been achieved *via* the decomposition of iron pentacarbonyl, $\text{Fe}(\text{CO})_5$.^{8,10} Other precursors such as iron oleate and iron bis(trimethylsilyl)amide have been used to achieve the formation of iron nanocubes.¹¹ However, the ease of nanoparticle synthesis and scalability is limited with these processes; $\text{Fe}(\text{CO})_5$ is volatile and highly toxic,⁷ other precursors are either air-sensitive,^{11b} or require high temperature for decomposition.^{11a} Recently, we have reported the synthesis of iron/iron oxide core/shell nanoparticles *via* the decomposition of an iron organometallic sandwich compound, $\text{Fe}(\text{C}_5\text{H}_5)(\text{C}_6\text{H}_7)$, in a closed reaction vessel, under a hydrogen atmosphere.¹²

Here we report the bench-top synthesis of superparamagnetic iron/iron oxide core/shell nanoparticles *via* the thermal decomposition of a new, easy to handle, symmetrical iron organometallic sandwich compound, bis(η^5 -1,3,5-*exo*-6-tetramethylcyclohexadienyl) iron(II), $[\text{Fe}(\eta^5\text{-C}_6\text{H}_3\text{Me}_4)_2]$. This non-carbonyl iron precursor was chosen for its simple synthesis,¹³ and is air stable compared to $\text{Fe}(\text{CO})_5$. In comparison to the precursor previously reported by our group, this compound has a symmetrical structure and is found to decompose more rapidly, producing iron nanoparticles with a relatively short reaction time.

The Fe precursor was synthesized according to literature methods,¹³ and the precursor structure and iron nanoparticle synthesis are outlined in Scheme 1. Briefly, $\text{Fe}(\eta^5\text{-C}_6\text{H}_3\text{Me}_4)_2$ is thermally decomposed *via* instant hot injection at 300 °C in octadecene (ODE) with the presence of oleylamine (OLA) as a stabilizing agent. Upon injection, the temperature immediately dropped to 260 °C, and the reaction was maintained at this temperature for 2 h, before cooling to room temperature.



Scheme 1 Structure of iron precursor bis(η^5 -1,3,5-*exo*-6-tetramethylcyclohexadienyl) iron(II), $[\text{Fe}(\eta^5\text{-C}_6\text{H}_3\text{Me}_4)_2]$, and iron/iron oxide core/shell nanoparticle synthesis reaction scheme.

^a School of Chemical and Physical Sciences and The MacDiarmid Institute of Advanced Materials and Nanotechnology, Victoria University of Wellington, P.O. Box 600, Wellington, New Zealand. E-mail: richard.tilley@vuw.ac.nz

^b Malaghan Institute of Medical Research, P.O. Box 7060, Wellington, New Zealand

^c Industrial Research Limited, P.O. Box 31-310, Lower Hutt, New Zealand

† Electronic supplementary information (ESI) available: Materials and methods for nanoparticle synthesis and supporting TEM images, size-distributions and relaxivity data. See DOI: 10.1039/c1cc13416g

Once cooled, the nanoparticles were then isolated from the reaction mixture *via* magnetic separation and washed twice with toluene to remove excess OLA. The purification was done under ambient conditions and the exposure to air at this point leads to the surface oxidation forming iron/iron oxide core/shell nanoparticles. To render the nanoparticles water soluble, the stabilizing agent (OLA) was exchanged with dimercaptosuccinic acid (DMSA). DMSA was chosen due to ease of exchange with OLA due to the strong binding carboxylic acid groups,¹⁴ and its excellent safety profile.¹⁵ The DMSA-coated nanoparticles were readily dispersed in water and the core/shell structures were re-examined six months later by TEM and were found to be identical and the core/shell morphology maintained (Fig. S1).

A typical low magnification transmission electron microscopy (TEM) image of the nanoparticles obtained is shown in Fig. 1A. The nanoparticles are relatively monodisperse, with an average size of 14.0 ± 1.9 nm and with an average core size of 8.5 ± 2.5 nm and a shell with width of 2.9 ± 1.2 nm (calculated from 1000 nanoparticles, Fig. S2) obtained by

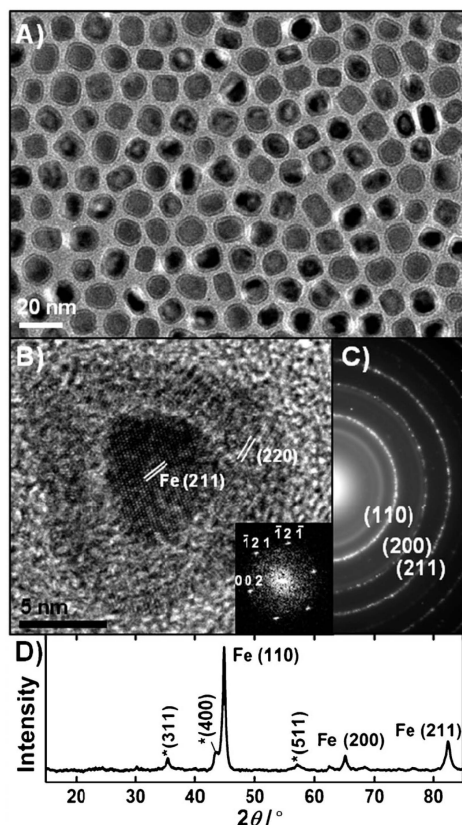


Fig. 1 (A) Low magnification TEM image of iron/iron oxide core/shell nanoparticles. (B) HRTEM showing single crystal α -Fe core with (211) planes observed across core area, and a polycrystalline iron oxide shell with (220) planes observed in sections of shell (inset) corresponding indexed FFT of the α -Fe core viewed down [2,1,0] zone axis. (C) SAED of iron/iron oxide core/shell nanoparticles. (D) XRD pattern of the iron/iron oxide core/shell nanoparticles, with diffraction peaks indexed to α -Fe and spinel iron oxide phase (*).

analysis of TEM images. The contrast of the nanoparticles show a darker core surrounded by a lighter shell that reveals a core/shell structure. High-resolution TEM (HRTEM) shows uniform lattice fringes across the entire core with spacings that correspond to α -Fe{211} indicating a single crystal α -Fe core (Fig. 1B). The nanoparticle shell is polycrystalline with multiple domains with various sections corresponding to the {220} planes of iron oxide. The selected area electron diffraction (SAED) of the nanoparticles in Fig. 1A is shown in Fig. 1C and the most intense rings can be indexed to the (110), (200) and (211) reflections of *bcc* α -Fe. An X-ray diffraction pattern of the nanoparticles is shown in Fig. 1D and can be readily indexed to α -Fe and iron oxide peaks (*) corresponding to either magnetite (Fe_3O_4) or maghemite (γ - Fe_2O_3). The average crystallite size of the α -Fe core calculated using the Scherrer equation from the peak width of Fe(110) and Fe(211) is estimated to be 8.7 ± 1.6 nm. This value is consistent with TEM images. The XRD pattern shows broader iron oxide peaks compared to the α -Fe peaks indicating a smaller average crystallite size compared to α -Fe, and is consistent with a polycrystalline shell layer.

Magnetic measurements were carried out on the core/shell nanoparticles at 300 K (Fig. 2). The magnetization curve intercepts at the origin, indicating an absence of both a remnant magnetization (M_R) and coercivity (H_C) showing that nanoparticles have superparamagnetic behaviour (inset Fig. 2).⁶ The saturated magnetization of 148 emu g^{-1} (Fe) is consistent with previously reported magnetization values for iron/iron oxide core/shell nanoparticles of similar size.¹⁶ The presence of an α -Fe core in the sample induces a higher magnetization compared to pure iron oxide nanoparticles that typically have magnetization values ranging from 40 – 70 emu g^{-1} (Fe).^{2b,17}

To assess effectiveness of the core/shell nanoparticles at enhancing T_2 -weighted MR signal the contrast was compared to iron oxides nanoparticles. The iron oxide nanoparticles of similar size (15 ± 2 nm) were synthesized according to literature¹⁸ and coated with DMSA. Both nanoparticles were independently dispersed in agar at varying concentrations of iron (in $\mu\text{g}(\text{Fe}) \text{ mL}^{-1}$). The core/shell nanoparticles showed an improved negative contrast (darkening) compared to the oxide nanoparticles (Fig. 3A) at iron concentrations of 2.0 to $10.0 \mu\text{g}(\text{Fe}) \text{ mL}^{-1}$. The core/shell nanoparticles also showed

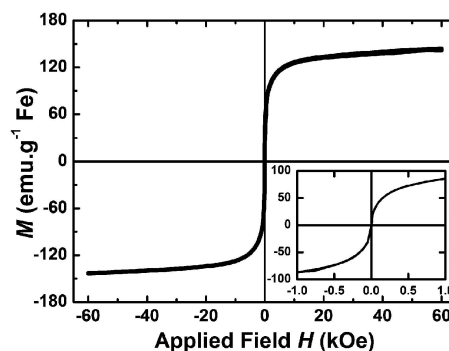


Fig. 2 Magnetization curve of iron/iron oxide core/shell nanoparticles at 300 K, with inset showing the low-field region.

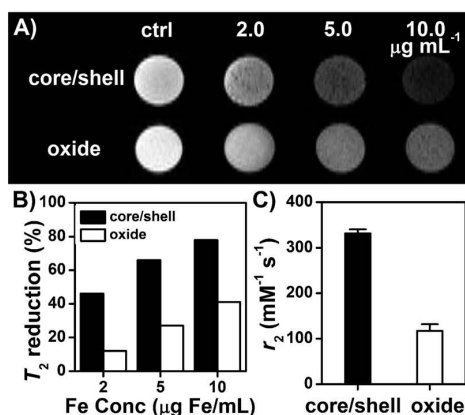


Fig. 3 (A) T_2 -weighted MR images at 9.4 T comparing the T_2 contrast (darkening) from core/shell and oxide nanoparticles in agar with concentration of 0.0 (control), 2.0, 5.0 and 10.0 $\mu\text{g(Fe)} \text{ mL}^{-1}$. (B) Bar graph comparing the % reduction of T_2 signal relative to that of control caused by core/shell and oxide nanoparticles. (C) Relaxivity (r_2) of the core/shell and oxide nanoparticles determined from the same sample.

greater percent in T_2 signal reduction (relative to that of the control) compared to that of the oxide. The core/shell nanoparticles reduced the T_2 -weighted signal by 46, 66 and 78% at 2.0, 5.0 and 10.0 $\mu\text{g(Fe)} \text{ mL}^{-1}$, respectively, compared to that of iron oxides, which reduced the T_2 -weighted signal by 12, 27 and 41%, respectively, at identical iron concentrations (Fig. 3B). The transverse relaxivity (r_2) of the iron/iron oxide core/shell nanoparticles was determined and compared with the r_2 of iron oxides (see Fig. S3, for plot of T_2 vs. $[\text{Fe}]$). The core/shell nanoparticles had an r_2 of $332 \text{ mM}^{-1} \text{ s}^{-1}$, nearly three-fold larger than that for iron oxide nanoparticles of $117 \text{ mM}^{-1} \text{ s}^{-1}$ (Fig. 3C). This is in agreement with the relaxivity of iron/iron oxide core/shell nanoparticles of similar size.¹² T_2 contrast enhancement of amorphous based iron core/shell nanoparticles relative to iron oxide nanoparticles have previously been reported, however little improvement in r_2 was observed.¹⁹ The large increase in r_2 shown by our iron/iron oxide core/shell nanoparticles indicates the importance of having a single-crystal α -Fe core present, and indicates a significant improvement of the MR signal that will enable greater detection at lower concentrations of iron compared to iron oxides.

Superparamagnetic iron/iron oxide core/shell nanoparticles were synthesized by a simple hot-injection method by decomposing an easy to handle iron organometallic precursor, $\text{Fe}(\eta^5\text{-C}_6\text{H}_5\text{Me}_4)_2$. Surface exchange with DMSA made the core/shell nanoparticles water soluble. The presence of a single-crystalline α -Fe core is shown to produce much greater negative contrast compared to pure iron oxide nanoparticles in T_2 -weighted MR imaging, and greatly improved the transverse relaxivity, which will contribute to further developments in magnetic resonance imaging and the next generation of contrast agents.

R.D.T, D.A.J.H, C.D.L and S.P. thank the Foundation of Research, Science and Technology (FRST) for funding through grants PROJ-13733-NMTS, CONT-20568-TTP, CONT-20707-NMTS-IRL and AMP for funding.

Notes and references

- (a) N. Tran and T. J. Webster, *J. Mater. Chem.*, 2010, **20**, 8760–8767; (b) R. Hao, R. Xing, Z. Xu, Y. Hou, S. Gao and S. Sun, *Adv. Mater.*, 2010, **22**, 2729–2742; (c) Q. A. Pankhurst, N. K. T. Thanh, S. K. Jones and J. Dobson, *J. Phys. D: Appl. Phys.*, 2009, **42**, 224001; (d) J.-s. Choi, H.-J. Choi, D.-C. Jung, J.-H. Lee and J. Cheon, *Chem. Commun.*, 2008, 2197–2199.
- (a) T. D. Schladt, K. Schneider, H. Schild and W. Tremel, *Dalton Trans.*, 2011; (b) H. B. Na, I. C. Song and T. Hyeon, *Adv. Mater.*, 2009, **21**, 2133–2148.
- H. B. Na, J. H. Lee, K. J. An, Y. I. Park, M. Park, I. S. Lee, D.-H. Nam, S. T. Kim, S.-H. Kim, S.-W. Kim, K.-H. Lim, K.-S. Kim, S.-O. Kim and T. Hyeon, *Angew. Chem., Int. Ed.*, 2007, **46**, 5397–5401.
- (a) E. Amstad, M. Textor and E. Reimhult, *Nanoscale*, 2011, DOI: 10.1039/c1nr10173k; (b) C.-C. Huang, K.-Y. Chuang, C.-P. Chou, M.-T. Wu, H.-S. Sheu, D.-B. Shieh, C.-Y. Tsai, C.-H. Su, H.-Y. Lei and C.-S. Yeh, *J. Mater. Chem.*, 2011, **21**, 7472–7479; (c) S. Laurent, D. Forge, M. Port, A. Roch, C. Robic, L. V. Elst and R. N. Müller, *Chem. Rev.*, 2008, **108**, 2064–2110.
- (a) J.-H. Lee, Y.-M. Huh, Y.-w. Jun, J.-w. Seo, J.-t. Jang, H.-T. Song, S. Kim, E.-J. Cho, H.-G. Yoon, J.-S. Suh and J. Cheon, *Nat. Med.*, 2007, **13**, 95–99; (b) Y.-w. Jun, Y.-M. Huh, J.-s. Choi, J.-H. Lee, H.-T. Song, KimKim, S. Yoon, K.-S. Kim, J.-S. Shin, J.-S. Suh and J. Cheon, *J. Am. Chem. Soc.*, 2005, **127**, 5732–5733.
- A.-H. Lu, E. L. Salabas and F. Schuth, *Angew. Chem., Int. Ed.*, 2007, **46**, 1222–1244.
- D. L. Huber, *Small*, 2005, **1**, 482–501.
- S. Peng, C. Wang, J. Xie and S. H. Sun, *J. Am. Chem. Soc.*, 2006, **128**, 10676–10677.
- C. M. Wang, D. R. Baer, L. E. Thomas, J. E. Amonette, J. Antony, Y. Qiang and G. Duscher, *J. Appl. Phys.*, 2005, **98**, 094308.
- (a) H. Lee, T.-J. Yoon and R. Weissleder, *Angew. Chem., Int. Ed.*, 2009, **48**, 5657–5660; (b) M. A. Willard, L. K. Kurihara, E. E. Carpenter, S. Calvin and V. G. Harris, *Int. Mater. Rev.*, 2004, **49**, 125–170.
- (a) A. Shavel, B. Rodriguez-Gonzalez, M. Spasova, M. Farle and L. M. Liz-Marzan, *Adv. Funct. Mater.*, 2007, **17**, 3870–3876; (b) F. Dumestre, B. Chaudret, C. Amiens, P. Renaud and P. Fejes, *Science*, 2004, **303**, 821–823; (c) L.-M. Lacroix, S. Lachaize, A. Falqui, M. Respaud and B. Chaudret, *J. Am. Chem. Soc.*, 2009, **131**, 549–557; (d) T. Hyeon, *Chem. Commun.*, 2003, 927–934.
- S. Cheong, P. Ferguson, K. W. Feindel, I. F. Hermans, P. T. Callaghan, C. Meyer, A. Slocombe, C.-H. Su, F.-Y. Cheng, C.-S. Yeh, B. Ingham, M. F. Toney and R. D. Tilley, *Angew. Chem., Int. Ed.*, 2011, **50**, 4206–4209.
- M. D. Clerk, M. J. Zaworotko, B. Borecka, T. S. Cameron, D. L. Hooper and A. Linden, *Can. J. Chem.*, 1990, **68**, 1923–1931.
- A. L. Miller, *Altern. Med. Rev.*, 1998, **3**, 199–207.
- J. J. Chisolm, *Clin. Toxicol.*, 2000, **38**, 365–375.
- (a) D. Farrell, S. A. Majetich and J. P. Wilcoxon, *J. Phys. Chem. B*, 2003, **107**, 11022–11030; (b) C. H. Griffiths, M. P. Ohoro and T. W. Smith, *J. Appl. Phys.*, 1979, **50**, 7108–7115.
- J. H. L. Beal, S. Prabakar, N. Gaston, G. B. Teh, P. G. Etchegoin, G. Williams and R. D. Tilley, *Chem. Mater.*, 2011, **23**, 2514–2517.
- T. R. Pisanic, J. D. Blackwell, V. I. Shubayev, R. R. Finones and S. Jin, *Biomaterials*, 2007, **28**, 2572–2581.
- C. G. Hadjipanayis, M. J. Bonder, S. Balakrishnan, X. Wang, H. Mao and G. C. Hadjipanayis, *Small*, 2008, **4**, 1925–1929.

Bibliography

- [1] T Erkinjuntti, L Ketonen, R Sulkava, J Sipponen, M Vuorialho, and M Iivanainen. Do white matter changes on mri and ct differentiate vascular dementia from alzheimer's disease? *J Neurol Neurosurg Psychiatr*, 50(1):37–42, Jan 1987.
- [2] C L Schultz, J R Haaga, B D Fletcher, R J Alfidi, and M A Schultz. Magnetic resonance imaging of the adrenal glands: a comparison with computed tomography. *AJR Am J Roentgenol*, 143(6):1235–40, Dec 1984.
- [3] Dushyant V Sahani, Sanjeeva P Kalva, Alan J Fischman, Rajagopal Kadavigere, Michael Blake, Peter F Hahn, and Sanjay Saini. Detection of liver metastases from adenocarcinoma of the colon and pancreas: comparison of mangafodipir trisodium-enhanced liver mri and whole-body fdg pet. *AJR Am J Roentgenol*, 185(1):239–46, Jul 2005.
- [4] Y Yamashita, J Machi, K Shirouzu, T Morotomi, H Isomoto, and T Kakegawa. Evaluation of endorectal ultrasound for the assessment of wall invasion of rectal cancer. report of a case. *Dis Colon Rectum*, 31(8):617–23, Aug 1988.
- [5] N J Emptage. Fluorescent imaging in living systems. *Curr Opin Pharmacol*, 1(5):521–5, Oct 2001.
- [6] Jae Hoon Shin, June-Key Chung, Joo Hyun Kang, Yong Jin Lee, Kwang Il Kim, Young So, Jae Min Jeong, Dong Soo Lee, and Myung Chul Lee. Noninvasive imaging for monitoring of viable cancer cells using a dual-imaging reporter gene. *J Nucl Med*, 45(12):2109–15, Dec 2004.
- [7] Paul T. Callaghan. *Principles of nuclear magnetic resonance microscopy*. Oxford University Press, 1991.
- [8] Kirk W Feindel. *Insights into the Performance of Proton-Exchange Membrane*

Fuel Cells Obtained from ^1H NMR Microscopy Experiments. PhD thesis, University of Alberta, 2006.

- [9] Malcolm H Levitt. *Spin dynamics: basics of nuclear magnetic resonance*. Springer, 2 edition, 2008.
- [10] S Stapf and Song-I Han. *Nuclear Magnetic Resonance Imaging in Chemical Engineering*. Wiley-VCH, 2006.
- [11] Dominik Weishaupt, Victor D. Köchli, and Borut Marinček. *How does MRI work?: an introduction to the physics and function of magnetic resonance imaging*. Springer, 2 edition, 2006.
- [12] R.K Harris, E.D Becker, S.M.C de Menezes, R Goodfellow, and P Granger. Nmr nomenclature. nuclear spin properties and conventions for chemical shifts:(iupac recommendations 2001). *Pure and applied chemistry*, 73(11):1795–1818, 2001.
- [13] Gustav K von Schulthess and Heinz-Peter W Schlemmer. A look ahead: Pet/mr versus pet/ct. *Eur J Nucl Med Mol I*, 36:3–9, 2009.
- [14] W.R Hendee and C.J Morgan. Magnetic resonance imaging part i—physical principles. *Western Journal of Medicine*, 141(4):491, 1984.
- [15] J Shen, D.C Shungu, and D.L Rothman. In vivo chemical shift imaging of gamma-aminobutyric acid in the human brain. *Magn. Reson. Med.*, 41(1):35–42, 1999.
- [16] D Le Bihan. Looking into the functional architecture of the brain with diffusion mri. *Nature Reviews Neuroscience*, 4(6):469–480, 2003.
- [17] Yaniv Assaf and Ofer Pasternak. Diffusion tensor imaging (dti)-based white matter mapping in brain research: a review. *J Mol Neurosci*, 34(1):51–61, 2008.
- [18] David D. Stark and William G. Bradley. *Magnetic resonance imaging, Volume 1*. C.V. Mosby, 1999.
- [19] Nikos K Logothetis. What we can do and what we cannot do with fmri. *Nature*, 453(7197):869–78, 2008.
- [20] P Caravan, J.J Ellison, T.J McMurry, and R.B Lauffer. Gadolinium (iii) chelates as mri contrast agents: structure, dynamics, and applications. *Chemical reviews*, 99(9):2293–2352, 1999.

- [21] HP Niendorf, J Haustein, I Cornelius, A Alhassan, and W Clauss. Safety of gadolinium dtpa: Extended clinical experience. *Magn. Reson. Med.*, 22(2):222–228, 1991.
- [22] D.R Broome. Nephrogenic systemic fibrosis associated with gadolinium based contrast agents: a summary of the medical literature reporting. *European Journal of Radiology*, 66(2):230–234, 2008.
- [23] M Rovaris and M Filippi. The role of magnetic resonance in the assessment of multiple sclerosis. *Journal of the Neurological Sciences*, 172:S3–S12, 2000.
- [24] AW Hsia and CS Kidwell. Developments in neuroimaging for acute ischemic stroke: Diagnostic and clinical trial applications. *Current atherosclerosis reports*, 10(4):339–46, 2008.
- [25] C Morgado and N Ruivo. Imaging meningo-encephalic tuberculosis. *European Journal of Radiology*, 55(2):188–192, 2005.
- [26] Silvio Aime, Zsolt Baranyai, Eliana Gianolio, and Enzo Terreno. *Molecular and Cellular MR Imaging*. Taylor and Francis, LLC, 2007.
- [27] R Agarwal, S.M Brunelli, K Williams, M.D Mitchell, H.I Feldman, and C.A Umscheid. Gadolinium-based contrast agents and nephrogenic systemic fibrosis: a systematic review and meta-analysis. *Nephrology Dialysis Transplantation*, 24(3):856, 2009.
- [28] D D Stark, R Weissleder, G Elizondo, P F Hahn, S Saini, L E Todd, J Wittenberg, and J T Ferrucci. Superparamagnetic iron oxide: clinical application as a contrast agent for mr imaging of the liver. *Radiology*, 168(2):297–301, 1988.
- [29] H.B Na, I.C Song, and T Hyeon. Inorganic nanoparticles for mri contrast agents. *Advanced Materials*, 21(21):2133–2148, 2009.
- [30] Claire Corot, Philippe Robert, Jean-Marc Idee, and Marc Port. Recent advances in iron oxide nanocrystal technology for medical imaging. *Adv. Drug Delivery Rev.*, 58(14):1471–1504, 2006.
- [31] S Weinstein, G Varallyay, E Dosa, S Gahramanov, B Hamilton, William D Rooney, L L Muldoon, and E A Neuwelt. Superparamagnetic iron oxide nanoparticles: diagnostic magnetic resonance imaging and potential therapeutic applications in neurooncology and central nervous system inflammatory

- pathologies, a review. *Journal of Cerebral Blood Flow and Metabolism*, 30(1):15–35, 2009.
- [32] A Roch, R.N Muller, and P Gillis. Theory of proton relaxation induced by superparamagnetic particles. *The Journal of chemical physics*, 110:5403, 1999.
 - [33] R.N Muller, P Gillis, F Moiny, and A Roch. Transverse relaxivity of particulate mri contrast media: from theories to experiments. *Magn. Reson. Med.*, 22(2):178–182, 1991.
 - [34] G Brix, LR Schad, and WJ Lorenz. Evaluation of proton density by magnetic resonance imaging: phantom experiments and analysis of multiple component proton transverse relaxation. *Physics in Medicine and Biology*, 35:53, 1990.
 - [35] J H Burdette, A D Elster, and P E Ricci. Acute cerebral infarction: quantification of spin-density and t2 shine-through phenomena on diffusion-weighted mr images. *Radiology*, 212(2):333–9, 1999.
 - [36] V L Stevenson, G J Parker, G J Barker, K Birnie, P S Tofts, D H Miller, and A J Thompson. Variations in t1 and t2 relaxation times of normal appearing white matter and lesions in multiple sclerosis. *Journal of the Neurological Sciences*, 178(2):81–7, 2000.
 - [37] E Tadamura, H Hatabu, W Li, P.V Prasad, and R.R Edelman. Effect of oxygen inhalation on relaxation times in various tissues. *Journal of Magnetic Resonance Imaging*, 7(1):220–225, 1997.
 - [38] Mukesh G Harisinghani, Jelle Barentsz, Peter F Hahn, Willem M Deserno, Shahin Tabatabaei, Christine Hulsbergen van de Kaa, Jean de la Rosette, and Ralph Weissleder. Noninvasive detection of clinically occult lymph-node metastases in prostate cancer. *N Engl J Med*, 348(25):2491–9, 2003.
 - [39] Dirk Baumjohann and Manfred Lutz. Non-invasive imaging of dendritic cell migration in vivo. *Immunobiology*, 211(6-8):587–597, 2006.
 - [40] Christoph Kleinschnitz, Martin Bendszus, Marco Frank, Laszlo Solymosi, Klaus V Toyka, and Guido Stoll. In vivo monitoring of macrophage infiltration in experimental ischemic brain lesions by magnetic resonance imaging. *Journal of Cerebral Blood Flow and Metabolism*, 23(11):1356–61, 2003.
 - [41] Andreas Saleh, Dirk Wiedermann, Michael Schroeter, Cornelia Jonkmanns,

- Sebastian Jander, and Mathias Hoehn. Central nervous system inflammatory response after cerebral infarction as detected by magnetic resonance imaging. *NMR in Biomedicine*, 17(4):163–9, 2004.
- [42] Lars Johansson, Cecilia Johnsson, Eva Penno, Atle Björnerud, and Håkan Ahlström. Acute cardiac transplant rejection: detection and grading with mr imaging with a blood pool contrast agent—experimental study in the rat. *Radiology*, 225(1):97–103, 2002.
- [43] S Kanno, Y J Wu, P C Lee, S J Dodd, M Williams, B P Griffith, and C Ho. Macrophage accumulation associated with rat cardiac allograft rejection detected by magnetic resonance imaging with ultrasmall superparamagnetic iron oxide particles. *Circulation*, 104(8):934–8, 2001.
- [44] T.K Jain, M.K Reddy, M.A Morales, D.L Leslie-Pelecky, and V Labhasetwar. Biodistribution, clearance, and biocompatibility of iron oxide magnetic nanoparticles in rats. *Molecular Pharmaceutics*, 5(2):316–327, 2008.
- [45] A.K Gupta and M Gupta. Synthesis and surface engineering of iron oxide nanoparticles for biomedical applications. *Biomaterials*, 26(18):3995–4021, 2005.
- [46] A Villanueva, M Cañete, A.G Roca, M Calero, S Veintemillas-Verdaguer, C.J Serna, M.P Morales, and R Miranda. The influence of surface functionalization on the enhanced internalization of magnetic nanoparticles in cancer cells. *Nanotechnology*, 20:115103, 2009.
- [47] S.J Park, S Kim, S Lee, G Zheong, K Char, and T Hyeon. Synthesis and magnetic studies of uniform iron nanorods and nanospheres. *Journal of the American Chemical Society*, 122(35):8581–8582, 2000.
- [48] Jeff W. M Bulte and D Kraitchman. Iron oxide mr contrast agents for molecular and cellular imaging. *NMR Biomed*, 17(7):484–99, 2004.
- [49] J Lodhia, G Mandarano, NJ Ferris, P Eu, and SF Cowell. Development and use of iron oxide nanoparticles (part 1): Synthesis of iron oxide nanoparticles for mri. *Biomedical Imaging and Intervention Journal*, 6(2):e12, 2010.
- [50] J Idee, M Port, I Raynal, and M Schaefer. *Superparamagnetic nanoparticles of iron oxides for magnetic resonance imaging applications*. Wiley, 2007.
- [51] EMA. Withdrawal assessment report for sinerem. *European Medicines Agency*:

Pre-authorisation Evaluation of Medicines for Human Use,
EMA/CHMP/11527/2008:1–18, May 2008.

- [52] Claire Corot, Philippe Robert, Jean-Marc Idee, and Marc Port. Recent advances in iron oxide nanocrystal technology for medical imaging. *Adv. Drug Delivery Rev.*, 58(14):1471–1504, 2006.
- [53] Taku Nakagawa, Steve R Martinez, Yasufumi Goto, Kazuo Koyanagi, Minoru Kitago, Tatsushi Shingai, David A Elashoff, Xing Ye, Frederick R Singer, Armando E Giuliano, and Dave S B Hoon. Detection of circulating tumor cells in early-stage breast cancer metastasis to axillary lymph nodes. *Clin Cancer Res*, 13(14):4105–10, Jul 2007.
- [54] Paul M Johnson, Geoff A Porter, Rocco Ricciardi, and Nancy N Baxter. Increasing negative lymph node count is independently associated with improved long-term survival in stage iiib and iiic colon cancer. *J Clin Oncol*, 24(22):3570–5, Aug 2006.
- [55] B K Kroon, S Horenblas, A P Lont, P J Tanis, M P W Gallee, and O E Nieweg. Patients with penile carcinoma benefit from immediate resection of clinically occult lymph node metastases. *J Urol*, 173(3):816–9, Mar 2005.
- [56] Bernd Misselwitz. Mr contrast agents in lymph node imaging. *European Journal of Radiology*, 58(3):375–382, June 2006.
- [57] Liucheng Wu, Yunfei Cao, Cun Liao, Jiahao Huang, and Feng Gao. Diagnostic performance of uspio-enhanced mri for lymph-node metastases in different body regions: A meta-analysis. *European journal of radiology*, Jan 2010.
- [58] M Harisinghani, J Barentsz, P Hahn, and W Deserno. Noninvasive detection of clinically occult lymph-node metastases in prostate cancer. *New England Journal of Medicine*, Jan 2003.
- [59] M F Bellin, L Lebleu, and J B Meric. Evaluation of retroperitoneal and pelvic lymph node metastases with mri and mr lymphangiography. *Abdominal imaging*, 28(2):155–63, Jan 2003.
- [60] T Tallheden, U Nannmark, M Lorentzon, O Rakotonirainy, B Soussi, F Waagstein, A Jeppsson, E Sjögren-Jansson, A Lindahl, and E Omerovic. In

vivo mr imaging of magnetically labeled human embryonic stem cells. *Life Sci*, 79(10):999–1006, Aug 2006.

- [61] Walter J Rogers, Craig H Meyer, and Christopher M Kramer. Technology insight: in vivo cell tracking by use of mri. *Nat Clin Pract Cardiovasc Med*, 3(10):554–62, Oct 2006.
- [62] J W Bulte, T Douglas, B Witwer, S C Zhang, E Strable, B K Lewis, H Zywicke, B Miller, P van Gelderen, B M Moskowitz, I D Duncan, and J A Frank. Magnetodendrimers allow endosomal magnetic labeling and in vivo tracking of stem cells. *Nat Biotechnol*, 19(12):1141–7, Dec 2001.
- [63] Jun Chen, Zhen-Yu Jia, Zhan-Long Ma, Yuan-Yuan Wang, and Gao-Jun Teng. In vivo serial mr imaging of magnetically labeled endothelial progenitor cells homing to the endothelium injured artery in mice. *PLoS ONE*, 6(6):e20790, Jan 2011.
- [64] Anna Moore, Jan Grimm, Bingye Han, and Pere Santamaria. Tracking the recruitment of diabetogenic cd8+ t-cells to the pancreas in real time. *Diabetes*, 53(6):1459–66, Jun 2004.
- [65] T C Yeh, W Zhang, S T Ildstad, and C Ho. In vivo dynamic mri tracking of rat t-cells labeled with superparamagnetic iron-oxide particles. *Magn Reson Med*, 33(2):200–8, Feb 1995.
- [66] Zhen Su, Jens Dannull, Axel Heiser, Donna Yancey, Scott Pruitt, John Madden, Doris Coleman, Donna Niedzwiecki, Eli Gilboa, and Johannes Vieweg. Immunological and clinical responses in metastatic renal cancer patients vaccinated with tumor rna-transfected dendritic cells. *Cancer research*, 63(9):2127–33, May 2003.
- [67] B Thurner, I Haendle, C Röder, D Dieckmann, P Keikavoussi, H Jonuleit, A Bender, C Maczek, D Schreiner, P von den Driesch, E B Bröcker, R M Steinman, A Enk, E Kämpgen, and G Schuler. Vaccination with mage-3a1 peptide-pulsed mature, monocyte-derived dendritic cells expands specific cytotoxic t cells and induces regression of some metastases in advanced stage iv melanoma. *The Journal of Experimental Medicine*, 190(11):1669–78, 1999.
- [68] Robert A Seder, Patricia A Darrah, and Mario Roederer. T-cell quality in memory and protection: implications for vaccine design. *Nature Reviews Immunology*, 8(4):247–58, Apr 2008.

- [69] J Banchereau, F Briere, C Caux, J Davoust, S Lebecque, Y.J Liu, B Pulendran, and K Palucka. Immunobiology of dendritic cells. *Annual review of immunology*, 18(1):767–811, 2000.
- [70] H.L Tang and J.G Cyster. Chemokine up-regulation and activated t cell attraction by maturing dendritic cells. *Science*, 284(5415):819, 1999.
- [71] C Fayolle, E Deriaud, and C Leclerc. In vivo induction of cytotoxic t cell response by a free synthetic peptide requires cd4+ t cell help. *The Journal of Immunology*, 147(12):4069, 1991.
- [72] S Lederman, MJ Yellin, A Krichevsky, J Belko, JJ Lee, and L Chess. Identification of a novel surface protein on activated cd4+ t cells that induces contact-dependent b cell differentiation (help). *The Journal of Experimental Medicine*, 175(4):1091, 1992.
- [73] Jinfang Zhu and William E Paul. Peripheral cd4+ t-cell differentiation regulated by networks of cytokines and transcription factors. *Immunol Rev*, 238(1):247–62, Nov 2010.
- [74] KA Fleming, A McMichael, JA Morton, J Woods, and JO McGee. Distribution of hla class 1 antigens in normal human tissue and in mammary cancer. *Journal of Clinical Pathology*, 34(7):779, 1981.
- [75] Kathryn J Farrand, Nina Dickgreber, Patrizia Stoitzner, Franca Ronchese, Troels R Petersen, and Ian F Hermans. Langerin+ cd8alpha+ dendritic cells are critical for cross-priming and il-12 production in response to systemic antigens. *J Immunol*, 183(12):7732–42, 2009.
- [76] G.F Gao, Z Rao, and J.I Bell. Molecular coordination of [alpha][beta] t-cell receptors and coreceptors cd8 and cd4 in their recognition of peptide-mhc ligands. *Trends Immunol*, 23(8):408–413, 2002.
- [77] J J Mond and M E Schaefer. Control of b cell differentiation by t cells. *Surv Immunol Res*, 2(3):216–9, 1983.
- [78] D Samuel, F Denizot, M Suzan, B Rubin, and P Golstein. Control of t- and b-lymphocyte differentiation: preliminary characterization of lymphocyte promoter factor(s) made by fcs-induced t-cell line and clones. *Cellular immunology*, 71(1):139–47, 1982.

- [79] Nicole L Yonkers, Benigno Rodriguez, Kimberly A Milkovich, Robert Asaad, Michael M Lederman, Peter S Heeger, and Donald D Anthony. Tlr ligand-dependent activation of naive cd4 t cells by plasmacytoid dendritic cells is impaired in hepatitis c virus infection. *J Immunol*, 178(7):4436–44, 2007.
- [80] Marshall D Behrens, Wolfgang M Wagner, Christopher J Krco, Courtney L Erskine, Kimberly R Kalli, James Krempski, Ekram A Gad, Mary L Disis, and Keith L Knutson. The endogenous danger signal, crystalline uric acid, signals for enhanced antibody immunity. *Blood*, 111(3):1472–9, 2008.
- [81] Shinichiro Fuse, Weijun Zhang, and Edward J Usherwood. Control of memory cd8+ t cell differentiation by cd80/cd86-cd28 costimulation and restoration by il-2 during the recall response. *J Immunol*, 180(2):1148–57, 2008.
- [82] M C Rissoan, V Soumelis, N Kadowaki, G Grouard, F Briere, R de Waal Malefyt, and Y J Liu. Reciprocal control of t helper cell and dendritic cell differentiation. *Science*, 283(5405):1183–6, 1999.
- [83] Adam J Linley, Murrium Ahmad, and Robert C Rees. Tumour-associated antigens: considerations for their use in tumour immunotherapy. *Int J Hematol*, 93(3):263–73, 2011.
- [84] Weiping Shen, Kelly Stone, Alessandra Jales, David Leitenberg, and Stephan Ladisch. Inhibition of tlr activation and up-regulation of il-1r-associated kinase-m expression by exogenous gangliosides. *J Immunol*, 180(7):4425–32, 2008.
- [85] Trina J Stewart and Mark J Smyth. Improving cancer immunotherapy by targeting tumor-induced immune suppression. *Cancer Metastasis Rev*, 30(1):125–40, 2011.
- [86] R.S Goldszmid, J Idoyaga, A.I Bravo, R Steinman, J Mordoh, and R Wainstok. Dendritic cells charged with apoptotic tumor cells induce long-lived protective cd4+ and cd8+ t cell immunity against b16 melanoma. *The Journal of Immunology*, 171(11):5940, 2003.
- [87] Eli Gilboa. Dc-based cancer vaccines. *Journal of Clinical Investigation*, 117(5):1195–203, 2007.
- [88] K Palucka, H Ueno, and J Banchereau. Recent developments in cancer vaccines. *The Journal of Immunology*, 186(3):1325–1331, 2011.

- [89] Derry Ridgway. The first 1000 dendritic cell vaccinees. *Cancer Invest*, 21(6):873–86, 2003.
- [90] S.A Rosenberg, J.C Yang, and N.P Restifo. Cancer immunotherapy: moving beyond current vaccines. *Nature Medicine*, 10(9):909–915, 2004.
- [91] M Docherty and R Smith. The case for structuring the discussion of scientific papers. *Bmj*, 318(7193):1224, 1999.
- [92] J.W.M Bulte and D.L Kraitichman. Iron oxide mr contrast agents for molecular and cellular imaging. *NMR in Biomedicine*, 17(7):484–499, 2004.
- [93] Soshan Cheong, Peter Ferguson, Kirk W Feindel, Ian F Hermans, Paul T Callaghan, Claire Meyer, Angela Slocombe, Chia-Hao Su, Fong-Yu Cheng, Chen-Sheng Yeh, Bridget Ingham, Michael F Toney, and Richard D Tilley. Simple synthesis and functionalization of iron nanoparticles for magnetic resonance imaging. *Angew. Chem. Int. Ed.*, 2011.
- [94] M Green, L Pratt, and G Wilkinson. Spectroscopic studies of some organoiron complexes. *J. Chem. Soc.*, (Mar):989–997, 1960.
- [95] II Pisanic, R Thomas, J.D Blackwell, V.I Shubayev, R.R Finones, and S Jin. Nanotoxicity of iron oxide nanoparticle internalization in growing neurons. *Biomaterials*, 28(16):2572–2581, 2007.
- [96] N Fauconnier, J Pons, J Roger, and A Bee. Thiolation of maghemite nanoparticles by dimercaptosuccinic acid. *J. Colloid Interface Sci.*, 194(2):427–433, 1997.
- [97] M.B Lutz, N Kukutsch, and A.L.J Ogilvie. An advanced culture method for generating large quantities of highly pure dendritic cells from mouse bone marrow. *Journal of immunological methods*, 223(1):77–92, 1999.
- [98] A Lee, K.J Farrand, N Dickgreber, C.M Hayman, S Jurs, I.F Hermans, and G.F Painter. Novel synthesis of [alpha]-galactosyl-ceramides and confirmation of their powerful nkt cell agonist activity. *Carbohydrate research*, 341(17):2785–2798, 2006.
- [99] Ian Hermans, J Silk, J Yang, M Palmowski, U Gileadi, C McCarthy, M Salio, F Ronchese, and V Cerundolo. The vital assay: a versatile fluorometric technique for assessing ctl- and nkt-mediated cytotoxicity against multiple targets in vitro and in vivo. *J Immunol Methods*, 285(1):25–40, 2004.

- [100] Daniel L J Thorek and Andrew Tsourkas. Size, charge and concentration dependent uptake of iron oxide particles by non-phagocytic cells. *Biomaterials*, 29(26):3583–90, 2008.
- [101] Sheng Tong, Sijian Hou, Zhilan Zheng, Jun Zhou, and Gang Bao. Coating optimization of superparamagnetic iron oxide nanoparticles for high t2 relaxivity. *Nano Letters*, 10(11):4607–13, 2010.
- [102] I Abarkan, T Doussineau, and M Smiaili. Tailored macro/microstructural properties of colloidal silica nanoparticles via microemulsion preparation. *Polyhedron*, 25(8):1763–1770, 2006.
- [103] Sophie Laurent. Magnetic iron oxide nanoparticles: Synthesis, stabilization, vectorization, physicochemical characterizations, and biological applications. *Chemical Reviews*, 108:2064–2110, 2008.
- [104] S Calvin, MM Miller, R Goswami, S.F Cheng, SP Mulvaney, LJ Whitman, and VG Harris. Determination of crystallite size in a magnetic nanocomposite using extended x-ray absorption fine structure. *J. Appl. Phys.*, 94:778, 2003.
- [105] Soshan Cheong, Peter Ferguson, Kirk W Feindel, Ian F Hermans, Paul T Callaghan, Claire Meyer, Angela Slocombe, Chia-Hao Su, Fong-Yu Cheng, Chen-Sheng Yeh, Bridget Ingham, Michael F Toney, and Richard D Tilley. Simple synthesis and functionalization of iron nanoparticles for magnetic resonance imaging. *Angew. Chem. Int. Ed.*, 50(18):4206–4209, 2011.
- [106] S D Konda, M Aref, S Wang, M Brechbiel, and E C Wiener. Specific targeting of folate-dendrimer mri contrast agents to the high affinity folate receptor expressed in ovarian tumor xenografts. *Magnetic Resonance Materials in Physics, Biology and Medicine*, 12(2-3):104–13, 2001.
- [107] R M. Cornell and Udo Schwertmann. The iron oxides: structure, properties, reactions, occurrences, and uses. *Wiley-VCH*, 2:664, 2003.
- [108] Massimo Corradi and Antonio Mutti. Metal ions affecting the pulmonary and cardiovascular systems. *Met Ions Life Sci*, 8:81–105, 2011.
- [109] E A Malecki. Manganese toxicity is associated with mitochondrial dysfunction and dna fragmentation in rat primary striatal neurons. *Brain Res Bull*, 55(2):225–8, 2001.

- [110] RH Chewning and K Murphy. Gadolinium-based contrast media and the development of nephrogenic systemic fibrosis in patients with renal insufficiency. *Journal of Vascular and Interventional Radiology*, 18(3):331–333, 2007.
- [111] S Benderbous, C Corot, P Jacobs, and B Bonnemain. Superparamagnetic agents: physicochemical characteristics and preclinical imaging evaluation. *Acad Radiol*, 3 Suppl 2:S292–4, 1996.
- [112] D.L.J Thorek, A.K Chen, J Czupryna, and A Tsourkas. Superparamagnetic iron oxide nanoparticle probes for molecular imaging. *Annals of biomedical engineering*, 34(1):23–38, 2006.
- [113] Y Jun, Y Huh, J Choi, J Lee, H Song, and S Kim. Nanoscale size effect of magnetic nanocrystals and their utilization for cancer diagnosis via ... *J. Am. Chem. Soc*, 2005.
- [114] Jae-Hyun Lee, Yong-Min Huh, Young-wook Jun, Jung-wook Seo, Jung-tak Jang, Ho-Taek Song, Sungjun Kim, Eun-Jin Cho, Ho-Geun Yoon, Jin-Suck Suh, and Jinwoo Cheon. Artificially engineered magnetic nanoparticles for ultra-sensitive molecular imaging. *Nature Medicine*, 13(1):95–9, 2007.
- [115] D Huber. Synthesis, properties, and applications of iron nanoparticles. *Small*, 1(5):482–501, 2005.
- [116] S Peng, C Wang, J Xie, and S Sun. Synthesis and stabilization of monodisperse fe nanoparticles. *Journal of the American Chemical Society*, 128(33):10676–10677, 2006.
- [117] C.M Wang, D.R Baer, L.E Thomas, J.E Amonette, J Antony, Y Qiang, and G Duscher. Void formation during early stages of passivation: Initial oxidation of iron nanoparticles at room temperature. *Journal of applied physics*, 98:094308, 2005.
- [118] A Shavel, B Rodríguez-González, M Spasova, M Farle, and L.M LizÀMarzán. Synthesis and characterization of iron/iron oxide core/shell nanocubes. *Advanced Functional Materials*, 17(18):3870–3876, 2007.
- [119] Frédéric Dumestre, Bruno Chaudret, Catherine Amiens, Philippe Renaud, and Peter Fejes. Superlattices of iron nanocubes synthesized from $\text{Fe}[\text{N}(\text{SiMe}_3)_2]_2$. *Science*, 303(5659):821–3, 2004.

- [120] D Astruc. Organo-iron complexes of aromatic compounds. applications in synthesis. *Tetrahedron*, 39(24):4027–4095, 1983.
- [121] Ludwig Reimer and Helmut Kohl. *Transmission electron microscopy: physics of image formation*, volume 36 of *Springer Series in Optical Sciences*. Springer, 5 edition, 2008.
- [122] C Cao, L Tian, Q Liu, W Liu, G Chen, and Y Pan. Magnetic characterization of noninteracting, randomly oriented, nanometer-scale ferrimagnetic particles. *J. Geophys. Res*, 115, 2010.
- [123] M.F Toney, A.J Davenport, L.J Oblonsky, M.P Ryan, and C.M Vitus. Atomic structure of the passive oxide film formed on iron. *Physical review letters*, 79(21):4282–4285, 1997.
- [124] S Gangopadhyay, G Hadjipanayis, B Dale, C Sorensen, K Klabunde, V Papaefthymiou, and A Kostikas. Magnetic properties of ultrafine iron particles. *Phys Rev, B Condens Matter*, 45(17):9778–9787, 1992.
- [125] Song Zhang, Xiangjian Chen, Chunrong Gu, Yu Zhang, Jindan Xu, Zhiping Bian, Di Yang, and Ning Gu. The effect of iron oxide magnetic nanoparticles on smooth muscle cells. *Nanoscale Research Letters*, 4(1):70–77, 2009.
- [126] J Chisolm Jr. Safety and efficacy of meso-2, 3-dimercaptosuccinic acid (dmsa) in children with elevated blood lead concentrations. *Clinical Toxicology*, 38(4):365–75, 2000.
- [127] A L Miller. Dimercaptosuccinic acid (dmsa), a non-toxic, water-soluble treatment for heavy metal toxicity. *Altern Med Rev*, 3(3):199–207, 1998.
- [128] Caroline R A Valois, Juliana M Braz, Eloiza S Nunes, Marco A R Vinolo, Emilia C D Lima, Rui Curi, Wolfgang M Kuebler, and Ricardo B Azevedo. The effect of dmsa-functionalized magnetic nanoparticles on transendothelial migration of monocytes in the murine lung via a beta2 integrin-dependent pathway. *Biomaterials*, 31(2):366–74, 2010.
- [129] J.H Lee, Y Jun, S.I Yeon, J.S Shin, and J Cheon. Dual mode nanoparticle probes for high performance magnetic resonance and fluorescence imaging of neuroblastoma. *Angewandte Chemie*, 118(48):8340–8342, 2006.
- [130] E.N Taylor and T.J Webster. Multifunctional magnetic nanoparticles for

- orthopedic and biofilm infections. *International Journal of Nanotechnology*, 8(1):21–35, 2011.
- [131] K.L Chen, S.E Mylon, and M Elimelech. Aggregation kinetics of alginate-coated hematite nanoparticles in monovalent and divalent electrolytes. *Environmental science and technology*, 40(5):1516–1523, 2006.
 - [132] Z Chen, Y Zhang, S Zhang, J Xia, J Liu, K Xu, and N Gu. Preparation and characterization of water-soluble monodisperse magnetic iron oxide nanoparticles via surface double-exchange with dmsa. *Colloids and Surfaces, A: Physicochemical and Engineering Aspects*, 316(1-3):210–216, 2008.
 - [133] Peter Reimer and Thomas Balzer. Ferucarbotran (resovist): a new clinically approved res-specific contrast agent for contrast-enhanced mri of the liver: properties, clinical development, and applications. *European Radiology*, 13(6):1266–76, 2003.
 - [134] Chongmin Wang, Donald R Baer, James E Amonette, Mark H Engelhard, Jiji Antony, and You Qiang. Morphology and electronic structure of the oxide shell on the surface of iron nanoparticles. *Journal of the American Chemical Society*, 131(25):8824–32, 2009.
 - [135] Gerhard H Simon, Jan Bauer, Olaf Saborovski, Yanjun Fu, Claire Corot, Michael F Wendland, and Heike E Daldrup-Link. T1 and t2 relaxivity of intracellular and extracellular uspio at 1.5t and 3t clinical mr scanning. *European Radiology*, 16(3):738–45, 2006.
 - [136] A Cabot, V.F Puentes, E Shevchenko, Y Yin, L Balcells, M.A Marcus, S.M Hughes, and A.P Alivisatos. Vacancy coalescence during oxidation of iron nanoparticles. *Journal of the American Chemical Society*, 129(34):10358–10360, 2007.
 - [137] Y Qiang, J Antony, M.G Marino, and S Pendyala. Synthesis of core-shell nanoclusters with high magnetic moment for biomedical applications. *Magnetics, IEEE Transactions on*, 40(6):3538–3540, 2004.
 - [138] Y Qiang, J Antony, A Sharma, J Nutting, and D Sikes. Iron/iron oxide core-shell nanoclusters for biomedical applications. *Journal of Nanoparticle Research*, 2006.
 - [139] Tae-Jong Yoon, Hakho Lee, Huilin Shao, and Ralph Weissleder. Highly magnetic

core-shell nanoparticles with a unique magnetization mechanism. *Angew Chem Int Ed Engl*, 50(20):4663–6, 2011.

- [140] V.F Puntès, K.M Krishnan, and A.P Alivisatos. Colloidal nanocrystal shape and size control: the case of cobalt. *Science*, 291(5511):2115, 2001.
- [141] S Sun, CB Murray, D Weller, L Folks, and A Moser. Monodisperse fept nanoparticles and ferromagnetic fept nanocrystal superlattices. *Science*, 287(5460):1989, 2000.
- [142] F Grasset, N Labhsetwar, D Li, DC Park, N Saito, H Haneda, O Cador, T Roisnel, S Mornet, and E Duguet. Synthesis and magnetic characterization of zinc ferrite nanoparticles with different environments: Powder, colloidal solution, and zinc ferrite-silica core-shell nanoparticles. *Langmuir*, 18(21):8209–8216, 2002.
- [143] Elena V Shevchenko, Dmitri V Talapin, Andrey L Rogach, Andreas Kornowski, Markus Haase, and Horst Weller. Colloidal synthesis and self-assembly of copt(3) nanocrystals. *Journal of the American Chemical Society*, 124(38):11480–5, 2002.
- [144] J Park, K An, Y Hwang, J.G Park, H.J Noh, J.Y Kim, J.H Park, N.M Hwang, and T Hyeon. Ultra-large-scale syntheses of monodisperse nanocrystals. *Nature Materials*, 3(12):891–895, 2004.
- [145] Masanori Horie, Hiroko Fukui, Keiko Nishio, Shigehisa Endoh, Haruhisa Kato, Katsuhide Fujita, Arisa Miyauchi, Ayako Nakamura, Mototada Shichiri, Noriko Ishida, Shinichi Kinugasa, Yasuo Morimoto, Etsuo Niki, Yasukazu Yoshida, and Hitoshi Iwahashi. Evaluation of acute oxidative stress induced by nio nanoparticles in vivo and in vitro. *J Occup Health*, 53(2):64–74, 2011.
- [146] Omid Veisesh, Jonathan W Gunn, and Miqin Zhang. Design and fabrication of magnetic nanoparticles for targeted drug delivery and imaging. *Advanced drug delivery reviews*, 62(3):284–304, 2010.
- [147] Jeff W. M Bulte. In vivo mri cell tracking: Clinical studies. *American Journal of Roentgenology*, 193(2):314–325, 2009.
- [148] Eric Farrell, Piotr Wielopolski, Predrag Pavljasevic, Sandra van Tiel, Holger Jahr, Jan Verhaar, Harrie Weinans, Gabriel Krestin, Fergal J O’Brien, Gerjo van Osch, and Monique Bernsen. Effects of iron oxide incorporation for long term cell

tracking on msc differentiation in vitro and in vivo. *Biochemical and Biophysical Research Communications*, 369(4):1076–81, 2008.

- [149] Mikhal E Cohen, Naser Muja, Nina Fainstein, Jeff W. M Bulte, and Tamir Ben-Hur. Conserved fate and function of ferumoxides-labeled neural precursor cells in vitro and in vivo. *J Neurosci Res*, 88(5):936–944, 2010.
- [150] Annelies Crabbe, Caroline Vandeputte, Tom Dresselaers, Angel Ayuso Sacido, Jose Manuel Garcia Verdugo, Jeroen Eyckmans, Frank P Luyten, Koen Van Laere, Catherine M Verfaillie, and Uwe Himmelreich. Effects of mri contrast agents on the stem cell phenotype. *Cell Transplantation*, 19(8):919–936, 2010.
- [151] Fernando Callera and Cláudio M T P de Melo. Magnetic resonance tracking of magnetically labeled autologous bone marrow cd34+ cells transplanted into the spinal cord via lumbar puncture technique in patients with chronic spinal cord injury: Cd34+ cells’ migration into the injured site. *Stem Cells Dev*, 16(3):461–6, 2007.
- [152] C Toso, J-P Vallee, P Morel, F Ris, S Demuylder-Mischler, M Lepetit-Coiffe, N Marangon, F Saudek, A M James Shapiro, D Bosco, and T Berney. Clinical magnetic resonance imaging of pancreatic islet grafts after iron nanoparticle labeling. *Am J Transplant*, 8(3):701–6, 2008.
- [153] B.K Rutt and D.H Lee. The impact of field strength on image quality in mri. *Journal of Magnetic Resonance Imaging*, 6(1):57–62, 1996.
- [154] D Horák, M Babic, P Jendelová, V Herynek, M Trchová, K Likavcanová, M Kapcalová, M Hájek, and E Syková. Effect of different magnetic nanoparticle coatings on the efficiency of stem cell labeling. *Journal of Magnetism and Magnetic Materials*, 321(10):1539–1547, 2009.
- [155] Martina Rudelius Heike E Daldrup-Link, Robert A J Oostendorp, Marcus Settles, Guido Piontek, Stefan Metz, Hilkea Rosenbrock, Ulrich Keller, Ulrich Heinzmann, Ernst J Rummeny, Jürgen Schlegel, and Thomas M Link. Targeting of hematopoietic progenitor cells with mr contrast agents. *Radiology*, 228(3):760–7, 2003.
- [156] Gerrit Fleige, Florian Seeberger, Daniela Laux, Mayk Kresse, Matthias Taupitz, Herbert Pilgrim, and Claus Zimmer. In vitro characterization of two different

- ultrasmall iron oxide particles for magnetic resonance cell tracking. *Investigative Radiology*, 37(9):482–8, 2002.
- [157] J W Bulte, P G Laughlin, E K Jordan, V A Tran, J Vymazal, and J A Frank. Tagging of t cells with superparamagnetic iron oxide: uptake kinetics and relaxometry. *Acad Radiol*, 3 Suppl 2:S301–3, 1996.
- [158] Hui Li Ma, Yu Feng Xu, Xian Rong Qi, Yoshie Maitani, and Tsuneji Nagai. Superparamagnetic iron oxide nanoparticles stabilized by alginate: pharmacokinetics, tissue distribution, and applications in detecting liver cancers. *Int J Pharm*, 354(1-2):217–26, 2008.
- [159] R Handgretinger, P Lang, M Schumm, G Taylor, S Neu, E Koscielnak, D Niethammer, and T Klingebiel. Isolation and transplantation of autologous peripheral cd34+ progenitor cells highly purified by magnetic-activated cell sorting. *Bone Marrow Transplant*, 21(10):987–93, 1998.
- [160] G.J Doherty and H.T McMahon. Mechanisms of endocytosis. *Annual review of biochemistry*, 78:857–902, 2009.
- [161] U Schoepf, EM Marecos, RJ Melder, RK Jain, and R Weissleder. Intracellular magnetic labeling of lymphocytes for in vivo trafficking studies. *Biotechniques*, 24(4):642, 1998.
- [162] Stephan Metz, Gabriel Bonaterra, Martina Rudelius, Marcus Settles, Ernst J Rummeny, and Heike E Daldrup-Link. Capacity of human monocytes to phagocytose approved iron oxide mr contrast agents in vitro. *European Radiology*, 14(10):1851–8, 2004.
- [163] S Anastase, D Letourneur, and J Jozefonvicz. Affinity chromatography of human anti-dextran antibodies. isolation of two distinct populations. *J Chromatogr B, Biomed Appl*, 686(2):141–50, 1996.
- [164] LX Tiefenauer, A Tschirky, G Kuhne, and RY Andres. In vivo evaluation of magnetite nanoparticles for use as a tumor contrast agent in mri. *Magn Reson Imaging*, 14(4):391–402, 1996.
- [165] Yijen L Wu, Qing Ye, Lesley M Foley, T Kevin Hitchens, Kazuya Sato, John B Williams, and Chien Ho. In situ labeling of immune cells with iron oxide particles:

an approach to detect organ rejection by cellular mri. *Proc Natl Acad Sci USA*, 103(6):1852–7, 2006.

- [166] Isabelle Raynal, Philippe Prigent, Sophie Peyramaure, Abderrahim Najid, Cecile Rebuzzi, and Claire Corot. Macrophage endocytosis of superparamagnetic iron oxide nanoparticles: mechanisms and comparison of ferumoxides and ferumoxtran-10. *Invest Radiol*, 39(1):56–63, 2004.
- [167] Stephan Metz, Stefanie Lohr, Marcus Settles, Ambros Beer, Klaus Woertler, Ernst J Rummeny, and Heike E Daldrup-Link. Ferumoxtran-10-enhanced mr imaging of the bone marrow before and after conditioning therapy in patients with non-hodgkin lymphomas. *European Radiology*, 16(3):598–607, 2006.
- [168] Z.M Qian, H Li, H Sun, and K Ho. Targeted drug delivery via the transferrin receptor-mediated endocytosis pathway. *Pharmacological reviews*, 54(4):561, 2002.
- [169] A.K Gupta and A.S.G Curtis. Lactoferrin and ceruloplasmin derivatized superparamagnetic iron oxide nanoparticles for targeting cell surface receptors. *Biomaterials*, 25(15):3029–3040, 2004.
- [170] C Sun, R Sze, and M.Q. Zhang. Folic acid-peg conjugated superparamagnetic nanoparticles for targeted cellular uptake and detection by mri. *Journal of Biomedical Materials Research Part A*, (78A):550–557, 2006.
- [171] Costas G Hadjipanayis, Revaz Machaidze, Milota Kaluzova, Liya Wang, Albert J Schuette, Hongwei Chen, Xinying Wu, and Hui Mao. Egrfviii antibody-conjugated iron oxide nanoparticles for magnetic resonance imaging-guided convection-enhanced delivery and targeted therapy of glioblastoma. *Cancer Res*, 70(15):6303–12, Aug 2010.
- [172] Chunfu Zhang, Manfred Jugold, Eva C Woenne, Twan Lammers, Bernd Morgenstern, Margareta M Mueller, Hanswalter Zentgraf, Michael Bock, Michael Eisenhut, Wolfhard Semmler, and Fabian Kiessling. Specific targeting of tumor angiogenesis by rgd-conjugated ultrasmall superparamagnetic iron oxide particles using a clinical 1.5-t magnetic resonance scanner. *Cancer Res*, 67(4):1555–62, 2007.
- [173] Christopher M Long, Hanneke W M Van Laarhoven, Jeff W. M Bulte, and Hyam I Levitsky. Magnetovaccination as a novel method to assess and quantify

- dendritic cell tumor antigen capture and delivery to lymph nodes. *Cancer Research*, 69(7):3180–7, 2009.
- [174] A Moore, E Marecos, A Bogdanov, and R Weissleder. Tumoral distribution of long-circulating dextran-coated iron oxide nanoparticles in a rodent model. *Radiology*, 214(2):568, 2000.
- [175] P Ros, P Freeny, S Harms, S Seltzer, P Davis, T Chan, A Stillman, L Muroff, V Runge, and M Nissenbaum. Hepatic mr imaging with ferumoxides: a multicenter clinical trial of the safety and efficacy in the detection of focal hepatic lesions. *Radiology*, 196(2):481–8, 1995.
- [176] J Schnorr, M Taupitz, S Wagner, H Pilgrimm, J Hansel, and B Hamm. Age-related blood half-life of particulate contrast material: experimental results with a uspio in rats. *J Magn Reson Imaging*, 12(5):740–4, 2000.
- [177] *Feridex injectable solution insert revision 08*. Bayer Healthcare Pharmaceuticals, Wayne, NJ 07470, May 2007.
- [178] C Corot, KG Petry, R Trivedi, A Saleh, C Jonkmanns, JF Le Bas, E Blezer, M Rausch, B Brochet, P Foster-Gareau, D Baleriaux, S Gaillard, and V Dousset. Macrophage imaging in central nervous system and in carotid atherosclerotic plaque using ultrasmall superparamagnetic iron oxide in magnetic resonance imaging. *Investigative Radiology*, 39(10):619–25, 2004.
- [179] Bao-An Chen, Nan Jin, Jun Wang, Jiahua Ding, Chong Gao, Jian Cheng, Guohua Xia, Feng Gao, Yin Zhou, Yue Chen, Guina Zhou, Xiaomao Li, Yu Zhang, Men Tang, and Xuemei Wang. The effect of magnetic nanoparticles of Fe_3O_4 on immune function in normal icr mice. *Int J Nanomedicine*, 5:593–9, 2010.
- [180] Jae-Hyun Lee, Yong-Min Huh, Young wook Jun, Jung wook Seo, Jung tak Jang, Ho-Taek Song, Sungjun Kim, Eun-Jin Cho, Ho-Geun Yoon, Jin-Suck Suh, and Jinwoo Cheon. Artificially engineered magnetic nanoparticles for ultra-sensitive molecular imaging. *Nature Medicine*, 13(1):95–9, 2007.
- [181] David Schrama, Ralph A. Reisfeld, and Jürgen C. Becker. Antibody targeted drugs as cancer therapeutics. *Nature Reviews Drug Discovery*, 5:147–157, 2006.
- [182] Fran Balkwill and Alberto Mantovani. Inflammation and cancer: back to virchow? *The Lancet*, (357):539–45, 2001.

- [183] Hiroya Hashizume, Peter Baluk, Shunichi Morikawa, John W. McLean, Gavin Thurston, Sylvie Roberge, Rakesh K. Jain, and Donald M. McDonald. Openings between defective endothelial cells explain tumor vessel leakiness. *Am J Pathol*, 156(4):1363–1380, 2000.
- [184] J Freyer. Role of necrosis in regulating the growth saturation of multicellular spheroids. *Cancer Res*, (48):2432–2439., 1988.
- [185] Van Beers B, A Roche, D Mathieu, Y Menu, M Delos, JB Otte, L Lalonde, and J Pringot. Epithelioid hemangioendothelioma of the liver: Mr and ct findings. *J Comput Assist Tomogr.*, 16(3):420–4, 1992.
- [186] Daly JM Outwater E, Tomaszewski JE and Kressel HY. Hepatic colorectal metastases: correlation of mr imaging and pathologic appearance. *Radiology*, 180(2):327–32, 1991.
- [187] I Fidler J Price, S Naito. Growth in an organ microenvironment as a selective process in metastasis. *Clinical and Experimental Metastasis*, 6(1):91–92, 1988.
- [188] Stefania Bellone, Michela Palmieri, Murat Gokden, Jabbar Joshua, Juan J. Roman, Sergio Pecorelli, Martin J. Cannon, and Alessandro D. Santin. Selection of her-2/neu-positive tumor cells in early stage cervical cancer: implications for herceptin-mediated therapy. *Gynecologic Oncology*, (91):231–240, 2003.
- [189] Costas G Hadjipanayis, Revaz Machaidze, Milota Kaluzova, Liya Wang, Albert J Schuette, Hongwei Chen, Xinying Wu, and Hui Mao. Egrfviii antibody-conjugated iron oxide nanoparticles for magnetic resonance imaging-guided convection-enhanced delivery and targeted therapy of glioblastoma. *Cancer Res*, 70(15):6303–12, 2010.
- [190] Matthias Kloor, Christina Becker, Axel Benner, Stefan M Woerner, Johannes Gebert, Soldano Ferrone, and Magnus von Knebel Doeberitz. Immunoselective pressure and human leukocyte antigen class i antigen machinery defects in microsatellite unstable colorectal cancers. *Cancer research*, 65(14):6418–24, Jul 2005.
- [191] Liucheng Wu, Yunfei Cao, Cun Liao, Jiahao Huang, and Feng Gao. Diagnostic performance of uspio-enhanced mri for lymph-node metastases in different body regions: A meta-analysis. *European journal of radiology*, 2010.

- [192] MW Van den Brekel, J.A Castelijns, and G.B Snow. The size of lymph nodes in the neck on sonograms as a radiologic criterion for metastasis: how reliable is it? *American journal of neuroradiology*, 19(4):695, 1998.
- [193] M Guichard, A Courdi, B Fertil, and E P Malaise. Radiosensitivity of lymph node metastases versus initial subcutaneous tumors in nude mice. *Radiat Res*, 78(2):278–85, 1979.
- [194] Yoshikazu Sado, Satoko Inoue, Yasuko Tomono, and Hiroyuki Omori. Lymphocytes from enlarged iliac lymph nodes as fusion partners for the production of monoclonal antibodies after a single tail base immunization attempt. *Acta Histochem. Cytochem.*, 39(3):89–94, 2006.
- [195] R.P Bucy, R.D Hockett, C.A Derdeyn, M.S Saag, K Squires, M Sillers, R.T Mitsuyasu, and J.M Kilby. Initial increase in blood cd4 lymphocytes after hiv antiretroviral therapy reflects redistribution from lymphoid tissues. *J Clin Invest*, 103(10):1391, 1999.
- [196] Leslie E W LaConte, Nitin Nitin, Omar Zurkiya, Daniela Caruntu, Charles J O'Connor, Xiaoping Hu, and Gang Bao. Coating thickness of magnetic iron oxide nanoparticles affects r2 relaxivity. *J Magn Reson Imaging*, 26(6):1634–41, 2007.
- [197] Matthias Nahrendorf, Farouc A. Jaffer, Kimberly A. Kelly, David E. Sosnovik, Elena Aikawa, Peter Libby, and Ralph Weissleder. Noninvasive vascular cell adhesion molecule-1 imaging identifies inflammatory activation of cells in atherosclerosis. *Circulation*, 11:1504–1511, 2006.
- [198] Hui-Li Ma, Xian-Rong Qi, Wu-Xiao Ding, Yoshie Maitani, and Tsuneji Nagai. Magnetic targeting after femoral artery administration and biocompatibility assessment of superparamagnetic iron oxide nanoparticles. *Journal of biomedical materials research Part A*, 84(3):598–606, 2008.
- [199] Nohyun Lee, Hyongsu Kim, Seung Hong Choi, Mihyun Park, Dokyoon Kim, Hyo-Cheol Kim, Yoonseok Choi, Shunmei Lin, Byung Hyo Kim, Hye Seung Jung, Hyeonjin Kim, Kyong Soo Park, Woo Kyung Moon, and Taeghwan Hyeon. Magnetosome-like ferrimagnetic iron oxide nanocubes for highly sensitive mri of single cells and transplanted pancreatic islets. *Proceedings of the National Academy of Sciences*, 108(7):2662–7, 2011.

- [200] D Hanahan and R A Weinberg. The hallmarks of cancer. *Cell*, 100(1):57–70, Jan 2000.
- [201] Douglas Hanahan and Robert A Weinberg. Hallmarks of cancer: The next generation. *Cell*, 144(5):646–674, Mar 2011.
- [202] Eric A Engels, Robert J Biggar, H Irene Hall, Helene Cross, Allison Crutchfield, Jack L Finch, Rebecca Grigg, Tara Hylton, Karen S Pawlish, Timothy S McNeel, and James J Goedert. Cancer risk in people infected with human immunodeficiency virus in the united states. *Int J Cancer*, 123(1):187–94, Jul 2008.
- [203] R Kim, M Emi, and K Tanabe. Cancer immunoediting from immune surveillance to immune escape. (7). *Immunology*, 121(7):1–14., 200.
- [204] MWL Teng, JB Swann, CM Koebel, RD Schreiber, and MJ Smyth. Immune-mediated dormancy: an equilibrium with cancer. *J. Leukoc. Biol.*, 84(988-993), 200.
- [205] M Smyth, GP Dunn, and R.D. RD Schreiber. Cancer immunosurveillance and immunoediting: the roles of immunity in suppressing tumor development and shaping tumor immunogenicity. *Adv. Immunol.*, (90):1–50, 2006.
- [206] Trina J Stewart and Mark J Smyth. Improving cancer immunotherapy by targeting tumor-induced immune suppression. *Cancer Metastasis Rev*, 30(1):125–140, Mar 2011.
- [207] Thomas Boehm. Design principles of adaptive immune systems. *Nature Publishing Group*, 11(5):307–317, Apr 2011.
- [208] Sarah L Clarke, Gareth J Betts, Andrea Plant, Kate L Wright, Tariq M El-Shanawany, Richard Harrop, Jared Torkington, Brian I Rees, Geraint T Williams, Awen M Gallimore, and Andrew J Godkin. Cd4+cd25+foxp3+ regulatory t cells suppress anti-tumor immune responses in patients with colorectal cancer. *PLoS ONE*, 1:e129, Jan 2006.
- [209] Jens Ruter, Brian G Barnett, Ilona Kryczek, Michael J Brumlik, Benjamin J Daniel, George Coukos, Weiping Zou, and Tyler J Curiel. Altering regulatory t cell function in cancer immunotherapy: a novel means to boost the efficacy of cancer vaccines. *Front Biosci*, 14:1761–70, Jan 2009.

- [210] C. Diaz-Montero, Mohamed Salem, Michael Nishimura, Elizabeth Garrett-Mayer, David Cole, and Alberto Montero. Increased circulating myeloid-derived suppressor cells correlate with clinical cancer stage, metastatic tumor burden, and doxorubicin–cyclophosphamide chemotherapy. *Cancer Immunology, Immunotherapy*, 58:49–59, 2009. 10.1007/s00262-008-0523-4.
- [211] Antonio Sica and Vincenzo Bronte. Altered macrophage differentiation and immune dysfunction in tumor development. *The Journal of Clinical Investigation*, 117(5):1155–1166, 5 2007.
- [212] Paola Allavena, Antonio Sica, Cecilia Garlanda, and Alberto Mantovani. The yin-yang of tumor-associated macrophages in neoplastic progression and immune surveillance. *Immunological Reviews*, 222(1):155–161, 2008.
- [213] Kevin W. Moore, Rene de Waal Malefyt, Robert L. Coffman, and Anne O’Garra. Interleukin-10 and the interleukin-10 receptor. *Annual Review of Immunology*, 19(1):683–765, 2001.
- [214] Carmela De Santo, Paolo Serafini, Ilaria Marigo, Luigi Dolcetti, Manlio Bolla, Piero Del Soldato, Cecilia Melani, Cristiana Guiducci, Mario P Colombo, Manuela Iezzi, Piero Musiani, Paola Zanovello, and Vincenzo Bronte. Nitroaspirin corrects immune dysfunction in tumor-bearing hosts and promotes tumor eradication by cancer vaccination. *Proc Natl Acad Sci USA*, 102(11):4185–90, Mar 2005.
- [215] Julie Vincent, Grégoire Mignot, Fanny Chalmin, Sylvain Ladoire, Mélanie Bruchard, Angélique Chevriaux, François Martin, Lionel Apetoh, Cédric Rébé, and François Ghiringhelli. 5-fluorouracil selectively kills tumor-associated myeloid-derived suppressor cells resulting in enhanced t cell-dependent antitumor immunity. *Cancer research*, 70(8):3052–61, Apr 2010.
- [216] Ronald H. Schwartz. T cell anergy. *Annual Review of Immunology*, 21(1):305–334, 2003.
- [217] P Romero, J Cerottini, and D Speiser. Monitoring tumor antigen specific t-cell responses in cancer patients and phase i clinical trials of peptide-based vaccination. *Cancer Immunology*, 53(3):249–255, 2004.
- [218] T.M Clay, A.C Hobeika, P.J Mosca, H.K Lysterly, and M.A Morse. Assays for monitoring cellular immune responses to active immunotherapy of cancer. *Clinical Cancer Research*, 7(5):1127, 2001.

- [219] A Müllbacher. The long-term maintenance of cytotoxic t cell memory does not require persistence of antigen. *The Journal of Experimental Medicine*, 179(1):317, 1994.
- [220] M J Pittet, D Valmori, P R Dunbar, D E Speiser, D Liénard, F Lejeune, K Fleischhauer, V Cerundolo, J C Cerottini, and P Romero. High frequencies of naive melan-a/mart-1-specific cd8(+) t cells in a large proportion of human histocompatibility leukocyte antigen (hla)-a2 individuals. *The Journal of Experimental Medicine*, 190(5):705–15, Sep 1999.
- [221] CL Slingluff, GV Yamshchikov, KT Hogan, SC Hibbitts, GR Petroni, EA Bissonette, JW Patterson, PY Neese, WW Grosh, and KA Chianese-Bullock. Evaluation of the sentinel immunized node for immune monitoring of cancer vaccines. *Annals of surgical oncology*, 15(12):3538–3549, 2008.
- [222] D.S Ritchie, I.F Hermans, J.M Lumsden, C.B Scanga, J.M Roberts, J Yang, R.A Kemp, and F Ronchese. Dendritic cell elimination as an assay of cytotoxic t lymphocyte activity in vivo. *Journal of immunological methods*, 246(1-2):109–117, 2000.
- [223] Amy E Anderson, David J Swan, Bethan L Sayers, Rachel A Harry, Angela M Patterson, Alexei von Delwig, John H Robinson, John D Isaacs, and Catharien M. U Hilkens. Lps activation is required for migratory activity and antigen presentation by tolerogenic dendritic cells. *J Leukocyte Biol*, 85(2):243–250, 2009.
- [224] J Banchereau and A.K Palucka. Dendritic cells as therapeutic vaccines against cancer. *Nature Reviews Immunology*, 5(4):296–306, 2005.
- [225] S Oehen and K Brduscha-Riem. Differentiation of naive ctl to effector and memory ctl: correlation of effector function with phenotype and cell division. *J Immunol*, 161(10):5338–46, Nov 1998.
- [226] W Barchet, S Oehen, P Klenerman, D Wodarz, G Bocharov, A L Lloyd, M A Nowak, H Hengartner, R M Zinkernagel, and S Ehl. Direct quantitation of rapid elimination of viral antigen-positive lymphocytes by antiviral cd8(+) t cells in vivo. *Eur J Immunol*, 30(5):1356–63, May 2000.
- [227] A Molano, H Erdjument-Bromage, D.H Fremont, I Messaoudi, P Tempst, and J Nikolic-Zugic. Peptide selection by an mhc h-2kb class i molecule devoid of the central anchor (" c") pocket. *The Journal of Immunology*, 160(6):2815, 1998.

- [228] J Yang, S.P Huck, R.S McHugh, I.F Hermans, and F Ronchese. Perforin-dependent elimination of dendritic cells regulates the expansion of antigen-specific cd8+ t cells in vivo. *Proceedings of the National Academy of Sciences of the United States of America*, 103(1):147, 2006.
- [229] I.F Hermans, D.S Ritchie, J Yang, J.M Roberts, and F Ronchese. Cd8+ t cell-dependent elimination of dendritic cells in vivo limits the induction of antitumor immunity. *The Journal of Immunology*, 164(6):3095, 2000.
- [230] B Ludewig, W.V Bonilla, T Dumrese, B Odermatt, R.M Zinkernagel, and H Hengartner. Perforin-independent regulation of dendritic cell homeostasis by cd8+ t cells in vivo: implications for adaptive immunotherapy. *Eur J Immunol*, 31(6):1772–1779, 2001.
- [231] M Smyth. Granzymes: exogenous proteases that induce target cell apoptosis. *Immunology today*, 16(4):202–206, 1995.
- [232] J.A Heibein, I.S Goping, M Barry, M.J Pinkoski, G.C Shore, D.R Green, and R.C Bleackley. Granzyme b-mediated cytochrome c release is regulated by the bcl-2 family members bid and bax. *The Journal of Experimental Medicine*, 192(10):1391, 2000.
- [233] V.R Sutton, J.E Davis, M Cancilla, R.W Johnstone, A.A Ruefli, K Sedelies, K.A Browne, and J.A Trapani. Initiation of apoptosis by granzyme b requires direct cleavage of bid, but not direct granzyme b-mediated caspase activation. *The Journal of Experimental Medicine*, 192(10):1403, 2000.
- [234] V.R Sutton, M.E Wolk, M Cancilla, and J.A Trapani. Caspase activation by granzyme b is indirect, and caspase autoprocessing requires the release of proapoptotic mitochondrial factors. *Immunity*, 18(3):319–329, 2003.
- [235] D Huang, M Hahne, M Schroeter, K Frei, A Fontana, A Villunger, K Newton, J Tschopp, and A Strasser. Activation of fas by fasl induces apoptosis by a mechanism that cannot be blocked by bcl-2 or bcl-xl. *Proceedings of the National Academy of Sciences of the United States of America*, 96(26):14871, 1999.
- [236] P.B Watchmaker, J.A Urban, E Berk, Y Nakamura, R.B Mailliard, S.C Watkins, S.M van Ham, and P Kalinski. Memory cd8+ t cells protect dendritic cells from ctl killing. *The Journal of Immunology*, 180(6):3857, 2008.

- [237] D Ashany, A Savir, N Bhardwaj, and K.B Elkon. Dendritic cells are resistant to apoptosis through the fas (cd95/apo-1) pathway. *The Journal of Immunology*, 163(10):5303, 1999.
- [238] V.P Badovinac, S.E Hamilton, and J.T Harty. Viral infection results in massive cd8+ t cell expansion and mortality in vaccinated perforin-deficient mice. *Immunity*, 18(4):463–474, 2003.
- [239] K Kogawa, S.M Lee, J Villanueva, D Marmer, J Sumegi, and A.H Filipovich. Perforin expression in cytotoxic lymphocytes from patients with hemophagocytic lymphohistiocytosis and their family members. *Blood*, 99(1):61, 2002.
- [240] J Wang, L Zheng, A Lobito, F.K.M Chan, J Dale, M Sneller, X Yao, J.M Puck, S.E Straus, and M.J Lenardo. Inherited human caspase 10 mutations underlie defective lymphocyte and dendritic cell apoptosis in autoimmune lymphoproliferative syndrome type ii. *Cell*, 98(1):47–58, 1999.
- [241] S.N Mueller, C.M Jones, A.T Stock, M Suter, W.R Heath, and F.R Carbone. Cd4+ t cells can protect apc from ctl-mediated elimination. *The Journal of Immunology*, 176(12):7379, 2006.
- [242] Kate A Andrew, Helen M A Simkins, Sabine Witzel, Rachel Perret, Jenny Hudson, Ian F Hermans, David S Ritchie, Jianping Yang, and Franca Ronchese. Dendritic cells treated with lipopolysaccharide up-regulate serine protease inhibitor 6 and remain sensitive to killing by cytotoxic t lymphocytes in vivo. *J Immunol*, 181(12):8356–62, 2008.
- [243] S.R Scheffer, H Nave, F Korangy, K Schlote, R Pabst, E.M Jaffee, M.P Manns, and T.F Greten. Apoptotic, but not necrotic, tumor cell vaccines induce a potent immune response in vivo. *International journal of cancer*, 103(2):205–211, 2003.
- [244] F.O Nestle, A Farkas, and C Conrad. Dendritic-cell-based therapeutic vaccination against cancer. *Current opinion in immunology*, 17(2):163–169, 2005.
- [245] J.C Sun and M.J Bevan. Defective cd8 t cell memory following acute infection without cd4 t cell help. *Science*, 300(5617):339, 2003.
- [246] K Palucka and J Banchereau. Dendritic cells: a link between innate and adaptive immunity. *Journal of clinical immunology*, 19(1):12–25, 1999.
- [247] Ruggero Ridolfi, Angela Riccobon, Riccardo Galassi, Gianluigi Giorgetti,

- Massimiliano Petrini, Laura Fiammenghi, Monica Stefanelli, Laura Ridolfi, Andrea Moretti, Giuseppe Migliori, and Giuseppe Fiorentini. Evaluation of in vivo labelled dendritic cell migration in cancer patients. *J Transl Med*, 2(1):27, 2004.
- [248] H Miles Prince, Dominic M Wall, David Ritchie, Dirk Honemann, Simon Harrison, Hang Quach, Mick Thompson, Rodney Hicks, Eddie Lau, Jill Davison, Maureen Loudovaris, Jude Moloney, Bruce Loveland, Jacques Bartholeyns, Andrew Katsifis, and Linda Mileshekin. In vivo tracking of dendritic cells in patients with multiple myeloma. *J Immunother*, 31(2):166–79, 2008.
- [249] Michael D Cahalan and Ian Parker. Imaging the choreography of lymphocyte trafficking and the immune response. *Current opinion in immunology*, 18(4):476–82, 2006.
- [250] C.H Schimmelpfennig, S Schulz, C Arber, J Baker, I Tarner, J McBride, C.H Contag, and R.S Negrin. Ex vivo expanded dendritic cells home to t-cell zones of lymphoid organs and survive in vivo after allogeneic bone marrow transplantation. *American Journal of Pathology*, 167(5):1321, 2005.
- [251] Dirk Baumjohann, Andreas Hess, Lubos Budinsky, Kay Brune, Gerold Schuler, and Manfred B Lutz. In vivo magnetic resonance imaging of dendritic cell migration into the draining lymph nodes of mice. *Eur J Immunol*, 36(9):2544–2555, 2006.
- [252] I.J.M de Vries, W.J Lesterhuis, J.O Barentsz, P Verdijk, J.H van Krieken, O.C Boerman, W.J.G Oyen, J.J Bonenkamp, J.B Boezeman, and G.J Adema. Magnetic resonance tracking of dendritic cells in melanoma patients for monitoring of cellular therapy. *Nat Biotechnol*, 23(11):1407–1413, 2005.
- [253] E Ahrens, M Feili-Hariri, H Xu, G Genove, and P Morel. Receptor-mediated endocytosis of iron-oxide particles provides efficient labeling of dendritic cells for in vivo mr imaging. *Magn. Reson. Med.*, 49(6):1006–1013, 2003.
- [254] Gregory A Dekaban, Jonatan Snir, Bradly Shrum, Sonali de Chickera, Christy Willert, Mia Merrill, Elias A Said, Rafick-Pierre Sekaly, Paula J Foster, and Peta J O’Connell. Semiquantitation of mouse dendritic cell migration in vivo using cellular mri. *J Immunother*, 32(3):240–51, 2009.
- [255] Fauline Verdijk, Tom Scheenen, W Lesterhuis, Giulio Gambarota, Andor Veltien, Piotr Walczak, Nicole Scharenborg, Jeff W. M Bulte, Cornelis Punt, Arend

- Heerschap, Carl Figdor, and I Jolanda M de Vries. Sensitivity of magnetic resonance imaging of dendritic cells for in vivo tracking of cellular cancer vaccines. *Int. J. Cancer*, 120(5):978–984, 2007.
- [256] A Nencioni, F Grünebach, S.M Schmidt, M.R Müller, D Boy, F Patrone, A Ballestrero, and P Brossart. The use of dendritic cells in cancer immunotherapy. *Crit Rev Oncol Hematol*, 65(3):191–199, 2008.
- [257] Peter Hersey, Scott W Menzies, Gary M Halliday, Tam Nguyen, Margaret L Farrelly, Chitra DeSilva, and Margaret Lett. Phase i/ii study of treatment with dendritic cell vaccines in patients with disseminated melanoma. *Cancer Immunol Immunother*, 53(2):125–34, 2004.
- [258] Michelle A Neller, J. Alejandro Lopez, and Christopher W Schmidt. Antigens for cancer immunotherapy. *Seminars in Immunology*, 20(5):286–295, 2008.
- [259] K Shimizu, E.K Thomas, M Giedlin, and J.J Mulé. Enhancement of tumor lysate-and peptide-pulsed dendritic cell-based vaccines by the addition of foreign helper protein. *Cancer Res*, 61(6):2618, 2001.
- [260] D.J Shedlock and H Shen. Requirement for cd4 t cell help in generating functional cd8 t cell memory. *Science*, 300(5617):337, 2003.
- [261] H.T Khong and N.P Restifo. Natural selection of tumor variants in the generation of "tumor escape" phenotypes. *Nature immunology*, 3(11):999–1005, 2002.
- [262] T.J de Vries, A Fourkour, T Wobbles, G Verkroost, D.J Ruiter, and G.N.P van Muijen. Heterogeneous expression of immunotherapy candidate proteins gp100, mart-1, and tyrosinase in human melanoma cell lines and in human melanocytic lesions. *Cancer Res*, 57(15):3223, 1997.
- [263] M Ahmad, R.C Rees, and S.A Ali. Escape from immunotherapy: possible mechanisms that influence tumor regression/progression. *Cancer Immunology, Immunotherapy*, 53(10):844–854, 2004.
- [264] F Berard, P Blanco, J Davoust, E.M Neidhart-Berard, M Nouri-Shirazi, N Taquet, D Rimoldi, J.C Cerottini, J Banchereau, and A.K Palucka. Cross-priming of naive cd8 t cells against melanoma antigens using dendritic cells loaded with killed allogeneic melanoma cells. *The Journal of Experimental Medicine*, 192(11):1535, 2000.

- [265] E.M Neidhardt-Berard, F Berard, J Banchereau, and A.K Palucka. Dendritic cells loaded with killed breast cancer cells induce differentiation of tumor-specific cytotoxic t lymphocytes. *Breast Cancer Res*, 6(4):R322–R328, 2004.
- [266] S.J Prasad, K.J Farrand, S.A Matthews, J.H Chang, R.S McHugh, and F Ronchese. Dendritic cells loaded with stressed tumor cells elicit long-lasting protective tumor immunity in mice depleted of cd4+ cd25+ regulatory t cells. *The Journal of Immunology*, 174(1):90, 2005.
- [267] CM Britten, S Janetzki, L Ben-Porat, TM Clay, M Kalos, H Maecker, K Odunsi, M Pride, L Old, and A Hoos. Harmonization guidelines for hla-peptide multimer assays derived from results of a large scale international proficiency panel of the cancer vaccine consortium. *Cancer Immunology, Immunotherapy*, 58(10):1701–1713, 2009.
- [268] J.S Yu, G Liu, H Ying, W.H Yong, K.L Black, and C.J Wheeler. Vaccination with tumor lysate-pulsed dendritic cells elicits antigen-specific, cytotoxic t-cells in patients with malignant glioma. *Cancer Res*, 64(14):4973, 2004.
- [269] M Salcedo, N Bercovici, R Taylor, P Vereecken, S Massicard, D Duriau, F Vernel-Pauillac, A Boyer, V Baron-Bodo, and E Mallard. Vaccination of melanoma patients using dendritic cells loaded with an allogeneic tumor cell lysate. *Cancer Immunology, Immunotherapy*, 55(7):819–829, 2006.
- [270] J Sprent, JF Miller, and GF Mitchell. Antigen-induced selective recruitment of circulating lymphocytes. *Cellular immunology*, 2(2):171, 1971.
- [271] U Hurtenbach, H Gleichmann, N Nagata, and E Gleichmann. Immunity to d-penicillamine: genetic, cellular, and chemical requirements for induction of popliteal lymph node enlargement in the mouse. *The Journal of Immunology*, 139(2):411, 1987.
- [272] S Man, E.E Ubogu, and R.M Ransohoff. Inflammatory cell migration into the central nervous system: a few new twists on an old tale. *Brain Pathology*, 17(2):243–250, 2007.
- [273] B Webster, E.H Ekland, L.M Agle, S Chyou, R Ruggieri, and T.T Lu. Regulation of lymph node vascular growth by dendritic cells. *The Journal of Experimental Medicine*, 203(8):1903, 2006.

- [274] David Masopust, Sang-Jun Ha, Vaiva Vezys, and Rafi Ahmed. Stimulation history dictates memory cd8 t cell phenotype: implications for prime-boost vaccination. *J Immunol*, 177(2):831–9, 2006.
- [275] V Kalia, S Sarkar, T.S Gourley, B.T Rouse, and R Ahmed. Differentiation of memory b and t cells. *Current opinion in immunology*, 18(3):255–264, 2006.
- [276] D Masopust, V Vezys, A.L Marzo, and L Lefrançois. Preferential localization of effector memory cells in nonlymphoid tissue. *Science*, 291(5512):2413, 2001.
- [277] F Sallusto, D Lenig, R Förster, M Lipp, and A Lanzavecchia. Two subsets of memory t lymphocytes with distinct homing potentials and effector functions. *Nature*, 402:34–38, 1999.
- [278] E.J Wherry, V Teichgräber, T.C Becker, D Masopust, S.M Kaech, R Antia, U.H von Andrian, and R Ahmed. Lineage relationship and protective immunity of memory cd8 t cell subsets. *Nature Immunology*, 4(3):225–234, 2003.
- [279] P R Walker, T Ohteki, J A Lopez, H R MacDonald, and J L Maryanski. Distinct phenotypes of antigen-selected cd8 t cells emerge at different stages of an in vivo immune response. *J Immunol*, 155(7):3443–52, Oct 1995.
- [280] C.S Hinrichs, Z.A Borman, L Cassard, L Gattinoni, R Spolski, Z Yu, L Sanchez-Perez, P Muranski, S.J Kern, and C Logun. Adoptively transferred effector cells derived from naive rather than central memory cd8+ t cells mediate superior antitumor immunity. *Proceedings of the National Academy of Sciences*, 106(41):17469, 2009.
- [281] J Hall and B Morris. The immediate effect of antigens on the cell output of a lymph node. *British journal of experimental pathology*, 46(4), 1965.
- [282] RN Cahill, H Frost, and Z Trnka. The effects of antigen on the migration of recirculating lymphocytes through single lymph nodes. *The Journal of Experimental Medicine*, 143(4):870, 1976.
- [283] WL Ford. Duration of the inductive effect of sheep erythrocytes on the recruitment of lymphocytes in the rat. *Immunology*, 15(4):609, 1968.
- [284] DA Rowley, JL Gowans, RC Atkins, WL Ford, and M.E Smith. The specific selection of recirculating lymphocytes by antigen in normal and preimmunized rats. *The Journal of Experimental Medicine*, 136(3):499, 1972.

- [285] S Stoll, J Delon, T.M Brotz, and R.N Germain. Dynamic imaging of t cell-dendritic cell interactions in lymph nodes. *Science*, 296(5574):1873, 2002.
- [286] C.R Mackay, W Marston, and L Dudler. Altered patterns of t cell migration through lymph nodes and skin following antigen challenge. *Eur J Immunol*, 22(9):2205–2210, 1992.
- [287] JG Hall, B Morris, G.D Moreno, and M.C Bessis. The ultrastructure and function of the cells in lymph following antigenic stimulation. *The Journal of Experimental Medicine*, 125(1):91, 1967.
- [288] J.B Hay and B.B Hobbs. The flow of blood to lymph nodes and its relation to lymphocyte traffic and the immune response. *The Journal of Experimental Medicine*, 145(1):31, 1977.
- [289] I McConnell and J Hopkins. Lymphocyte traffic through antigen-stimulated lymph nodes. i. complement activation within lymph nodes initiates cell shutdown. *Immunology*, 42(2):217, 1981.
- [290] J Hopkins, I McConnell, and JD Pearson. Lymphocyte traffic through antigen-stimulated lymph nodes. ii. role of prostaglandin e2 as a mediator of cell shutdown. *Immunology*, 42(2):225, 1981.
- [291] J.B Huppa, M Gleimer, C Sumen, and M.M Davis. Continuous t cell receptor signaling required for synapse maintenance and full effector potential. *Nature Immunology*, 4(8):749–755, 2003.
- [292] U H von Andrian. Intravital microscopy of the peripheral lymph node microcirculation in mice. *Microcirculation*, 3(3):287–300, 1996.
- [293] W Weninger, M.A Crowley, N Manjunath, and U.H Von Andrian. Migratory properties of naive, effector, and memory cd8+ t cells. *The Journal of Experimental Medicine*, 194(7):953, 2001.
- [294] M.D Cahalan and G.A Gutman. The sense of place in the immune system. *Nature Immunology*, 7(4):329–332, 2006.
- [295] U.H von Andrian and T.R Mempel. Homing and cellular traffic in lymph nodes. *Nature Reviews Immunology*, 3(11):867–878, 2003.
- [296] CN Arnold, EC Butcher, and DJ Campbell. Antigen-specific lymphocyte

sequestration in lymphoid organs: lack of essential roles for alpha 1 and alpha 4 integrin-dependent adhesion or g alpha i protein-coupled receptor signaling. *The Journal of Immunology*, 173(2):866, 2004.

- [297] S Mandala, R Hajdu, J Bergstrom, E Quackenbush, J Xie, J Milligan, R Thornton, G.J Shei, D Card, and C.A Keohane. Alteration of lymphocyte trafficking by sphingosine-1-phosphate receptor agonists. *Science*, 296(5566):346, 2002.
- [298] H Rosen and E.J Goetzl. Sphingosine 1-phosphate and its receptors: an autocrine and paracrine network. *Nature Reviews Immunology*, 5(7):560–570, 2005.
- [299] R Pappu, S.R Schwab, I Cornelissen, J.P Pereira, J.B Regard, Y Xu, E Camerer, Y.W Zheng, Y Huang, and J.G Cyster. Promotion of lymphocyte egress into blood and lymph by distinct sources of sphingosine-1-phosphate. *Science*, 316(5822):295, 2007.
- [300] S.H Wei, H Rosen, M.P Matheu, M.G Sanna, S.K Wang, E Jo, C.H Wong, I Parker, and M.D Cahalan. Sphingosine 1-phosphate type 1 receptor agonism inhibits transendothelial migration of medullary t cells to lymphatic sinuses. *Nature Immunology*, 6(12):1228–1235, 2005.
- [301] Z Moodie, L Price, C Gouttefangeas, A Mander, S Janetzki, M Löwer, M J P Welters, C Ottensmeier, S H van der Burg, and Cedrik M Britten. Response definition criteria for elispot assays revisited. *Cancer Immunol Immunother*, 59(10):1489–501, 2010.
- [302] Medsafe. Medsafe regulatory information - licensed medicine manufacturing sites, 2008.
- [303] I.J.M de Vries, M.R Bernsen, W.J Lesterhuis, N.M Scharenborg, S.P Strijk, M.J.P Gerritsen, D.J Ruiter, C.G Figdor, C.J.A Punt, and G.J Adema. Immunomonitoring tumor-specific t cells in delayed-type hypersensitivity skin biopsies after dendritic cell vaccination correlates with clinical outcome. *Journal of clinical oncology*, 23(24):5779, 2005.
- [304] CS Chin and HD Bear. Sentinel node mapping identifies vaccine-draining lymph nodes with tumor-specific immunological activity. *Annals of surgical oncology*, 9(1):94–103, 2002.

- [305] Stanley P L Leong, Eugene T Morita, Martin Südmeyer, Jeffrey Chang, David Shen, Theodore A Achtem, Robert E Allen, and Mohammed Kashani-Sabet. Heterogeneous patterns of lymphatic drainage to sentinel lymph nodes by primary melanoma from different anatomic sites. *Clin Nucl Med*, 30(3):150–8, 2005.
- [306] T.L Whiteside. Immune suppression in cancer: effects on immune cells, mechanisms and future therapeutic intervention. *Seminars in cancer biology*, 16(1):3–15, 2006.
- [307] C Carbonneil, H Saidi, V Donkova&Petrini, and L Weiss. Dendritic cells generated in the presence of interferon&± stimulate allogeneic cd4+ t&cell proliferation: modulation by autocrine il&10, enhanced t&cell apoptosis and t regulatory type 1 cells. *International immunology*, 16(7):1037, 2004.
- [308] H Jonuleit, E Schmitt, G Schuler, J Knop, and A.H Enk. Induction of interleukin 10-producing, nonproliferating cd4+ t cells with regulatory properties by repetitive stimulation with allogeneic immature human dendritic cells. *The Journal of Experimental Medicine*, 192(9):1213, 2000.
- [309] K Sato, N Yamashita, M Baba, and T Matsuyama. Modified myeloid dendritic cells act as regulatory dendritic cells to induce anergic and regulatory t cells. *Blood*, 101(9):3581, 2003.
- [310] JF Griffith, ACW Chan, AT Ahuja, SF Leung, LTC Chow, SCS Chung, and C Metreweli. Neck ultrasound in staging squamous oesophageal carcinoma—a high yield technique. *Clinical radiology*, 55(9):696–701, 2000.
- [311] J Dashe and DD McIntire. Maternal obesity limits the ultrasound evaluation of fetal anatomy. *Journal of Ultrasound in Medicine*, (28):1025–1030, 2009.
- [312] N Andreasen. Brain imaging: applications in psychiatry. *Science*, 239(4846):1381–1388, Jan 1988.
- [313] U S FDA. Approved gadolinium based contrast agents, June 2011.
- [314] R F J Browne, C Zwirewich, and W C Torreggiani. Imaging of urinary tract infection in the adult. *European Radiology*, 14 Suppl 3:E168–83, Mar 2004.
- [315] T Grobner. Gadolinium—a specific trigger for the development of nephrogenic fibrosing dermopathy and nephrogenic systemic fibrosis? *Nephrology Dialysis Transplantation*, 21(4):1104, 2006.

- [316] RH Chewning and K Murphy. Gadolinium-based contrast media and the development of nephrogenic systemic fibrosis in patients with renal insufficiency. *Journal of Vascular and Interventional Radiology*, 18(3):331–333, Jan 2007.
- [317] M Vorobiov, A Basok, D Tovbin, A Shnaider, L Katchko, and B Rogachev. Ironâemobilizing properties of the gadolinium–dtpa complex: clinical and experimental observations. *Nephrology Dialysis Transplantation*, 18(5):884, 2003.
- [318] J Mann. Stability of gadolinium complexes in vitro and in vivo. *Journal of computer assisted tomography*, 17(S1):S19–S23, Jan 1993.
- [319] C.D Wiginton, B Kelly, A Oto, M Jesse, P Aristimuno, R Ernst, and G Chaljub. Gadolinium-based contrast exposure, nephrogenic systemic fibrosis, and gadolinium detection in tissue. *American Journal of Roentgenology*, 190(4):1060, 2008.
- [320] Henrik S Thomsen and Peter Marckmann. Extracellular gd-ca: differences in prevalence of nsf. *European journal of radiology*, 66(2):180–3, May 2008.
- [321] H.S Thomsen. Gadolinium-based contrast media may be nephrotoxic even at approved doses. *European Radiology*, 14(9):1654–1656, 2004.
- [322] G Schieren, N Wirtz, P Altmeyer, L.C Rump, S.M Weiner, and A Kreuter. Nephrogenic systemic fibrosis-a rapidly progressive disabling disease with limited therapeutic options. *Journal of the American Academy of Dermatology*, 61(5):868–874, 2009.
- [323] S E Cowper. Nephrogenic fibrosing dermopathy [icnsfr website]. In <http://www.icnsfr.org>, 2011.
- [324] A Deo, M Fogel, and S. E Cowper. Nephrogenic systemic fibrosis: A population study examining the relationship of disease development to gadolinium exposure. *Clinical Journal of the American Society of Nephrology*, 2(2):264–267, Feb 2007.
- [325] D G Cameron, E H Bensley, P Wood, and V Grayston. Treatment of iron deficiency anaemia with saccharated iron oxide given by the intravenous route. *Can Med Assoc J*, (64):27–30, 1951.
- [326] G Stoll and M Bendszus. Imaging of inflammation in the peripheral and central nervous system by magnetic resonance imaging. *Neuroscience*, 158(3):1151–60, Feb 2009.

- [327] H.B Na, I.C Song, and T Hyeon. Inorganic nanoparticles for mri contrast agents. *Advanced Materials*, 21(21):2133–2148, 2009.
- [328] R Heesakkers, A Hovels, and G Jager. Mri with a lymph-node-specific contrast agent as an alternative to ct scan and lymph-node dissection in patients with prostate cancer: a prospective multicohort study. *The lancet oncology*, 9, Issue 9, Pages 850 - 856,(9):850–856, Jan 2008.
- [329] W. M Klerkx, L Bax, W. B Veldhuis, A. P. M Heintz, W. Pthm Mali, P. H. M Peeters, and K. G. M Moons. Detection of lymph node metastases by gadolinium-enhanced magnetic resonance imaging: Systematic review and meta-analysis. *JNCI Journal of the National Cancer Institute*, 102(4):244–253, Feb 2010.
- [330] Olivia Will, Sanjay Purkayastha, Christopher Chan, Thanos Athanasiou, Ara W Darzi, Wady Gedroyc, and Paris P Tekkis. Diagnostic precision of nanoparticle-enhanced mri for lymph-node metastases: a meta-analysis. *The lancet oncology*, 7(1):52–60, Jan 2006.
- [331] Samdeep K Mouli, Lee C Zhao, Reed A Omary, and C Shad Thaxton. Lymphotropic nanoparticle enhanced mri for the staging of genitourinary tumors. *Nature reviews Urology*, (7):84–93, Feb 2010.
- [332] Isaiah J Fidler. The pathogenesis of cancer metastasis: the 'seed and soil' hypothesis revisited. *Nature Reviews Cancer*, 3(6):453–8, Jun 2003.
- [333] H Degani, M Chetrit-Dadiani, L Boginora, and Edna Furman-Haran. Magnetic resonance imaging of tumor vasculature. *Thrombosis and Haemostasis*, 88(6):888–1067, Jan 2002.
- [334] L W Nunes, M D Schnall, E S Siegelman, C P Langlotz, S G Orel, D Sullivan, L A Muenz, C A Reynolds, and M H Torosian. Diagnostic performance characteristics of architectural features revealed by high spatial-resolution mr imaging of the breast. *AJR Am J Roentgenol*, 169(2):409–15, Aug 1997.
- [335] B Webster, E.H Ekland, L.M Agle, S Chyou, R Ruggieri, and T.T Lu. Regulation of lymph node vascular growth by dendritic cells. *The Journal of Experimental Medicine*, 203(8):1903, 2006.

- [336] A Krongrad. Laparoscopic radical prostatectomy. *Curr Urol Rep*, 1(1):36–40, May 2000.
- [337] A. Krongrad. The demise of combidex/sinerem. In <http://www.wellsphere.com/cancer-article/the-demise-of-combidex-160-sinerem/1058235>, 2010.
- [338] Enzo Terreno, Simonetta Geninatti Crich, Simona Belfiore, Luigi Biancone, Claudia Cabella, Giovanna Esposito, Andrea D Manazza, and Silvio Aime. Effect of the intracellular localization of a gd-based imaging probe on the relaxation enhancement of water protons. *Magn Reson Med*, 55(3):491–7, Mar 2006.
- [339] Siegfried Trattnig, Ahmed Ba-Ssalamah, Iris-Melanie Noebauer-Huhmann, Markus Barth, Stefan Wolfsberger, Katja Pinker, and Engelbert Knosp. Mr contrast agent at high-field mri (3 tesla). *Top Magn Reson Imaging*, 14(5):365–75, Oct 2003.
- [340] C Cabella, S Geninatti Crich, D Corpillo, A Barge, C Ghirelli, E Bruno, V Lorusso, F Uggeri, and S Aime. Cellular labeling with gd(iii) chelates: only high thermodynamic stabilities prevent the cells acting as ‘sponges’ of gd3+ ions. *Contrast Media & Molecular Imaging*, 1(1):23–9, Jan 2006.
- [341] Naser Muja and Jeff W. M Bulte. Magnetic resonance imaging of cells in experimental disease models. *Prog Nucl Mag Res Sp*, 55(1):61–77, Jan 2009.
- [342] Z Shi, K Neoh, and E Kang. Bifunctional eu3+ doped gd2o3 nanoparticles as a luminescent and t1 contrast agent for stem cell labeling. *Contrast Media & Molecular Imaging*, 5(2):105–111, Jan 2010.
- [343] Jeff W. M Bulte. In vivo mri cell tracking: Clinical studies. *American Journal of Roentgenology*, 193(2):314–325, Jan 2009.
- [344] B Rutt. Cell tracking and single cell imaging by mri. *IFMBE Proceedings*, 25(13):218–220, Jan 2009.
- [345] A Crabbe, C Vandeputte, T Dresselaers, A.A Sacido, J.M.G Verdugo, J Eyckmans, F.P Luyten, K Van Laere, C.M Verfaillie, and U Himmelreich. Effects of mri contrast agents on the stem cell phenotype. *Cell Transplantation*, 19(8):919–936, 2010.

- [346] Walter J Rogers, Craig H Meyer, and Christopher M Kramer. Technology insight: in vivo cell tracking by use of mri. *Nat Clin Pract Cardiovasc Med*, 3(10):554–562, Oct 2006.
- [347] L Kostura, D Kraitchman, and A Mackay. Feridex labeling of mesenchymal stem cells inhibits chondrogenesis but not adipogenesis or osteogenesis. *NMR in Biomedicine*, 17(7):513–517, Jan 2004.
- [348] A Lepore, P Walczak, M Rao, and I Fischer. Mr imaging of lineage-restricted neural precursors following transplantation into the adult spinal cord. *Experimental neurology*, 201(1):49–59, Jan 2006.
- [349] I Siglienti, M Bendszus, and C Kleinschnitz. Cytokine profile of iron-laden macrophages: implications for cellular magnetic resonance imaging. *Journal of Neuroimmunology*, 173(1):166–173, Jan 2006.
- [350] Alan Trounson. New perspectives in human stem cell therapeutic research. *BMC medicine*, 7:29, Jan 2009.
- [351] Cancer vaccine approval could open floodgates. *Nature Medicine*, 16(6):615, Jun 2010.
- [352] M W Wilson. Hepatocellularcarcinoma:regional therapy with a magnetic targeted carrier bound to doxorubicin in a dual mr imaging/conventional angiography suite—initial experience with four patients. *Radiology*, (230):287–93, 2004.
- [353] C S Brazel. Magnetothermally-responsive nanomaterials: combining magnetic nanostructures and thermally-sensitive polymers for triggered drug release. *Pharmaceutical Res.*, (26):644–56, 2009.
- [354] F Scherer. Magnetofection:enhancingand targeting gene delivery by magnetic force in vitro and in vivo. *Gene Ther.*, (9):102–9, 2002.
- [355] S Hughes, A J El Haj, and J Dobson. Magnetic micro- and nanoparticle mediated activation of mechanosensitive ion channels. *Med. Eng. Phys.*, (27):754–62, 2005.
- [356] N Wang and D E Ingber. Probing transmembrane mechanical coupling and cytomechanics using magnetic twisting cytometry. *Biochem. Cell Biol.*, (73):327–35, 1995.
- [357] Assaf A Gilad, Keren Ziv, Michael T McMahon, Peter C. M van Zijl, Michal

- Neeman, and Jeff W. M Bulte. Mri reporter genes. *Journal of Nuclear Medicine*, 49(12):1905–1908, Jan 2008.
- [358] S J De Nardo. Development of tumor targeting bioprobes (in-111-chimeric l6 monoclonal antibody nanoparticles) for alternating magnetic field cancer therapy. *Clin. Cancer Res.*, 11(11)(Suppl. 19):7087S–92S, 2005.
- [359] A Jordan, R Scholz, P Wust, and H Fähling. Magnetic fluid hyperthermia (mfh): Cancer treatment with ac magnetic field induced excitation of biocompatible superparamagnetic nanoparticles. *Journal of Magnetism and Magnetic Materials*, 201(1-3):413–419, 1999.
- [360] Thomas R McCauley, Matthew D Rifkin, and Cheryl A Ledet. Pelvic lymph node visualization with mr imaging using local administration of ultra-small superparamagnetic iron oxide contrast. *J Magn Reson Imaging*, 15(4):492–7, Apr 2002.
- [361] L L Muldoon, P Varallyay, D F Kraemer, G Kiwic, K Pinkston, S L Walker-Rosenfeld, and E A Neuwelt. Trafficking of superparamagnetic iron oxide particles (combidex) from brain to lymph nodes in the rat. *Neuropathol Appl Neurobiol*, 30(1):70–9, Feb 2004.
- [362] S Gandhi, M Brown, and J Wong. Mr contrast agents for liver imaging: What, when, how. *Radiographics*, 26(6):1621–1630, Jan 2006.
- [363] John Watt. *Communication with John Watt, Project manager of magnetic nanoparticle patent NZ573797 with VicLink, Victoria University of Wellington*, 2011.